University of Alberta

Three-Dimensional Discrete Element Modeling of Tunneling in Sand

By

ASM Masud Karim

A thesis submitted to the Faculty of Graduate Studies and Research in partial fulfillment
of the requirements for the degree of Doctor of Philosophy

In

Geotechnical Engineering

Department of Civil and Environmental Engineering

Edmonton, Alberta
Fall, 2007

Library and
Archives Canada

Published Heritage
Branch

395 Wellington Street
Ottawa ON K1A 0N4
Canada

Bibliothèque et
Archives Canada

Direction du
Patrimoine de l'édition

395, rue Wellington
Ottawa ON K1A 0N4
Canada

Your file Votre référence
ISBN: 978-0-494-32990-0
Our file Notre référence
ISBN: 978-0-494-32990-0

NOTICE:
The author has granted a non-exclusive license allowing Library and Archives Canada to reproduce, publish, archive, preserve, conserve, communicate to the public by telecommunication or on the Internet, loan, distribute and sell theses worldwide, for commercial or non-commercial purposes, in microform, paper, electronic and/or any other formats.

The author retains copyright ownership and moral rights in this thesis. Neither the thesis nor substantial extracts from it may be printed or otherwise reproduced without the author's permission.

AVIS:
L'auteur a accordé une licence non exclusive permettant à la Bibliothèque et Archives Canada de reproduire, publier, archiver, sauvegarder, conserver, transmettre au public par télécommunication ou par l'Internet, prêter, distribuer et vendre des thèses partout dans le monde, à des fins commerciales ou autres, sur support microforme, papier, électronique et/ou autres formats.

L'auteur conserve la propriété du droit d'auteur et des droits moraux qui protège cette thèse. Ni la thèse ni des extraits substantiels de celle-ci ne doivent être imprimés ou autrement reproduits sans son autorisation.

In compliance with the Canadian Privacy Act some supporting forms may have been removed from this thesis.

While these forms may be included in the document page count, their removal does not represent any loss of content from the thesis.

Conformément à la loi canadienne sur la protection de la vie privée, quelques formulaires secondaires ont été enlevés de cette thèse.

Bien que ces formulaires aient inclus dans la pagination, il n'y aura aucun contenu manquant.

Canada

ABSTRACT

This thesis uses three dimensional discrete element modeling (DEM) to examine: (1) laboratory triaxial tests on Ottawa sand; (2) centrifuge testing of a tunnel in Fontainebleau sand; and (3) surface settlement along a 6.5-m-diameter shallow tunnel in mixed face conditions where the upper layer was sand.

Laboratory triaxial tests on Ottawa sand were used to establish the micro-parameters, namely, particle elastic properties and contact friction, for the DEM used to simulate the centrifuge tests and the shallow tunnel. Assemblies of smooth spherical particles as well as 'clustered' particles at both dense and loose densities at different confining pressures were modeled. Both rigid single and segmental walls were used as lateral boundaries. It was found that while the size or scale effect can be minimized the particle shape influences the peak strength of the synthetic material. Perfectly spherical particles underestimated the peak strength. The volumetric response was found to be insensitive to either particle size or shape.

DEM, using smooth spherical particles, was used to simulate a centrifuge test of a shallow tunnel in sand. The collapse pressure and near face displacements from the DEM simulations were in close agreement with the results from the centrifuge test and analytical results.

Three-dimensional DEM was used to simulate surface settlement of a recently constructed 6.5-m-diameter tunnel excavated within the City of Edmonton. The tunnel was excavated by earth pressure balanced shield tunnel boring machine and traversed in both uniform and mixed face condition. The findings from the numerical modeling suggest that the geology of the

mixed-face tunneling conditions was likely the controlling factor in reducing the surface settlements.

DEDICATION

I am dedicating this thesis to my elder son, ASM Safwan Karim, who was diagnosed with Mitochondrial Disorder during the third year of this research.

To Safwan, who is my strength

ACKNOWLDGEMENTS

I want to express my sincere and grateful thanks to my supervisors, Prof. Derek Martin and Dr. Richard Brachman for their guidance and support during the period of this research. I am grateful for their exceptional patience, encouragement, and exceptional research inspiring thoughts. Their directions, advice and expertise were instrumental in accomplishing this research.

I would also like to acknowledge and thank my examiners, especially Profs. Richard Bathurst and Dwayne Tannant for their invaluable suggestions and comments. Appreciation is extended to all my teachers and other staff at the University of Alberta.

I am deeply indebted to my family, especially to my wife, Mehetaj, for her love, patience, support, and continued encouragement during the period of this research.

TABLE OF CONTENTS

ABSTRACT

CHAPTER 1 INTRODUCTION PAGE

1.1 **PROBLEM STATEMENT** 1

1.2 **SCOPE OF RESEARCH** 2

1.3 **DISCRETE OR DISTINCT ELEMENT METHOD** 3

1.4 **OUTLINE OF THESIS** 3

CHAPTER 2 TUNNELING IN SAND

2.1 **DIFFICULTIES IN TUNNELING IN SAND** 6

2.2 **SOFT GROUND TUNNELING: DESIGN CONSIDERATIONS**

- 2.2.1 Tunneling methods in sand 7
- 2.2.2 Drained stability 8
- 2.2.3 Ground deformation: fundamentals 11
- 2.2.4 Ground deformation: modeling and prediction
  - 2.2.4.1 Analytical solutions 12
  - 2.2.4.2 Numerical solution by finite element analyses 14
  - 2.2.4.3 Physical modeling 16
- 2.2.5 Discontinuum modeling 17

CHAPTER 3 MICROMECHANICAL APPROACH LEADING TO COMPUTATIONAL GRANULAR MECHANICS

3.1 MICRO OR PARTICULATE MECHANICS

3.1.1 Continuum vs. Discontinuum 26

3.1.2 Micro-structure 27

3.1.2.1 Definition of stress 29

3.1.3 Micro-scale deformation during slow and quasi-static loading 31

3.1.4 Plasticity at micro-scale 35

3.1.5 Numerical modeling of discontinua 35

3.2 DISTINCT ELEMENT METHOD AND PROGRAM PFC3D

3.2.1 Fundamental concepts

3.2.1.1 Representation of contacts 37

3.2.1.2 Representation of solid material 40

3.[illegible] Numerical Implementation 40

3.2.2 Particle flow code or PFC^{3D}

3.2.2.1 Basic entities 42

3.2.2.2 Contact models 42

3.2.2.3 Damping 43

3.2.2.4 Time step 43

3.2.2.5 Tracking equilibrium 44

3.2.3 Micro-parameters

3.2.3.1 Measurements of interparticle friction coefficient 45

3.3 SUMMARY 46

CHAPTER 4 DISCRETE ELEMENT ANALYSIS OF TRIAXIAL COMPRESSION TESTS ON UNIFORM SAND

4.1 TRIAXIAL TEST AND SAND BEHAVIOR

4.1.1 Conventional triaxial compression test 54

4.1.2 Triaxial response of sand 54

4.2 MODELLING DETAILS FOR TRIAXIAL COMPRESSION TEST

4.2.1 Particle shape 55
4.2.2 Particle size 56
4.2.3 Particle contact 57

4.2.4 Stages of analysis Shearing

4.2.4.1 Sample generation 57
4.2.4.2 Isotropic Consolidation 58
4.2.4.3 Application of Deviatoric Stress 58

4.2.5 Boundary conditions

4.2.5.1 Properties of loading platens 59
4.2.5.2 Lateral boundary condition 60
4.2.6 Numerical damping 61
4.2.7 Contact model 61
4.2.8 Initial porosity 62

4.3 PARAMETRIC STUDIES WITH SMOOTH SPHERICAL PARTICLES

4.3.1 Particle size and number of particles 64
4.3.2 Elastic properties of particles 65
4.3.3 Interparticle friction 66
4.3.4 Effect of particle rotation 68
4.4 PARAMETRIC STUDIES WITH NON- SPHERICAL PARTICLES 69

4.5 COMPARISON WITH MEASURED TRIAXIAL COMPRESSION RESULTS

4.5.1 Dense sample 71
4.5.2 Loose sample 72
4.5.3 Effect of confining stress 73
4.6 SUMMARY 74

CHAPTER 5 SIMULATION OF CENTRIFUGE TESTING OF TUNNEL IN SAND

5.1 PHYSICAL TESTING AND ANALYTICAL PREDICTIONS

5.1.1 Centrifuge modeling of tunnel face stability 109
5.1.2 Analytical results 111

5.2 SIMULATING CENTRIFUGE TESTS WITH DEM

5.2.1 Model description 111
5.2.2 Particle characteristics 112
5.2.3 Boundary conditions 113
5.2.3 Initial conditions and tunnel construction 113

5.3 COLLAPSE PRESSURE AND NEAR FACE DISPLACEMENTS

5.3.1 DEM Modeling: Evolution of Tunnel Face 114
    5.3.1.1 DEM curve using best-fit parameters 115
    5.3.1.2 Parametric Studies 116
5.3.2 Effect of geometry 117

5.3.3 Collapse Pressure and Failure Mechanism

    5.3.3.1 Collapse pressure 118
    5.3.3.2 Near face displacements 119
5.3.4 Sand flow into tunnel 120
5.3.5 Solution Time 121

5.4 SUMMARY 122

CHAPTER 6 SURFACE SETTLEMENT ABOVE A 6.5 M DIAMETER TUNNEL

6.1 SOUTH LIGHT RAIL TRANSIT PROJECT BACKGROUND 141

6.2 GEOTECHNICAL CARACTERISTICS OF SOIL 143
6.3 FIELD MONITORING 143

6.4 MODELING PROCEDURE

6.4.1 Model description 145
6.4.2 Boundary conditions 147
6.4.3 Initial Conditions and Tunnel Construction 147

6.5 PARAMETRIC STUDIES

6.5.1 Elastic cap to model fill and clay layer 150
6.5.2 Magnitude of gaps between shield and liner 151
6.5.3 Modeling gaps 152

6.6 SURFACE SETTLEMENT
6.6.1 Uniform face: sand
6.6.1.1 Cover to depth (C/D) ratio equal to 1 153
6.6.2 Other C/D ratios and mixed face 155

6.7 SUMMARY 157

CHAPTER 7 CONCLUSIONS AND RECOMMENDATIONS

7.1 CONCLUSIONS 179
7.2 RECOMMENDATIONS 182

REFERENCES 184

APPENDICES 192

LIST OF TABLES

CHAPTER 2

Page

Table 2.1 Soft ground tunneling conditions (after Terzaghi, 1950) ---------- 19

CHAPTER 3

Table 3.1 Discrete mechanical quantities in 3D (after Satake, 1997) ---------- 47

Table 3.2 Attributes to the four classes of discrete element method (modified from Cundall and Hart, 1992) ---------- 47

Table 3.3 Elastic properties of selected continuum materials (at room temperature) (after Santamarina, 2001) ---------- 47

Table 3.4 Friction properties of selected continuum materials (at room temperature) (after Santamarina, 2001) ---------- 48

CHAPTER 4

Table 4.1 Bond properties of clusters ---------- 76

Table 4.2 Different cases ramp up the platen velocity ---------- 76

Table 4.3 Different cases of lateral boundary conditions ---------- 76

Table 4.4 Initial Porosities (r_{min}=1.5 mm) ---------- 77

Table 4.5 Initial Porosities (r_{min}=1.0 mm) ---------- 78

Table 4.6 Configuration of different PFC samples ---------- 78

Table 4.7 Average sample void ratios at different particle friction ---------- 79

Table 4.8 Physical and mechanical properties of Ottawa sand ---------- 80

Table 4.9 Fundamental Input Parameters in PFC^{3D} for material calibration ---------- 81

CHAPTER 5

Table 5.1 Properties of Fontainbleau sand ---------- 123

Table 5.2 Range of parameters in Chambon & Corte (1994) study ---------- 123

Table 5.3 Particle size distributions in DEM tunnel model ---------- 123

Table 5.4 Parallel bond properties of tunnel tube particles ---------- 123

Table 5.5 Initial conditions (5.0 m diameter tunnel simulation ---------- 123

Table 5.6 Collapse pressures by DEM analyses (Tunnel Diameter, D=5.0 m, C/D=2.0) ---------- 124

Table 5.7 Comparison between experimental, theoretical and numerical results for collapse Pressure ---------- 125

Table 5.8 Solution time for 3D discrete element modeling of tunneling ---------- 126

CHAPTER 6

Table 6.1 Geotechnical engineering parameters for major stratigraphic units---------------------------------- 160

Table 6.2 Ball size distributions (material discretization) in DEM tunnel model------------------------------ 161

Table 6.3 Magnitude of gap around shield and liner--- 161

Table 6.4 Modeling options considered in DEM --- 162

Table 6.5 Initial conditions in DEM model (specified porosity = 0.4, 1g gravity, C/D=1.0) ---------------- 162

LIST OF FIGURES

CHAPTER 2 Page

Figure 2.1 Tunnel heading in soft ground--20
Figure 2.2 Three dimensional sliding mechanism (after Horn 1961)------------------------------------20
Figure 2.3 Effective support pressure s' (after Anagnostou and Kovari, 1996)------------------------20
Figure 2.4 Typical patterns of face failure (after Vermeer and Ruse 2000) ----------------------------21
Figure 2.5 Experimentally determined and computed support pressures as a function of tunnel Diameter
for dry sands (modified after Anagnostou & Kovari , 1996)--------------------------------------21
Figure 2.6 Components of ground movements by shield tunneling ---------------------------------------22
Figure 2.7 Reference diagram for surface settlement over a tunnel (modified after Wood, 2000) ----------22
Figure 2.8 Computed failure mechanisms for drained soil conditions,
γ=20 kN/m3, c=5 kPa, φ=27.5^0, D=5 m (after Vermeer and Ruse 2000) -----------------------23
Figure 2.9 Schematic of centrifuge model (modified from Chambon & Corte,1994) ------------------------23

CHAPTER 3

Figure 3.1 Fabric elements of granular sand (after Oda, 1972)--49
Figure 3.2 Contact normals, contact vectors, and contact forces
(after Bathurst & Rothenburg, 1998)--49
Figure 3.3 A dilatancy model for granular materials (after Oda, 1997)----------------------------------50
Figure3.4 Kinematics at a contact : rolling and sliding (after Bardet,1994)--------------------------------50
Figure 3.5 Particle graph (after M. Satake, 1997)--50
Figure 3.6 Basic contact model (after Bardet, 1998)--51
Figure 3.7 Contact force-displacement relationship---51
Figure 3.8 Calculation scheme in distinct element method (after Dorby and Ng, 1992)----------------51
Figure 3.9 Basic PFC configuration – assembly of balls bounded by walls (plane view) -----------------52

CHAPTER 4

Figure 4.1 Typical response of triaxial test on sand --82
Figure 4.2 Grain shape and size of Ottawa sand (sieve no. 20-30, ASTM C-190) and
shape of a cluster in PFC simulation---82
Figure 4.3 Particle size distributions of numerical samples and Ottawa sand-----------------------------83

Figure 4.4 Effect of parameters to ramp up the platen velocity on simulated dense constitutive behavior (Sample size: 50×21×21 mm, $G=1.0$ GPa, $\nu=0.2$, $D=0.8$, $\mu=0.5$ and $V=0.01$ m/s) ---------- 83

Figure 4.5 Effect of platen velocity on stress equilibrium of dense PFC samples ---------- 84

Figure 4.6 Effect of loading platen roughness on simulated dense constitutive behavior (Sample size: 50×21×21 mm, $G=1.0$ GPa, $\nu=0.2$, $D=0.8$, $\mu=0.5$ and $V=0.01$ m/s) ---------- 85

Figure 4.7 Configuration of a typical assembly of particles for triaxial test ---------- 86

Figure 4.8 Segmental lateral boundary in numerical triaxial test ---------- 86

Figure 4.9 Macro deformation pattern of dense PFC sample (smooth spherical particles, ($\sigma_3=100$ kPa): (a) initial condition (b) rigid single walls (c) rigid discretized walls ---------- 87

Figure 4.10 Effect of lateral boundary on simulated dense stress-strain-strength and volumetric behavior (Sample size: 165×70×70 mm, $G=1.0$ GPa, $\nu=0.2$, $D=0.8$, $\mu=0.5$ and $V=0.01$ m/s) ---------- 87

Figure 4.11 Effect of numerical damping on simulated dense constitutive behavior (Sample size: 50×21×21 mm, $G=1.0$ GPa, $\nu=0.2$, $\mu=0.5$ and $V=0.01$ m/s) ---------- 88

Figure 4.12 Size and locations of measurement spheres within a pfc sample ---------- 89

Figure 4.13 Effect of particle size on dense simulated stress-strain-strength and volumetric behavior (Sample size: 165×70×70 mm, $G=1.0$ GPa, $\nu=0.2$, $\alpha=0.8$, $\mu=0.5$ and $V=0.01$ m/s) - 90

Figure 4.14 Effect of particle size on dense simulated peak strength ---------- 91

Figure 4.15 Size effect on simulated dense peak strength (Sample size: 50×21×21 mm, $G=1.0$ GPa, $\nu=0.2$, $\mu=0.5$ and $V=0.01$ m/s) ---------- 91

Figure 4.16 Effect of particle size on loose simulated stress-strain-strength and volumetric behavior (Sample size: 165×70×70 mm, $G=1.0$ GPa, $\nu=0.2$, $D=0.8$, $\mu=0.5$ and $V=0.1$ m/s) --- 92

Figure 4.17 Effect of particle elastic properties on simulated dense stress-strain-strength and volumetric behavior (Sample size: 165×70×70 mm, $D=0.8$, $\mu=0.5$ and $V=0.01$ m/s) ---------- 93

Figure 4.18 Effect of particle elastic properties on simulated loose stress-strain-strength and volumetric behavior (Sample size: 165×70×70 mm, $D=0.8$, $\mu=0.5$ and $V=0.1$ m/s) ---------- 94

Figure 4.19 Effect of μ during shear on simulated dense stress-strain-strength and volumetric behavior (Sample size: 165×70×70 mm, $G=1.0$ GPa, $\nu=0.2$, $D=0.8$ and $V=0.01$ m/s) ---------- 95

Figure 4.20 Effect of μ during shear on simulated dense peak strength ---------- 96

Figure 4.21 Effect of μ during shear on simulated loose stress-strain-strength and volumetric behavior (Sample size: 165×70×70 mm, $G=1.0$ GPa, $\nu=0.2$, $D=0.8$ and $V=0.1$ m/s) ---------- 97

Figure 4.22 Effect of particle rotation on simulated dense constitutive behavior (Sample size: 50×21×21 mm, $G=1.0$ GPa, $\nu=0.2$, $\mu=0.5$, $D=0.8$ and $V=0.01$ m/s) ---------- 98

Figure 4.23 Variation of average incremental particle rotational velocities versus axial strain: free rotation (a) middle-third of sample and (b) top one-third of sample ---------- 99
Figure 4.24 Variation of average incremental particle rotational velocities (top one-third of sample) versus axial strain: fixed rotation (middle-third) ---------- 100
Figure 4.25 Effect of clustering (overlap) on simulated dense constitutive behavior (Sample size: 50×21×21 mm, k_n=ks=1.0×e^6 N/m, D=0.8, μ=0.5 and V=0.01 m/s) ---------- 101
Figure 4.26 Effect of clustering (particle size but no overlap) on simulated dense constitutive behavior (Sample size: 50×21×21 mm, k_n=ks=1.0×e^6 N/m, D=0.8, μ=0.5 and V=0.01 m/s) ---------- 102
Figure 4.27 Variability in friction angle of Ottawa sand ---------- 103
Figure 4.28 Matched constitutive behavior (dense) between physical test and PFC simulation (G=1.0 GPa, ν=0.2, μ=0.5 and V=0.01 m/s) ---------- 104
Figure 4.29 Matched constitutive behavior (loose) between physical test and PFC simulation (G=1.0 GPa, ν=0.2, μ=0.5 and V=0.1 m/s) ---------- 105
Figure 4.30 Dense simulated and physical constitutive relationships at different confining stresses (PFC general: G=1.0 GPa, ν=0.2 and μ=0.5) ---------- 106
Figure 4.31 Loose simulated and physical constitutive relationships at different confining stresses (PFC general: G=1.0 GPa, ν=0.2 and μ=0.5) ---------- 107

CHAPTER 5

Figure 5.1 Centrifuge model in container: 1,200 × 800 mm (after Chambon & Corte, 1994) ---------- 127
Figure 5.2 Cylindrical tunnel model in centrifuge test (after Chambon & Corte, 1994) ---------- 127
Figure 5.3 Evolution of tunnel face: horizontal displacement with decreasing confining pressure (after Chambon & Corte, 1994) ---------- 128
Figure 5.4 Variation of face collapse pressure with tunnel diameter (after Chambon & Corte, 1994) ---- 128
Figure 5.5 Failure bulb for fully lined tunnel (after Chambon et al, 1991) ---------- 129
Figure 5.6 Experimentally determined and computed support pressures as a function of tunnel diameter for dry and clean sands (modified after Anagnostou & Kovari, 1996) ---------- 129
Figure 5.7 Comparison of the physical and DEM model dimensions ---------- 130
Figure 5.8 Material discretization in DEM model to simulate small-scale centrifuge test of shallow tunnel ---------- 130
Figure 5.9 Three dimensional discrete element model of centrifuge testing of shallow tunnel ---------- 131
Figure 5.10 Pre-failure DEM material behavior ---------- 132
Figure 5.11 Flow chart for DEM centrifuge tunnel simulation ---------- 133
Figure 5.12 Tunnel face evolution: DEM (G=1.0 GPa, ν=0.2 and μ=0.5) versus physical data ---------- 134

Figure 5.13 Comparison of DEM modeling of shallow tunnel for different particle friction Coefficient- 134

Figure 5.14 Comparison of DEM modeling of tunneling in sand for different particle damping coefficient (μ=0.6) ---------- 135

Figure 5.15 Comparison of DEM modeling of tunneling in sand for different particle sizes (μ=0.6, Dc=0.8) ---------- 135

Figure 5.16 Comparison of DEM modeling of tunneling in sand for two different model sizes (D/d_{50} = 11.5, μ=0.6 and Dc=0.8) ---------- 136

Figure 5.17 Comparison of DEM modeling of tunneling in sand for two different timestep (μ=0.6, Dc=0.8, D/d_{50}=11.5) ---------- 136

Figure 5.18 Comparison of DEM modeling of tunneling in sand for different face pressure increment (D/d_{50} = 11.5, μ=0.6 and Dc=0.8) ---------- 137

Figure 5.19 Failure bulbs for different C/D ratios observed in small-scale model (after Chambon & Corte, 1994) ---------- 137

Figure 5.20 Failure bulb from discontinuum modeling (D=5.0 m, C/D=2.0) ---------- 138

Figure 5.21 Failure bulb from discontinuum modeling (D=5.0 m, C/D=0.5) ---------- 138

Figure 5.22 Initial face condition (a) and subsequent flow of granular material into collapsed tunnel (b) from discontinuum modeling: plane view (D=5.0 m, C/D=2.0) ---------- 139

Figure 5.23 Dwasplacement vectors under complete tunnel collapse: plane view (D=5.0 m, C/D=2.0) ---------- 140

CHAPTER 6

Figure 6.1 Project location plan and simplified geology (after Bobey et al, 2004) ---------- 163

Figure 6.2a Longitudinal section and face section of Lovat EPB-TBM used for constructing the City of Edmonton LRT tunnels (figures provided by Lovat) ---------- 164

Figure 6.2b Face section of Lovat EPB-TBM used for constructing the City of Edmonton LRT tunnels (figures provided by Lovat) ---------- 165

Figure 6.3 Photograph of the Lovat EPB_TBM in position to commence the driving of the southbound LRT tunnel. Note the approximately 6-m of cover (1 tunnel diameter) above the tunnel crown (photo taken during a tour of the site by the author) ---------- 166

Figure 6.4 The cutting head of the Lovat EPB-TBM after breaking through on the Northbound tunnel (photo taken during a tour of the site by the author) ---------- 167

Figure 6.5 Variability in grain size distribution of soils in outwash deposit (after Boone et al, 2004) ---------- 168

Figure 6.6 Profile of natural water content related to elevation ---------- 168

Figure 6.7 Photograph showing the clean nature of the outwash sand exposed in the open-cut excavation for the TBM portal (photo taken during a tour of the site by the author) ---------- 169

Figure 6.8 Observed shallow settlements during construction of Southbound tunnel with proximity to TBM face, from Portal to Education Car Park (after Bosse, 2005)---------------------------- 170

Figure 6.9 Observed shallow settlements during construction of Southbound tunnel with proximity to TBM face, Education Car Park (after Marc Bosse) --- 170

Figure 6.10 Observed shallow settlements during construction of Southbound tunnel and mixed-face condition (after Bosse, 2005) -- 171

Figure 6.11 Three-dimensional view of shallow tunnel model by DEM (118999 particles) --------------- 172

Figure 6.12 DEM model of SLRT tunnel construction -- 172

Figure 6.13 Tunnel model used in SLRT modeling and X-section along the tunnel lining and surrounding ground --- 173

Figure 6.14 Uniform radial displacement of Shield/Liner in DEM to create the gaps between the TBM shield/liner and the tunnel bore-- 174

Figure 6.15 Location of measurement spheres to measure stresses around the tunnel --------------------- 174

Figure 6.16 Flow chart for SLRT simulation using--- 175

Figure 6.17 Quantification of 'clay cap' in DEM model of 6.5 m-diameter tunnel in sand: uniform face and C/D=1.0 (G=1 GPa, ν=0.2, μ=0.6, spherical particles)---------------------- 175

Figure 6.18 Quantification of gaps in DEM model of 6.5 m-diameter tunnel in sand: uniform face and C/D=1.0 (G=1 GPa, ν=0.2, μ=0.6, spherical particles) -------------------- 176

Figure 6.19 Quantification of particle velocity to produce gaps in DEM model of 6.5 m-diameter tunnel in sand: uniform face and C/D=1.0 (G=1 GPa, ν=0.2, μ=0.6, spherical particles) -- 176

Figure 6.20 Surface settlement from DEM model of 6.5 m-diameter tunnel in sand: uniform face (G=1 GPa, ν=0.2, μ=0.6, spherical particles) ------------------------------------ 177

Figure 6.21 Surface settlement from DEM model of 6.5 m-diameter tunnel in sand: uniform face (C/D=0.5, G=1 GPa, ν=0.2, μ=0.6, spherical particles) ------------------------ 177

Figure 6.22 Surface settlement from DEM model of shallow tunnel in sand: mixed face consisting 90 percent 'idealized' till (C/D=2, G=1 GPa, ν=0.2, μ=0.6, spherical particles) ------------- 178

Figure 6.23 Settlement variation with tunnel geology -- 178

List of Symbols

C – depth of soil cover above tunnel crown or overburden
D – tunnel diameter
R – tunnel radius
P - length of the pressure chamber in front of face
σ_T - face support pressure
ϕ' - friction angle
c' is the effective cohesion
p_f – face collapse pressure
α_s – weighting factor
α_γ - weighting factor
γ - soil unit weight
γ_d - soil dry unit weight
γ' - soil effective unit weight
F_0, F_1, F_2 and F_3 – dimensionless coefficients
h_0 – water table elevation
h_F – piezometric head in the chamber
τ_f - shearing resistance of soil
K_0 - coefficient of lateral earth pressure
Ka - active earth pressure coefficient
σ_z – vertical stress
z_0 – depth below ground surface
i - transverse distance to the point of inflection of the settlement trough
S(x) - settlement at a distance x from the tunnel centerline
S_{max} - maximum settlement for x=zero
k - trough width parameter
Vs - transverse surface settlements (per meter length of tunnel)
V_t – ground loss
C_n – coordination number
k_n – normal contact stiffness
k_s – tangential contact stiffness
a – contact area
N- normal force
T – tangential force
μ - interparticle friction coefficient
α– damping constant
Δt – time step
Δt_{cr} – critical time step
G – particle shear modulus
ν - particle Poisson's ratio
Dr- relative density
σ_1, σ_2, σ_3 – major, intermediate and minor principal stress, respectively
ε_1 – axial strain
d – particle size

D_0 – sample size
v – velocity
n_0 – initial porosity
Cu – uniformity coefficient
e – void ratio
ρ_d – particle density
g – gravitational acceleration
r_{min} – minimum particle radius
r_{max} – maximum particle radius
K_{n1}, K_{n2} – normal strength and stiffness of parallel bond
K_{s1}, K_{s2} - shear strength and stiffness of parallel bond

CHAPTER 1

Introduction

1.1 Problem statement

One of the key challenges of any geotechnical numerical analysis is to incorporate an accurate description of soil and rock behaviour. Continuum models, which are commonly used, required development of constitutive models to describe the soil/rock behaviour. With the introduction of the discrete element method by Cundall (1971) and Cundall and Strack (1979), the requirement to prescribe the constitutive behaviour of the macro-scale response was changed to describing the micro-contact behaviour that captured the macro-scale response. It was argued by Cundall that this presented a significant step forward for modeling of particulate materials such as soil.

The issue with discrete element models is the determination of the micro-scale or contact parameters to represent the macro-scale response. This can be done on laboratory samples where the stress-strain response is recorded for various stress paths. However, once the micro-scale parameters are determined the application of these micro-parameters to engineering boundary value problems remains uncertain. In addition, the issue of practical modeling the correct particle shape (shape other than spherical) is significant. This is the focus of this thesis; to determine if the micro-parameters obtained from triaxial tests on sand irrespective of particle shape can be used to assess the deformations above a 6.5 meter diameter shallow tunnel in sandy soils.

This research has been undertaken with the following objectives:

- Establishing micro-macro property relationship through element tests on synthetic discrete element samples consisting of both spherical and non-spherical shaped particles and calibrate the synthetic response against physical triaxial test results on sands at low to medium stress levels. Determining what other modeling parameters influence the corresponding macro-behaviour in addition to the micro-scale parameters.

- Apply the micro-parameters obtained from the triaxial test to the simulation of a centrifuge tests. The centrifuge tests assess the collapse face pressure of a shallow tunnel in clean sand. The predicted face collapse pressure will be compared to measured.
- Apply the micro-parameters obtained from the triaxial tests to the simulation of a shallow 6.5-m-diameter tunnel in mixed faced ground conditions. The measured surface settlement above the tunnel will be compared to the predicted settlement.

1.2 Scope of research

The scope of this research was to examine the potential of the discrete element method (DEM) for application ~~to~~ tunneling in dry uniform cohesionless soil and therefore, condition of drained stability prevails.

In line with the objectives of the research, a three-step approach will be followed within the framework of DEM, namely:

(1) modeling of triaxial test on uniform sand
(2) modeling of a small scale centrifuge test of a shallow tunnel in sand and finally
(3) modeling of full scale shallow tunnel in uniform and mixed face conditions.

It is intended to see the constraints in each of the steps and how those constraints affected the outcome of the next step. In other words, through each step the number of modeling factors will be reduced in order to reduce the time and effort of the next step.

Steps (2) and (3) are unique to this research. However, step (1) is the very first step of any DEM modeling as it involves the smallest modeling size at the level of laboratory sample scale. Step (2) is an intermediate but important step towards attaining the main objective of this research that is the applicability of DEM to assess the material deformation by a full scale tunnel in sand.

1.3 Discrete or Distinct Element Method

Cundall and Hart (1992) differentiated the terms 'discrete element method' and 'distinct element method'. According to Cundall and Hart (1992) 'discrete element method' applies to any computer program that: (1) allows finite displacements and rotations of discrete bodies, including complete detachment, and (2) recognizes new contacts automatically as the calculation progresses. The term 'distinct element method' was coined by Cundall and Strack (1978) to refer to the particular discrete element scheme that uses deformable contacts and explicit, time-domain solution of the original equations of motion (Cundall and Hart, 1992).

It is obvious from the above that the term 'discrete element method' is the general term applicable to any DEM based computer code. This author believes the term 'discrete' is more appropriate than 'distinct' once the simulation and modeling of an assembly of discrete particles are involved, as is the case of this research. Therefore, in the following chapters, the term 'discrete element method' will be used to describe and discuss the findings from this research; the term 'distinct element method' will be used to quote previous research only to keep the originality of the previous publications.

1.4 Outline of thesis

In the following chapters (Chapter 2 through Chapter 6), the thesis has been documented based on the above mentioned objectives and scope of work. Chapters 2 and 3 describe the findings of literature search on modeling/prediction of shallow or soft ground tunneling and on state-of-the-art of discrete element method. In Chapter 2, the challenges of soft ground tunneling despite significant advances in terms of both understanding the deformation/failure mechanism as well as state-of-the-art construction techniques are outlined. Emphasis will be given on the numerical modeling of such an otherwise complex engineering works. The review will be restricted to bored tunneling in urban environment using closed face machine such as pressurized shield tunneling.

Two different fields of approach for micromechanics based granular material research can be identified: theoretical based micro-structural continuum approach or the multi-scale approach used in continuous media and computer simulation by discrete numerical models. In Chapter 3, only the later approach i.e. computer based discrete modeling will mainly be reviewed, as it will be used as the fundamental tool in this research. However, some of the concepts are the same and are considered the fundamental to any micro-mechanical approach. Therefore, first, an overview of micro-mechanically based granular modeling is given. This includes the definition and the concept of the approach and the fundamental differences with the continuum approach. In addition, different variables classically used to describe the approach are outlined. This is then followed by a description of the basic characteristics of discrete modeling of granular behaviour i.e. discrete element method. Outline of the commercially available DEM tool used in this research, Particle Flow Code (PFC) is presented. Finally, discussion on micro-scale parameters needed as input parameters in any DEM simulations is also presented.

Chapter 4 documents the results of numerical triaxial tests on synthetic samples and comparisons with real experimental data for uniform sands. The primary goal is to find the values of a best set of micro-parameters and other parameters necessary to formulate a boundary value problem i.e. tunneling in sand by discrete element method. A spherical particle in DEM can be considered a single discretization unit or element in the problem domain that is being considered. This is similar to the discretization in finite element method (FEM). Like FEM, however, general shaped element other than spherical can also be generated in DEM and will be considered and compared with the results involving only spherical particles. In any realistic calibration of synthetic sample behaviour against laboratory data, an ideal case would be to simulate flexible boundary during an element test. A different but comparatively easy technique has been developed and used to allow the PFC sample to bulge. A comparison of the synthetic sample behaviour between single rigid and multiple rigid boundaries will also be presented.

Once the material properties are calibrated, formulation and simulation of tunnel responses in uniform ground by discrete element method and comparisons with physical data are described in Chapter 5. Chambon and Corte (1991, 1994) investigated the face stability of shallow tunnel construction in uniform dry sand (Fontainebleau sand, a fine sand) using centrifuge tests. Their results are chosen as the reference data for the calibration of PFC model. Like the triaxial test simulations, systematic parametric studies are undertaken first to observe the effects of various DEM parameters (micro and others) on the tunnel response. This is then followed by the prediction of collapse pressure and failure mechanism of a shallow tunnel under uniform pressure by DEM. The predictions are then compared to the results from the centrifuge tests.

Finally applicability of DEM to simulate a 6.5-m-diameter tunnel is examined in Chapter 6 which compares the predicted surface settlement with the measured surface settlement. Recently constructed southern extension of the Light Rail Transit (SLRT) at the University of Alberta campus provided valuable field data against which the model results are calibrated. Not all the real physical aspects of the tunneling are simulated, as modeling of tunnel construction is quite complex. For example, the advancement of tunnel, stresses on liner, etc are not considered. Emphasis is given on the prediction of the magnitude and pattern of surface settlement due to tunneling using an earth pressure balanced (EPB) shield machine. The principal intention in this chapter is to extend and judge the capability of DEM modeling from small scale (Chapter 5) to full scale modeling. Therefore, many of the DEM parameters are simplified such as using perfectly spherical particles. Both tunneling in uniform and mixed faced (sand/till or bedrock) tunneling are considered.

Chapter 7 provides the key research findings and recommends future research needs for DEM based geotechnical engineering modeling, particularly for the problem involving material flow.

CHAPTER 2

Tunneling in Sand

A soft ground tunnel may be distinguished as one constructed in soil which will be unstable, or only marginally stable, if left unsupported and which will collapse due to gross plastic distortions in the ground (Potts, 1976). The term 'soft ground tunneling' is synonymous with shallow tunneling (since relatively soft soils usually do not exists at great depths). As tunneling in sand falls into this definition, it is necessary to define and clarify the term. In general, a shallow tunnel is different from a deep tunnel in its interference with ground surface and subsequent occurrence of surface settlement. As mentioned in Chapter 1, among the three most important aspects of soft ground tunnel design, namely stability, ground deformation, and lining performance, the prediction of stability and ground deformation are the focus of this research project and therefore, will be reviewed here.

2.1 DIFFICULTIES IN TUNNELING IN SAND

The technique of mining (or tunneling) through earth (or soft ground) depends chiefly on the bridge-action period of the earth above the roof (of the tunnel) and on the position of the tunnel with reference to the water table (Proctor and White, 1946). Terzaghi (1946) defines the bridge action period (also commonly known as stand up time) of a geologic medium related to tunnel excavation as the time which elapses between the excavation of the tunnel face and ground instability around the excavation leading to complete collapse of the unsupported face. As discussed by Terzaghi (1946), the stand up time for cohesionless sand or badly broken rock without cementing material is almost zero; hence, excessive overbreak or collapse is inevitable if not supported properly. On the other hand, the same for cohesive material may ranges between several hours and several days (Terzaghi, 1946).

Material with no cohesion, such as clean sand or gravel, is commonly referred to as running ground regardless of whether it is located below or above the water table (Proctor and White, 1946). Terzaghi (1950) discussed in details the geologic aspects of soft ground tunneling and mentioned six principal categories of soft ground, namely, firm, raveling, running, flowing, squeezing and swelling ground. Table 2.1 shows the characteristics and examples of different ground from the tunneling perspective (after Terzaghi, 1950).

As the tunnel face and roof must be supported before the stand up time expires, tunneling in sand requires special tunneling techniques. In urban environments, where shallow tunneling is usually done under sensitive buildings, roads, etc., the process of tunnel design, especially the design for support system, becomes more complex.

2.2 SOFT GROUND TUNNELING: DESIGN CONSIDERATIONS

2.2.1 Tunneling methods in sand

In an urban environment tunneling in soft unstable ground, such as sand above or below water table, where the face requires support at all times, is usually carried out using closed face tunneling machines which operate on the principle of a pressurized face (positive face control) (Eisenstein, 2000). Three common types are: (1) compressed air, (2) slurry (bentonite) or BS shield, and (3) earth pressure balance or EPB shield. They are also known as shielded tunnel boring machine or TBM. The compressed air is now obsolete because of its health hazard and the risk of blow-out, i.e. sudden reduction of support pressure on account of rapid loss of air. This will not be discussed further. The difference in the mechanics of face support in BS and EPB TBM are discussed by Eisenstein (2000) and Anagnostou and Kovari (1994, 1996). In a slurry shield, a pressurized mixture of bentonite or clay and water provides the temporary support of the face hydraulically. The method is most effective in water bearing granular soils (Mair and Taylor, 1998). As discussed by Eisenstein (2000), the method can control either a total stress or a neutral (water) pressure. It cannot support directly the effective stress in the chamber. On the other hand, EPB machines are being universally applied to any types of soft unstable ground (Eisenstein, 2000). A uniform pressure is applied at face using freshly excavated soil in the pressure chamber (required face pressure is achieved by controlling the entry of soil and water through the cutter face and spoil removed through a screw conveyor). The EPB can only work in either a total stress or an effective (grain-to-grain) stress mode (Eisenstein, 2000).

2.2.2 Drained stability

Tunnels in predominantly sandy soil (dry or saturated) are driven under drained conditions. Tunnel face stability under drained condition has been studied by number of researchers under various face support conditions (Peck, 1969; Leca and Dormieux, 1990; Anagnostou and Kovari, 1994, 1996a, 1996b). Most of these works were done analytically based on plasticity solutions and calibrated against centrifuge model tests and/or continuum numerical modeling. Drained stability of a shallow tunnel heading was also studied by researchers in France with the Laboratoire Central des Ponts et Chaussees (LCPC) centrifuge. In general, parameters controlling the stability of a tunnel heading are (Figure 2.1): the tunnel diameter (D); depth of soil cover (C); the length of the pressure chamber in front of face (P) and the soil type (represented by the unit weight and shear strength) as well as face support pressure (σ_T). For tunnel in dry sand, the shear strength is characterized by friction angle, ϕ' only.

There are special issues related to maintaining the required face pressure of any shield machine. Anagnostou and Kovari (1994, 1996) analyzed the problem of face stability for slurry and EPB machines. They consider a collapse mechanism consisting of a wedge and prismatic body that extends from the tunnel crown to the surface (Figure 2.2). The circular cross-section of the tunnel is approximated by a square having the same area. The ground is considered homogeneous and isotropic.

As discussed by Anagnostou and Kovari (1994), for the case of slurry shield, the safety factor was found to be time-dependent. This is due to the gradual infiltration of bentonite suspension into the ground. Therefore, permeability of the ground as well as effective grain size plays a critical role in maintaining required support pressure. Maintaining support pressure at EPB face is more complex as resultant face pressure depends on the effective support pressure as well as piezometric head in the work chamber. The position of water table in the undisturbed soil also influences the face pressure. The shear resistance of the muck should also be kept as low as possible. It was found by Anagnostou and Kovari (1994) that a constant effective support pressure is difficult to maintain for sandy soil.

Mair and Taylor (1998) did a comprehensive review on tunnel face stability and concluded that the effective support pressure required preventing collapse of a tunnel in dry cohesionless soil was very small, irrespective of whether it was a two dimensional circular tunnel or a three dimensional heading. It was also independent of tunnel depth; however, collapse support pressure in dry sand was found to vary significantly with tunnel diameter. Probably the first theoretical approach of tunnel face stability in dry sand, taking into consideration the full three-dimensional nature of the problem, was proposed by Leca and Dormieux (1990). The limiting face collapse pressure, p_f, based on a three dimensional failure mechanism was derived as:

$$p_f = \alpha_s.\sigma_s + \alpha_\gamma.\gamma D \tag{2.1}$$

where α_s and α_γ are weighting factors which depend on the angle of internal friction, ϕ' and C/D ratio and can be obtained from pre-established charts. γ is the soil unit weight. σ_s is the surcharge loading. All other parameters have been defined above and are shown in Figure 2.1.

Based on the failure mechanism as shown in Figure 2.2, Anagnostou and Kovari (1996) derived the following formula to calculate necessary limiting collapse pressure, with earth-pressure balanced shields (Figure 2.3):

$$p_f = F_0\lambda' D - F_1 c' + F_2\gamma'\Delta h - F_3 c'\frac{\Delta h}{D} \tag{2.2}$$

where: F_0 to F_3 are dimensionless coefficients that depend on the friction angle ϕ', on the geometric parameters C/D and (h_0-D)/D, and on the ratio of the dry to the submerged unit weight γ_d / γ'. C, D, and Δh are the overburden, tunnel diameter, and head difference between elevation of the water table (h_0) and piezometric head in the chamber (h_F), respectively. c' is the effective cohesion.

The theoretical minimum face support pressure for tunneling in dry soil (having only dry unit weight γ_d instead of γ' in equation 2.2) is, therefore, given by:

$$p_f = F_0\lambda_d D - F_1 c' \tag{2.3}$$

Vermeer and Ruse (2000) considered, as the basic idea for analyzing tunnel face stability, that failure was associated with an active sliding wedge as indicated in Figure 2.4. Vermeer and Ruse (2000) modified the method proposed by Anagnostou and Kovari (1996) by introducing horizontal force on top of the wedge (the collapse mechanism consists of a wedge and right-handed prism, see Figure 2.4). As discussed by Vermeer and Ruse (2000), the method of Anagnostou and Kovari is not based on a kinematically admissible collapse mechanism, as this would imply sliding between the rectangle (prism) and the wedge. The authors make the following assumptions (see Figure 2.4):

- The inclination angle of the wedge is a preset value of $45^0+\phi/2$,
- Shear stresses on the vertical sides are neglected,
- The shearing resistance on the top of the wedge, τ_f and
- The vertical stress on top of the wedge is considered according to the silo theory by Janssen (1895) which was also used by Terzaghi (1954):

$$\sigma_z = \frac{\langle \gamma R - 2c \rangle}{2K_0 \tan\phi}\left(1 - e^{-2K_0 \tan\phi . \frac{C}{R}}\right) \tag{2.4}$$

where: R is the radius of the tunnel; c is the cohesion; ϕ is the friction angle; γ is the unit weight; K_0 the coefficient of lateral earth pressure at rest and C is the depth to tunnel crown.

Using the classical earth pressure theory, the failure face pressure, p_f was derived by Vermeer and Ruse (2000) as:

$$p_f = \left(\frac{1}{2}\gamma D + \sigma_z\right)K_a - \left(3c + \sigma_z \tan\phi\right)\sqrt{K_a} \tag{2.5}$$

where

$K_a = \dfrac{1-\sin\phi}{1+\sin\phi}$ is the active earth pressure coefficient. Other terms have been defined above.

Predictions based on the equation (2.3), for an average friction angle of 40 degrees, were compared by Anagnostou and Kovari (1996) with the centrifugal model test results of Chambon and Corte (1994) as well as model of Leca and Dormieux (equation 2.1)) concerning face stability in dry cohesionless soils and is reproduced here as Figure 2.5. Prediction based on the equation (2.5) for a friction angle of 40 degrees and c equal to zero is also included in Figure 2.5. For a given tunnel diameter, for a dry, clean sand ($\phi = 40^0$, c = 0), the analytical predictions were always higher than that of experimental one. Among the analytical methods, the failure mechanism adopted by Vermeer and Ruse (2000) gave the results closest to the physical results. The centrifuge results will be discussed in detail in Chapter 5.

2.2.3 Ground deformation: fundamentals

In closed face shield tunneling, the possible sources of ground deformation or ground loss into tunnel, measured as m^3/m, as shield progresses, are shown in Figure 2.6. The corresponding evolution of surface settlements along the length of tunnel is also shown. While settlement in front of the face (although usually negligible, even ground heave can occur for a well-controlled face) largely depends on the face pressure applied, the major source of ground loss is at the tail void. However, field observations of tunnel excavation by EPB machine in predominantly sandy ground showed surprisingly larger settlements along the length of TBM (Maconochie and Suwansawat, 2001; Bosse, 2005). Shirlaw et al. (2003) discussed this settlement due to overcut i.e. component 2 in Figure 2.6. According to Shirlaw et al. (2003), typical values for overcutting, for a 6.5 m diameter machines, expressed as a percentage of the face area are:

- Minimum overcut: 0.5 %
- Additional overcut due to 50 mm look-up or overhang: 1.1%
- Additional overcut due to 100 mm extension of copy-cutters: 4.8%

In a flowing ground condition, like sand, the overcut is likely to close immediately as the machine moves forward. Conventionally, grouting at tail void is carried out through the ports in the tunnel lining rings and can only start once the seals at the tail of the machine have passed the grout port. In a cohesionless soil, this will result in a large tail void closure before the grouting can start. The situation can become worse if lining deflection is allowed.

Loss of ground at a localized region in a soil at depth z_0 below the ground surface gives rise to axisymmetric strains which, where there is a continuous line of such punctuated ground loss, form a cone of depression at ground surface (Wood, 2000). Figure 2.7 shows the settlement trough of depression, with a shape often assumed as that of a normal distribution curve. The distribution of surface settlement is represented by the parameter, *i*, the transverse distance to the point of inflection of the settlement trough. The various attempts to define the parameter *i* have been described in the following section.

2.2.4 Ground deformation: modeling and prediction

Often ground movements associated with the surface settlements govern the design of shallow urban tunnel construction. Prediction of ground movements, especially the magnitude and distribution of surface settlement is an important part of the design process. The estimation of the required face pressure and calculation of the ground displacement under that pressure is, therefore, routinely carried out by soft ground tunnel designers. An important consideration during the design of a shallow tunnel would be the evolution of the face displacement against decreasing face pressure to evaluate the critical face pressure below which face collapse will occur. In practice, different predictive methods are being used from simple analytical/empirical method to sophisticated three-dimensional numerical modeling.

2.2.4.1 Analytical solutions

Sagaseta (1998) reviewed analytical solutions for the evaluation of soil deformation around tunnels. As discussed by the author, the problem can be divided into two parts, of very different nature: near field and far field deformations. The magnitude and distribution of the former are strongly dependent on the soil mechanical behaviour and tunnel construction process and thereby, difficult to consider (analytically), given the three-dimensional character of the problem, non-linearity, etc. On the other hand, for the distribution of the far field movements, the influence of construction details and tunnel precise geometry is not so important, due to attenuation with distance.

Peck (1969) and Schmidt (1969) proposed that surface settlements could be estimated using transverse distribution of surface settlements:

$$S(x) = S_{\max} e^{-\frac{x^2}{2i^2}} \tag{2.6}$$

where S(x) is the settlement at a distance x from the tunnel centerline, $S_{\max}$ the maximum settlement for x=zero and *i* has been defined above.

Two different expressions have been used for i, as follows, with success (Moh et al., 1996):

$$i = kz_0 \tag{2.7}$$

$$i = \left(\frac{D}{2}\right)\left(\frac{z_0}{D}\right)^{0.8} \tag{2.8}$$

where z_0 is the vertical distance from surface to center of tunnel; k is a trough width parameter and D is the tunnel diameter.

Equation (2.6) was proposed by O'Reilly and New (1982) based on observations of tunnels driven in the United Kingdom and equation (2.7) was proposed by Clough and Schmidt (1981). Coefficient k for sands and gravels is 0.25. In any case, *i* is expected to be dependent on soil properties and it is thus necessary to establish relationships based on local experience (Moh et al., 1996). Width of the transverse settlement trough above tunnels in granular soils depends to some extent on the magnitude of settlement as noted by Cording (1991), with larger settlements tending to cause a narrower trough consistent with the "chimney" failure mechanism in sand (Mair and Taylor, 1998).

The volume of settlements (per meter length of tunnel), V_s, is given by the integral of (2.8) as:

$$V_s = \sqrt{2\pi} * i * S_{\max} \tag{2.9}$$

As discussed by Wood (2000), for granular soil, the phenomenon of ground movement is visualized as intergranular movement under gravitational force. The relationship between 'ground loss' or V_t as explained in section 2.2.3 and V_s, volume of transverse surface settlement trough per unit length of tunnel, will depend on the initial state of the soil. In case of tunneling in dense dilating sands $V_t/V_s > 1$ and for loose sand $V_t/Vs < 1$.

The above empirical expression (equation 2.9) works well for clays but is found to overestimate settlement in dense sands above the water table (Personal Notes, Dr. Eisenstein). There have been attempts to find theoretical solutions for the distribution of surface settlements (Sagaseta, 1987, Verruijt and Booker, 1996, Sagaseta, 1998). However, these solutions have been proposed for undrained, cohesive case and to date no solution have been proposed for the dilatant cohesionless case.

2.2.4.2 Numerical solution by finite element analyses

Numerical analyses are now routinely used to simulate tunneling in soil and rock. The excavation/construction steps can be simulated in these analyses with a degree of accuracy, which in principle is limited only by the required computational effort (Gioda and Swoboda, 1999). Another distinct advantage is the ability to incorporate various soil models, which can capture some of the aspects of soil behaviour relevant to tunnel construction.

Two-dimensional plane strain approximation along the tunnel axis can be used to investigate many tunneling problems. Shin et al. (2002) mentioned some of the shortcomings of this way of modeling of tunnel problem, such as, it provide no information on the behaviour of tunnel heading and in particular on the behaviour of soil as the tunnel approaches. As was also discussed by the authors, axisymmetric analyses, in which the tunnel axis is taken as the axis of symmetry, are not applicable to shallow tunnels, where the presence of the ground surface and the effect of gravity have a significant influence on behaviour. It is now generally accepted that realistic modeling of shallow soft ground tunnel can only be achieved with three-dimensional (3D) models. There are, therefore, attempts to incorporate 3D effects in two dimensional (2D) finite element analyses as 2D analyses are still being commonly adopted in design using the percentage unloading method (Panet and Guenot, 1982), the reduced stiffness method (Swoboda, 1979), the gap method (Rowe et al., 1983) and recently the volume loss method (Potts and Addenbrooke, 1997). However, all of these consider empirical factors (Shin et al., 2002), such as determination of load reduction factors and appropriate stiffness in the first two methods, respectively.

As discussed by Mair and Taylor (1998), there are still very few examples of published three dimensional (3D) finite element (FE) analyses case histories where detailed comparisons are made between the predictions and the measurements. However, there are few attempts recently to capture some aspects of shallow tunnel response by 3D-FEM (Vermeer and Ruse, 2000; Shin et al., 2002; Augarde et al., 1998, 2001). The majority of analyses still deal with clays due to well-established Cam Clay Model and few of these are discussed below.

Vermeer and Ruse (2000) validated the analytical solution of both undrained and drained face stability by non-linear 3D-FEM. For the analytical solution, the three-dimensional collapse mechanism was of the same type as considered by Anagnostou and Kovari (1994, 1996). For drained analyses elastic-perfectly plastic soil model along with Mohr-Coulomb failure criterion was used. However, soil is assumed to be non-dilatant. Figure 2.8 shows the computed failure mechanisms shadings in terms of displacement increments of the very last calculation steps (lighter the shading the larger the incremental displacements). Though the authors described a chimney type of failure, nothing was mentioned about the exact extension of the failure zone in longitudinal and transverse directions.

Shin et al. (2002) described a three dimensional modeling of a shallow tunneling in decomposed granite by New Austrian Tunneling Method (NATM). The tunnel-heading problem was analyzed using Fourier Series Aided Finite Element Method (FSAFEM). The excavation process in NATM tunneling is simulated sequentially (2 m/day) based on the real cycle time of tunneling works. Lining installation is simulated by installing the liner in a very short period once an increment of the excavation is completed. The real tunnels usually had a horseshoe cross-section, with a height of 8.2 meters and a width of 10.6 meters. However, the numerical model assumed a circular tunnel of equivalent area resulting in a 9.2 meters tunnel diameter. A 70 meters tunnel excavation was simulated and the behaviour of tunnel face at 60 m distance was examined. The numerical results were then compared with field measurements of field tunnel construction. Although the maximum settlement compared well with a single settlement measurement at a point far behind the tunnel face, the shape of both the transverse and longitudinal surface settlement could not be verified because of very limited field data.

Augarde et al. (1998, 2001) formulated a three-dimensional finite element model to study the effects of subsidence from soft ground tunneling on adjacent surface structures. The later paper concerned only the numerical model for tunnel installation. A non-linear, elasto-plastic material formulation was used to model an overconsolidated clay deposit. The ground loss in terms of face loss and tail void loss associated with the tunneling (thus excavation by shield tunneling was simulated) were incorporated in the model. Face was unsupported and tail loss was simulated by uniform hoop shrinkage of the lining elements in a plane normal to the tunneling center. The hoop shrinkage was achieved by the application of a suitable set of radial forces within the tunnel liner. According to the authors, the fictitious stresses within the liner because of the shrinkage did not affect the way in which ground and liner interact, as the liner was elastic.

The problem involving sand is more complicated due to complex constitutive behaviour of sand and its proper implementation into a finite element code. In 1987 Professor R. F. Scott wrote, "…none of the constitutive models can currently represent the behaviour of very dense sand or heavily overconsolidated clay, where failure is accompanied by the development of slip surfaces." Professor Scott continued, "In finite element models, the choice of element and its associated shape function controls the possible deformation modes of the element. For that class of material, which exhibits failure surfaces or slip zones during loading, a different calculation approach may be useful. As noted by Mair and Taylor (1998), general difficulty in comparing finite element analyses with field data is that discrepancies could be due to one or more of the following: (a) deficiencies in the soil model (b) the soil parameters adopted (c) idealizations in the modeling, especially with respect to the boundary conditions, and (d) possible uncertainties in the field measurements. However, according to this author, the last two difficulties are common problems for any numerical modeling technique.

2.2.4.3 Physical modeling

The centrifuge modeling of shallow tunnel is a viable alternative to numerical modeling because self-weight of the soil influences the stability and deformations. This is probably the reason while it is hard to find any extensive three dimensional finite element case histories of tunneling in sand while the publications of centrifuge model tests on tunnels in sands is relatively large. The initial studies (Atkinson et al., 1977; Atkinson and Potts, 1977; Chambon et al., 1991; Chambon and Corte, 1994) involve uniform sand and simple tunnel models. The objectives of these works were to investigate the face stability and failure mechanism. In those tests, therefore, the tunneling process was not replicated. More recent studies (Honda et al., 2001; Nomoto et al., 1999; Imamura et al., 1996; Nomoto et al., 1996; Bolton et al., 1996) tried to model the construction process of shield tunneling in uniform sand and layered soil and associated earth pressure distribution as well as ground deformation.

As already discussed, the process of tunneling, especially shield tunneling is highly complex. Reproducing all details of the tunneling process within a small-scale centrifuge model would obviously be impossible and approximations need to be made (Taylor, 1995). A typical set up of centrifuge test for tunnel analyses is shown in Figure 2.9 (dimensions are for 5 m prototype tunnel: 50g acceleration). Taylor (1995, 1998) discussed various issues related to modeling of tunnel behaviour by centrifuge testing.

Among the simple centrifuge modeling (uniform ground and without tunnel movement) analysis by Chambon and Corte (1994) represented a three-dimensional face and therefore, some of the results from Chambon and Corte (1994)'s investigations will be discussed in Chapter 5, as the numerical modeling results from this research will be compared with the centrifuge testing results.

2.2.5 Discontinuum modeling

Soils, particularly sands, consist of discrete particles at micro level interacting with each other at contact points. It is now generally accepted that interaction of particles at micro scale, through particles as well as contact properties, governs the overall or macro behaviour. The unavailability of computational tools to numerically calculate the interaction of thousands of particles restricted the application of theory until early 70's when Peter Cundall developed discrete element method for discontinuum analyses applicable to both soil and rock (Cundall, 1971; Cundall and Strack, 1979).

One of the greatest strengths of discrete element method is that constitutive law of material is inherent in the code and need not be defined explicitly as in finite element method. The material constitutive law can be defined by micro parameters with physical meaning as opposed to continuum constitutive law of sand with large number of experimentally determined parameters. The values of micro properties in discrete element method, however, must be established indirectly, through calibration. In 2001, Peter Cundall wrote, "Rather than inventing a constitutive model that mimics overall sand behaviour through a set of manufactured (but essentially gratuitous) equations, the physical behaviour may be reproduced simply by representing directly the granular material on the computer."

As numerical modeling will continue to play greater role over other methods of analyses in analyzing complex engineering problem, an alternative to finite element modeling is desirable to solve engineering problem involving sand. This research project was, therefore, undertaken keeping this prospect in mind. The next chapter has been devoted in understanding the fundamentals of discrete element modeling and micro-mechanical analyses in general.

Table 2.1 Soft ground tunneling conditions (after Terzaghi, 1950)

Ground Category	Characteristics	Example	Stand-up time
Firm	Tunnel heading can be advanced without any roof support. Permanent lining can be constructed before the ground will start to move	Loess above the above the water table Calcareous clay with low plasticity	> 24 hours
Raveling	Chunks or flakes of material begin to drop out of the roof or the sides some time after the ground has been exposed. - Fast or slow raveling	Fast raveling: residual soil or sand with a clay binder located below the water table Slow raveling: same soil as fast raveling but above the water table	Between 24 hours and 5 minutes
Running	Material flows like granulated sugar until the slope angle becomes equal to angle of repose. Cohesive running where the run is preceded by brief period of raveling.	Clean, loose gravel and in clean, coarse or medium sand above the water table Cohesive running: clean, fine, moist sand	Zero
Flowing	Ground moves like a viscous liquid. - If the flow is not stopped, it continues until the tunnel is completely filled.	In any ground with an effective grain size in excess of about 0.005 millimeter, provided the tunnel is below water table	Zero
Squeezing	Ground slowly advances into the tunnel without any signs of fracturing and without perceptible increase of the water content of the ground surrounding the tunnel	Soft or medium clay	"Not mentioned"
Swelling	Like squeezing ground, moves slowly into the tunnel, but the movement are associated with a very considerable volume increase of the ground surrounding the tunnel.	Heavily overconsolidated clays with a plasticity index in excess of about 30	"Not mentioned"

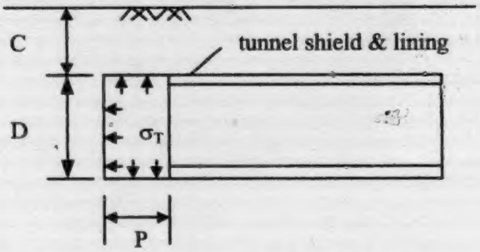
C
tunnel shield & lining
D
σ_T
P

Figure 2.1 Tunnel heading in soft ground

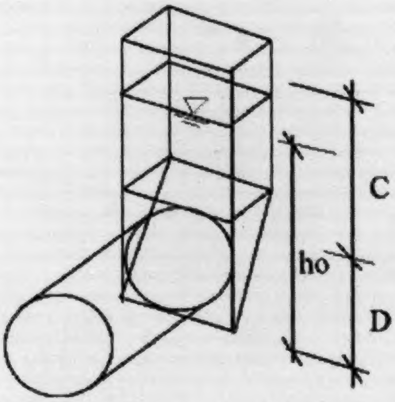

Figure 2.2 Three-dimensional sliding mechanism (after Horn 1961)

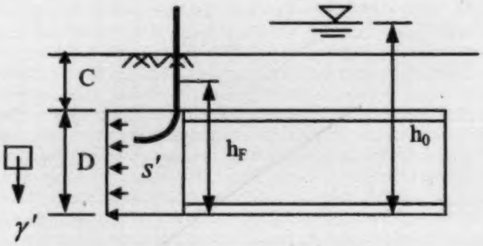
C
D
s'
h_F
h_0
γ'

Figure 2.3 Effective support pressure s' (after Anagnostou and Kovari, 1996)

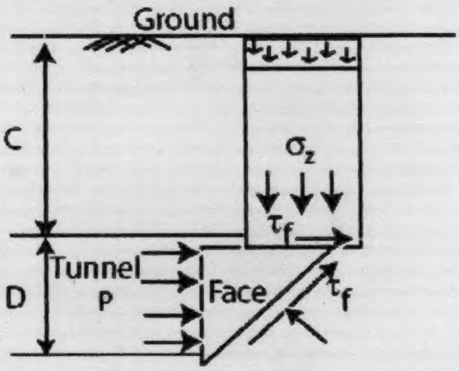
Ground
C
σ_z
τ_f
Tunnel
P
D
Face
τ_f

Figure 2.4 Typical patterns of face failure (after Vermeer and Ruse 2000)

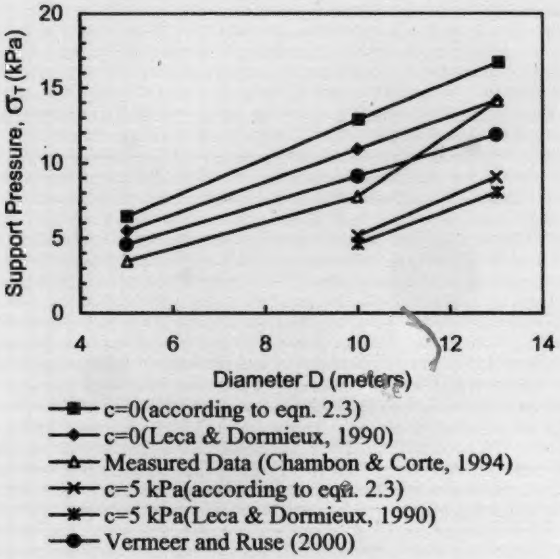

Figure 2.5 Experimentally determined and computed support pressures as a function of tunnel diameter for dry sands (modified after Anagnostou & Kovari, 1996)

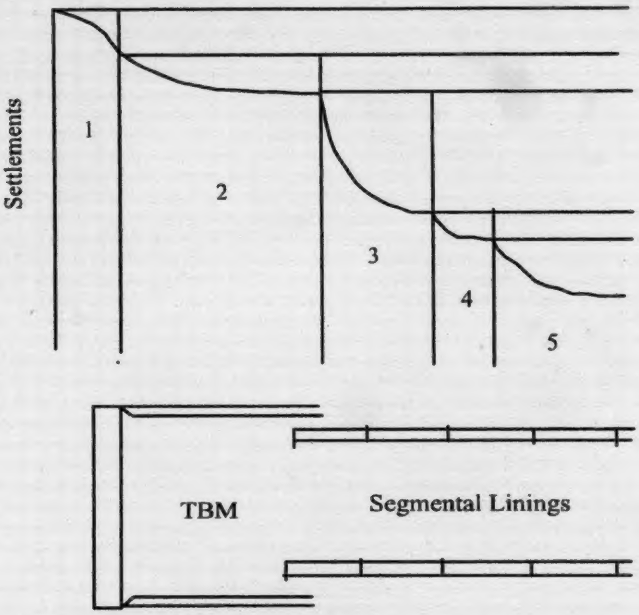
Settlements
1
2
3
4
5
TBM
Segmental Linings

Components of Ground Movements by Shield Tunneling:

1 - ground movement above and ahead the face
2 - ground movements along the TBM (overcut closure)
3 - ground movements induced at the tail void
4 - ground movements due to lining deflection
5 - ground movements due to long term settlement (soft clay only)

Figure 2.6 Components of ground movements by shield tunneling (after Maconochie et al, 2001)

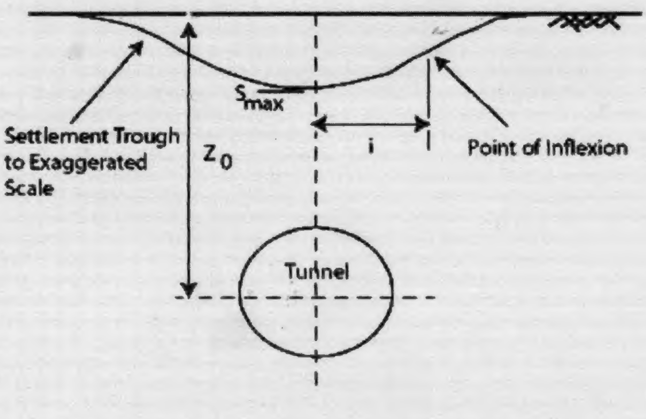
Settlement Trough to Exaggerated Scale
Smax
Z0
i
Point of Inflexion
Tunnel

Figure 2.7 Transverse settlement trough over a tunnel

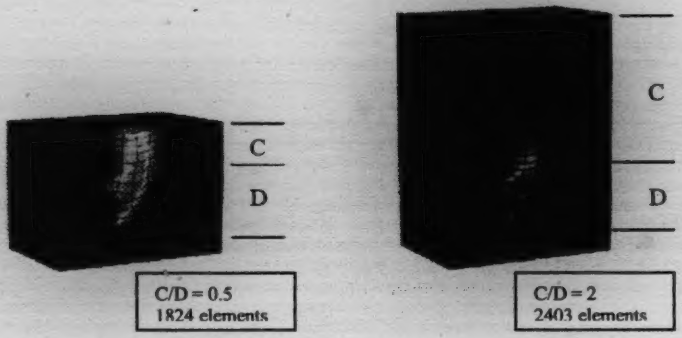
C
D
C/D = 0.5
1824 elements
C
D
C/D = 2
2403 elements

Figure 2.8 Computed failure mechanisms for drained soil conditions, γ=20 kN/m^3, c=5 kPa, ϕ=27.5^0, D=5 m (after Vermeer and Ruse 2000)

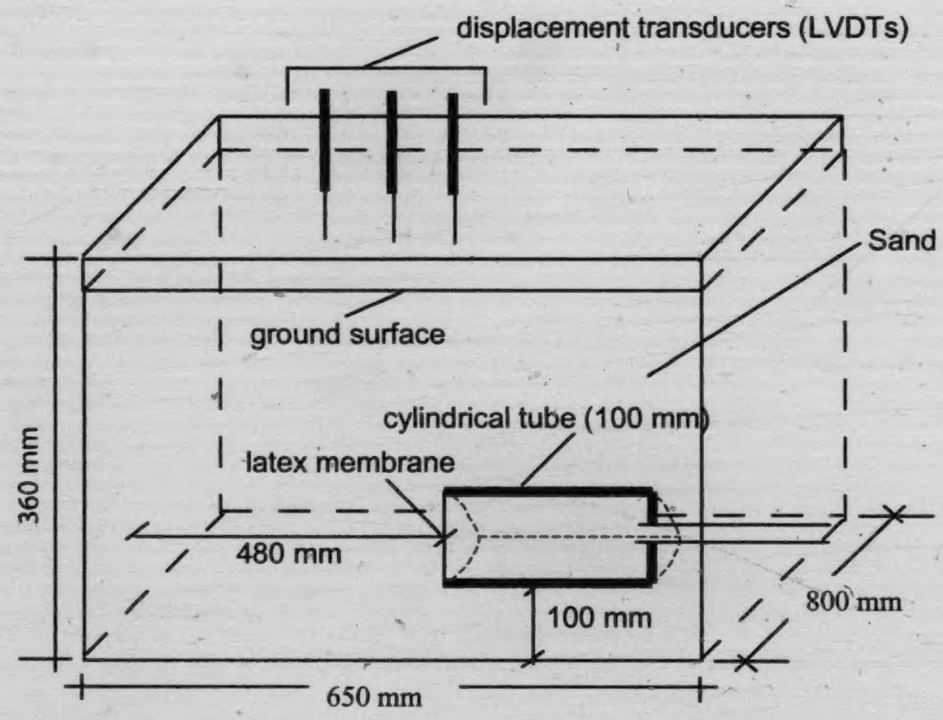
displacement transducers (LVDTs)
Sand
ground surface
cylindrical tube (100 mm)
latex membrane
360 mm
480 mm
100 mm
800 mm
650 mm

Figure 2.9 Schematic of centrifuge model (modified from Chambon & Corte, 1994)

CHAPTER 3

Micromechanical Approach Leading to Computational Granular Mechanics

As discussed in Chapter 2, until recently, most studies involving granular or particulate materials have utilized macro-scale behaviour or equivalent continuum approach. The continuum approach is required to solve large boundary value problems of practical engineering interests. This still remains the main approach today. However, granular materials like sands are fundamentally discrete in their nature composed of interacting discrete solid elements. Therefore, micro-scale behaviour of particle interaction influences the macro-scale properties.

Two different fields of approach for micromechanics based granular material research can be identified: (1) indirectly by theoretical based micro-structural continuum approach or the multi-scale approach and (2) direct approach of computer simulation by discrete numerical models. In the micro-mechanical approach, constitutive law for a granular assembly is derived, via a homogenization procedure, from the equilibrium, the kinematics, and force-displacement relations of two particles in contact. The objective is to derive any constitutive behaviour to be used in continuum based numerical method, from the knowledge of the local or microscale behaviour and microstructure. The coefficients in the resulting constitutive formulation can then be directly related to micro-scale properties, such as contact stiffness, particle density and particle size (Suiker et al., 2000).

The discrete numerical approach has evolved owing to the tremendous development of computer hardware and software in the 1970's, which is continuing to date. The fundamental assumption in this approach is that granular material is an assembly of discrete particles, which interact only at contact points. This has virtually eliminated the need to achieve constitutive behaviour from micromechanical approach and then incorporate into the continuum method to solve boundary value problems as can be seen in some earlier researches on micro-mechanical numerical models (Chang and Misra, 1989b; Chang and Misra, 1990a, 1990b; Chang et al., 1991a, 1991b; Wan and Guo, 2000). Instead the constitutive law is inherent in this new approach and the method has the potential to be used directly to simulate practical engineering problems.

Only the computer based discrete modeling will be reviewed as it will be used as the fundamental tool in this research. In the following, an overview of micro-mechanically based granular modeling is given. This includes definition and concept of the approach and fundamental differences with the continuum approach. Also different variables classically used to describe the approach are outlined. This is then followed by description of basic characteristics of discrete modeling of granular behaviour i.e. discrete element method (DEM). Outline of the commercially available DEM tool, Particle Flow Code (PFC) is presented (Itasca, 1999). Finally, a discussion on micro-scale parameters needed as input parameters in any DEM simulations is presented.

3.1 Micro or Particulate mechanics

Micro-mechanics is a broad subject area covering experimental investigation, analytical prediction and numerical modeling. This is quite distinct from traditional physical tests on soils where measurements inside the samples are difficult and is generally overlooked. The macroscopic (overall or averaged) behaviour of granular materials is determined not only by how discrete grains are arranged in space, but also by what interactions are operating among them (Satake et al., 1999). In other words, as discussed by Oda (1972), macroscopic response is the interplay of various micro parameters of which most noticeable are 'fabric' or microstructure of an assemblage and constitutive law of individual particle (particle stiffness and friction). As a result of this new insight into granular material behaviour, micro-scale deformation is being studied in greater details and theories are being laid out about micro-deformation. In fact, plasticity in geomaterials is now seen as a direct result of micro-scale particle sliding and rolling (Bardet, 1994; Cambou, 1998; Iwashita and Oda, 2000). In section 3.2.2 these basic micro parameters are defined and elaborated as well as mechanisms of plastic deformation at micro or grain scale is discussed.

Cundall (2001) laid out an impressive and appealing case of a future for numerical modeling in geomechanics based on discontinuum. Some of the fundamental differences between continuum and micro-mechanics based discontinuum approaches and their relative merits/demerits are discussed in section 3.2.1. Although granular micro-mechanics are being investigated by experimental, analytical as well as numerical modeling, only the numerical discrete modeling has caught much attention in recent years. An overview of this approach is given in section 3.2.3.

Only the concepts dealing with the quasi-static behaviour of granular materials as relates to this research, in which inertia is negligible, have been covered. It should be reminded that, as discussed by Satake et al. (1999), the subject area is complex and vast and full framework of micro-mechanical analyses has not yet been firmly established.

3.1.1 Continuum vs. Discontinuum

From a microscopic point of view, all material bodies are composed of discrete molecules (particles), which are connected to each other by forces of mutual attraction and repulsion (Harr, 1977). However, mechanical behaviour of all engineering materials, from man made materials such as steel to geological materials such as soils and rocks, is simplified by the assumption of displacement continuity within the material.

One of the major assumptions of continuum mechanics is that the material properties can be scaled from small laboratory samples to large material masses using constitutive relations (Bardet, 1998). Finite elements analyses could be more useful for explaining and predicting displacements if satisfying constitutive equations were available (Biarez and Hicher, 1987). Therefore constitutive law plays a major role in successful application of continuum principles to solve engineering problems. Unfortunately, stress-strain relationship of geological materials is not as straightforward as man made materials; for example, pressure and initial void ratio dependency; non-linearity even at small strain; effect of dilation on strength; softening after peak strength; effect of intermediate principle stress; anisotropy are few of the complexity involved. Hence, as discussed by Imam (1999), the literature on constitutive modeling of granular materials is extensive extending from simple elasto-plastic to more sophisticated (strain or work-hardening plasticity) and advanced models such as Lade's curved yield surface model (1977); double hardening model (Vermeer, 1978); bounding surface plasticity (Bardet, 1986); hypoplasticity (Kolymbas and Herle, 1998); etc. are the few among them. An overview of constitutive models for sands, as those mentioned above and others, is given by Reza Imam (1999). The shortcomings of the traditional continuum based constitutive models of sands have been discussed by various authors (Tordesillas et al., 2004; Scott, 1987a,b). As noted by Tordesillas et al. (2004), the overwhelming majority of these models can be classed as phenomenological, as they contain no direct link to the underlying cause of bulk deformation, namely particle motion and interactions. Specifically, these models are expressed in terms of curve-fitting parameters, which require considerable calibration through laboratory experiments, and even then there is still no guarantee that these parameters agree with those obtained in situ. In most of the cases the number of constants are too many and some of them without any physical meaning (Scott, 1987a). Scott (1987a) showed that the number of constants increased from two to 40 during the period 1960 to 1987. Obviously, the scenario gets more complicated when three-dimensional constitutive laws are to be formulated. As discussed by Bardet (1998), another difficulty with the continuum approach as applied to granular materials lie in modeling shear banding or bifurcation phenomenon which is commonly observed in soils and rock.

An alternative path to modeling granular material behaviour would be to consider their discrete nature and get rid of the complex continuum mathematical formulations with many coefficients. In fact, many of the features of granular materials such as dilation and local nonhomogeneity depend on its particulate nature. In this alternative approach, which is generally termed discontinuum as oppose to continuum, the continuum is replaced with an assembly of particles. The complex behaviour observed in sand derives, in large part, from microscopic geometric changes induced by loading, and, to a lesser extent, from basic contact laws between particle pairs (Cundall, 2001). Discrete modeling can be of great help to continuum mechanics, for not only developing constitutive models based on physics, but also for understanding physical origins of material instability, and the limitations of continuum mechanics (Bardet, 1998).

3.1.2 Micro-structure

Two fundamental components of a micro-mechanical modeling are (i) particles and (ii) particle contacts. Particles are considered to be the idealization of grains in any granular material, e.g., sand grains. The size and gradation of particles as well as shape are one of the concerns. For simplicity circular or disk shaped in two dimensional and spherical in three-dimensional are usually considered. Existence of contacts or interfaces between particles is a unique characteristic of micro-mechanics that distinguishes it from continuum approach. At the heart of the micro-mechanical modeling exists a contact relation or contact constitutive law. Various contact laws are available and used in the literature (Misra, 1995; Johnson, 1985;). Details of particles and their contacts will be discussed later in section 3.2.4. Here the discussion will be limited to various parameters defining microstructure of an assemblage of particles at micro-scale and their relation to macroscopic stress and strain.

The primary goal of the researchers in micromechanics of granular behaviour is to formulate a suitable macro behaviour in terms of micro-parameters. Many researchers have been working towards this goal with varying success (e.g. see Mason and Martinez, 2001; Misra, 1995; Chang et al., 1992a,b; Chang and Misra, 1990a,b). In order to transfer the discrete parameters to corresponding macro parameters, the local internal structure (called microstructure or fabric) of a granular mass and parameters those define that must be understood. First of all, it is important to know what 'fabric' is meant in a granular mass from a micro-mechanics point of view.

Oda (1972) made an important contribution in establishing relationships between microstructure of sand and its mechanical properties. He defined 'fabric' as a concept to represent the spatial arrangement of solid particles and associated void. Two important parameters defining fabric are: (1) orientation of an individual particle, and (2) position of the particle and its mutual relationship to other particles or packing. The orientation of a nonspherical particle can be represented by the inclination of the longest and the shortest axes of the grain to the fixed directions (Figure 3.1). Oda (1972) showed that the characteristics of fabric of a sand mass closely related to the shape of particles and manner in which they were deposited. It was found that orientation fabric of sand, consisting of relatively spherical particles, almost isotropic. One of the findings, which will have a great significance later in formation of synthetic samples in chapter 4, was that, mobilized strength of dense sand samples consisting of relatively spherical particles was almost independent of their initial fabric character. This is because, according to the author, when samples of spherical particles are deformed, rearrangement and re-orientation of sand grains may occur easily resulting in a similar ultimate fabric at regardless of their initial fabric.

The packing or mutual relation of individual particles to neighboring particles is best represented by a parameter called co-ordination number. The coordination number (of a particle),

C_n, is the average number of contacts per particle. The average coordination number of an assembly or a represented volume of the assembly is

$$C_n = \frac{M_V}{P} \tag{3.1}$$

where M_V=total number of contacts within the assembly volume

P=total number of particles

The coordination number characterizes the density of the packing between particles of a given granular medium. Researchers have shown that high correlation exists between C_n and global density variables (void ratio, density, porosity). It is postulated that the greater the value of C_n, the higher the stability of the packing. Oda (1977) analyzed the co-ordination number in the random assemblies of glass particles to evaluate the stability of cohesionless soils against applied external forces. Oda (1977) concluded that mean value of co-ordination number is closely related to the mean value of void ratio.

3.1.2.1 Definition of stress

Stress is a continuum quantity and therefore does not exist at each point in a particle assembly, because the medium is discrete (PFC manual, 1999). However, various researchers have tried to formulate micro-structural equivalent stress tensor for granular materials. Here there is no meaning to the term "stress at a point," because forces may fluctuate widely from point to point; therefore, an estimate of stress is only possible over a finite volume of space (PFC manual, 1999). A generally accepted description of average stress tensor in terms of the summation of discrete contact forces and fabric can be expressed as (Bathurst and Rothenburg, 1988):

$$\overline{\sigma}_{ij} = \frac{1}{V}\sum_{c\in V} f_i^c l_j^c \quad \text{I, j = 1,2 [two dimensional]} \tag{3.2}$$

where f_i^c and l_j^c refer to scalar components of contact forces $\mathbf{f}^c$ and contact vectors $\mathbf{l}^c$ at contact locations (see Figure 3.2).

With the aid of the virtual work principle, equivalent expressions for three-dimensional idealized granular assemblies have been reported by Christoffersen et al. (1981) as:

$$\overline{\sigma}_{ij} = \frac{1}{n}\sum_{\alpha=1}^{N} t_{ij}^{\alpha} \equiv \langle t_{ij} \rangle,\ t_{ij}^{\alpha} = nf_i^{\alpha} l_j^{\alpha} \text{ (}\alpha\text{ not summed),} \tag{3.3}$$

where n is the number of contacts in volume V (taken as the unit of volume). Similar to the two dimensional case (equation 3.2), f_i^{α} and l_j^{α} refer to scalar components of contact force $\mathbf{f}^{\alpha}$ at contact α and contact vector $\mathbf{l}^{\alpha}$ that connects the centroid of two grains in contact at α; the stress is assumed to be symmetric.

As discussed by Bathurst and Rothenburg (1988), the above is an approximation to the stress tensor of continuum mechanics for granular media comprising large but finite number of rigid particles. Hence stress calculated from equation (3.2) or (3.3) would be expected to fluctuate from subvolume to subvolume. The fluctuations can be expected to become smaller as the subdomain volume becomes larger (hence, number of particles). It is also an accurate analogue to the continuum stress tensor for finite but large number of particles. However, it requires exact knowledge of contact forces and contact vector terms for all particles (Bathurst and Rothenburg, 1988). Hence an alternate definition is sought by some researchers using a purely static approach and considering that for a particulate material, stresses exist only in the particles. The average stress tensor $\overline{\sigma}_{ij}$ in a volume V of material with N_p particles, is defined by

$$\overline{\sigma}_{ij} = \frac{1}{V}\sum_{N_p} \overline{\sigma}_{ij}^{(p)} V^{(p)} \tag{3.4}$$

where $\overline{\sigma}_{ij}^{\ (p)}$ is the average stress tensor in particle (p); $V^{(p)}$ volume V containing N_p particles.

The average stress tensor in a particle (p) is given by

$$\overline{\sigma}_{ij}^{(p)} = \frac{1}{V^{(p)}} \int_{v(p)} \sigma_{ij}^{(p)} dV^{(p)} \tag{3.5}$$

3.1.3 Micro-scale deformation during slow and quasi-static loading

Unlike continuum materials, deformation of granular materials like sand produces movement of individual particles. Although the particles themselves may deform, this deformation is localized near contacts, and deformation of granular material results primarily from the shifting of particle centers (Kuhn, 1997). This fundamental assumption is quite reasonable for hard quartz particles and is well accepted. There have been few attempts to quantify and visualize the deformation that results from particle movements i.e. microscale deformation. The most rigorous among them are the theoretical as well as experimental description of Oda (1972, 1997); Oda et al. (1980, 1982); and Satake (1992, 1993) known as particle chain and particle graph method, respectively. In the followings, these two methods are described with the intention that they will enable us to understand what's happening in granular medium subjected to slow loading.

Method 1: Particle chain and deformation measures

In this method deformation is viewed as a combination of stretches and shears along the chains or "solid paths" (Kuhn, 1999). The method had its inception in early stress-dilatancy studies (Rowe 1962; Horn 1965a,b). Oda (1997), by means of optical analysis using microscope and thin sections on five different sands, experimentally established and viewed the method as development of column-like structure extending parallel to the major principal stress direction up to failure (Figure 3.3a). The axial stress is mainly transmitted through this column and gradually increases until peak stress and finally starts to buckle (Figure 3.3b). Oda tried to relate these column structures to large voids inside shear band and proposed a possible dilatancy model for granular soil. During strain hardening process, small voids between the columns are connected to make ellipsoidal ones (Figure 3.3a) and in the strain softening process, voids are gradually enlarged between the buckling columns. Also particle rotation and resistance to it plays crucial role during the shear banding in addition to slipping at contacts. Hence, traditional sliding based concept of micro mechanical deformation is replaced by both sliding and rolling at contact. Numerical simulation of idealized granular media by Oda et al. (1982) and Bardet and Proubet (1991, 1992) had also confirmed the above finding.

Hence at the heart of particle chain method developed by Oda is particle rotation as the dominant micro deformation phenomenon, especially when interparticle friction is large. Two technical terms, rolling and rotation, must be carefully distinguished (Iwashita and Oda, 1998). The former denotes a micro-mechanism of deformation taking place at contacts, while the later denotes pure rotation with respect to a reference axis. Following is the theoretical background on micro deformation mechanism based on rolling and sliding at contact between two particles (Bardet, 1994 and Iwashita and Oda, 1998).

Deformation Measures: Rolling and Sliding

For simplicity, let us consider a plane strain condition of assembly of particles, which is being incrementally deformed. Two particles 1 and 2 are in contact during the small time step from t to t + dt, as shown in Figure 3.4. The terms in the figure are explained below:

C and C' - contact points before and after deformation

C_1' and C_2' – position of material point at C after deformation at particles 1 and 2, respectively

$\boldsymbol{n}$ and $\boldsymbol{n}'$ – unit vectors normal to the contact surfaces at C and C'

$d\beta$ - angle between $\boldsymbol{n}$ and $\boldsymbol{n}'$

$d\theta_1$ and $d\theta_2$ – incremental rotations (in radian) of particles 1 and 2, respectively (counterclockwise rotation being positive).

The arc lengths CC'_1 and $C'C_2'$, which represent the displacement of the contact point C on each particle, are given by

$$da = r_1(d\theta_1 - d\beta) \qquad db = r_2(d\theta_2 - d\beta)$$

where r_1 and r_2 are the radii of particles 1 and 2, and da and db are positive when measured counterclockwise

The relationship between da and db represents the condition of the nature of deformation between two contacting particles. If da equals –db, pure rolling occur. If da equals db, pure sliding occurs without contact rotation. These are the two extreme cases; contacts may be successively and/or simultaneously rolling and sliding. da and db can now be expressed in terms of rolling (dUr) and sliding (dUs) displacements as follows:

$$da = dUr + dUs; \qquad db = -dUr + dUs$$

Or $$dUr = (da - db)/2 \qquad dUs = (da + db)/2$$

where minus sign for dUr in db indicates that rolling causes opposite signs for da and db. It should be noted that a displacement component dUn also takes place parallel to contact normal **n**.

A contact constitutive model can now be defined based on the above description of contact normal (dUn), contact rolling (dUr) and contact sliding (dUs) displacements. This important representation of contact constitutive law will be further illustrated in section 2.3.3.

Method 2: Void based Deformation measure – Particle Graph Method

This method is based upon the graph-theoretical work of Satake (1992, 1993). The method explicitly considers the void between particles in a granular assembly. It is assumed that the particles are circular and rigid and overall deformation is caused only by relative displacements at contact points. The method is basically developed for two-dimensional assembly of particles.

As is shown in Figure 3.5, an assembly of granules is replaced by a graph called the *particle graph*. The three elements of particle graph; point, branch and loop correspond to those of the assembly; particle, contact and void, respectively. In case of three dimensional, number of elements in a particle graph becomes four and the correspondence between elements of the graph and those of the assembly is explained in Table 3.1.

Details of the mathematical background of this method are omitted here due to its limited application and lack of general acceptance to micromechanical research. However, the underlying concept of the method has a potential application in visualizing the micro deformation through numerical experiments as is described below.

Application of particle graph method

Recently Kuhn (1999) applied the method to numerical experiments on a large two-dimensional assembly of circular disks. In order to measure deformation of individual voids at microscale, void cell geometry and their evolution during biaxial compression were described. In its initial state, the particle graph had contained 3950 void cells, 7727 contacts and 3777 load bearing particles. The following changes were observed during the biaxial test.

- As biaxial compression proceeds, the number of void cells is reduced, and their average size increases.
- The void cells become monotonically larger and more elongated in the direction of compression, primarily due to loss of contacts between particles and their horizontally oriented neighbors.
- The more vertically elongated void cells tend to dilate; whereas, horizontally flattened void cells tend to compress.
- Slipping and energy dissipation occurs at particle contacts, which form the edges of a particle graph; whereas, deformation occurs within the void cells that form the faces of the graph.

The last point is used to explain the initial contraction and subsequent dilation of dense granular material. The apparent discrepancy between overall, macroscale compression while the average void cell size and effective void ratio grow continually larger is due to the fact: average void cell shape is initially isotropic and hence void cell elongation initially has no effect on volume change. The early reduction in void ratio is a consequence of an increasing mean stress, which pushes the particles more closely together. As the vertical stress increases and the voids become vertically elongated, their average behaviour becomes increasingly more dilatant, eventually causing the entire assembly to expand.

One of the important conclusions drawn by the authors was that local void fabric and deformation was interrelated. The interrelation was dynamic, with void fabric changing significantly as deformation proceeds and, in turn, affecting the subsequent deformation.

3.1.4 Plasticity at micro-scale

Plasticity theories have been an important development in engineering to analyse failure and flow. One of the fundamental questions to the theoretical investigator as well as practitioner is why soils behave as they do when stresses become too severe (Davis and Selvadurai, 2002). So far the continuum theory of plasticity has enabled us to explain the macroscopic inelastic response of soil as observed through the laboratory tests. This has been an important development and enhanced our understanding of soil behaviour. However, to better understand the phenomenon of failure in soil, there is now renewed interest to analyse soil response at micro-scale and how grain contact deformation is related to overall inelastic response.

All the classic stability problems in soil mechanics such as slopes, retaining walls, tunnel as well as foundations are the result of intense deformation manifested along shear bands or discontinuities (Davis and Selvadurai, 2002). This intense shear strains occur because of large shear stresses. As the shear strain grows, particle structure or fabric is disrupted. This could be result of particle rearrangement and/or from particles fracturing or crushing. However, at low stress, only particle rearrangement can trigger the fabric change (Oda, 1977). These two mechanisms, fracture and rearrangement, combine to produce the irreversible effects we call plasticity (Davis and Selvadurai, 2002). For non-cohesive granular material such as sand, a typical feature is the absence of the elastic domain even for small shear loading, but the immediate occurrence of plastic flow (Ehlers et al., 2001). This may certainly be the result of rearrangement. These observations indicate that inelasticity observed in granular mass could be direct result of micro-scale particle movements.

It is now generally understood that global recoverable strain is due to elastic deformations of the contacts between particles and that irrecoverable global strain is linked to sliding and rolling occurring between particles in contact (Cambou, 1998). In fact, many experimental results (Oda et al., 1982, Bardet, 1994) seem to demonstrate that the prevailing phenomenon to explain inelastic or plastic strain is the rolling between particles. This point has already been discussed above.

3.1.5 Numerical modeling of discontinua

As is seen above, one of the requirements of micro-mechanical analyses of granular assembly is to measure discrete quantities such as forces between particles and displacements and rotations of individual particles. This is difficult in physical experiments. Possibly the most powerful way of modeling assemblies of discs and spheres is by numerical techniques. Numerical modeling is more flexible in application than analytical modeling and has the advantage over physical modeling that any data are accessible at any stage of the test (Cundall and Strack, 1979). The rapid advancement of computer during 70's has revolutionized the modeling by introduction of the computer code BALL by Cundall (Cundall and Strack, 1978) and shifts the focus of micro-mechanical modeling from analytical/experimental to computer simulations.

Cundall and Hart (1992) identified three important aspects of numerical modeling of discontinua, popularly known as discrete element program as:

1. the representation of contacts,
2. the representation of solid material, and
3. the scheme used to detect and revise the set of contacts

According to the authors, any discrete element program should be capable of (1) allowing finite displacements and rotations of discrete bodies, including complete detachment, and (2) recognizing new contacts automatically as the calculation progresses. There were four main classes of computer programs that conform to the proposed definition of discrete element method (Cundall and Hart, 1992). Table 3.2 summarizes the attributes, advantages and shortcomings of the methods. Later Bardet (1998) add four more to this class of program namely, contact dynamics, structural mechanics methods, mean field and energy minimization method.

The choice of program for this research project i.e. particle flow code in three-dimensional or PFC^{3D} belongs to discrete element method, popularly known as DEM. It is therefore natural to present an in-depth discussion on DEM and is done in the following section.

3.2 Discrete element method and Program PFC^{3D}

Initially discrete element method (term 'distinct element method' was used in the publication) was introduced by Cundall (1971) for the analysis of rock mechanics problems. Later Cundall and Strack (1979) applied the method to soils. A thorough description of the method is given in the two-part paper by Cundall (1988) and Hart et al.. (1988). In section 3.3.2, the method is presented in relation to the points of most important aspects of a discrete numerical modeling i.e. representation of contacts and solid materials and scheme to detect and revise set of contacts. There are some DEM codes which are currently being used namely TRUBAL; UDEC; 3DEC; DIBS; 3DSHEAR; JP2 and most recent PFC^{2D}/PFC^{3D}. The idea of PFC originated from the need to simulate the caving process, the flow of broken rock in mining (Guest and Cundall, 1994). A description of the code is given in section 3.3.3.

3.2.1 Fundamental concepts

3.2.1.1 Representation of contacts

In DEM individual particles or bodies may be rigid or deformable, but contacts are always deformable. Hence, the interface stiffness that connect force and displacements at particle contacts, play a central role. This so called 'soft contact' concept was explained by Cundall and Strack (1979) and Cundall and Hart (1992). Since contact forces are related to contact displacements, one body must interpenetrate the other to produce any finite value of contact force. What really happens is that surface deformation occurs rather than interpenetration. This overlapping behaviour, in fact, represents particle deformation for particles with simple geometry e.g. sphere and overlaps are small in relation to the particle sizes.

In order to calculate the unbalanced contact force from the relative movement at a contact point, contact behaviour is idealized, as discussed by Oda and Iwashita (2000) and Fortin et al. (2002), by using a set of elastic springs (to provide repulsive force), dashpots (to dissipate a portion of the relative kinetic energy) and shear slider. Figure 3.6 represents the force-displacement relationship (contact model) between two disks without rotational stiffness and friction. The contact relationship is activated when the disks overlap. The character and values of the contact stiffness, k_n (normal) and k_s (tangential), together with interparticle friction, μ, therefore, plays a major role in simulating intergranular behaviour (c represents cohesion and is not considered for granular simulations).

An excellent study of interface stiffness including every possible interface conditions was presented by Misra (1995). The author described the expressions for stiffnesses and their backgrounds in details for a generalized contact relation, which also includes torsional and rolling or rotational stiffness. However, most of the DEM's including PFC consider contact relation without rotational stiffness that is rolling occurs freely without providing any resistance against it. The absence of rotational stiffness in conventional DEM such as PFC can be compensated by non-spherical shaped particles. Also, for simplicity, only interface of smooth cylindrical or spherical elastic particles are assumed. Therefore, in the following paragraphs, only a summary of derivations for k_n and k_s are given.

The first organized study of force-deformation behaviour of particle interface is credited to Hertz (1885), who studied the contact of frictionless non-conforming elastic bodies under normal loads. Later Mindlin (1949) and Mindlin and Deresiewicz (1953) extended the theory to combined normal and tangential loads. A brief presentation of Hertz-Mindlin contact law is given below.

Considering the contact area to be circular with a parabolic pressure distribution, the deformation of the particle in the vicinity of the point of contact is obtained using the linear elasticity theory of pressure load on elastic half space (Johnson, 1985). This leads to the expression of the radius of the contact area, *a*, in terms of the normal force at the interface, *N*, and the elastic properties of the particles, as follows:

$$a = \left(\frac{3NR}{8E}\right)^{1/3} \tag{3.6}$$

where

$$\frac{1}{E} = \frac{1-\nu_1}{2G_1} + \frac{1-\nu_2}{2G_2}, \qquad \frac{1}{R} = \frac{1}{2}\left(\frac{1}{R_1} + \frac{1}{R_2}\right)$$

G_1 and G_2 are the shear moduli, ν_1 and ν_2 are the Poisson's ratios, R_1 and R_2 are the radii of the particles in contact.

Noting that $\delta_n = \frac{a^2}{R}$, rearranging equation (3.6) gives:

$$N = \frac{4}{3}E(R\delta_n^{\,3})^{1/2} \tag{3.7}$$

where N is the total normal force and δ_n is the normal relative displacement of particle centers

The resultant normal stiffness is expressed by

$$k_n = \frac{dN}{d\delta_n} = 2E\left(\frac{3NR}{8E}\right)^{1/3} = 2Ea \tag{3.8}$$

The resulting force-displacement relationship defined by equation (3.7) indicates a non-linear behaviour (Figure 3.7a). This study, originated by Hertz (1885), was extended by Mindlin (1949) to take into account the supplementary influence of a tangential force T at the contact of two spheres by introducing Coulomb's friction law along the surface of the contact zone. Under a monotonically increasing tangential force, Mindlin (1949) demonstrated that, for a constant normal force N, the effect of applying a tangential force $T<\mu N$ is to cause a small relative tangential motion or slip, over part of the contact area and localized on an annular surface and form an annulus of slip. When T becomes equal to μN, this zone (annulus of slip) extends to the entire zone of contact and, consequently, relative displacement of the two spheres takes place.

Mindlin and Deresiewicz (1953) generalized the theory by taking into account the effect of oscillating tangential force accompanied by varying normal force. Thornton and Randall (1988) provided a concise form of the resulting tangential stiffness as follows

$$k_s = 8Ga\left(\frac{1}{\theta} \pm \frac{\Delta N \tan\phi_\mu}{\Delta T}\left[\frac{1}{\theta} - 1\right]\right)^{-1} \tag{3.9}$$

where

$$\frac{1}{G} = \frac{2-\upsilon_1}{G_1} + \frac{2-\upsilon_2}{G_2}$$

$$\theta^3 = 1 - \left(\frac{T}{N\tan\phi_\mu} + \frac{\Delta N}{N}\right) \qquad \text{(virgin loading)}$$

$$\theta^3 = 1 - \left(\frac{T^* - T}{2N \tan \phi_\mu} + \frac{\Delta N}{N} \right) \qquad \text{(unloading)}$$

$$\theta^3 = 1 - \left(\frac{T^{**} - T}{2N \tan \phi_\mu} + \frac{\Delta N}{N} \right) \qquad \text{(reloading)}$$

and T* and T** are the loading and unloading reversal points, respectively, as shown in Figure 3.7b.

As indicated in section 3.1.3, relative displacement at a contact point can, in general, be decomposed into two components: sliding and rolling. In the conventional DEM like PFC^{3D}, rolling occurs freely without providing any resistance against it.

3.2.1.2 Representation of solid material

The material comprising the individual particle may be assumed rigid or deformable. The assumption of material rigidity is a good one when most of the deformation in a physical system is accounted for by movement of discontinuities or discrete particles along interfaces. At a low to medium stress level, the deformation of a packed-particle assembly, or a granular assembly such as quartz sand, as a whole is described well by this assumption, since the deformation results primarily from the sliding and rotation of the particles as rigid bodies and the opening and interlocking at interfaces and not from individual particle deformation.

As this research work deals only with the hard quartz minerals (like Ottawa sand grain) the case of deformable particles, which is more appropriate to model particle breakage, will not be considered hereafter.

3.2.1.3 Numerical Implementation

Figure 3.8 represents the basic calculation scheme in DEM (Dobry and Ng, 1992). The algorithm of any DEM simulation consists essentially of two stages. First of all, forces are computed from the relative displacement using an interaction law that allows particle to interpenetrate each other. Movements result from the propagation through the particle system of disturbances caused by a specified wall and particle motion and/or body forces. In the second stage, Newton's second law is used to determine, for each particle, the resulting acceleration, which is then time-integrated to find the new particle positions. This process is repeated i.e. force-displacement law continues to update the contact forces and Newton's second law determine the motion of each particle arising from the new contact forces in addition to the body forces, until convergence is achieved. Hence, this is a dynamic process in which speed of propagation depends on the physical properties of the discrete system.

A timestepping algorithm in which it is assumed that the velocities and accelerations are constant within each time-step represents the dynamic behaviour numerically. The completion of the above two stages constitutes one calculation cycle and represents an increment of time equal to the time-step. The solution scheme is identical to that used by the explicit finite-difference method for continuum analysis. Thus modeling follows a sequence of locally determined dynamic equilibrium states rather than a series of globally determined static equilibrium states (Last and Harkness, 1991). In order for the equilibrium to be assessed locally in this way, the incremental time-step between successive sets of calculations must be small enough to prevent propagation of information beyond neighboring calculation points within such a step (the scheme is conditionally stable).

For static problems one possibility is the use of the technique called 'dynamic relaxation', in association with the finite difference method; the computations are set up as for a dynamic problem, but in which the damping is artificial (Scott, 1987a). As also discussed by the author, the significant advantage of the dynamic relaxation technique used with the finite difference operation lies in its application to non-linear problems, and particularly those involving unstable material behaviour.

3.2.2 Particle Flow Code in 3D (PFC^{3D})

PFC can be viewed as a simplified implementation of the DEM because of the restriction to rigid spherical particles (a general DEM can handle any arbitrarily shaped of particles as well as deformable particles). Hence, all the foregoing discussion on micro-mechanics and discrete element method mentioned in section 3.2 and 3.3, respectively is also applicable to PFC. Details of the logics involving formulation and simulation of a model by PFC can be found in four volume PFC manuals. Cundall and Carranza-Torres (2004) summarized the details of calculation cycle performed in PFC including law of motion and force-displacement law.

3.2.2.1 Basic entities

The two basis entities in PFC are particles, which is termed as 'balls' in three-dimension, and walls (Figure 3.9). The term 'particle' denotes a body that occupies a finite amount of space as opposed to more usual definition in the field of mechanics where it occupies only a single point in space. The particles can be free (usual for the case of unbonded material such as sand) or can be bonded together at their contact points (to model solid materials). The granular material is approximated as a compacted assembly of many small particles. Figure 3.9 shows such an assembly bounded by four walls. A wall is a plane that has arbitrarily defined contact properties. A wall has one 'active' side, which only can interact with particles. Walls are used in PFC both to define boundaries of a model and assist with the generation and compaction of particles.

The particles and walls interact with one another via the forces that arise at contacts (due to external excitation). In Figure 3.9 the black lines denote the contact forces between particles and particle and wall. Forces acting on a wall do not influence its motion. Instead, its motion is specified by the user and remains constant regardless of the contact forces acting upon it.

3.2.2.2 Contact models

In PFC, the contact constitutive model consists of three parts: a stiffness model; a slip model; and a bonding model (for cohesive or rock materials). The normal stiffness is a secant (total) and shear or tangential stiffness is in incremental form. Two contact-stiffness models are provided by PFC^{3D}: a linear model; and a simplified Hertz-Mindlin model.

PFC^{3D} allows particles to be bonded together at contacts. Two bonding models are supported: a contact-bond model and a parallel-bond model. Both bonds can be envisioned as a kind of glue joining the two particles. The contact bond can only transmit a force, while the parallel bond can transmit both a force and a moment.

3.2.2.3 Damping

As has been discussed above the current DEM operates in dynamic mode and so does PFC. However, the program can be used to model both static or dynamic problems. But the full dynamic equations of motion are solved even when the static solutions are required. This is advantageous to follow such phenomena as failure and ‘flow’ of material in a realistic manner. For a static problem, the system either reaches equilibrium or starts to collapse. By default, PFC operates in ‘static’ mode – that is, internal damping is applied that causes the system of particles to reach equilibrium in a minimum number of cycles. The type of damping embodied in PFC acts to suppress accelerating motion rather than velocity i.e. local non-viscous damping is available to dissipate energy, in addition to frictional sliding, by effectively damping the equation of motions. The damping force is controlled by the damping constant α which is related to the ‘specific loss’ as defined by Kolsky (1963) as the ratio of energy lost per cycle to maximum energy stored. An additional force vector is added to the unbalanced force vectors. Similar is also applied to the rotational degrees of freedom.

3.2.2.4 Time step

For any given time step, force displacement equations are evaluated for all contacts assuming velocities and positions are fixed; the laws of motion are applied by assuming all forces and moments are fixed (Cundall, 2004). As a requirement of central difference scheme the integration method requires that the time step Δt is smaller than a critical value, Δt_{cr}, which can be calculated from the mass and stiffness properties of the complete element assemblage (Bathe and Wilson, 1976). In PFC, the solution stability is estimated by

$$\begin{aligned} \Delta t_{cr} &= \left\{ \sqrt{m / k^{tran}} \right\} \\ \Delta t_{cr} &= \left\{ \sqrt{I / k^{rot}} \right\} \end{aligned} \tag{3.10}$$

where k^{tran} and k^{rot} are the translational and rotational stiffness, respectively, m is a single point mass, and I is the moment of inertia of the particle.

A critical timestep is found for each particle by applying Eq.3.10 separately to each degree-of-freedom and assuming that the degrees-of-freedom are uncoupled. The stiffness is estimated by summing all contributions (e.g., stiffness of all contacts with a particle) for that degree of freedom. The final critical timestep is taken to be the minimum of all critical timestep computed for all degrees-of-freedom of all particles.

A detailed explanation of each of the terms in equation 3.9 can be found in PFC^{3D} manual, Theory and Application (Itasca, 1999).

3.2.2.5 Tracking equilibrium

The use of an explicit, as opposed to an implicit, numerical scheme makes PFC possible to simulate the non-linear interaction of a large number of particles without excessive memory requirements or the need for an iterative procedure. The interpretation of results may be more difficult than with a conventional continuum code that produces a 'solution' at the end of its calculation phase. However, there are several indicators available to assess the state of the PFC model i.e. whether the system is stable, unstable or at continuous flow of particles. These are:

- Diagnostic forces – For the entire assembly of particles, maximum and mean unbalanced force* as well as maximum and mean contact force and the ratios of unbalanced to contact force (both mean and maximum) are calculated automatically during timestepping in a PFC^{3D} run. These ratios can be used to establish a limiting condition to denote equilibrium. The default on both is 0.01 (1% 'error').
- Tracking movement of particles during timestepping in the region of interest.
- Energy tracking
- Measurement spheres – can be used to measure porosity, stress, strain-rate, coordination number and sliding fraction (fraction of contacts contained within the measurement sphere that are slipping).

*The unbalanced force is the net force acting on each particle and indicates when a mechanical equilibrium state (or the onset of granular flow) is reached in static analysis. Forces are contributed to each particle through its contacts with other particles or walls. The model is in perfect equilibrium when the net force vector at each particle centroid is zero (i.e., the forces acting in each particle are nearly in balance). If the "unbalanced" or "out-of-balance" forces approach a non-zero value, this indicates that continuous movement of particles is occurring within the model.

If the unbalanced force approaches a constant non-zero value, this probably indicates that failure and granular flow are occurring within the model.

3.2.3 Micro-parameters

Micro-scale parameters of an assembly of granular mass can be defined in two categories: contact parameters and particle physical properties. It is clear by now that DEM such as PFC utilizes only three contact parameters with clear physical meaning, namely the two contact stiffness (linear contact) or elastic properties of particle i.e. shear modulus G and Poisson ratio ν (Hertz-Mindlin) and interparticle friction coefficient μ. In the physical properties category falls the particle density.

It is, therefore, necessary to have a clear understanding about possible ranges of values of above properties found in natural soil grains for effective simulation of boundary value problem involving natural soil by DEM. Although values of micro-properties for a particular material will be eventually evaluated through calibration process, as described in Chapter 4, this is important to check the validity of micro-properties assigned to PFC particles. Average values of elastic properties for selected materials are presented in Table 3.3.

3.2.3.1 Measurements of interparticle friction coefficient (μ)

As discussed by Proctor and Barton (1974), μ is generally taken to be the average coefficient of kinetic friction generated when one 'typical' soil particle surface is caused to slide slowly over another through a significant displacement. Various workers in soil mechanics have tried to measure μ by laboratory investigation based on the common approach of a 'constant μ' defined in the form μ or $\tan\phi_\mu=T/N$. Proctor and Barton (1974) summarized the earlier works and tried to build a general consensus on the matter discussing various environments affecting its value. Table 3.4 shows the values of μ of different mineral tested.

The results were found to be independent of: (a) apparatus tested, (b) range of normal force employed, (c) shearing direction, and (d) speed of traverse.

3.3 Summary

The discussion in this chapter revealed that a different but distinct mechanism exists, called discrete element method or DEM, other than traditional continuum based methods of numerical modeling,. The fundamental principle of DEM is that only few parameters with physical meaning are needed to formulate a boundary value problem compared to many and often not so clear parameters in continuum based methods. This hypothesis has been tested and described in the subsequent chapters starting with the material calibration in Chapter 4 by simulation of triaxial tests to determine a best set of micro parameters to describe the macro behaviour of a particular soil and formulation and simulation of boundary value problems involving that soil in Chapters 5 and 6.

Table 3.1 Discrete mechanical quantities in 3D (after Satake, 1997)

	Particle	Contact	Dual contact	Void cell
Particle graph	Point	Branch	Loop	Cell
Mech. Quantities	f_p, u_p	f_c, u_c	f_d, u_d	f_v, u_v

Table 3.2 Attributes to the four classes of discrete element method (after Cundall and Hart, 1992)

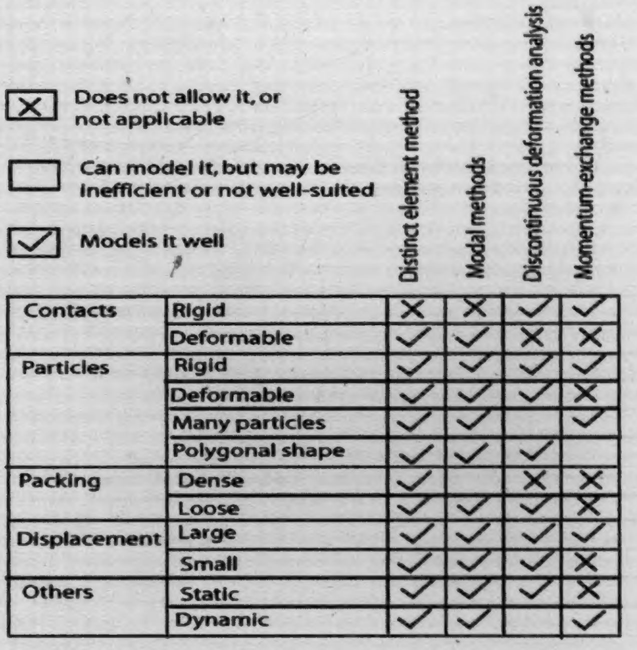

☒ Does not allow it, or not applicable

☐ Can model it, but may be inefficient or not well-suited

☑ Models it well

		Distinct element method	Modal methods	Discontinuous deformation analysis	Momentum-exchange methods
Contacts	Rigid	✗	✗	✓	✓
	Deformable	✓	✓	✗	✗
Particles	Rigid	✓	✓	✓	✓
	Deformable	✓	✓	✓	✗
	Many particles	✓	✓		✓
	Polygonal shape	✓	✓	✓	
Packing	Dense	✓		✗	✗
	Loose	✓	✓	✓	✗
Displacement	Large	✓	✓	✓	✓
	Small	✓	✓	✓	✗
Others	Static	✓	✓	✓	✗
	Dynamic	✓	✓		✓

Table 3.3 Elastic properties of selected continuum materials (at room temperature): (after Santamarina, 2001)

Material	Elastic modulus E (GPa)	Shear modulus G (GPa)	Poisson's ratio
Quartz	76	29	0.31
Steel	207	83	0.27
Wood	0.2 - 16	-	-
Granite	10 – 86	7 – 70	0 – 0.3
Shale	0.4 – 68	5 – 30	0.01 – 0.34
Glass	55	-	0.25
Limestone	2 – 97	1.6 – 38	0.01 – 0.32
Salt	31 – 40	10 – 16	0.25 – 0.27

Table 3.4 Friction properties of selected continuum materials (at room temperature): (after Santamarina, 2001)

Saturated or Dry	Material	Particle-particle		Particle-plane	
		Mean ϕ_μ, degrees	Standard deviation, degrees	Mean ϕ_μ, degrees	Standard deviation, degrees
Saturated	Glass ballotini	17.9	± 2.8	15.5	± 5.1
	Stainless steel ballotini	8.1	± 2.1	8.6	± 1.7
	Quartz	26	*	22.2	± 2.3
	Feldspar	*	-	28.9	± 1.1
Dry	Glass ballotini	5 – 10	*	5 – 10	*
	Quartz	*	-	17.4	± 0.6

* Insufficient data to give meaningful values.

- No tests performed

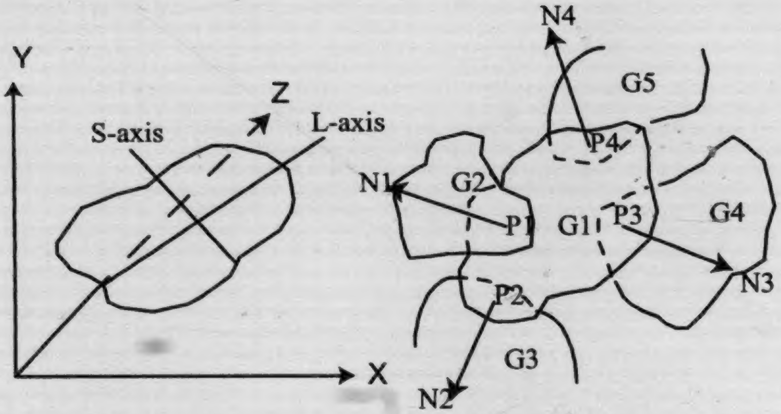
Y
Z
S-axis
L-axis
X
N4
G5
P4
N1
G2
P1
G1
P3
G4
N3
P2
G3
N2

(1) Orientation (2) Relative Configuration

G - grain, P - contact, Ni - contact normal, L-axis: long axis

Figure 3.1 Fabric elements of granular sand (after Oda, 1972)

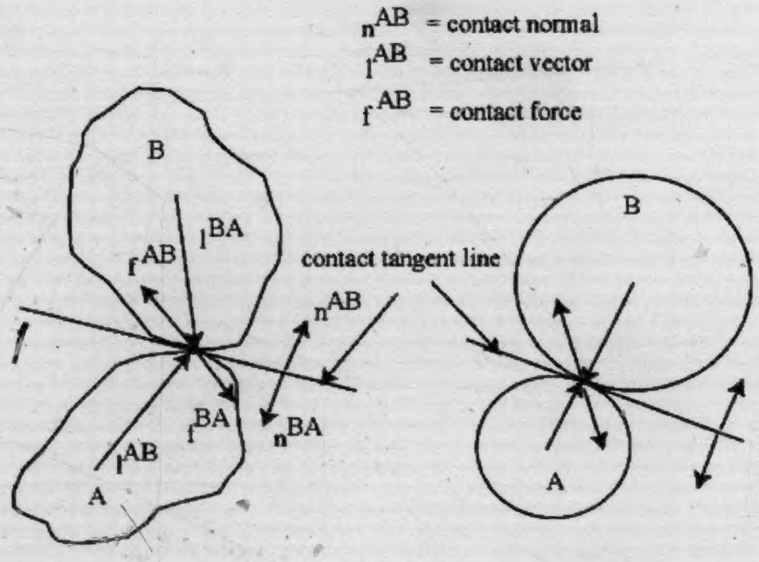
n^AB = contact normal
l^AB = contact vector
f^AB = contact force
B
l^BA
f^AB
contact tangent line
n^AB
f^BA
n^BA
l^AB
A
B
A

a) Non-circular particle b) Disc-shaped particle

Figure 3.2 Contact normals, contact vectors, and contact forces (after Bathurst & Rothenburg, 1988)

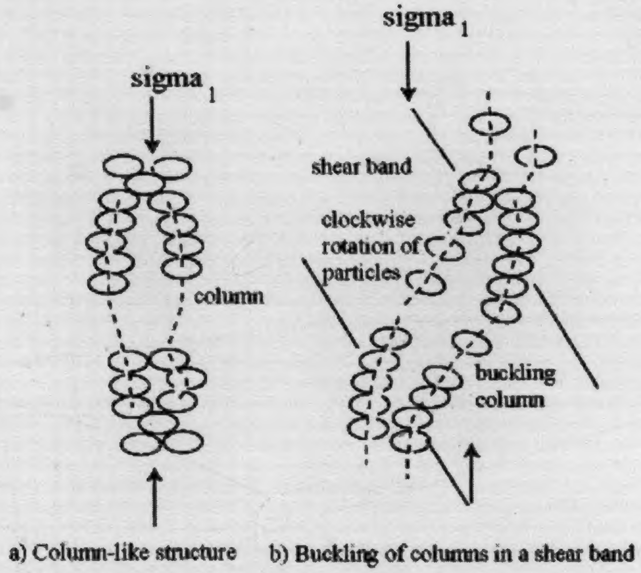
sigma 1
sigma 1
shear band
clockwise rotation of particles
column
buckling column
a) Column-like structure
b) Buckling of columns in a shear band

Figure 3.3 A dilatancy model for granular materials (after Oda, 1997)

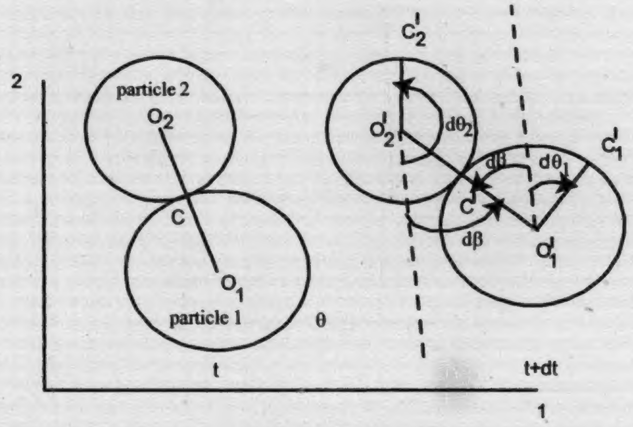
2
particle 2
O2
C
O1
particle 1
θ
t
C'2
O'2
dθ2
dβ
dθ1
C'1
C'
dβ
O'1
t+dt
1

Figure 3.4 Kinematics at a contact: rolling and sliding (after Bardet, 1994)

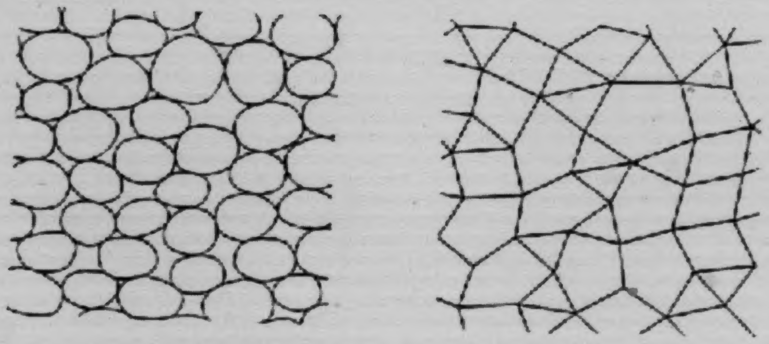

Figure 3.5 Particle graph (after M. Satake, 1997)

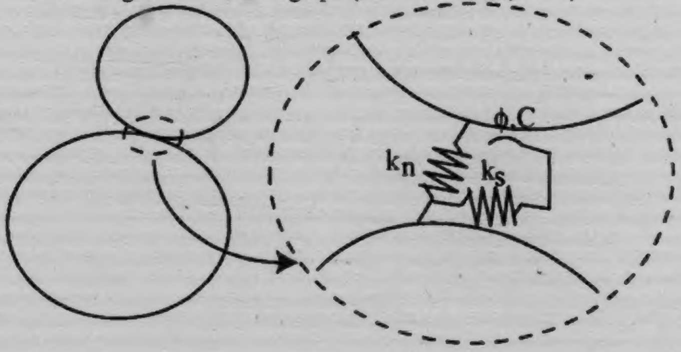

Figure 3.6. Basic contact model (after Bardet, 1998)

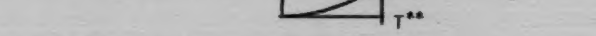

a) Normal b) Tangential

Figure 3.7. Contact force-displacement relationship

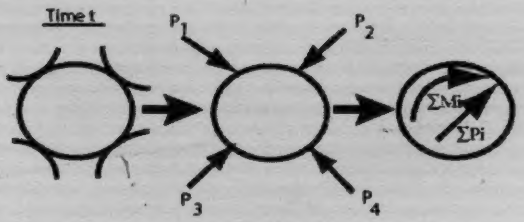
Time t
P1
P2
ΣMi
ΣPi
P3
P4

ΣPi produces acceleration of particle
ΣMi produces angular acceleration (spin) of particle

Time step is assumed to be small such that accelerations and velocities are constant in this small time.

Time t + Δt
- Particle occupies new position due to acceleration
- New Pi's, Mi's are computed for new position
- ΣPi . ΣMi and process is repeated

Figure 3.8 Calculation scheme in distinct element method (after Dobry and Ng, 1992)

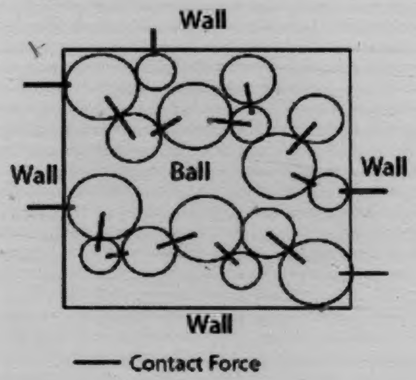
Wall
Wall
Ball
Wall
Wall
Contact Force

Figure 3.9 Basic PFC configurations – assembly of balls bounded by walls (plane view)

CHAPTER 4

Discrete Element Analyses of Triaxial Compression Tests on Uniform Sand

The Discrete Element Method or DEM has attracted a great deal of research in the geotechnical engineering due to its perceived capability to model soil grains. Material calibration is a useful starting point for any numerical modeling method as it involves a small volume of material with clearly defined boundary conditions. Details of the calibration of material response formulated by DEM against laboratory test data will be presented. Only data from standard Ottawa sand was considered due to its favorable grain shape i.e. round to sub-round which could easily be modeled using spherical particles or clustered of spherical particles.

The following key questions were considered:

1. What are the key factors affecting stress-strain-volumetric and strength behaviour of a DEM sample as observed through testing in simulated triaxial tests? What is the role the shape and size of the DEM particle play on the calculated response?
2. How the behaviour from the simulations compares with the observed laboratory behaviour of natural sand (Ottawa sand)?
3. What are the appropriate values of the micro scale material parameters that closely relate the relevant macro-scale properties of sand and hence could be used to formulate a boundary value problem by discontinuum modeling?

First of all, the physical triaxial test environment and the constitutive behaviour of uniform quartz sand (sub-rounded to rounded in shape) as observed through conventional compression tests ($\sigma_2 = \sigma_3$) will be briefly reviewed in section in 4.1. The review will be restricted to the engineering behaviour of sand mass where individual particles do not undergo inelastic deformations and/or rupture caused by elevated stress or temperature. This is consistent with the scope of this research work. Hence, stress-strain-strength and volumetric behaviour under low to medium stress conditions will be discussed. Influence of grain ruptures are beyond the scope of this work. Also only the behaviour of dry sand or fully drained behaviour is considered.

In the following the terms PFC and DEM are used interchangeably.

4.1 TRIAXIAL TEST AND SAND BEHAVIOUR

4.1.1 Conventional triaxial compression test

Laboratory test results on granular soil samples are interpreted by relating stresses and strains, presuming that the granular material under consideration is a continuous medium (Hicher, 1998). In the case of granular soil, an element of finite volume contains particles, which are discontinuously in contact with each other. The initial condition in the laboratory triaxial test is usually a state of isotropic stress ($\sigma'_1 = \sigma'_2 = \sigma'_3$). Compression at a constant strain rate follows ($\sigma'_1 > \sigma'_2 = \sigma'_3$). σ'_1, σ'_2 and σ'_3 are the major, intermediate and minor effective principle stresses.

A typical response of cohesionless granular medium from conventional triaxial compression test is shown in Figure 4.1. A brief description of the differences between dense and loose sample is provided below.

4.1.2 Triaxial response of sand

Hicher (1998) summarized the experimental behaviour of granular material. As discussed by Hitcher (1998), the key points of the behaviour of sand as observed through triaxial compression test are:

- In a loose state (defined by relative density, Dr, $0<Dr<0.3$) a continuous increase of deviatoric stress ($\sigma'_1-\sigma'_3$) is observed until it attains a maximum value unaffected by further changes in axial strain (ε_1). This final state is termed perfect plasticity.
- In a dense state, strain softening is observed after the peak. However, depending on the boundary conditions and slenderness of the specimen, the softening or post-peak response could be abrupt with out achieving perfect plasticity or could be smooth i.e. stress-strain curve continue to reduce after peak. The former is well known as effect

of strain localization i.e. the existence of a very pronounced peak followed by relatively sharp drop in deviatoric stress. Reducing the slenderness of a specimen and minimizing the friction between the rigid end platens and the specimen can lead to the later response i.e. smoother post-peak behaviour.

- The relation of volumetric strain to axial strain is also distinct between the loose and dense specimen. In a loose state, the volume change tends to attain a constant value as axial strain (ε_1) increases and no further volume change occurs consistent with the perfect plasticity condition of loose stress-strain behaviour. In a dense condition, the specimen is initially contractant (decrease in void ratio) and then void ratio starts to increase resulting in dilatant behaviour. This phenomenon of increase void ratio even under compressive stresses is well known for dense granular media and is called "dilatancy".

Lee and Seed (1967) investigated the effect of increasing confining pressures on the stress-strain and volume change characteristics of sand. For a dense sample, the effects of increasing confining pressure are:

- the brittle characteristics of stress-strain curve are reduced,
- the strain to failure is increased, and
- the tendency to dilate is decreased.

In case of loose samples, the tendency for dilation at low pressures is not so strong as for dense sands, while at high pressures the tendency for compression is greater. One interesting observation was that at each confining pressure the void ratios at failure were the same for all samples regardless of their initial void ratios.

4.2 MODELLING DETAILS FOR TRIAXIAL COMPRESSION TEST

4.2.1 Particle shape

Ottawa sand particles are round to subround (Salgado et al, 2000). Norris (1977) discussed the definition of sphericity and roundness which formulate the shape of sand particles. Koerner

(1968) points out that Ottawa sand consists of soil particles of well rounded shapes having high sphericities (sphericity = 0.71). As discussed by Norris (1977), unlike sphericity, which relates to the length to width ratio of a particle, roundness makes some assessment of the corner in a particle. Based on the discussion of Norris (1977) no natural sand particles are completely spherical (sphericity of 1).

In this research study a non-spherical particle is created by the concept of a 'cluster'. Several particles may be bonded together to form a cluster that can act like a particle of non-spherical shape. In this analysis a cluster has been defined as a bonding of two particles in order to get a shape closer to that of an Ottawa sand grain (Figure 4.2). It was ensured that cluster would behave as a single rigid body with a deformable boundary and would not break apart, regardless of the forces acting upon it. This was achieved by bonding the pair in a cluster with high bond strength and stiffness. Table 4.1 shows the assigned values of bond properties at a contact between two spherical particles in a cluster.

4.2.2 Particle size

Figure 4.3 shows the grain size distributions of Ottawa sand and DEM particles (spherical particles). DEM samples contain particles whose sizes are just horizontal translation of grain size of sand as explained below. Total of 5 different sizes of DEM particles are chosen in order to show the effect of particle size on the constitutive behaviour of DEM samples. A closer look of the size distribution of Ottawa sand reveals that the whole curve can be divided into two distinct zones: (1) 0.2 to 0.4 mm and (2) 0.4 to 0.6 mm with d_{10}=0.28 mm and d_{60}=0.42 mm, where $d_{10 \text{ or } 60}$ is the grain size by which 10% or 60% by mass are finer than that grain size. Initial simulations were run generating particles of two sizes and single size ranges. No difference was found in the macro behaviour. Hence, all of the following simulations were conducted using one size range between d_{10} and d_{60} of Ottawa sand but multiplied by a factor to make the number of particles within the practical limit of computer power. Using an upscaling factor of 10 (Achmun and Rahman, 2002) the corresponding d_{10} and d_{60} for DEM particles become 2.8 and 4.2 mm, respectively. DEM samples were created generating particles with plus or minus of this size range.

In case of non-spherical or clustered particles the same grain size distribution as shown in Figure 4.3 applies as, in this work, a clustered particle is just made of two overlapping spherical particles. In other words, only particle shape is altered by bonding two equal size particles making up the same particle size distribution of Figure 4.3.

4.2.3 Particle contact

The Hertz-Mindlin contact law (Mindlin and Deresiewicz, 1953) models the contact behaviour for simulations involving spherical particles. This is advantageous over the simple linear model, in which k_n and k_s are constants independent of the history of N and T at that contact (Dobry and Ng, 1992).

However, the above contact law could not be used for the case of clustered particles. Both contact and parallel bonds are present in a clustered particle. The PFC ver.2.0 does not allow Hertz-Mindlin law to be used along with contact bond. Therefore, linear contact law was used in simulations involving clustered particles

4.2.4 Stages of the analysis

4.2.4.1 Sample generation

The objective of this stage of the analysis is to generate particles with a particular size and distribution within a parallelepiped sample and compact the assembly to achieve a target porosity. Compaction of the assembly was performed during particle generation to obtain the target porosity. Two different techniques were followed for spherical and non-spherical particles (PFC User's Guide, 1999). In the case of spherical samples, particles were generated with a radius smaller than the required size and later expanded until the desired porosity was obtained. This is a trial-and-error process and all the necessary spheres were generated based on the required porosity and particle size distribution. In the case of bonded particles, each pair in a bonded particle was generated at a time including the overlap, if any, to the desired position and porosity was calculated after each pair was created. The particle generation process would be automatically halted once the porosity became less than the target porosity.

During the above process the lateral boundary of the sample defined by the six walls remain fixed in position i.e. zero lateral displacement. Note that all synthetic DEM samples are parallelepiped rather than the cylindrical shaped soil sample in a real triaxial test.

4.2.4.2 Isotropic consolidation

The second stage of the analysis deals with the application of equal and all-around confining pressures to the sample through the six frictionless walls. Wall stresses were brought to the desired confining stresses in an iterative manner. A tolerance limit of 0.5% (ratio of difference between calculated stress at the walls and required stress to the required stress expressed as a percentage of the required stress) was used in all the simulations performed.

Interparticle friction coefficient, μ, was then assigned to all particles at this stage compared to zero friction during sample preparation stage. For a dense assembly, the value assigned to μ was found to have no effect on the porosity of the sample during sample generation; however in the case of a loose assembly, it was found that μ was required to be greater than zero to retain the required porosity. In all the numerical simulations described below (dense and loose), μ was set equal to the 0.5, which is presumed to be the value of natural sand grains.

4.2.4.3 Application of deviatoric stress

In this third and final stage of the triaxial simulation, deviatoric stress was applied to the numerical sample up to the desired strain level. The specimen was loaded by controlling the axial strain. This was achieved by moving the top and bottom platens toward one another at a constant velocity (v). In order to minimize effects from dynamic impact to the sample, the velocity was applied in stages. This was done by adjusting the velocities to reach the final value in a sequence of specified number of stages (_nsteps) over a specified number of cycles (_nchunks). An attempt was taken to see the effect of different values of the above parameters to ramp up the platen velocity on the simulated results. The different scenarios are shown in Table 4.2. Figure 4.4 shows little effect on stress-strain-volumetric response as both the above parameters have been changed except a narrow band in the stress-strain curve beyond the peak deviatoric stress. In the remainder of the section the values in Case A5 was considered as it showed an average value in the band.

Throughout the loading process, the confining stress was kept constant by adjusting the lateral-wall velocities in such a way as to reduce the difference between the measured stress and the required stress. Unlike the physical test where lateral confinement is done through a flexible membrane, in PFC^{3D} rigid walls were used to apply the confinement. The value for μ was set to its final value, which was required to correctly simulate the strength of the DEM sample.

At each stage of the analysis the history of the mean unbalanced force with timestepping, the ratio of mean unbalanced force to mean contact force and the history of movements of particles at critical locations of the entire sample were assessed to ensure that the numerical calculation reached a stable solution. Each of these indicators to assess the state of the DEM model (stable, unstable or continuous flow of particles) has been described in Chapter 3.

4.2.5 Boundary conditions

4.2.5.1 Properties of loading platens

As was discussed in section 3.2 of Chapter 3, contact forces in DEM are directly related to the external velocity applied and therefore, it is essential to assess the dynamic impact of loading platen on stress condition inside the sample. This was done by setting the platen velocities to zero at different axial strain increments, and noting the changes in stress components; if the changes were too large, the whole test was repeated at lower platen velocities. The influence of platen velocity on the calculated results for a dense simulation (void ratio, e=0.56) with spherical particles is presented in Figure 4.5. These results were obtained by applying an increment in platen velocity and then cycling until equilibrium was attained (ratio of the mean unbalanced force to the mean contact force equal to 0.005). For a platen velocity of 0.25 m/s, there was a large (60-100 kPa) decrease in deviatoric stress when cycling to equilibrium. The drop increased with increasing axial strain. Reducing the platen velocity reduced the magnitude of this decrease. A value of V=0.01 m/s was able to minimize the drop to close to zero. However, note that the V=0.01 m/s was obtained for a dense sample under a 100 kPa confining stress. Similar analyses were undertaken for dense sample at other confining stresses as well as loose sample with different confining stresses. It was found that equilibrium platen velocity depends on both void ratio and confining stress level. In the simulation results described below, the platen velocity mentioned was the required value at which an equilibrium condition could be maintained.

The effect of the roughness of the platen on the calculated response is examined in Figure 4.6. These results were obtained from small-scale simulations (50×21×21 mm sample) of a dense material. Three platen roughness values (μ_p) of 0, 0.2 and 0.5 (referred to as cases B1, B2 and B3, respectively) were considered. Figure 4.6 shows that both the peak stress and dilation increases with increasing roughness of the loading platen. However, both the initial contraction and initial dilation at low to medium strain (zero to two percent) was unaffected. In addition, platen roughness seemed to affect the strain level at which peak stress develop; higher the roughness smaller the peak strain. A clear pointed peak was developed for μ_p=0.5 friction coefficient while peak was smoother for μ_p=0.2 and 0.The calculated results show a similar trend to the physical observation by Vardoulakis and Drescher (1985) that the onset of post-peak strain-softening is earlier in the case of rough platens due to the formation of rigid cones at the boundaries.

4.2.5.2 Lateral boundary condition

The lateral boundary condition in a laboratory triaxial test would impose constant radial pressure on the sample. This would be achieved by flexible rubber membrane that surrounds the sample, which is loaded by fluid pressure. This boundary condition would permit lateral displacement along these boundaries (i.e., sample bulging). In PFC^{3D}, the feature exists to impose an average pressure along a boundary, but this boundary wall is rigid (Figure 4.7). The consideration of a 'rigid wall' only option could be due to the simplicity of the analyses and bulging may not be important for rock material. This would result in uniform lateral displacement along the boundary and not allow the sample to bulge more in the middle than at the ends of the specimen. There is still no efficient method to simulate flexible boundary in DEM. Recently Tang Tat-Ng (2004) presented a historical perspective on the subject along with discussion on his proposed method to simulate flexible boundary. As discussed by Tang Tat-Ng (2004), the only method developed so far is the placement of additional boundary particles to simulate the rubber membrane. However, the method increases the computational effort significantly. Tang Tat-Ng (2004) developed a method, which simulates the water pressure and not the rubber membrane itself. The method has yet to gain any general acceptance.

An alternate approach of using multiple rigid wall segments is presented here. The premise being that bulging along the lateral boundary can be simulated using the available rigid wall option provided that enough segments are employed along the boundary. Figure 4.8 illustrates the approach of dividing the lateral boundary into a number of segments.

Three cases were considered to examine the influence of the effect of lateral bulging on the calculated results. The first (C1) involved a single rigid wall segment for each lateral boundary. In Cases C2 and C3, each of the four lateral walls was discretized in several vertical (along the height: n_H) and horizontal (along the width: n_W) segments, as given in Table 4.3. The segments were free to move, as they were not interconnected. In case of Series C3 the heights of the middle three vertical segments were smaller relative to the top and bottom segments in anticipation that sample will bulge more in the middle. The three horizontal segments in the direction of sample width were of equal width. The particular case of a dense sample with smooth spherical particles was considered.

Figure 4.9 show the sample deformation at an axial strain of 20% for single and discretized lateral walls. The calculated results for Cases C1-C3 are presented in Figure 4.10. In general, allowing the sample to deform freely (approximately here) in the lateral directions resulted in higher peak stress compared to rigid walls. An increase of 8.4 and 5.4 percent in peak stress was observed as the lateral walls were discretized from C1 to C2 and C3, respectively. A slight drop in peak stress at greater discretization could not be explained. However, flexibility of lateral walls did not show any changes in the initial stiffness. Similarly, C2 showed highest dilation compared to C1 and C3. A slight increase in dilation was observed in C3 compared to C1. Also the initial volumetric compaction was insensitive to the lateral wall discretization.

While it is difficult to judge the effect of lateral boundary stiffness on the constitutive behaviour the bulging in DEM sample similar to that of physical sample is obtained through multiple segment walls. Although the higher the number of segments the greater the computational difficulty, one more case with higher discretization than C3 was tried. The lateral walls were discretized in 10 vertical segments while horizontal segments remained three. Unfortunately the program crashed during the consolidation stage after completing few cycles. The probable reason could be that the boundary walls loose contact with the balls (remember that wall segments gets smaller) and if there is no contact PFC can not compute the wall stresses (it has a equation where some parameter has to be divided by the contact count).

This suggests that 7 vertical segments is the limit in the particular program used. Since only small changes occurred between C2 and C3, it appears that C3 case provides reasonable solution.

4.2.6 Numerical damping

The theoretical background behind damping in PFC has been described in Chapter 3. To investigate the effect of damping constant (α) on the calculated response, analyses were carried out using sample size of 50×21×21 mm. In the original case α was equal to 0.7, which is the default PFC value. Simulations were then run with $\alpha=0.5$ and $\alpha=0.8$. The three conditions are named as D1, D2 and D3, respectively. The results are presented in Figure 4.11. It was found that the value of the damping constant influenced obtaining stress equilibrium of the sample during shear. The smaller the value of the damping constant, the more steps DEM required to reach equilibrium. For example, for a model comprising of 495 particles, the case with $\alpha=0.5$ required 1150 steps compare to 860 steps for the case with $\alpha=0.8$. It is expected that the number of steps will increase with the number of particles as in DEM this local non-viscous damping is applied to each particle.

In the case of $\alpha=0.5$, the constitutive behaviour of DEM samples are somewhat inconsistent, especially after peak stress, compared to $\alpha=0.7$ and 0.8. The higher peak stress observed in $\alpha=0.5$ was probably due to the effect of accelerated motion of particles under reduced damping. Little changes in stress-strain relationship were observed for the cases of $\alpha=0.7$ and 0.8. Volumetric response was also somewhat inconsistent for the cases of $\alpha=0.5$ and 0.7 and higher dilation was observed as damping was reduced. The changing numerical damping was further investigated in conjunction with the varying particle size and is discussed below.

It is clear that a damping constant of 0.8 helped to reach a stable solution within a reasonable number of cycles as well as reduced the vibration in the calculated response. In the remainder of the analyses damping constant equal to 0.8 was used unless otherwise mentioned.

4.2.7 Contact model

The Hertz-Mindlin contact law as described in Chapter 3 modeled the contact behaviour for simulations involving spherical particles.

However, the above contact law could not be used for the case of clustered particles. Both contact and parallel bonds are present in a clustered particle. The PFC ver.2.0 does not allow Hertz-Mindlin law to be used along with contact bond. Therefore, linear contact law was used in simulations involving clustered particles.

4.2.8 Initial porosity

As has already been mentioned, during ball generation stage a porosity is specified. The number of balls generated depends on the specified porosity; the higher the porosity, the fewer the number of balls. Also the forces generated on the boundary walls at this stage depend on the porosity specified; the denser the assembly, the greater the forces exerted by balls on the walls. During the consolidation stage, as the forces on the lateral walls are changed to generate the required confining stresses so does the porosity. This is examined in detail by using a 50×21×21 mm sample (495 balls). The configuration of the measurement spheres and their locations are shown in Figure 4.12 The porosity is the average of the measurement spheres at top, middle and bottom of sample. Details of the porosity measurement are mentioned in Table 4.4 and important observations are summarized below:

- The measured porosities are always lower than the specified one at the end of sample creation stage.
- There are increases in normal stresses at the sample creation stage if the specified porosity is lowered from 0.38 to 0.35.
- The initial porosities at the end of isotropic consolidation depend on the required confining stress; the higher the confining stress, the lower the porosity.
- The sample is not uniform in terms of porosity from top to bottom.

In order to evaluate the effect of particle size on porosity, the same sample but smaller particle sizes (1671 balls) were investigated and the results are reported in Table 4.5. Only one porosity (n_o=0.38) was considered. Compared to the bigger size particle, higher wall forces were generated even at the specified porosity of 0.38. In general, the final porosities at the end of consolidation stage are lower than that of bigger size particle.

4.3 PARAMETRIC STUDIES WITH SMOOTH SPHERICAL

PARTICLES

4.3.1 Particle size and number of particles

Particle size and subsequently the number of particles are important considerations in DEM. As discussed by Cundall (2001), it is not possible to include in the numerical model every grain of sand presents in any real construction involving sand mass. Even discrete element samples cannot have the number of grains present in a laboratory triaxial sample. In this section, results from analyses conducted with different particle size are reported to examine their effect on the calculated stress-strain and volumetric behaviour. Also an attempt was made to reach a final conclusion on the value of damping constant in conjunction with the particle size. The particle sizes were constantly decreased until little changes on the constitutive behaviour due to changes in particle size were found keeping the sample size fixed at 165×70×70 mm. The sample size in the simulation was the same as the one used in the laboratory triaxial tests by Salgado et al. (2000) in order to minimize the simulation time during the actual calibration of the DEM sample. Table 4.6 provides the details of the particle size and number for the different cases analyzed. D_0 is the diameter of sample (i.e. D_0=W=2.4L) and d_{50} is the average particle size. Please refer to Figure 4.3 for comparison of particle size distribution between DEM sample and sand.

Figures 4.13 and 4.14 shows little effect on the overall stress-strain-strength as well as volumetric responses of dense samples for the different particle sizes considered . There are, however, differences when particle size was increased to 'D_0/d_{50}=8 (E1)' and 'D_0/d_{50}=11.2 (E2)'. Triaxial simulation on both these samples (E1 and E2) revealed that stress-strain response was less stiff and post-peak strain softening was not as smooth as other cases. A little higher peak stress as well as higher dilation after peak was observed compared to smaller particle sizes (D_0/d_{50}=18.66 to 46.66 i.e. E3 to E6).

The above study of particle size was extended to a much smaller sample size (50×21×21 mm) including only hundreds of particles. Only two cases of particle size distribution (minimum and maximum in Figure 4.13) were considered, namely D_0/d_{50}=21/3.75=5.6 and D_0/d_{50}=21/2.5=8.4. Once again it was found that the peak deviatoric stress was insensitive to the size effect only if the damping constant is equal to 0.8. This is shown in Figure 4.15.

The above finding is significant regarding selection of particle size (in relation to the model size) and the damping constant in DEM modeling. Size or scale effect was negligible provided that the average particle sizes (d_{50}) of numerical sample remains close to or less than 4 mm (for uniformity coefficient, C_u=1.5) for a model size equivalent to a triaxial sample but only with internal damping equal to 0.8.

Figure 4.16 shows the influence of particles size on the loose simulated behaviour. The number of cases were reduced to 3 compared to 5 as in dense sample, namely, E1, E3, and E5. These results were obtained with α=0.8. Notice that the platen velocity at which sample was in equilibrium has been changed from 0.01 m/s for the dense case to 0.1 m/s in the loose case. Similar to the dense case there is no significant difference in the stress-strain relationship using internal damping α=0.8. Also, except for the case of D_0/d_{50}=8, little effect of particle size variations on loose volumetric responses was found. The calculated results from cases E3 and E5 were very similar with higher deviatoric stress (by 20 kPa) beyond 4% axial strain. The case with a larger particle size (E1) showed higher stiffness and less contraction compared to E3 and E5.

4.3.2 Elastic properties of particles

Cohesionless, granular materials are commonly assumed to be composed of elastic-frictional particles, which obey Hertz-Mindlin contact theory (Morgan and Boettcher, 1999). As discussed in Chapter 3, the Hertz-Mindlin contact constitutive law at a particular contact is defined by two parameters: shear modulus G [$ML^{-1}T^{-2}$]; and Poisson's ratio ν [-] of contacting particles. The overall constitutive behaviour of a material, particularly the stiffness, is simulated in DEM by specifying appropriate values of these parameters. It is therefore important to know what impact would different values of these parameters have on the macro response of an unbonded granular assembly.

Four different combinations of G and ν were considered. They were named as F1 (G=1.0 GPa, ν=0.2); F2 (G=10.0 GPa, ν=0.2); F3 (G=1.0 GPa, ν=0.3) and F4 (G=1.0 GPa, ν=0.1). The reason to select these values was based on comparison of some preliminary DEM analyses to that of sand. The particle shear modulus, G, was found to affect the stiffness, peak deviatoric stress as well as dilation of dense sample; the higher the G, the greater the stiffness and dilation but the smaller the peak stress (Figure 4.17). However, initial contraction of the sample was found to be less compared to G equal to 1.0 GPa. Negligible effects of particle Poisson's ratio on the constitutive behaviour were found. This is similar to the findings of Borja and Regueiro (1998) who concluded that for a given particle assembly the predicted overall stress-strain response depended almost exclusively on the chosen value of G.

The value of particle shear modulus of G=1.0 GPa which was found to closely match the initial stiffness of Ottawa sand is 30 times lower than the typical value for a quartz mineral (see Table 3.3 of Chapter 3). This is probably because particle shape is perfectly spherical compared to sand particles (Borja and Regueiro, 1998). This will be further discussed in the calibration section of this chapter.

The influences of G and ν on loose sample responses are shown in Figure 4.18. The observations were quite similar to that of dense samples. G has only a direct effect on the stiffness of the sample; the predicted overall response becomes stiffer as G increases and subsequently the stress-strain curve shifts upward or downward based on the higher or lower value. On the other hand, changing G was found not to affect the volumetric response of the loose sample. As was observed for the dense sample, varying the particle's elastic Poisson's ratio has virtually no effect on the overall loose constitutive response.

4.3.3 Interparticle friction

In the physical world, the parameter μ is generally taken to be the average coefficient of kinetic (sliding) friction generated when one 'typical' soil particle surface is caused to slide slowly over another through a significant displacement (Proctor and Barton, 1974). The importance and significance of μ in relation to the overall strength of a granular mass has been discussed in section 4.1.2. It is therefore, important to measure this parameter in order to get the total available strength of a sand mass. Numerical experiments could be a viable alternative to the physical testing to measure interparticle friction or at least confirm the physical findings. One of the advantages of simulations is to see the role of contact friction on the macro behaviour of a granular mass.

The different cases were named as: G1 (μ=0.1); G2 (μ=0.5) and G3 (μ=1.0). These friction values were assigned to the particles after the consolidation stage and before the application of deviatoric stress in the simulated triaxial tests. The other parameters were G=1.0 GPa, ν=0.2, α=0.8 and V=0.01m/s. The following observations were made in case of dense specimens (Figures 4.19 and 4.20):

- Keeping other parameters constant, the peak deviatoric stress increases with increasing values of μ. It was also found that the higher the value of μ, the greater the strain softening. At μ = 0.1, there was no clearly defined peak in stress-strain curve. As μ increases from 0.1, the peak was more clearly seen.
- The effect of μ was also observed on volumetric response; the higher the value, the greater the dilation (Figure 4.19). This was consistent with the sample void ratio measured at any strain level during shearing (Table 4.9); the smaller the μ, the smaller the void ratio. Table 4.9 shows comparison of void ratios.
- The initial compaction during shearing also varied with μ; higher compaction was observed with higher values of μ (Figure 4.19).

Figure 4.21 shows the influence of particle friction coefficient on loose simulated sample behaviour. The stiffness of the stress-strain curve was changed based on different μ values: the higher the μ, the higher the stiffness. Subsequently the stress-strain curve moved upward as μ was increased (an increase in deviatoric stress of 142 % was observed at μ equal to 1.0 over μ equal to 0.1 at 8.5 % strain). Dramatic changes also were observed in sample volume change as μ was changed from 0.1 to 1.0. At μ equal to 0.1, the sample experienced the highest contraction within a short axial strain (less than 1 %). In other words, the loose DEM material compressed instantly to a large value at comparatively low μ value and continued compressing but at much lower rate as the sample was strained resulting in higher stiffness. On the other hand, for μ equal to 1.0, the material experienced first an initial contraction, reached a plateau and started to dilate at axial strain equal to 4 %. The contraction reduced greatly at both μ equal to 0.5 and 1.0. The observation was anticipated as lower friction values encourage rapid displacement and re-arrangement of particles at much lower boundary forces.

4.3.4 Effect of particle rotation

Due to computational simplicity most of the DEM research so far has been concentrated using perfectly smooth circular (2D) discs or spherical (3D) particles (e.g. Sitharam et al., 2002; Sitharam and Nimbkar, 2000; Thornton, 2000; Morgan and Boettcher, 1999a, 1999b; Bardet and Proubet, 1991 and 1992; Bathurst and Rothenburg, 1990). However, simple circular discs or spheres were found to roll excessively resulting in peak simulated friction angle often lower than those of soils (Oda and Iwashita, 2000; Thomas and Bray, 1999; Jensen et al., 1999; Bardet, 1994; Rothenburg and Bathurst, 1992). One of the options in DEM is to freeze the particle rotation. Although this option is not considered to be logical anymore (Iwashita and Oda, 1998; Jansen et al., 1999; Mirghasemi et al., 2002; Thomas and Bray, 1999), it is carried out as one of the parametric studies in this research to examine the particle rotations in detail and to confirm the previous research findings.

The effect of particle rotation on the simulated results is presented in Figure 4.22 for a dense sample. The dimension of the sample was chosen to be smaller (50×21×21 mm) than the previous cases to reduce the computational demand. All other conditions were similar to those of the previous simulations including particle size range of 3.0 to 4.5 mm. Three specific conditions were considered: (H1) rotations of all particles were fixed, (H2) rotations of particles along the middle-third of sample were fixed while keeping the top and bottom-third particles free, and (H3) all particles free to rotate. The case H3 was originated from the idea that in laboratory triaxial test bulging occurs mostly at the middle third of the sample and therefore the spherical particles at the middle third have the greater tendency to rotate.

Fixing the rotations (H1) increased the peak strength by a factor of 7 and at a higher axial strain (5 % compared to 1.5% in H3) and showed much larger initial volumetric compression that with the particles free to rotate. However, interestingly, fixing particle rotation only at the middle third of the sample generated stress-strain behaviour comparable close to that of free rotation case. The peak strength (H2) was increased by a factor of 1.5 only while volumetric strain closely follows to that of H3.

In addition to the effect on peak strength, degree of particle rotation has also effects on macro stiffness of the assembly; the smaller the particle rotation, the greater the stiffness.

The degree of particle rotation was examined at various locations of the DEM sample with free particle rotation. The average incremental rotational velocities in x, y and z directions are plotted against axial strain a[illegible]own in Figure 4.23. Details of particle rotations are presented in Appendix A. The o[illegible]ations are similar to those of Oda and Iwashita (2000) in that the rotational velocities are distributed uniformly with both positive and negative velocities so that the mean velocities are close to zero. As explained by Oda and Iwashita (2000), this is due to the fact that clockwise rotation of a particle makes its neighboring ones rotate counterclockwise in a sample where rotation is not controlled. Figure 4.24 shows the average particle rotational velocities of the top one-third of the sample where particle rotations at the middle-third of the sample were fixed. Comparing Figures 4.23 (b) and 4.24, clearly, there are fewer rotations at the top part of the sample up to axial strain of 4% due to fixing particle rotations in the middle of sample.

Hence, there is rotational resistance to all the particles in a sample during pre-peak and peak response in stress-strain behaviour and on average, simple smooth spherical particles acted like a natural sand grain having roughness and non-spherical shape. Having said that it was not intended to use this option any further as it represented just an arbitrary modeling option without broad application. The objective was to confirm the previous research finding of excessive rolling (smooth spherical particles) on peak strength of an granular assembly i.e. DEM simulations using simple disks or spheres with free rotation usually underestimates the shear strength of a granular medium subjected to uniform compressive loading.

4.4 PARAMETRIC STUDY WITH NON-SPHERICAL PARTICLES

Probably the most effective way to capture interlocking of natural soil particles and thus the true shear resistance between them by discrete element modeling is to model the shape of the soil particles as accurately as possible. The simple logic of 'particle clustering' has been explained in section 4.3 (see Figure 4.2). Two spherical particles can be bonded together to create a more natural looking Ottawa sand grain. Once again small-scale simulations were performed using few hundred particle 'clusters'. The individual particles were created using the size range of 2.0 to 3.5 mm to keep the clustered particle size close to that of non-clustered cases.

The investigation was intended to see the influence of overlap, x, and different particle size in a cluster on calculated results. In the first case, two equal size particle having three different overlaps were examined: I1 (x=R); I2 (x=0.8R) and I3 (x=0.5R). In the second case, three different particle sizes in a cluster of two particles touching each other (no overlap) were considered, namely, (R2=R1), (R2=0.8R1) and (R2=0.5R1).

Figures 4.25 and 4.26 show the result of this parametric study on a dense sample. As was expected, the smaller the distance x, the greater the angularity of the particle and hence, the higher the peak deviatoric stress (Figure 4.25). The rate of post-peak strain softening was also higher as x was increased. On the other hand, angularity of particle does not have any effect on the stiffness of the mass. This is exactly similar what is usually observed in physical tests between sub-rounded to sub-angular shaped quartz sand mass (Norris, 1977; Koerner, 1968). Volumetric response did not change between x=R and x=0.8R until x was reduced to half of R where much higher dilation was observed. This is also similar to the case of physical results where sand consisting of angular shaped grains have greater dilation compared to less angular shaped grains.

Similarly, as can be seen from Figure 4.25, both peak stress and dilation increased as the size of the second particle was increased from half of the first particle (R2=0.5R1) to being the equal of the first particle (R2=R1). This confirms the previous research using DEM on the effect of particle shape (Ni, 2000 and 2003) who defined the shape of a non-spherical particle by the term 'shape factor' as (R1+R2)/R1, where R1 and R2 are the radii of the larger and smaller spheres in a cluster. A single spherical particle has a shape factor of 1, whilst a particle comprising two spheres of the same size has a shape factor of 2. As discussed by Ni (2003), both the peak angle of shearing resistance and dilation increases with shape factor.

Finally, comparing Figures 4.22 (series E3) and 4.25 and 26, it is shown that a DEM sample comprising simple clusters of two spheres has the higher peak stress compared to a sample comprising smooth spheres. This is due to the availability of greater interlocking opportunity in a clustered sample. Similar calculations were obtained by Rothenburg and Bathurst (1992) using planar elliptical particles compared to that of disk-shaped particles in two-dimension.

4.5 COMPARISON WITH MEASURED TRIAXIAL COM-

PRESSION RESULTS

This section describes the comparison between results from measured physical triaxial data on Ottawa sand to that calculated from DEM comprising an assembly of spherical particles and general shaped particles (clustered particles). Please note that the Hertz-Mindlin contact law only applies to the case of spherical particles. It can not be used in the PFC code for the cluster particles and consequently, the linear contact law was used in the case of cluster particles.

The physical data against which the numerical results were calibrated is shown in Table 4.8. Ottawa sand, which is round to sub-round in shape (Salgado et al., 2000) was selected for this work. Various researchers have described the behaviour of Ottawa sand from triaxial compression tests (e.g. Salgado et al., 2000; Norris, 1977; Koerner, 1968; Holubec, 1966). Figure 4.27 shows the variability in peak friction angle of Ottawa sand for a wide range of confining pressures and densities under drained triaxial compression tests as tabulated in Table 4.8. Table 4.8 revealed that friction angles of dense to medium dense Ottawa sand varies among the different laboratories under different testing procedures.

Based on the findings of parametric studies in the previous section and literature review on elastic properties as well as interparticle friction of sand grains, Table 4.9 shows the various input parameters and their values for numerical triaxial simulation on DEM samples.

In the case of clustered simulations no changes were made to the values of micro-parameters used in the simulations involving spherical particles. This is acceptable as the objective was to model only the shape of the grains and not the grains itself. For segmental lateral walls only the case of seven (length) by three (width) segments at each side was considered.

4.5.1 Dense sample (σ_3=100 kPa)

The comparison of the constitutive behaviour calculated by DEM samples (dense) to that of Ottawa sand is shown in Figure 4.28. The number of particles for the cases of 'PFC spheres free and fixed' and 'PFC general' were 18154 spherical particles and 16560 particles, respectively. Regarding the overlap distance between two particles in a cluster, it was found that x equal to 0.9R (between the cases F1 and F2 in Figure 4.25) best represented the physical data in matching both peak stress and post-peak response. The overlapping distance of 0.8R and R overestimated and underestimated the peak stress, respectively. Therefore, data obtained from x equal to 0.9R is only shown in Fig 4.28. Very good matches have been obtained in overall stress-strain-volumetric responses, especially the hardening part of the stress-strain curve. The calculated peak stress of DEM sample is just little higher than that of the physical one (284 and 296 kPa for PFC spheres fixed and PFC general, respectively compared to value 282 kPa). However, the strain to failure of DEM sample is less than that of the physical one (2.13 and 2.18 % compared to 3.75 %). The rate at which the stress decreases after the peak is similar in both the physical and DEM stress-strain behaviour.

The volumetric response as observed in the DEM sample matched the general trend of the physical sample with initial volumetric contraction followed by an increase in volume. However, the calculated results are less than the measured volumetric strains from 0.5 to 3% axial strain and are larger than those measured beyond 3% strain. Also, the onset of dilation in both the physical and the DEM samples was before the peak stress but at smaller axial strains (0.5 %) in laboratory triaxial sample compared to 1 % in the DEM samples. This small difference in initial volumetric response could be attributed to the specified particle elastic properties, especially the particle shear modulus, in DEM samples.

4.5.2 Loose sample (σ_3=400 kPa)

The comparison of the constitutive behaviour obtained by DEM simulation of DEM samples (loose) to that of Ottawa sand is shown in Figure 4.29. The number of particles for the cases of 'PFC spheres free/fixed' and 'PFC general' were 15518 and 16284 particles, respectively. Input parameters were similar as mentioned in Table 4.9 except V and μ. V=0.1 m/s was chosen as it maintained the stress equilibrium under 400 kPa lateral stress (see discussion on parametric studies). The particle size distribution was kept similar to that of dense sample. However, the number of particles was less than that of dense sample because of the higher void ratio.

Very good agreement has been obtained using clustered particles. However, volumetric compression of DEM samples was higher than that of physical one. For example, at 2 % axial strain compression was overestimated by 0.4 %. Also the DEM materials were less stiff compared to the Ottawa sand. The stiffness increased as interlocking of grains were modeled accurately i.e. either by incorporating rotational resistance to spherical particles or shape of the Ottawa sand into the numerical model. Similarly rotational resistance of DEM particles has helped to reduce the rate of sample compression gradually similar to that of Ottawa sand. DEM samples of perfectly spherical particles (PFC spheres free) tended to compress at a high rate and deviated from the observed triaxial volumetric response at higher strain.

4.5.3 Effect of confining stresses

The physical triaxial laboratory data of Holubec (1966) on Ottawa sand were considered. Holubec (1966) conducted triaxial compression tests on both dense (e=0.55) and loose (e=0.66) sands at three different confining stresses (210, 415 and 690 kPa). The dimensions of DEM sample were 102 mm × 51 mm × 51 mm similar to the physical dimensions of 51 mm diameter and 102 mm height. Minimum particle radius was 1.0 mm and a ratio of rmax/rmin of 2.0 was used based on the grain size distribution of sand. Loading platens were smooth as was the case in laboratory tests. Values of the other required parameters were the same as mentioned in Table 4.9. Only the case of 'PFC general' with the overlapping distance between particles, x, equal to 0.9R was considered.

Once again stress equilibrium was checked during shearing by stopping the platen and cycling to equilibrium. The platen velocities at which no large stress drops were observed were 0.05 and 0.1 m/s for 210 kPa and 410 kPa and beyond, respectively. This is consistent with the previous simulation cases of 100 kPa and 400 kPa lateral stress for which 0.01 m/s and 0.1 m/s, respectively were needed to reach stress equilibrium. Figure 4.30 shows the comparison at different confining stress level for the dense sample. The results of the simulation from 100 kPa are also shown. First of all, DEM simulations captured the well-recognized behaviour of granular material i.e. peak stress is confining stress dependent. Secondly, there is a consistent pattern as the confining stress was increased; the tendency to overestimate the peak stress increased as the confining stress was increased including the curve at 100 kPa (see Figure 4.30).

The pattern of volumetric responses closely follow to that of the physical ones i.e. the higher the confining stress, the greater the initial contraction and smaller the dilation. Notice that the physical volumetric responses as obtained from Holubec (1966) did not show any significant changes with the changing confining stresses. Also as in the case of 100 kPa, the DEM curves underestimated the observed physical curves.

Figure 4.31 shows the comparison at different confining stress level for the loose sample. Once again the simulated curves closely follow to those of the physical ones i.e. loose sample tends to contract after a certain axial strain at lower confining stress. However, as noted earlier a perfect match was not obtained between the simulated and physical response. The DEM simulated loose volumetric response tends to overestimate the volumetric strain. However, as can be seen from Figure 4.29, the tendency to overestimate reduced at the lower confining stress.

In summary, the peak stress of the dense and volumetric strain of the loose DEM samples tend to match the respective responses of the physical samples better at lower confining stress.

4.6 Summary

Triaxial Compression tests on uniform sub-rounded sand were simulated using the discrete element program Particle Flow Code in three-dimension (PFC^{3D}). Assemblies of smooth spherical particles as well as 'clustered' particles at both dense and loose densities were modeled. The shape of Ottawa sand grain was modeled by clustering two equal spheres overlapping each other. Both rigid single and segmental walls were used as lateral boundaries. The concept of segmental walls as an alternative to flexible boundaries was introduced. It was shown that this more simplistic approach to otherwise complex flexible membrane in three-dimension has allowed the numerical sample to bulge.

First of all, detailed parametric studies were undertaken to explore and identify the sensitivity of the numerical output to the various input parameters such as particle size and shape, particle elastic properties and friction coefficient, particle rotation, as well as sample size. Next the calibrations of the simulated triaxial responses from DEM samples were done against laboratory triaxial data on Ottawa sand at both dense and loose conditions as well as at different confining stresses. The following conclusions were reached:

- Irrespective of density and confining pressures, the followings particle contact parameters (using the Hertz-Mindlin contact law) best fit the stress-strain-volumetric behaviour of Ottawa sand under triaxial compressive loading:

  - Particle shear modulus: 1.0 GPa
  - Particle Poisson's ratio: 0.2
  - Contact friction coefficient between particles: 0.5

- To capture peak strength as well as the modulus of uniform sand, the best modeling approach is for clustered particles using linear contact law.
- The stiffness of the numerical sample was insensitive to particle rotation or particle shape and was only affected by the particle elastic properties such as shear modulus, G and Poisson's ratio, ν.
- For a model size close to that of a triaxial sample (165 mm × 70 mm × 70 mm), the size or scale effect was negligible provided that the average particle size (d_{50}) of the numerical sample remains close to or less than 4 mm (for a uniformity coefficient, C_u=1.5) and with internal damping equal to 0.8.
- Bulging in DEM samples can be simulated by multiple wall segments. While each unit of the discretization is rigid the overall response is close to the rubber membrane as is used in laboratory tests of soil samples.
- The proposed modeling to capture the shape of Ottawa sand grain i.e. overlapping of two equal spheres, has worked well to replicate the laboratory peak strength of standard Ottawa sand.

Table 4.1 Bond properties of clusters

	Parallel bond				
Parameter	Normal strength, N/m^2	Shear strength, N/m^2	Normal stiffness, N/m^3	Shear stiffness, N/m^3	Radius multiplier*
PFC command	Pb_n	Pb_s	Pb_kn	Pb_ks	Pb_r
Value Used	1e20	1e20	1e13	1e13	1.0
	Contact bond				
Parameter	Normal strength, N/m^2	Shear strength, N/m^2			
PFC command	n_b	s_b			
Value Used	1e20	1e20			

*** such that parallel-bond radius equals this multiplier times the minimum radius of the two bonded balls**

Table 4.2 Different cases of ramp up the platen velocity

_nsteps (total cycle to reach final velocity) : 1	**_nchunks (number of steps): 2**	**Cycle in each step 3=1/2**	**Series**
1000	80	12.5~12	A1
4000	80	50	A2
2000	40	50	A3
2000	160	12.5~12	A4
2000	80	25	A5

Table 4.3 Different cases of lateral boundary conditions

Number of segments in Lateral Boundaries (Rigid Wall)	**Series**
One	C1
Three by three in each wall (n_H=n_W=3)	C2
Seven (length) by three (width) in each wall (n_H= 7, n_W=3)	C3

Table 4.4 Initial Porosities of PFC samples (r_{min}=1.5 mm)

Creating the sample (r_{min}=1.5 mm)		Isotropic consolidation	
Specified porosity	Measured average porosities	Confining stress (kPa)	Measured average porosities
n_0	n_0	σ_3	n_0
0.38	Top – 0.364 Middle – 0.367 Bottom – 0.37	30	Top – 0.367 Middle – 0.37 Bottom – 0.376
		100	Top – 0.364 Middle – 0.367 Bottom – 0.37
		500	Top – 0.35 Middle – 0.35 Bottom – 0.36
0.35	Top - 0.296 Middle – 0.29 Bottom – 0.29	30	Top – 0.37 Middle – 0.366 Bottom – 0.356
		100	Top – 0.365 Middle – 0.36 Bottom – 0.35

Table 4.5 Initial Porosities of PFC samples (r_{min}=1.0 mm)

Creating the sample (r_{min}=1.0 mm)		Isotropic consolidation	
Specified porosity	Measured average porosities	Confining stress (kPa)	Measured average porosities
n_0	n_0	σ_3	n_0
0.38	Top – 0.34 Middle – 0.336 Bottom – 0.334	30	Top – 0.366 Middle – 0.362 Bottom – 0.358
		100	Top – 0.363 Middle – 0.358 Bottom – 0.354
		500	Top – 0.353 Middle – 0.35 Bottom – 0.344

Table 4.6 Configuration of different PFC samples

Cases	Sample Size (D_0) to Particle Size (d) Ratio	Particle Size Range (mm)	Average Particle Size (d_{50}) (mm)	Number of Particles
E1	$D_0/d_{50} = 8$	7.0–10.5	8.75	1429
E2	$D_0/d_{50} = 11.2$	5.0 –6.25	5.62	3921
E3	$D_0/d_{50} = 18.66$	3.0 – 4.5	3.75	18154
E4	$D_0/d_{50} = 23.33$	2.4 – 3.6	3	35457
E5	$D_0/d_{50} = 28$	2.0 – 3.0	2.5	61270
E6	$D_0/d_{50} = 46.66$	1.2 – 1.8	1.5	283660

Table 4.7 Average sample void ratios at different particle friction

Particle friction (μ)	Initial void ratio	Void ratio at 10% strain
0.1	0.36	0.37
0.5	0.36	0.396
1.0	0.36	0.404

Table 4.8 Physical and mechanical properties of Ottawa sand

Designation (Reference)	C_u	e_{max}	e_{min}	e	D_r	σ_3 (kPa)	End Conditions	ϕ_{max} (degree)	Sample Size (mm) D=diameter, H=height
A (Holubec, 1966)	2.0	0.822	0.443	0.465	94	207 414 690	frictionless	38.3	D = 51 H = 102
				0.537 0.632	95.7 60.3	207 207		39.5 34.6	
B (Koerner, 1968)	1.25	0.796	0.524	0.555	70	207 414 690	frictionless	33.7	D = H = 102
C (Norris, 1977)	-	-	-	0.499 0.571 0.495 0.546 0.532 0.628	89 60.5 96.5 97 103 66	42 118 333 42 118 333	frictionless	38.5 34 37.7 41.8 39.9 34.4	D = H = 51
D (Salgado et al, 2000)	1.48	0.78	0.48	0.558 0.537 0.59 0.586	74.1 80.9 63.3 64.6	100 100 400 100	not known	35.9 36.5 34.7 34	D = 70 H = 165

Table 4.9 Fundamental Input Parameters in PFC^{3D} for material calibration

Name	Symbol	Value
Particle shear modulus	G	1.0 GPa
Particle Poisson's ratio	ν	0.2
Contact normal stiffness	k_n	1×10^6 N/m
Contact shear stiffness	k_s	1×10^6 N/m
Particle contact friction	μ	0.5
Particle density	ρ_d	2650 kg/m^3
Numerical damping	α	0.8
Loading Platen Friction	δ	0.0/0.2
Lateral wall normal stiffness	K_{nl}	1×10^6 N/m
Loading platen normal stiffness	K_{np}	1×10^8 N/m
Platen velocity $\sigma_3 \leq 100$ kPa $\sigma3 > 100 < 400$ kPa $\sigma_3 \geq 400$ kPa	v	 0.01 m/s 0.05 m/s 0.1 m/s
Particle size (diameter)	d	3.0 – 4.5 mm 2.0 – 4.0 mm
Overlapping distance in clustered particles	x	R, 1.1R and 1.2R R=particle radius

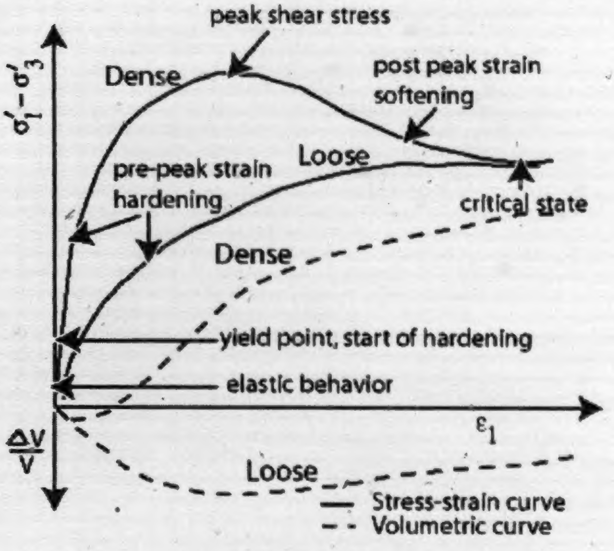
peak shear stress
$\sigma_1' - \sigma_3'$
Dense
post peak strain softening
Loose
pre-peak strain hardening
critical state
Dense
yield point, start of hardening
elastic behavior
ε_1
$\frac{\Delta V}{V}$
Loose
Stress-strain curve
Volumetric curve

Figure 4.1 Typical response of triaxial test on sand

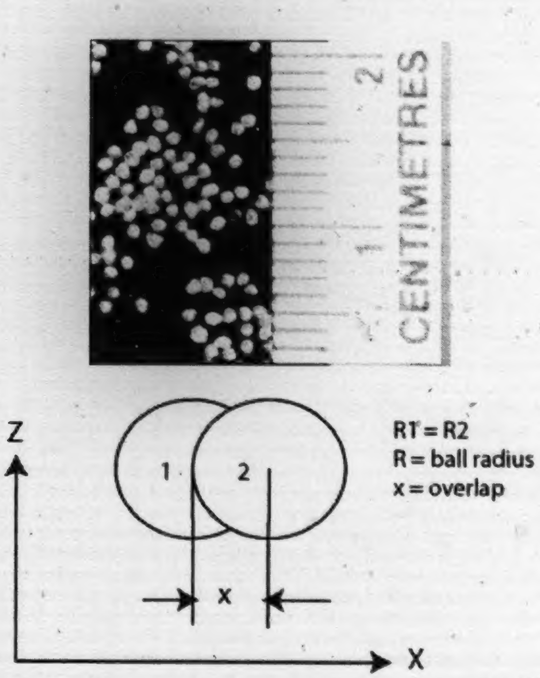
2
CENTIMETRES
1
Z
1
2
R1 = R2
R = ball radius
x = overlap
x
X

Figure 4.2 Grain shape and size of Ottawa sand (sieve no. 20-30, ASTM C-190) and shape of a cluster in DEM simulation

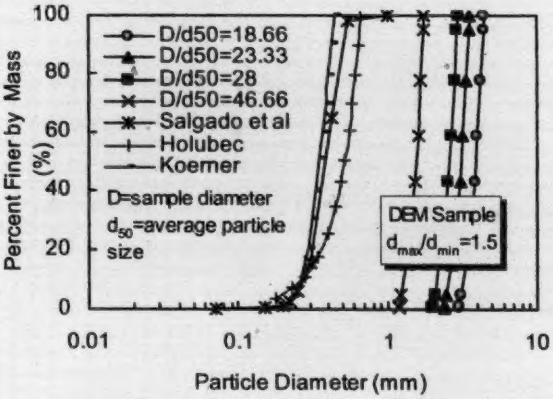

Figure 4.3 Particle size distributions of numerical samples and Ottawa sand

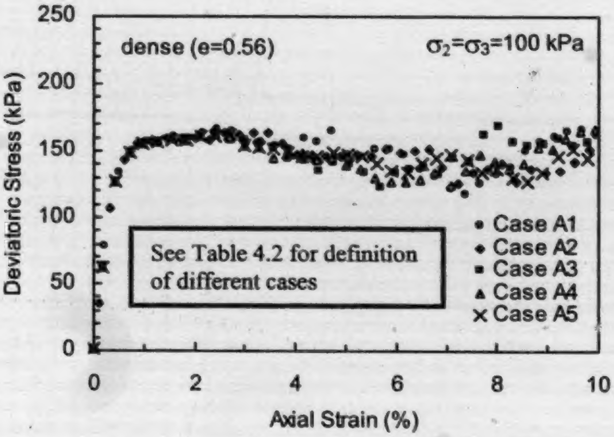

Figure 4.4 Effect of parameters to ramp up the platen velocity on simulated dense constitutive behavior (Sample size: 50×21×21 mm, G=1.0 GPa, ν=0.2, α=0.8, μ=0.5 and v=0.01 m/s)

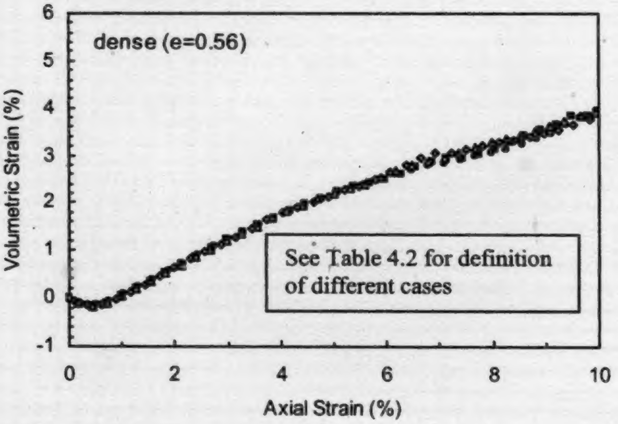

Figure 4.4 (Contd) Effect of parameters to ramp up the platen velocity on simulated dense constitutive behavior (Sample size: 50×21×21 mm, G=1.0 GPa, ν=0.2, α=0.8, μ=0.5 and v=0.01 m/s)

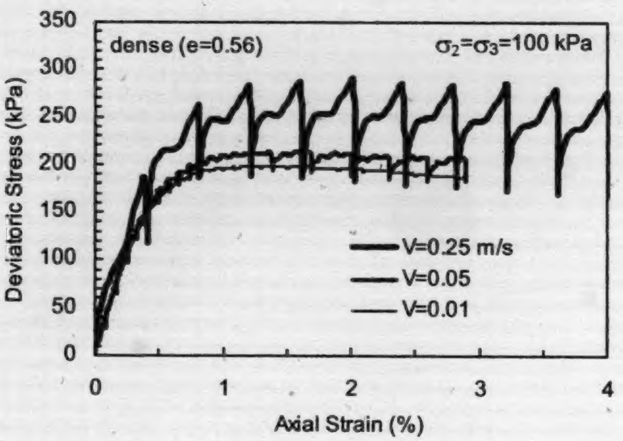

Figure 4.5 Effect of platen velocity on stress equilibrium of dense PFC samples

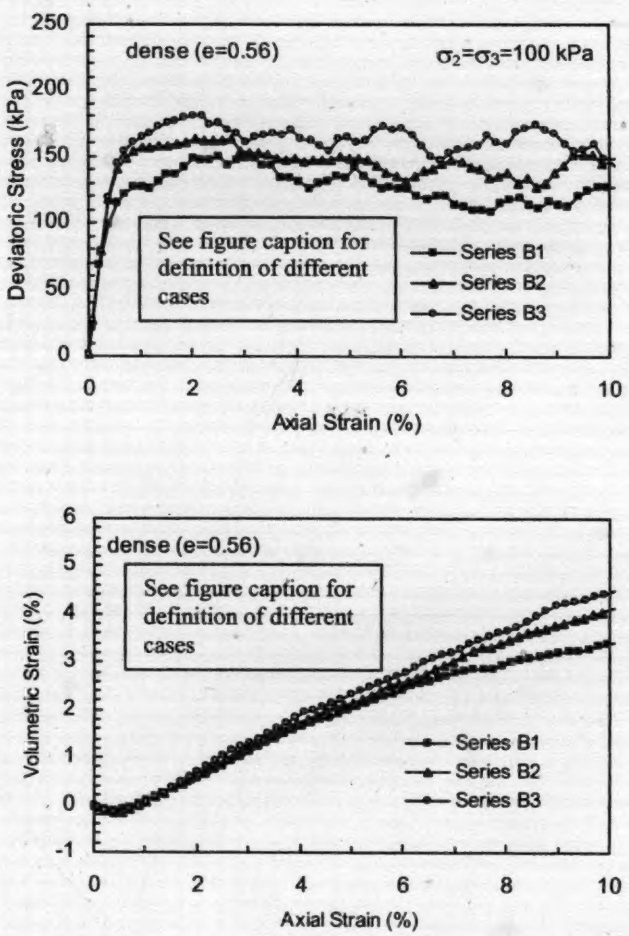

Figure 4.6 Effect of loading platen roughness on simulated dense constitutive behavior (Sample size: 50×21×21 mm, $G=1.0$ GPa, $\nu=0.2$, $\alpha=0.8$, $\mu=0.5$ and $v=0.01$ m/s; B1: $\mu_p=0$; B2: $\mu_p=0.2$; B3: $\mu_p=0.5$)

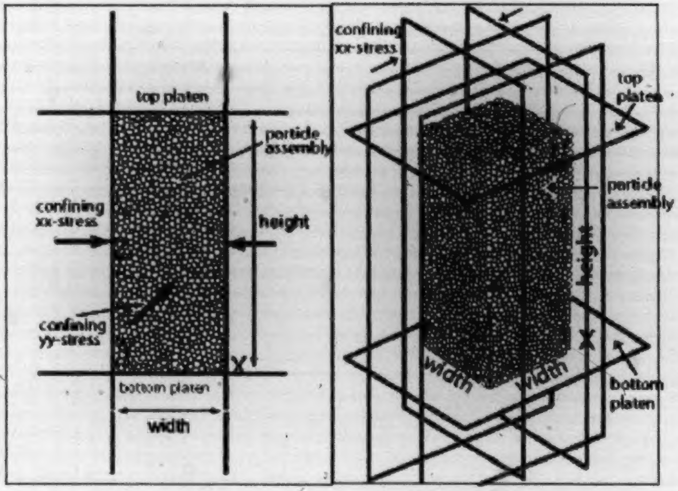
top platen
particle assembly
confining xx-stress
height
confining yy-stress
X
bottom platen
width
confining xx-stress
top platen
particle assembly
height
X
width
width
bottom platen

Figure 4.7 Configuration of a typical assembly of particles for triaxial test

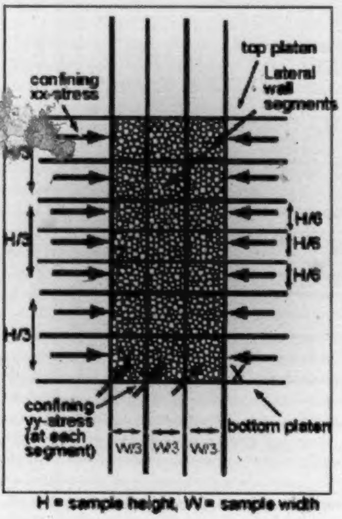
top platen
Lateral wall segments
confining xx-stress
H/3
H/3
H/3
H/6
H/6
H/6
X
confining yy-stress (at each segment)
W/3
W/3
W/3
bottom platen

H = sample height, W = sample width

Figure 4.8 Segmental lateral boundary in numerical triaxial test

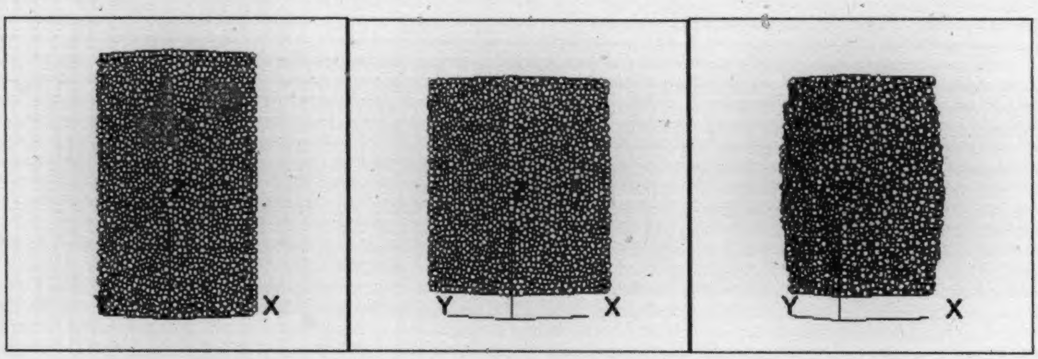

Figure 4.9 Macro deformation pattern of dense PFC sample (smooth spherical particles, (σ_3=100 kPa): (a) initial condition (b) rigid single walls (c) rigid discretized walls

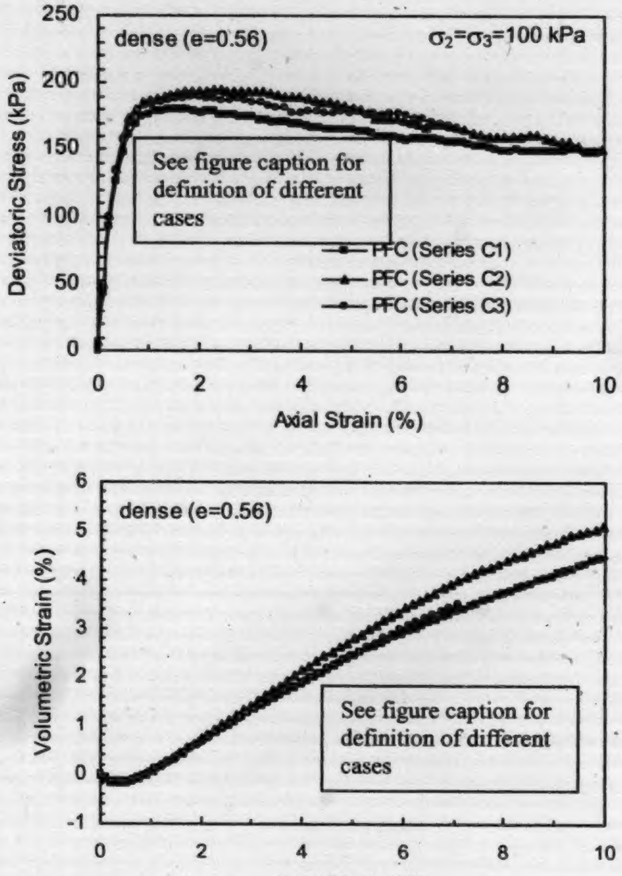

Figure 4.10 Effect of lateral boundary on simulated dense stress-strain-strength and volumetric behavior (Sample size: 165×70×70 mm, G=1.0 GPa, ν=0.2, α=0.8, μ=0.5 and v=0.01 m/s; C1: single wall; C2: 3 by 3 segments; C3: 7-along length by 3-along width segments)

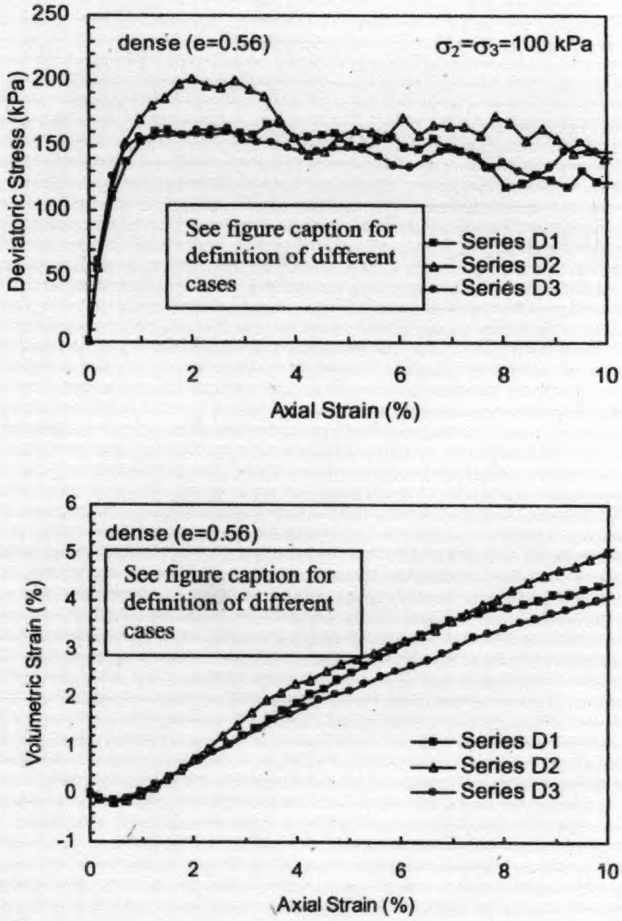

Figure 4.11 Effect of numerical damping on simulated dense constitutive behavior (Sample size: 50×21×21 mm, G=1.0 GPa, ν=0.2, μ=0.5 and v=0.01 m/s; D1 : α=0.7; D2 : α=0.5; D3 : α=0.8)

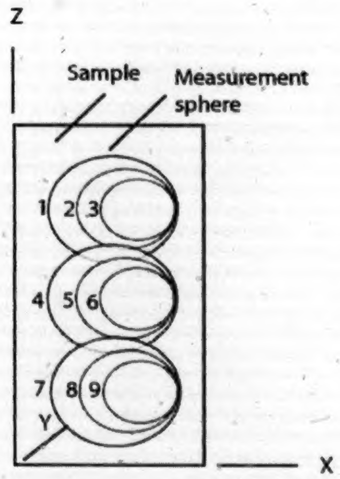
Z
Sample
Measurement sphere
1
2
3
4
5
6
7
8
9
Y
X

Figure 4.12 Size and locations of measurement spheres within a pfc sample

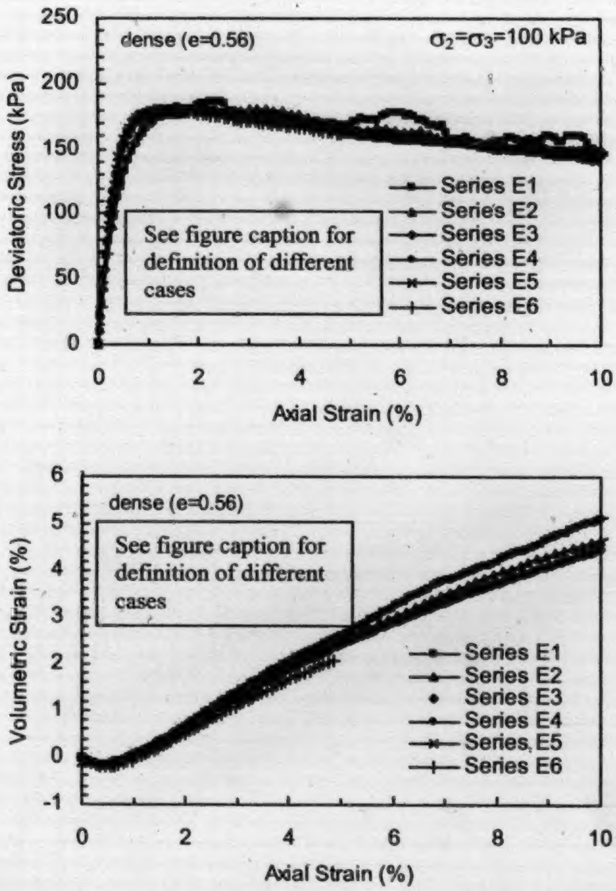

Figure 4.13 Effect of particle size on dense simulated stress-strain-strength and volumetric behavior (Sample size: 165×70×70 mm, G=1.0 GPa, ν=0.2, α=0.8, μ=0.5 and v=0.01 m/s; E1: D_0/d_{50} = 8; E2: D_0/d_{50} = 11.2; E3: D_0/d_{50} = 18.66; E4: D_0/d_{50} = 23.33; E5: D_0/d_{50} = 28 and E6: D_0/d_{50} = 46.66)

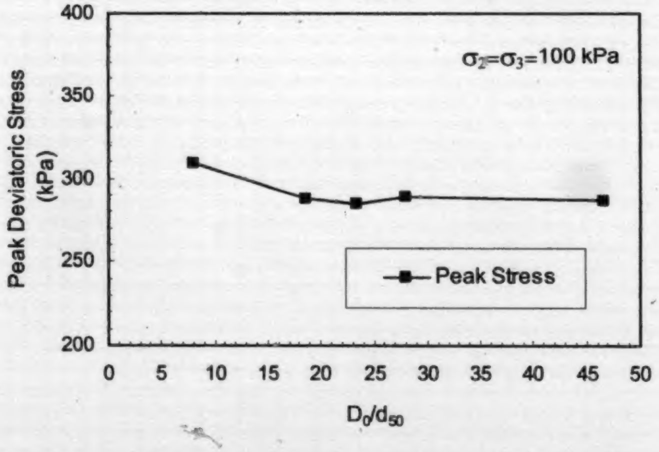

Figure 4.14 Effect of particle size on dense simulated peak strength
(Sample size: 165×70×70 mm, G=1.0 GPa, ν=0.2, α=0.8, μ=0.5 and v=0.01 m/s)

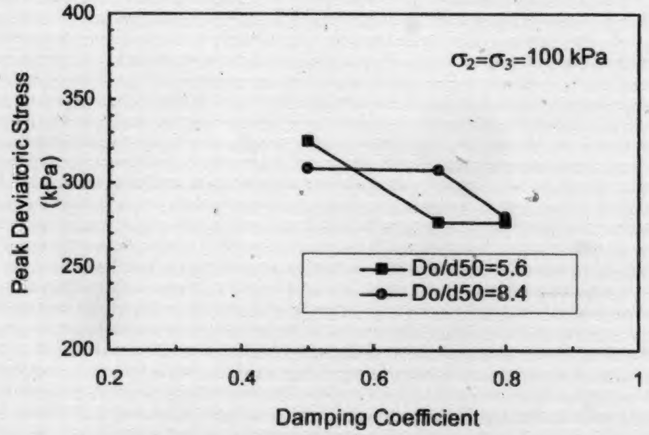

Figure 4.15 Size effect on simulated dense peak strength
(Sample size: 50×21×21 mm, G=1.0 GPa, ν=0.2, μ=0.5 and v=0.01 m/s)

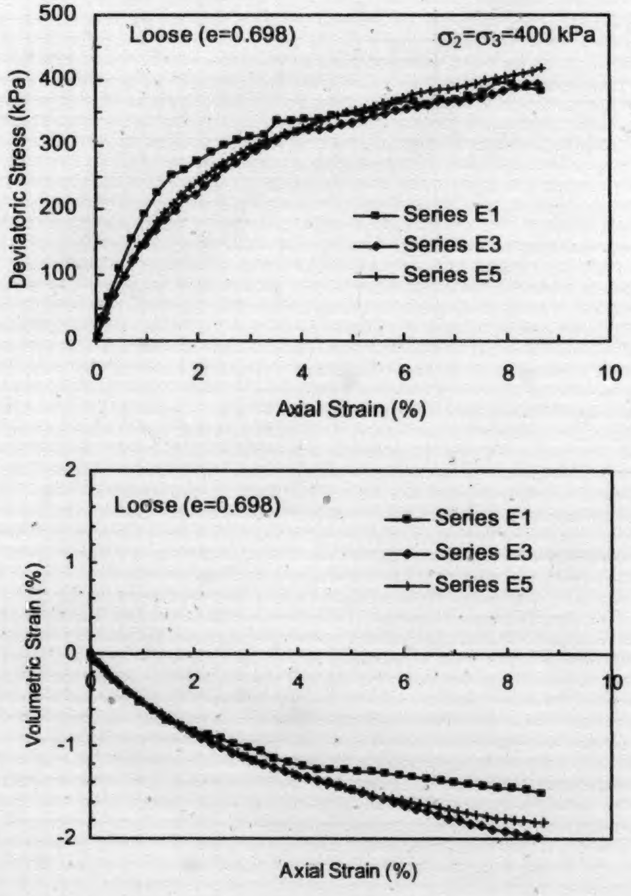

Figure 4.16 Effect of particle size on loose simulated stress-strain-strength and volumetric behavior (Sample size: 165×70×70 mm, G=1.0 GPa, ν=0.2, α=0.8, μ=0.5 and v=0.1 m/s)

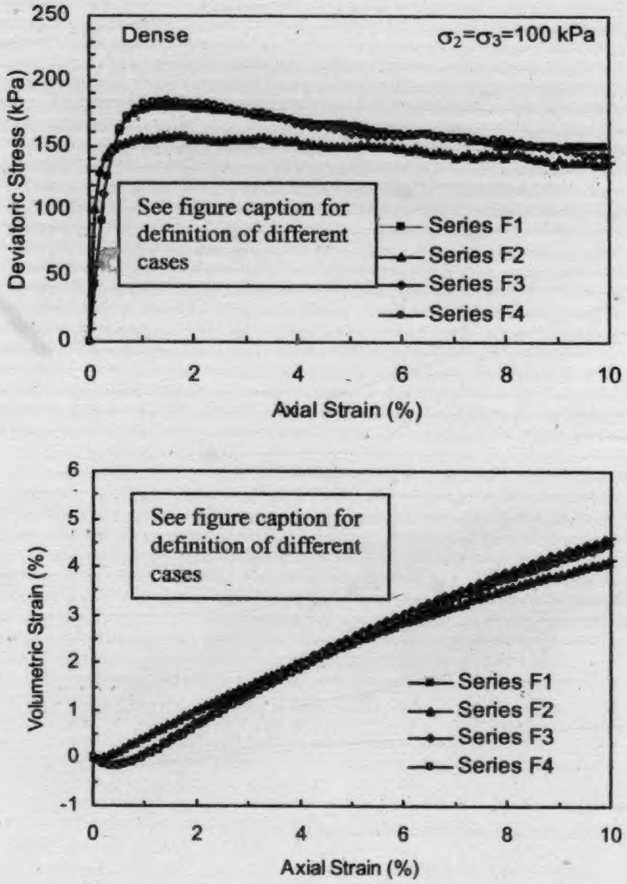

Figure 4.17 Effect of particle elastic properties on simulated dense stress-strain-strength and volumetric behavior (Sample size: 165×70×70 mm, α=0.8, μ=0.5 and v=0.01 m/s; F1: G=1.0 GPa, ν=0.2; F2: G=10.0 GPa, ν=0.2; F3: G=1.0 GPa, ν=0.3 and F4: G=1.0 GPa, ν=0.1)

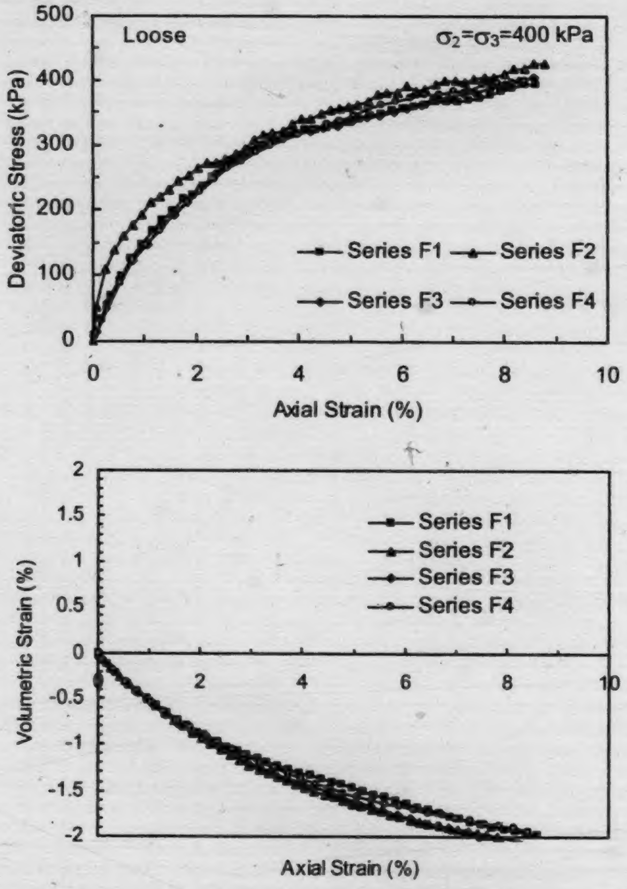

Figure 4.18 Effect of particle elastic properties on simulated loose stress-strain-strength and volumetric behavior (Sample size: 165×70×70 mm, α=0.8, μ=0.5 and v=0.1 m/s)

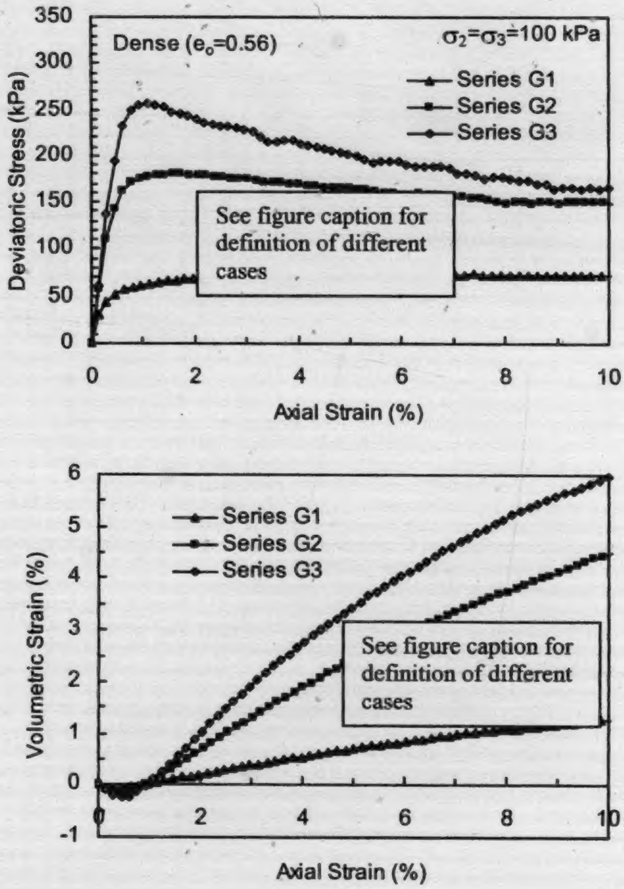

Figure 4.19 Effect of μ during shear on simulated dense stress-strain-strength and volumetric behavior (Sample size: 165×70×70 mm, G=1.0 GPa, ν=0.2, α=0.8 and v=0.01 m/s; G1: μ=0.1; G2: μ=0.5 and G3: μ=1)

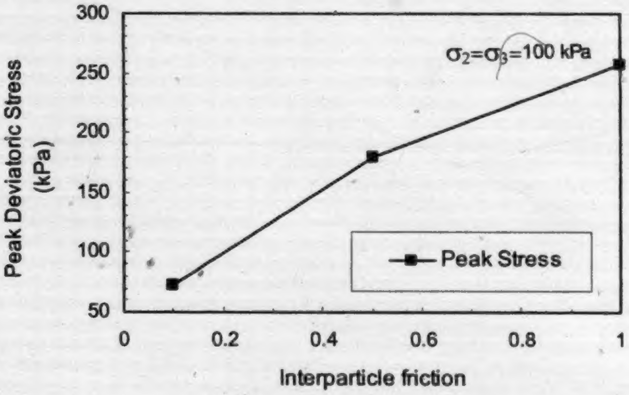

Figure 4.20 Effect of μ during shear on simulated dense peak strength

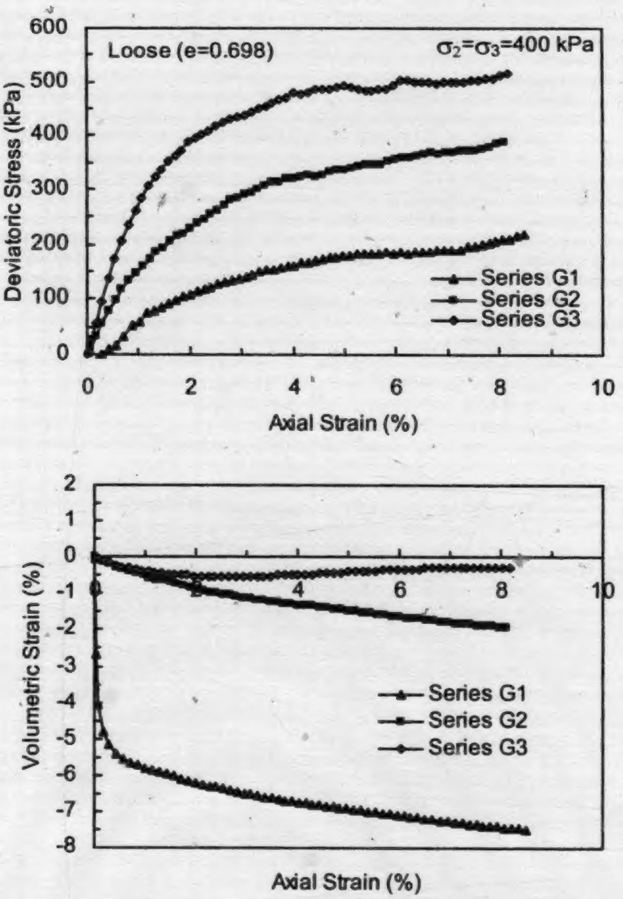

Figure 4.21 Effect of μ during shear on simulated loose stress-strain-strength and volumetric behavior (Sample size: 165×70×70 mm, G=1.0 GPa, ν=0.2, α=0.8 and v=0.1 m/s; G1: μ=0.1; G2: μ=0.5 and G3: μ=1)

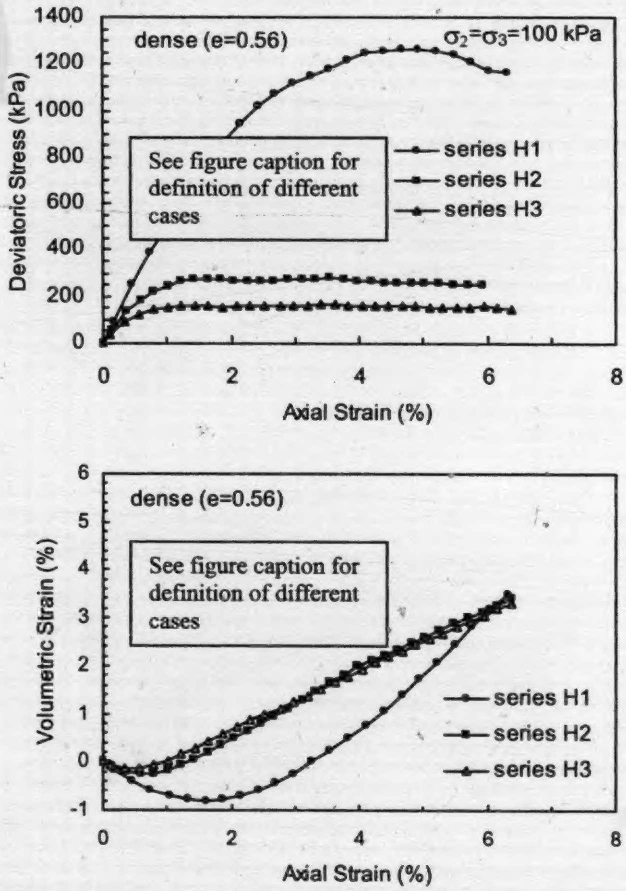

Figure 4.22 Effect of particle rotation on simulated dense constitutive behavior (Sample size: 50×21×21 mm, G=1.0 GPa, ν=0.2, μ=0.5, α=0.8 and v=0.01 m/s; H1: rotations of all particles were fixed; H2: rotations of particles along the middle-third of sample were fixed while keeping the top and bottom-third particles free; H3: all particles free to rotate)

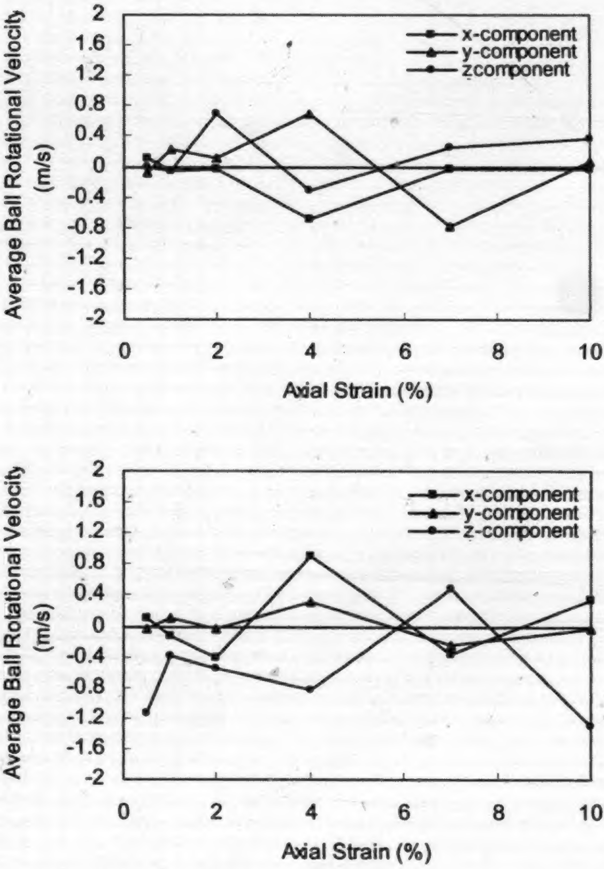

Figure 4.23 Variation of average incremental particle rotational velocities versus axial strain: free rotation (a) middle-third of sample and (b) top one-third of sample

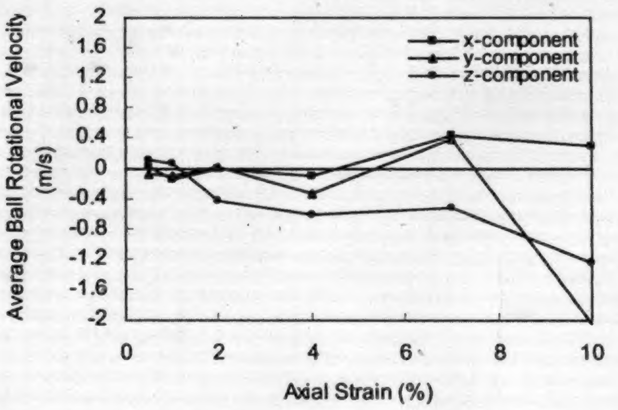

Figure 4.24 Variation of average incremental particle rotational velocities (top one-third of sample) versus axial strain: fixed rotation (middle-third)

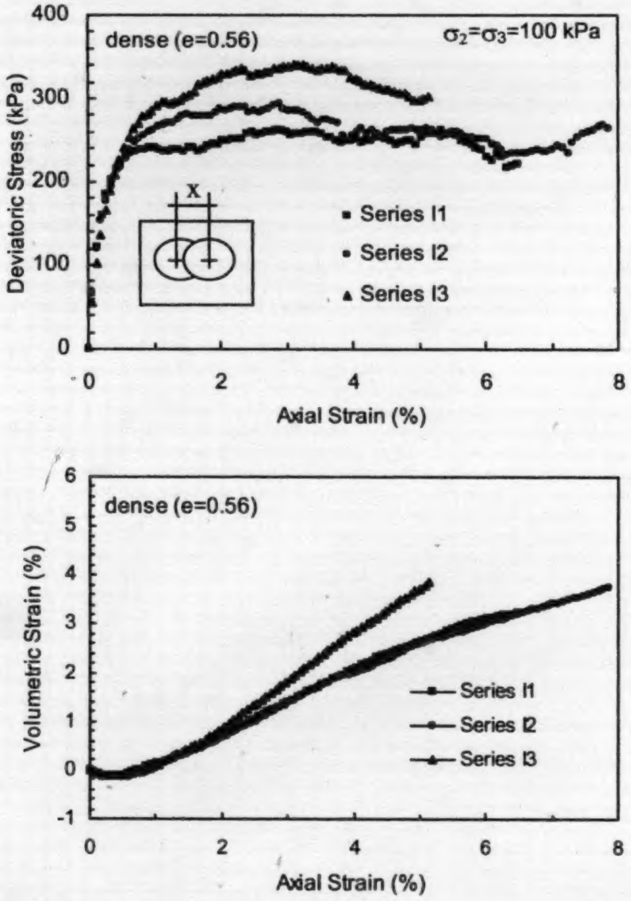

Figure 4.25 Effect of clustering (overlap) on simulated dense constitutive behavior (Sample size: 50×21×21 mm, k_n=ks=1.0×e^6 N/m, α=0.8, μ=0.5 and v=0.01 m/s; I1: x=R; I2: x=0.8R; I3: x=0.5R)

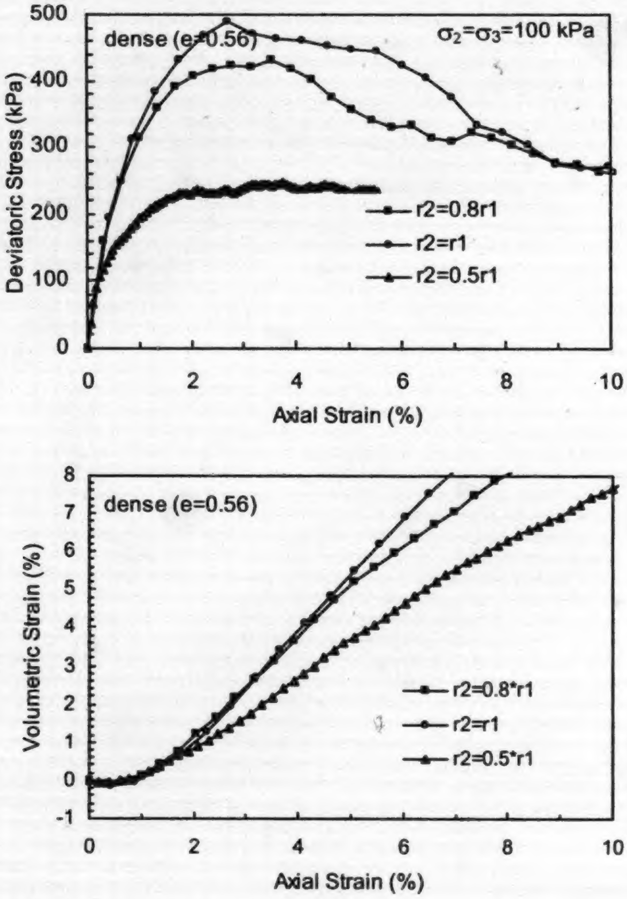

Figure 4.26 Effect of clustering (particle size but no overlap) on simulated dense constitutive behavior (Sample size: 50×21×21 mm, k_n=ks=1.0×e^6 N/m, α=0.8, μ=0.5 and v=0.01 m/s)

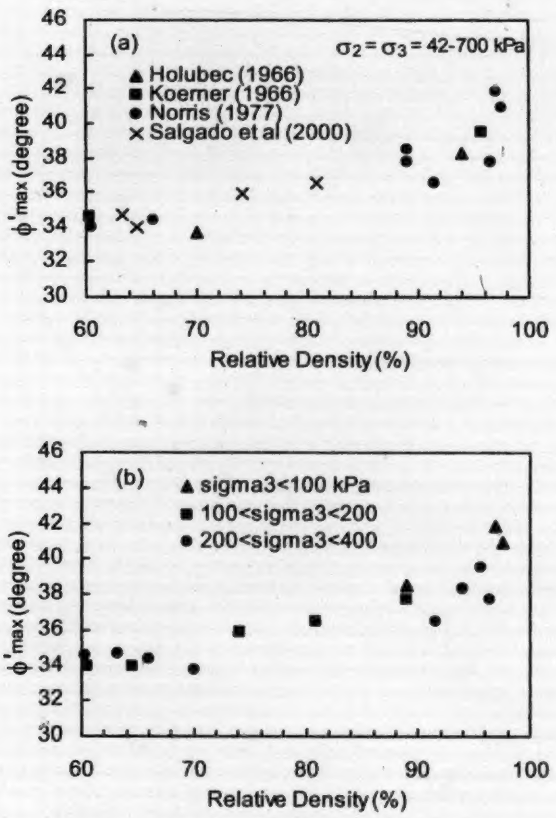

Figure 4.27 Variability in friction angle of Ottawa sand

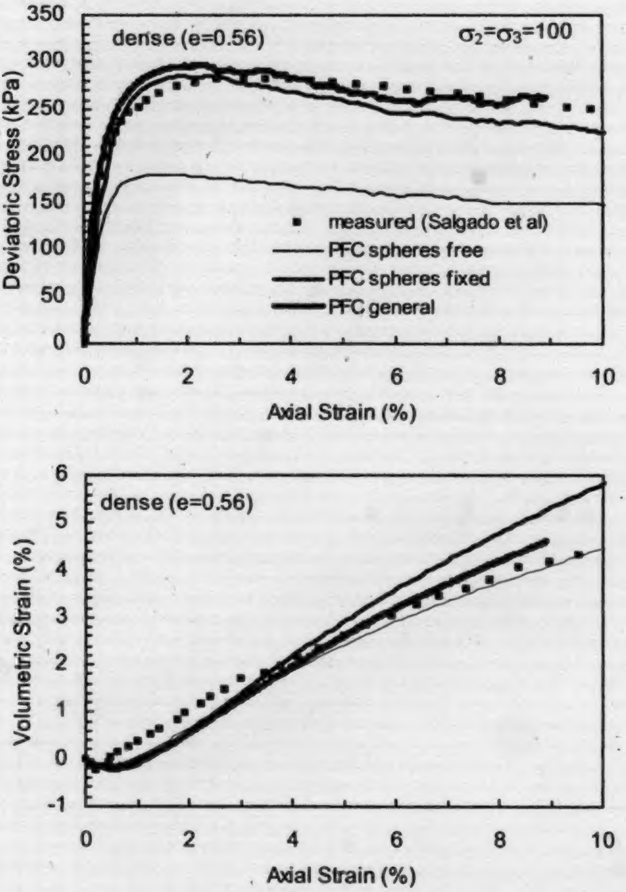

Figure 4.28 Matched constitutive behavior (dense) between physical test and PFC simulation (G=1.0 GPa, ν=0.2, μ=0.5 and v=0.01 m/s)

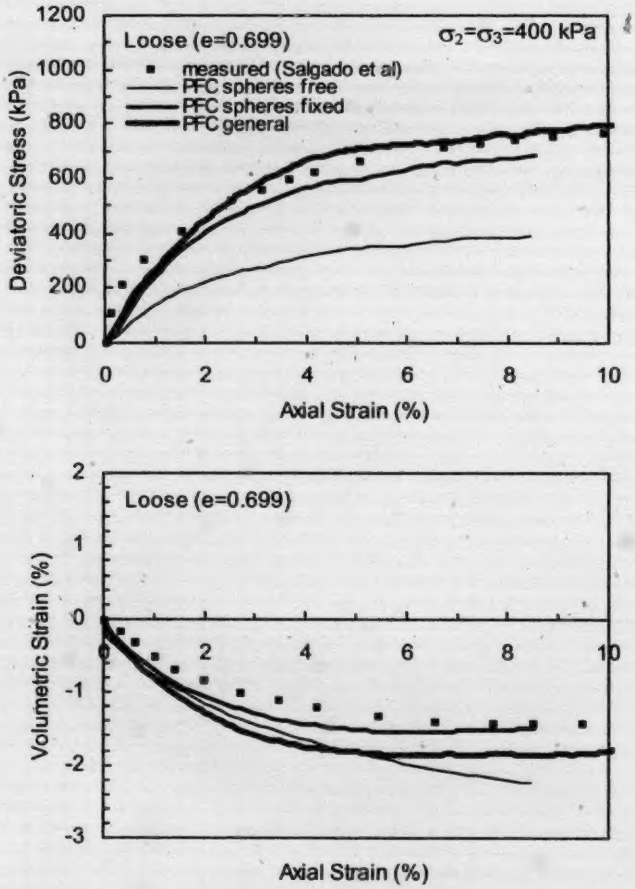

Figure 4.29 Matched constitutive behavior (loose) between physical test and PFC simulation (G=1.0 GPa, v=0.2, μ=0.5 and v=0.1 m/s)

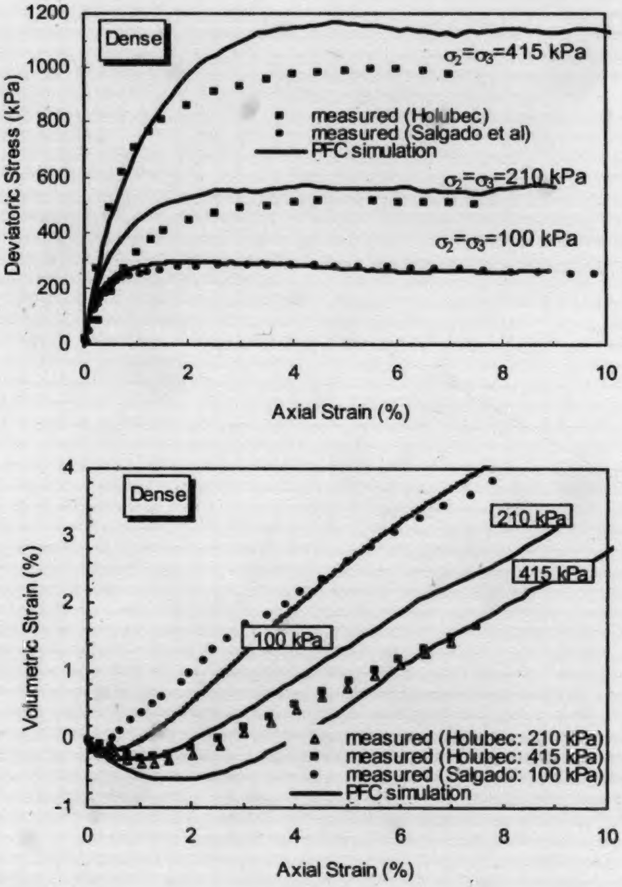

Figure 4.30 Dense simulated and physical constitutive relationships at different confining stresses (PFC general: G=1.0 GPa, ν=0.2 and μ=0.5)

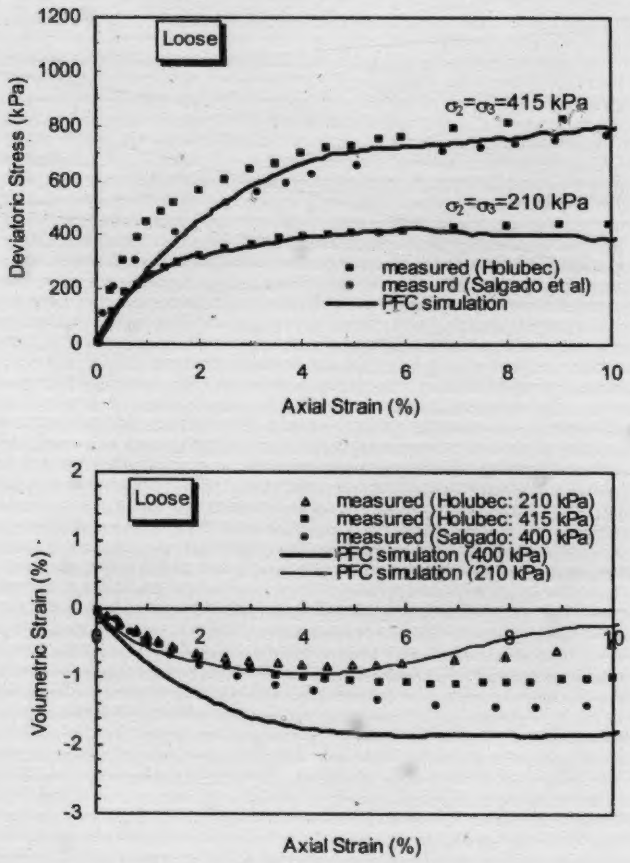

Figure 4.31 Loose simulated and physical constitutive relationships at different confining stresses (PFC general: G=1.0 GPa, ν=0.2 and μ=0.5)

CHAPTER 5

Discrete Element Modeling of Centrifuge Testing of a Shallow Tunnel in Sand

Soil behaviour is highly stress dependent. Consequently, a centrifuge modelling technique has been employed to a test small-scale model (1/Nth-scale) under high gravity (Ng) so that field-scale stress levels are reproduced. The centrifuge is a convenient tool to simulate field-scale in a small-scale model. Centrifuge testing is often conducted to simulate problems that challenge a model numerically. Chambon and Corte (1994) (hereafter, C and C [1994]), used centrifuge testing to investigate the near-face behaviour of circular tunnels in clean sand. They analyzed several tunnel diameters and various tunnel depths, and presented their findings in terms of face-pressure collapse and near-face deformation patterns. A discussion of C and C's results will be presented in section 5.1.1. In this chapter, discrete element modeling (DEM) was used to simulate the problems posed by C and C (1994). Results of discrete element modeling were compared to those of C and C (1994), and to results from closed form solutions (discussed in Chapter 3 and summarized in section 5.1.2).

First the numerical results are presented for a typical test of a tunnel in dry sand with a C/D of 2.0. A parametric study and a more in-depth discussion follow regarding the influence of various numerical variables on these results. Finally, comparisons are drawn between the numerical results and physically observed failure mechanisms.

The discrete element modeling used in this chapter to simulate the C and C (1994) centrifuge testing used the best-fit particle stiffness parameters (Table 4.8) established in Chapter 4 for clean sand. The grain size for the centrifuge simulation models was higher than the typical grain size considered during material calibration. The effect of grain size was studied in detail and is discussed in section 5.3. Also simulations in this work were limited to using spherical shaped particles only.

5.1 PHYSICAL TESTING AND ANALYTICAL PREDICTIONS

5.1.1 Centrifuge modeling of tunnel face stability

Chambon et al. (1991) and C and C (1994) investigated the face stability and near-face deformation patterns of circular tunnels in Fontainebleau sand (Table 5.1) using a series of centrifuge tests. The configuration of the centrifuge model used for all their tests is shown in Figure 5.1. The tunnel face was simulated with a thin (0.2 mm) latex membrane, with slack left to prevent mechanical influence on the face displacements. Details of the tunnel model are shown in Figure 5.2. The pressure in the tunnel model during preparation (spreading of sand in a rigid container) and during acceleration of the centrifuge was kept equal to the geostatic stress at the centerline of the tunnel. Pressure on the face was then gradually reduced until failure occurred. Two types of support for the tunnel face were reproduced: (1) a uniform pressure for the compressed-air shield; and (2) a hydrostatic pressure to simulate the pressure diagram in the case of a slurry shield. Specific details of the test procedure can be found in C and C (1994).

The physical properties of Fontainebleau sand are shown in Table 5.1 where C_u and e indicate coefficient of uniformity and void ratio, respectively. Unit weight of the sand ranged from 15.3 to 16.1 kN/m^3, corresponding to relative densities from 0.65 to 0.92. The well-rounded quartz and fine-grained Fontainebleau sand was white and clean (more than 99.5% SiO_2).

C and C (1994) investigated the effects on face stability of tunnel diameter and of depth below the ground surface. The level of acceleration used dictated the dimension of the prototype, as the principal scaling law applying to tunnelling problems is that of length. Prototype diameters of 5 m, 10 m, and 13 m were chosen corresponding to accelerations of 50 g, 100 g, and 130 g. C and C (1994) expressed their results in terms of a ratio of the depth of the tunnel (*C*), measured from the ground surface to the top of the tunnel, to tunnel diameter (*D*). The full range of parameters investigated is summarized in Table 5.2.

C and C (1994) found that for the case of uniform face pressure on the face of a fully lined tunnel (compressed-air shield) with C/D equal to 2.0, collapse occurs in three stages (Figure 5.3). No face movement was detected until the face pressure was decreased to 20 kPa as the pressure was decreased gradually from an initial value equal to the weight of the earth at the height of the tunnel centre line (K_0 condition). Any further decrease in internal pressure from 20 kPa, called the characteristic pressure (p_c) by C and C (1994), resulted in an increment of face movement (yielding). The limiting collapse pressure (p_f) corresponding to the onset of large deformations was detected by the sudden acceleration of movement (see Figure 5.3). C and C found that the collapse pressure was little affected by changes of geometry at the relative depths considered (C/D = 0.5, 1, 2, 4) or by the density of the soil. For instance, for a C/D ratio equal to 1, a change in density from 15.3 kN/m^3 to 16.1 kN/m^3 resulted in a change in collapse pressure of only 0.1 kPa. An increase of 0.6 kPa in the collapse pressure was found as the C/D ratio was changed from 0.5 to 2.0. On the other hand, the diameter of the tunnel has an approximate linear relationship with the collapse pressure, e.g., doubling the diameter requires an approximate doubling of the supporting pressure (Figure 5.4).

In addition to monitoring the face displacements, Chambon et al. (1991) and C and C (1994) investigated the deformation patterns ahead of the tunnel face. They used coloured sand to create horizontal planes in each sand block. After each test the sand blocks were moistened to provide an apparent cohesion induced by suction. The blocks were then cut along different vertical planes and the displacement pattern identified was carefully traced onto grid paper. Figure 5.5 shows the displaced coloured sand layers. By combining both deformation and face pressure Chambon et al. (1991) and C and C (1994) were able to clearly define the onset and extent of yielding.

C and C's centrifuge test simulates a complex problem involving shallow tunneling in soft ground. The tunnel model was assumed to be the finished tunnel (i.e., permanent tunnel lining installed). Therefore, the complete tunnel process involving tunnel advancement and associated changes in ground stress and displacement (radial loss, overcutting, etc.) around the tunnel were not modeled. Their experimental results are significant in understanding the parameters affecting the short-term deformation response in cohesionless soil, i.e., face stability and failure mechanism.

5.1.2 Analytical results

Details of the mechanism (three-dimensional) and prediction of the drained stability of shallow circular tunnel construction are discussed in section 2.3.2 of Chapter 2. As discussed by Sagaseta (1998), analytical solutions, used in conjunction with numerical methods and interpretation of actual observations, form a basis for the prediction of performance in engineering problems. This is particularly true for soil deformation around tunnels. Figure 2.5 (reproduced here as Figure 5.6) shows predictions of collapse pressure in a shallow tunnel using different analytical methods (equations 2.1 to 2.5 in section 2.2.2). Also shown in Figure 5.6 are the centrifuge results for dry and clean sand. For a given tunnel diameter, in a case of dry, clean sand ($\phi = 40^0$, c = 0), the analytical predictions of collapse pressure are always higher than predictions from centrifuge testing. For instance, for a 5.0 m diameter tunnel, the theoretical collapse pressure estimated by Vermeer and Ruse (2000), which was closest to the physical results, was 39.4 percent higher than the collapse pressure measured by C and C (1994).

Although analytical predictions are based on an idealized tunnel model and a simplified failure mechanism in the ground ahead of the face, they are still used in practice for design purposes. Due to their simplicity, analytical results are valuable in quantifying the face pressure required for face stability and therefore are compared here with the numerical results using discontinuum modeling.

5.2 SIMULATING CENTRIFUGE TESTS WITH DEM

5.2.1 Model Description

The dimensions of the actual centrifuge box (containing sand) used by C and C (1994) in their centrifuge tests was 1200×800×360 mm (see Figure 5.1). During the time of this analysis it was not practical, using desktop computers, to simulate the complete centrifuge box with particles of 2 mm diameter (approximate average grain size of Fontainebleau sand). In order to simplify the analyses and take advantage of symmetry, the DEM models were reduced to half of the physical model (Figure 5.7). In addition, because this research focused only on behaviour near the tunnel-face, grading of the particle size distribution was used to reduce the total number of particles, i.e., by increasing particle size toward the model boundaries (Figure 5.8). This is similar to the approach used commonly in the finite element method where finer discretization is used in the zone of interest and coarse discretization is used in approaching the model boundaries. Figure 5.9 shows the three-dimensional view of DEM material discretization.

The second issue in simulating the centrifuge tests was simulating the steel tube used to represent the tunnel lining. This was solved by identifying the space which would be occupied by the steel lining, and then bonding the particles in that region with bond properties that simulated a perfectly rigid body. To eliminate any kind of movements of the particles simulating the lining tube the particles were assigned zero velocities (x, y, and z components) and the velocities were then fixed. The excavation was modeled by deleting the particles inside the lining particles (see Figure 5.9). Forces equivalent to the required face pressure was specified to each particle occupying the face to simulate the face pressure. The force to each face particle was calculated by multiplying the required face pressure times the area and dividing by the number of particles. This process was different than that of physical modeling where pressurized flexible membrane was used to control pressure.

5.2.2 Particle Characteristics

It is important to note that the tunnel problem involves much smaller strain than the triaxial simulations and only the consideration of stress-stain behaviour up to pre-failure will suffice. Figure 5.10 shows the stress-strain-volumetric response of dense DEM material up to 2% axial strain. PFC-general refers to non-spherical particles and in Chapter 4 it was found that PFC-general captured the stress-strain behaviour including the initial modulus of real sand. Figure 5.3 shows that during stage 2 of face deformation and just before face collapse, material strain varies between zero and 0.7 percent. From Figure 5.10 the secant modulus is almost the same up to 0.1 percent and becomes 23 and 36 MPa at 0.7 percent strain for cases of smooth spherical and clustered simulations, respectively.

Due to the limitation of computer power, although the initial modulus of DEM material of spherical particles fell short compared to that of material consisting of non-spherical particles, it was decided to proceed with the simple spherical shaped particles in tunnel simulations rather than using the more computationally rigorous non-spherical particles. As will be shown later in this chapter, this worked well as it was found that a somewhat less stiff stress-strain relationship of DEM material obtained from using smooth spherical particles produced little deviation from the experimental result as far as comparison of collapse pressure was concerned. In the following simulations, therefore, spherical particles with free rotation were utilized.

The particle sizes in the area of the tunnel face (region 1 in Figure 5.8) were chosen using the ratio in the small-scale model of tunnel diameter (100 mm) to particle diameter (2 mm) as approximately 20. Table 5.3 shows the size distribution and number of particles in each zone shown in Figure 5.8 (for the standard simulation case shown in Figure 5.12).

5.2.3 Boundary Conditions

The six walls that provided boundaries for the centrifuge box were frictionless, rigid, and fixed in position. The top wall did not play any role as the particles in contact with the top wall moved downward under gravity during the generation of initial stress. Therefore, there was a free surface at the top of the model.

The tunnel tube was also rigid as described above. The particles were glued together by parallel bonds with high strength. The glue properties of the particles simulating the tube are described in Table 5.4. The surface friction of the particles comprising the liner was same as the particles that made up the material.

5.2.4 Initial Conditions and Tunnel Simulation

The procedure followed in the DEM simulation was similar to that used in centrifuge testing and constituted the following steps:

- After generating particles within the model boundaries, the tunnel tube was created and the particles inside the tube were deleted to form the tunnel.
- Required gravitational acceleration (here 50g to model a 5 m diameter tunnel) of the initial assembly of particles was specified and then cycled to equilibrium with the tunnel model in place.
- During cycling, face pressure in the DEM simulation was gradually increased to the

required pressure (geostatic horizontal stress at the centre line of the tunnel) while stresses in surrounding material were also increasing under 50 g.

- At the end of cycling, the tunnel face condition was checked for any cave-in or blowout of face material. The 2nd and 3rd steps were repeated with a revised internal face pressure value if any of these conditions were noticed.
- Finally, the unit weight of the DEM material was checked for vertical stress at a certain depth. The vertical stress was taken as the average of three measurement spheres installed at the required depth.

Two factors played a critical role during the gradual increase of face pressure in the DEM model: (1) the number of increment stages and (2) the total number of cycles. In addition to the required face pressure itself, the values assigned for the increment stages and total cycles also dictated the initial face condition, i.e., whether the face would blow out or cave-in. This was a trial-and-error process. Too few or too many cycles than actually required could result in blowout or cave-in, respectively, of the face.

Table 5.5 summarizes the initial conditions for the all the simulations for the 5.0 m diameter tunnel described below. Once the desired initial state was achieved, the face pressure (i.e., forces on the face particles calculated automatically from the new pressure) was gradually reduced until face collapse occurred. The model was cycled to equilibrium during each face pressure stage. A flow chart describing the procedure required for setting the initial conditions and subsequent testing is given in Figure 5.11.

The Hertz-Mindlin contact law was used to model the contact behaviour between spherical particles for the tunnel simulations described below.

5.3 CALIBRATION AGAINST PHYSICAL MODELING

5.3.1 DEM Modeling: Evolution of the Tunnel Face

Only three micro-parameters are needed to formulate and simulate a boundary value problem in DEM, namely: two contact stiffness or particle/particle elastic properties (shear modulus, G and Poisson's ratio, ν) and particle contact or interparticle friction, μ. The values for these micro parameters were established in Chapter 4 and were found to be G = 1.0 GPa, $\nu = 0.2$, and $\mu = 0.5$ regardless of particle shape. Although particle shape played an important part in matching the overall triaxial compression behaviour of the DEM sample to that of real sand, this was ignored in the following simulations as explained in section 5.2.2.

Regardless of the calibrated values of the above mentioned parameters, it was intended to see the effect of variation of these parameters on the tunnel response. In addition to the micro-properties, which were needed to simulate the interaction of particles, numerical damping was found to play a part. It was also found that model size and timestep affects the response of the DEM sample. Hence, in order to get a clear picture of the tunnel response using DEM, the effects of particle elastic properties and friction, damping, model size, and timestep were also investigated. Finally, the effect of particle size was investigated. The simulation was started with a size distribution of $r_{min} = 3.5$ mm and ratio $r_{max}/r_{min} = 1.5$ in the zone of interest up to $r_{min} = 5.5$ mm at the boundaries, which resulted in 67143 particles (Table 5.3). The particle sizes were reduced gradually while keeping in mind the limitation of computer power.

Unfortunately, Chambon and Corte (1994) published only one plot of horizontal face displacement versus internal support pressure for the case of a C/D ratio of 2.0, a tunnel diameter of 5.0 m, and uniform face pressure. Therefore, DEM simulations were performed mainly for the above case and were compared with the results of the centrifuge data of Chambon and Corte.

5.3.1.1 DEM curve using calibrated parameters

Figure 5.12 shows the comparison of the horizontal displacement of the tunnel face with decreasing confining pressure for a tunnel diameter of 5.0 m and a C/D ratio of 2.0. The micro parameters were obtained by calibration against triaxial data of uniform clean sand, i.e., G = 1.0 GPa, $\nu = 0.2$, and $\mu = 0.5$ (regardless of particle shape). Although the overall trend was consistent with the physical data, the DEM simulation showed 10 mm more settlement on average. The onset of yielding was also different, occuring at 10 kPa face pressure in the case of DEM compared to 15 kPa in the physical observation. Another noticeable difference was observed in the face deformation as the initial face pressure was gradually reduced to 10 kPa; the face deformed at a constant but slow rate unlike the physical case where virtually no face movement occurred until face pressure was reduced below 20 kPa.

First, the differences could be attributed to the way the face movement was measured. In the centrifuge model the face was represented by a thin (0.2 mm) latex membrane separating the inside and outside of the cavity. Figure 5.2 indicates a displacement transducer was attached to a rigid plate but it was not clear how it was fixed with the membrane or kept in place during face deformation. In other words, there is uncertainty as to how the deformation of the membrane was translated onto the transducer. In the DEM simulation, the measurement of face deformation was more direct as displacements of each particle comprising the face were counted and the average of the face particle displacements was used in the plot. It seems, therefore, that a membrane in a physical test could artificially restrict the face deformation while DEM measures the face deformation without any constraint.

Second, the differences could be due to the effect of particle shape as DEM material consisting of smooth spherical particles showed less initial modulus than material consisting of non-spherical shaped particles.

5.3.1.2 Parametric Studies

Figure 5.13 shows the effect of particle contact friction on the DEM simulation of tunneling in sand and a comparison with the physical result. The damping constant α was 0.8; particles were free to rotate and the default timestep was used. Better match with physical data, especially below 10 kPa, has been obtained for the case of $\mu = 0.6$. While no difference in simulation was found regardless of μ values while the face pressure remained at the high end, > 10 kPa, differences appeared at low internal pressure. Below 10 kPa, the tunnel face displacement curve for the case of $\mu = 0.5$ was stiffer than at $\mu = 0.6$ and also deviated from the physical data. The possible reason could be that at low confining stress, sliding between particles occurs more easily than at high pressure for similar particle contact friction, resulting in lower material strength.

Figure 5.14 shows the effect of damping on DEM simulation and a related comparison with centrifuge data. The other parameters or modeling conditions were: $\mu = 0.6$, free rotation of particles, and a default timestep. It was clear that a damping constant of 0.8 better matched the physical curve as it did in the case of triaxial simulations; particularly below 15 kPa face pressure.

Figure 5.15 shows the effect of particle size for the same model size as described above. The original analysis was based on a ratio of small-scale tunnel diameter (D = 100 mm) to an average particle diameter (d_{50}) of 11.5. The revised model uses a ratio of 16, i.e., the minimum particle diameter in the zone of interest was reduced from 7.0 mm to 5.0 mm. The smaller particle size (r_{min} = 2.5 mm instead of 3.5 mm) better matched the physical curve in the upper confinement range and reduced the gap between the DEM result and centrifuge data. This was consistent with the observation of triaxial simulation where the sample consisting of r_{min} equal to 3.5 mm showed greater modulus than that of the sample having r_{min} = 2.5 mm.

Figure 5.16 shows the effect of model size for the smaller particle size. The reduced model uses only three discretization zones (1, 4, and 5) instead of the six in the original model (see Figure 5.8) and subsequently the left boundary was moved from zone 3 to zone 1. Other boundary conditions were kept similar. There was a boundary effect on the tunnel response as can be seen from Figure 5.16 in accordance with the observation of boundary effects on other types of numerical modeling such as the finite element method. However, the deviation was not large. A difference in face movement in the order of only 1 mm was observed up to 15-kPa internal pressures; the gap widens a little bit thereafter but there was no major shift in the overall trend of face movement.

The effect of numerical timestep on the solution is shown in Figure 5.17. Although no effect on collapse pressure was observed, a significant deviation occurred in the final stage of pressure-displacement plot below 10 kPa; the path to reach collapse was different for different timesteps. The physical path (final stage) was somewhere between.

The numerical correctness of the result or sensitivity of the DEM analyses was also examined as different increments of face pressure were used while reducing the confinement. The above analyses were based on increments of face pressure higher than the physical testing, as the objective was to simply observe the interplay of various factors on the simulation results. Analysis of a particular case was then undertaken using lower increments of confinement. In the above DEM analyses (parametric studies) the increments of face pressure were: 80, 65, 50, 40, 30, 20, 15, 10, 5, 4.8, and 4.6 kPa when face collapsed. In the revised analysis the face pressure was reduced in the following increments: 10 kPa from 100 to 50 kPa; 5 kPa from 50 to 20 kPa; 2 kPa from 20 to 8 kPa; 1 kPa from 8 to 5 kPa, then 0.2 kPa until face collapse. The comparison of results is shown in Figure 5.18. No effects on the pressure-displacement curve were found until confinement was reduced to 10 kPa. Below 10 kPa the revised DEM curve (PFC_2 in Figure 5.18) first touched the physical curve and then followed the physical curve during the rest of the face pressure increments. Obviously at lower confinement just before face collapse, the pressure increment in numerical modeling should be as small as possible to capture the true plastic nature of the load-deformation curve.

5.3.2 Collapse Pressure and Failure Mechanism

5.3.3.1 Effect of geometry

As mentioned earlier, Chambon and Corte reported only the influence of geometry on the value of the limiting face pressure without showing pressure versus displacements plots. They found no significant difference in the effect of depth on the limiting pressure for a given diameter. However, tunnel diameter was found to play a significant role. DEM simulations were carried out for a C/D ratio equal to 0.5 for D = 5.0 m, and a C/D ratio equal to 1.0 for D = 10.0 m. The gravitational acceleration for the 10 m diameter tunnel was 10g. Material density was again 16.0 kN/m^3. The results will be discussed below.

5.3.3.2 Collapse pressure

In the centrifuge test of Chambon and Corte (1994), the limiting pressure at which face collapse occurred was determined from the shape of the diagram of horizontal face displacement, with special attention paid to the sudden acceleration of the movement. This was also followed in the numerical modeling. First of all, the collapse pressures as observed in parametric studies for a particular geometry are tabulated in Table 5.6. For convenience the parametric studies are named according to their figure number mentioned above. Comparison with the centrifuge result was then shown in Table 5.7. The range for collapse pressure in the case of a 5 m diameter tunnel and C/D ratio equal to 2.0 was obtained through the parametric studies described above. Theoretical collapse pressures in dry sand found by Anagnostou and Kovari (1996) and Vermeer and Ruse (2000) are also shown in Table 5.7.

A few important comments on Table 5.6 and 5.7 follow:

- DEM solutions for a collapse face pressure ranged from 3.4 kPa to 4.6 kPa; different variables were found to alter the value slightly. However, a particle contact friction coefficient equal to 0.6 (or $\phi_\mu = 31$ degrees) together with a damping constant of 0.8 gave a value close to the physical results. The slightly higher μ value compared to the calibration in Chapter 4 ($\mu = 0.5$) was probably due to the spherical particles used in tunnel simulation. This shows that in the DEM modeling of a real engineering problem involving hundreds of thousands of particles, simple shaped particles with higher particle friction coefficients could be used rather than computationally expensive non-spherical particles. As shown here the larger friction value might have compensated for the interlocking which arises due to the non-spherical shape.
- The insensitivity to different parameters of the collapse pressure probably was because strains were relatively small.
- Chambon and Corte reported a single value for collapse pressure for each 5 m and 10 m diameter tunnel whether the value actually varies based on the C/D ratio. For example, the value found for a C/D ratio equal to 2.0 for a 5 m diameter tunnel was 4 kPa. Keeping this in mind, the DEM results clearly show the collapse pressure tended to be close to the physical value as particle sizes were reduced; the model size was the same as the physical size and the increments of face pressure were close to the physical ones (see Table 5.6).
- The analytical solutions give higher values for collapse pressure compared to physical and numerical methods. Among the analytical methods, the Vermeer and Ruse method gave reasonable agreement with the numerical predictions for both 5.0 m and 10 m diameter tunnels.

5.3.3.2 Near face displacements

In the physical test, as discussed by Chambon and Corte (1994), the pattern of deformation was recorded after the test by wetting the sand and cutting the soil mass along different vertical planes. For each of these planes the displacement pattern was identified from a careful tracing onto paper of the position of the layers of colored sand. Figure 5.19 shows the failure envelope observed for different soil covers to the outside of tunnel diameter ratio C/D. As discussed by the authors, the bulb-shaped zone was limited by a vertical plane passing through the tunnel face and by a concave envelope that starts near the tunnel invert, extends a half-diameter in front of the face, and rejoins the vertical plane at a height of about one diameter above the face.

The ground surface was affected only with relative depths C/D < 1 (Figure 5.19). With deeper tunnels, the bulb closes and arching with force transfers to the crown of the tunnel.

A similar technique was adopted in numerical predictions. The incremental particle displacements under failure pressure at various vertical points along two longitudinal sections (y-direction) in front of the face were calculated. The limit of the displaced zone was determined by identifying the sudden acceleration of vertical movement relative to the neighboring particles. The simulation case in Figure 5.15 with D/d_{50} equal to 16 was used to check the DEM displacement pattern. Details of the settlement patterns at two transverse locations (x-direction) namely, at the plane of symmetry (x = 0.0) and half way (x = 1.0 m) from the plane of symmetry are shown in Appendix B. It was observed that no apparent sudden acceleration of vertical movement was found that can precisely determine the zone of failed soil mass. This was particularly true above the crown. The limit of the area of movement toward the tunnel was, however, defined by observing change in the gradient of particle displacements. Below the crown there were only movements of particles within the displaced zone; there were zero movements or heave outside the zone of failure. Figure 5.20 shows the predicted and physical displacement pattern (side view at model plane of symmetry, i.e., x = 0.0 m) for a C/D ratio equal to 2.0 and a tunnel diameter 5.0 m. Measurements of heave or opposite movements of particles were taken as zero displacement.

Figure 5.20 also shows the near face displacement pattern for C/D equal to 2.0 as was observed in the physical test. The vertical extension of the near face displacement zone from DEM modeling was shorter (0.8 times the tunnel diameter) compared to the physical test which was one diameter above the crown. There was also wider extension in a longitudinal direction (0.8 times the diameter compared to half the diameter).

The above procedure was repeated for a C/D ratio equal to 0.5 (D = 5.0 m, D/d_{50} = 11.5). Details of the settlement pattern at one transverse location (x-direction) is shown in Appendix B.

Clearly, the displacement has extended to the ground surface, as was the case in the physical test. Figure 5.21 shows the corresponding failure mechanism that could possibly be defined from the longitudinal extension of the particle displacement at various vertical locations (excluding the area where the displacement rate was constant). The longitudinal extension was the same as predicted in the case of C/D equal to 2.0; 0.8 times the diameter. The shape of the displacement pattern from DEM was somewhat irregular compared to the physically observed pattern (see Figure 5.21).

Figures 5.20 and 5.21 support the analytical assumption that failure occurs as a movement of blocks consisting of a wedge and a right-angled prism extending from the tunnel invert to the surface.

5.3.3 Sand flow into the tunnel

One of the benefits of DEM is the large strain capability, which enables one to observe the flow of material into the tunnel. In order to see a completely collapsed tunnel face under zero face pressure, one of the models described above was taken to its final stage, i.e., face pressure was reduced to zero. For this analysis the model described in Figure 5.15 but with D/d_{50} equal to 11.5 was used. Figure 5.22 shows the resulting flow of sand in a plane along the line of symmetry (see Figure 5.9). Rows of particles were marked as black dots in order to get a clear pattern of displacement in front and above the face. Displacement vectors of the collapsed tunnel along the same plane are shown in Figure 5.23. It was clear that sand flow stabilized at the angle of repose. Figure 5.23 indicates the failure zone, which was a chimney failure as observed in previous physical and numerical modeling. The darker and longer the arrow the greater the displacement. Figures 5.22 and 5.23 reveal that the chimney did not propagate to the surface even under zero face pressure.

5.3.4 Solution Time

The number of cycles to complete a run involving tunneling was obviously much higher compared to element tests discussed in the previous chapter. The minimum number of particles as in the case of the original model (Figures 5.12 and 5.13) was 66801 and the maximum number of particles as in the case of the original model with smaller particle size (Figure 5.15) was 145100. Table 5.8 shows the details of each model described above regarding the total number of cycles, timestep, and number of hours to complete a run. Computer power was similar to that of element tests. As can be seen from the table the timestep in PFC was calculated based on the number of particles and the fraction of critical timestep specified by the user along with the contact stiffness, which was constant in all cases.

5.4 Summary

1. Particle stiffness parameters needed to model small-scale centrifuge tests of shallow tunneling in uniform and clean sand were obtained from the results of triaxial calibration studies. A slightly higher interparticle friction coefficient (0.6 instead of 0.5) obtained through calibration was used to better match the physical results of tunnel face evolution, especially under 10 kPa face pressure.
2. Additional parameters related to DEM modeling were checked, for example, the ratio of particle size to model size, to evaluate the sensitivity of results.
3. The collapse face pressure from all tests ranged from 3.6 to 4.6 kPa for a C/D ratio of 2.0 and a tunnel diameter of 5.0 m. The measured face collapse pressure in the centrifuge test was 4.0 kPa for a C/D ratio of 2.0. Simulated collapse pressure converged with the measured physical value as particle size was reduced.
4. The discretization technique for distributing particle sizes used in these analyses provided acceptable results.
5. The near face displacement pattern from DEM simulations reasonably matched the physical observations, at least qualitatively. With the deeper tunnel, the displacement stops at a certain distance above the tunnel crown and does not propagate to the surface. The opposite was observed for shallower depth where displacement, starting at the face, continued to the surface.

Table 5.1 Properties of Fontainbleau sand

Properties	d_{50} (mm)	Cu	e_{min}	e_{max}	Particle Shape
Values	0.17 – 0.22	1.4 – 1.5	0.6	0.9	Well-rounded

Table 5.2 Range of parameters in Chambon & Corte (1994) study

Diameter (m)	Depth (m)	C/D
5	2.5	0.5
	5	1
	10	2
10	10	1
13	52	4

Table 5.3 Particle size distributions in DEM tunnel model

Particle Zone	Particle Size Distribution, millimeters	Number of Particles
1	$r_{min} = 3.5$, $r_{max} = 5.25$	20697
2	$r_{min} = 4.5$, $r_{max} = 6.75$	9738
3	$r_{min} = 5.5$, $r_{max} = 8.25$	4000
4	$r_{min} = 4.5$, $r_{max} = 6.75$	4869
5	$r_{min} = 5.5$, $r_{max} = 8.25$	10505
6	$r_{min} = 5.5$, $r_{max} = 8.25$	17334
Total number of particles, before excavation		67143

Table 5.4 Parallel bond properties of tunnel tube particles

Parallel bond normal strength, N/m^2	Parallel bond shear strength, N/m^2	Parallel bond normal stiffness, N/m^3	Parallel bond shear stiffness, N/m^3	Parallel bond radius multiplier*
1e20	1e20	1e10	1e10	1.0

Table 5.5 Initial conditions (5.0 m diameter tunnel simulation)

Initial Face Pressure, kPa	Gravitational Acceleration, m/sec^2	Unit Weight, kN/m^3	Velocities and Displacements of particles
110	50g	16	zero

Table 5.6 Collapse pressures by DEM analyses (Tunnel Diameter, D=5.0 m, C/D=2.0)

	DEM Variables											
Figure Number	**μ (α=0.8)**		**D (μ=0.6)**		**Particle size (μ=0.6, α=0.8)**		**Model size (D/d_{50}=16)**		**Timestep**		**Face Pressure Increment**	
	0.5	0.6	0.7	0.8	D/d_{50} =11.5	D/d_{50} =16	800×400 ×430	200×300 ×430	t_{cr}=0.8t	t_{cr}=0.5t	DEM_1	DEM_2
	Collapse, Pressure, Pf (kPa)											
5.13	4.6	3.6										
5.14			4.6	3.6								
5.15					3.6	4						
5.16							4	4.6				
5.17									3.6	3.4		
5.18											3.6	3.8

Table 5.7 Comparison between experimental, theoretical and numerical results for collapse pressure

Different studies	**Collapse Pressure, kPa**			**Reference:**
	Diameter D		**Cover/Diameter**	
	5 m	10 m	C/D	
PFC^{3D}	4.6 – 3.6		2.0	Present study
		10.0*	1.0	
	3.6*		0.5	
Experimental (Centrifuge Testing)	4.0		2.0	Chambon & Corte (1994)
		7.4	1.0	
	3.3		0.5	
Analytical	6.25	12.5	Little effect for $\phi > 30^0$	Anagnostou & Kovari (1996): Equation. 2.3
	4.6		2.0	Vermeer and Ruse (2000): Equation 2.5
		9.4	1.0	

***Ball damping coefficient=0.7; ball contact friction=0.5; D/d$_{50}$=11.5 mm and model size=400×650×430 mm**

Table 5.8 Solution time for 3D discrete element modeling of tunneling

Fraction of Critical Timestep	Figure Number	Cycles to reach initial condition	Total cycles up to collapse pressure	Timestep (second)	Solution Time (hours)
0.8 (default)	5.13 & 5.14 (μ=0.6, α=0.8)	20000	225000	5.98×10^{-6}	72
	5.15 (D/d_{50}=16)	40000	288000	4.31×10^{-6}	187
	5.16 (reduced model: D/d_{50}=16)	40000	259100	4.37×10^{-6}	84
	5.18	20000	249000	5.98×10^{-6}	79
0.5	5.17	20000	251002	3.7×10^{-6}	76

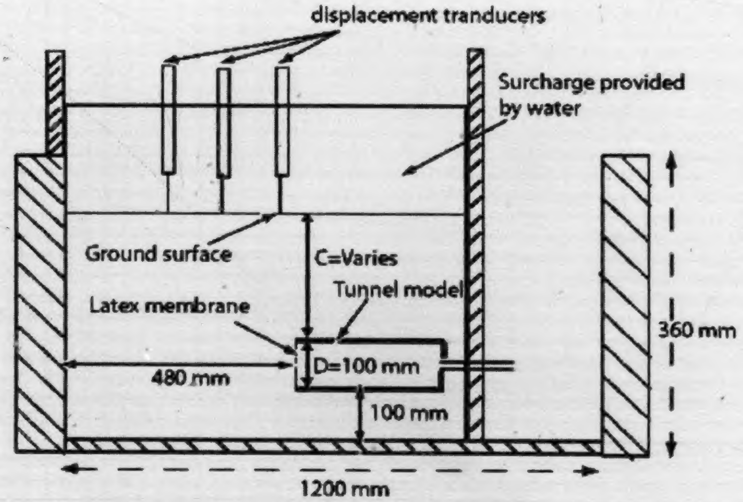
displacement tranducers
Surcharge provided by water
Ground surface
C=Varies
Tunnel model
Latex membrane
D=100 mm
480 mm
100 mm
360 mm
1200 mm

Figure 5.1 Cross sectional view of the centrifuge model and container: 1,200 × 800 mm (after Chambon & Corte, 1994)

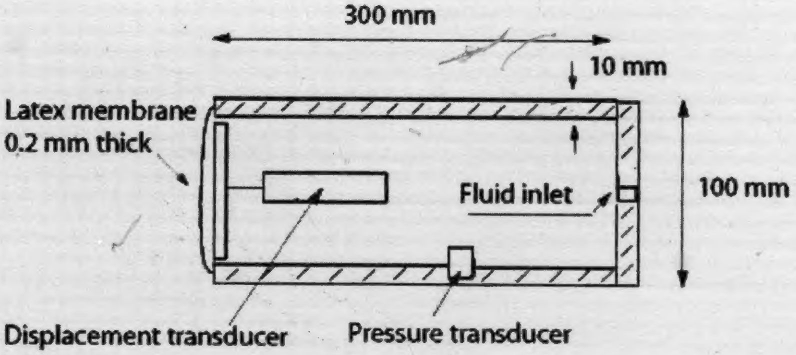
300 mm
10 mm
Latex membrane
0.2 mm thick
Fluid inlet
100 mm
Displacement transducer
Pressure transducer

Figure 5.2 Cross sectional view of the cylindrical tunnel model in centrifuge test (after Chambon & Corte, 1994)

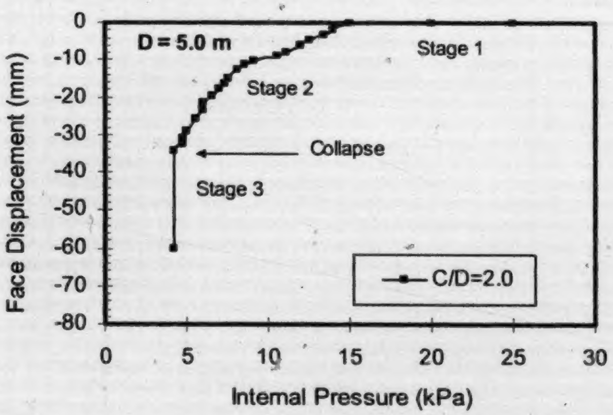

Figure 5.3 Evolution of tunnel face: horizontal displacement with decreasing confining pressure (after Chambon & Corte, 1994)

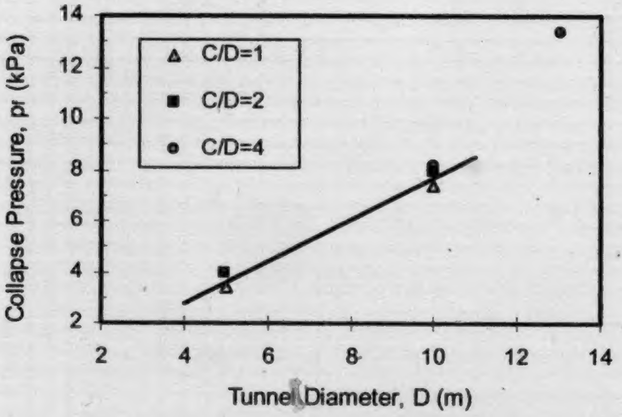

Figure 5.4 Variation of face collapse pressure with tunnel diameter (after Chambon & Corte, 1994)

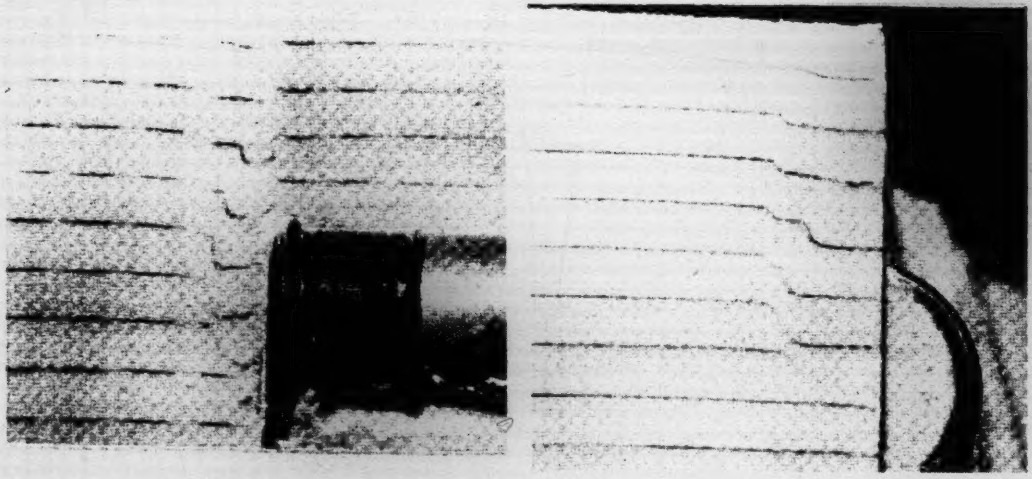

Figure 5.5 Failure bulb for fully lined tunnel (after Chambon et al, 1991)

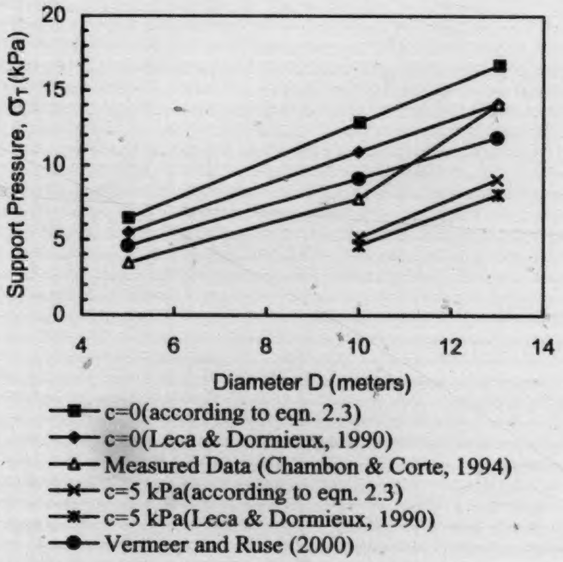

Figure 5.6 Experimentally determined and computed support pressures as a function of tunnel diameter for dry and clean sands (modified after Anagnostou & Kovari, 1996)

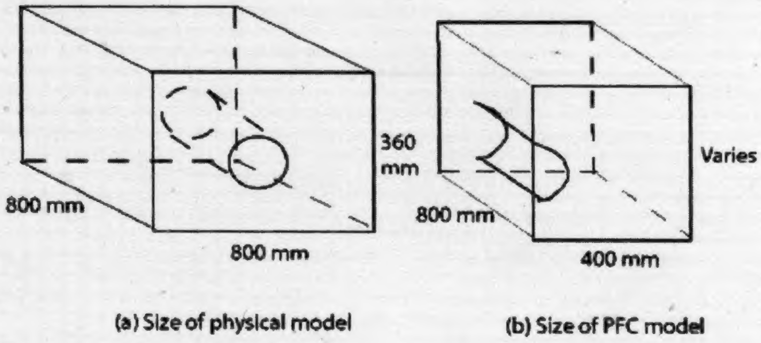
360 mm
800 mm
800 mm
Varies
800 mm
400 mm
(a) Size of physical model
(b) Size of PFC model

Figure 5.7 Comparison of the physical and DEM model dimensions

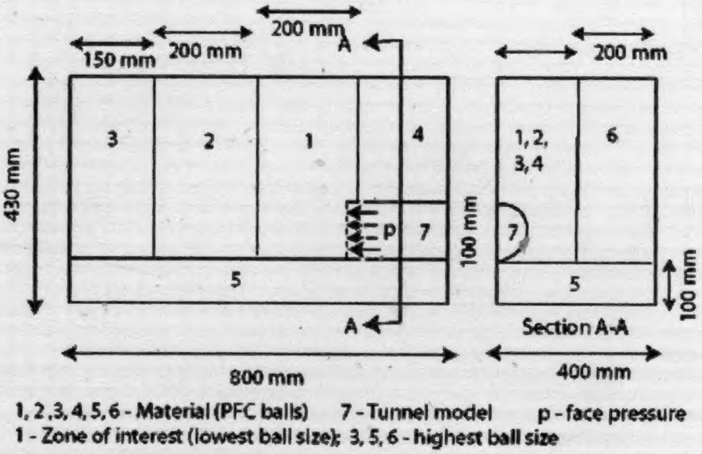
200 mm
150 mm
200 mm
200 mm
A
A
430 mm
3
2
1
4
p
7
5
100 mm
1, 2, 3, 4
6
7
5
100 mm
Section A-A
800 mm
400 mm
1, 2 ,3, 4, 5, 6 - Material (PFC balls)
7 - Tunnel model
p - face pressure
1 - Zone of interest (lowest ball size); 3, 5, 6 - highest ball size

Figure 5.8 Material discretization in DEM model to simulate small-scale centrifuge test of shallow tunnel

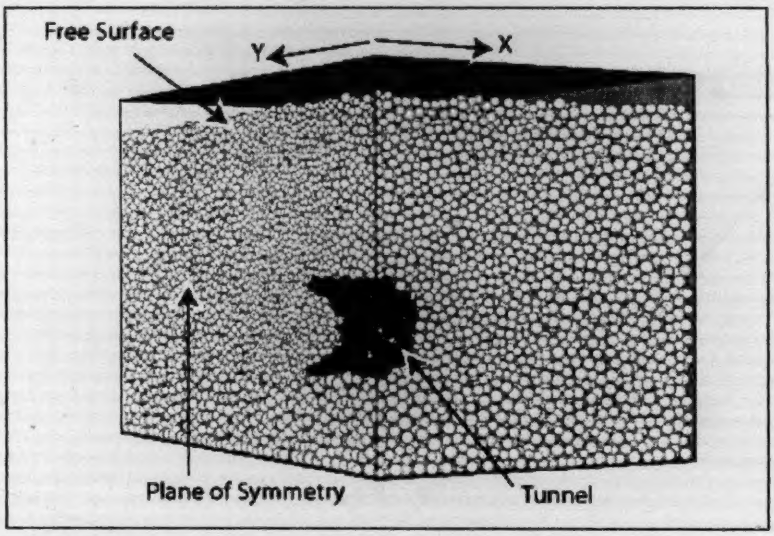
Free Surface
Y
X
Plane of Symmetry
Tunnel

Figure 5.9 Three-dimensional discrete element model of centrifuge testing of shallow tunnel

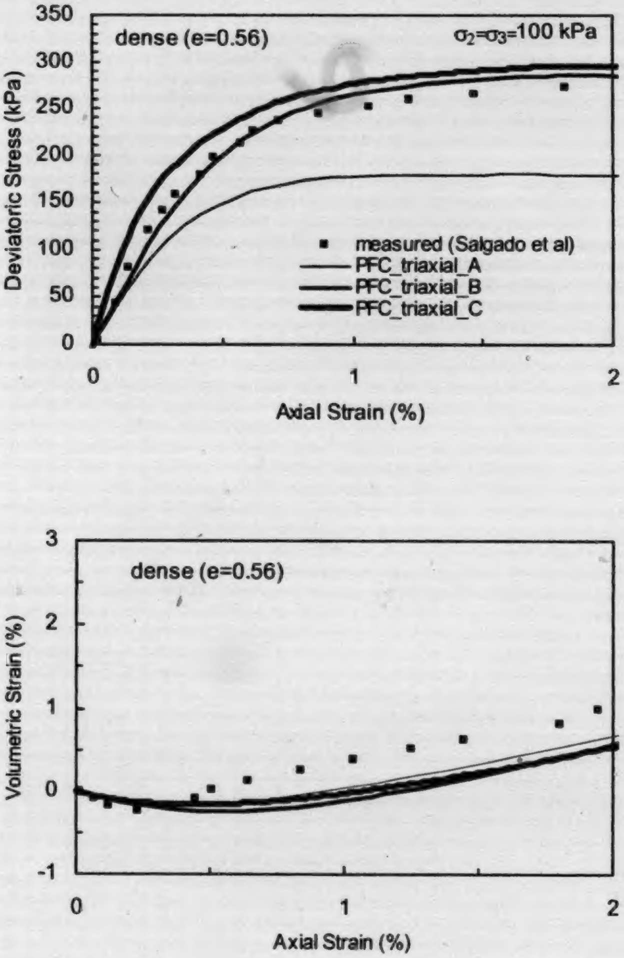

Figure 5.10 Pre-failure DEM material behavior

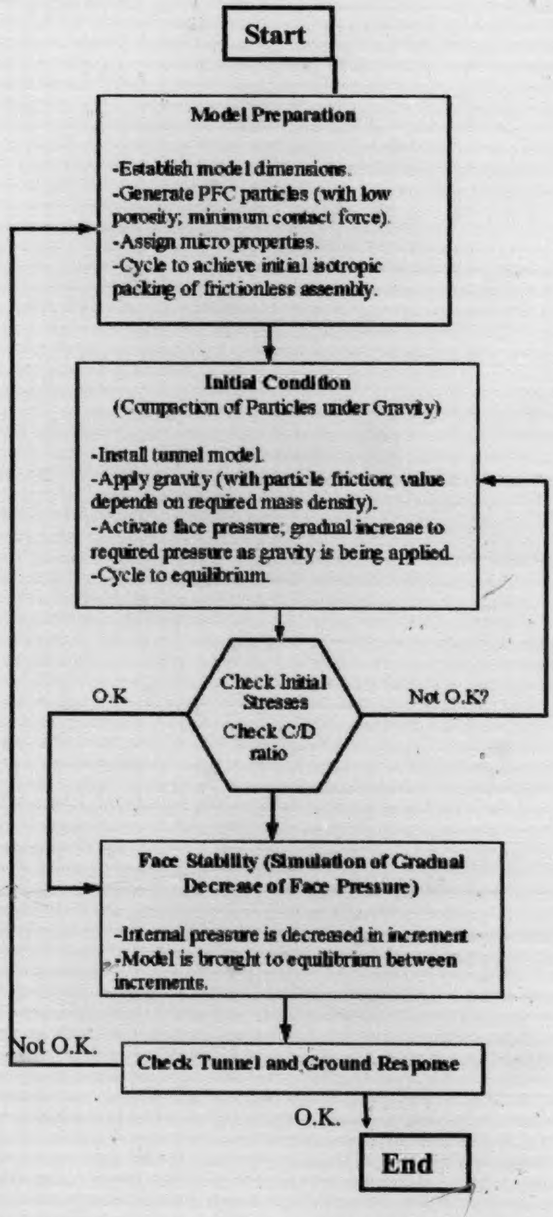
Start
Model Preparation
-Establish model dimensions.
-Generate PFC particles (with low porosity; minimum contact force).
-Assign micro properties.
-Cycle to achieve initial isotropic packing of frictionless assembly.
Initial Condition
(Compaction of Particles under Gravity)
-Install tunnel model.
-Apply gravity (with particle friction; value depends on required mass density).
-Activate face pressure; gradual increase to required pressure as gravity is being applied.
-Cycle to equilibrium.
Check Initial Stresses
Check C/D ratio
O.K
Not O.K?
Face Stability (Simulation of Gradual Decrease of Face Pressure)
-Internal pressure is decreased in increment
-Model is brought to equilibrium between increments.
Not O.K.
Check Tunnel and Ground Response
O.K.
End

Figure 5.11 Flow chart for DEM centrifuge tunnel simulation

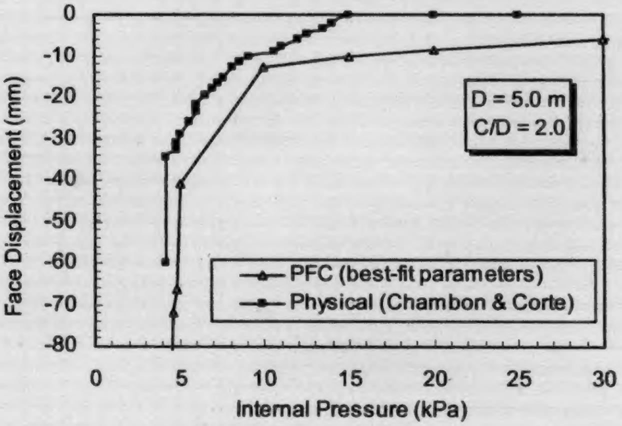

Figure 5.12 Tunnel face evolution: DEM (G=1.0 GPa, ν=0.2 and μ=0.5) versus physical data

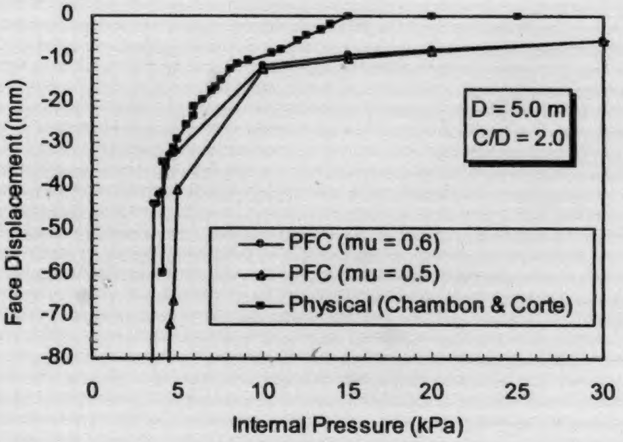

Figure 5.13 Comparison of DEM modeling of tunnel face displacement for different particle friction coefficient

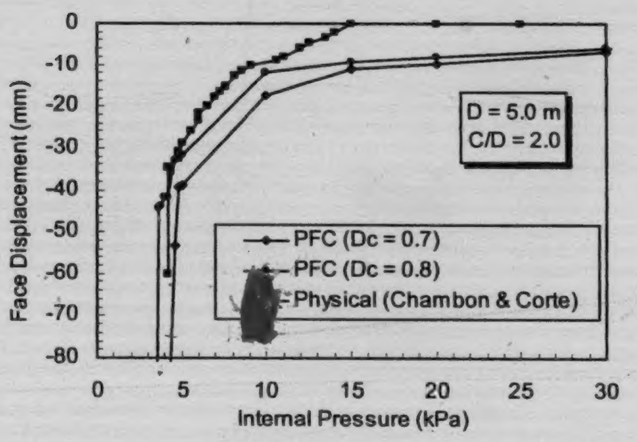

Figure 5.14 Comparison of DEM modeling of tunnel face displacement for different particle damping coefficient (μ=0.6)

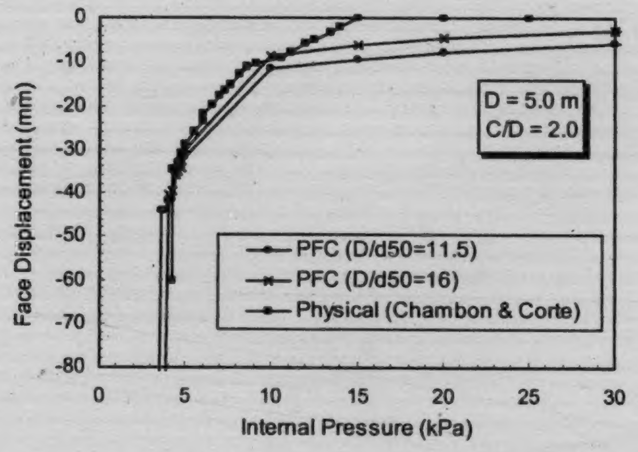

Figure 5.15 Comparison of DEM modeling of tunnel face displacement for different particle sizes (μ=0.6, α=0.8)

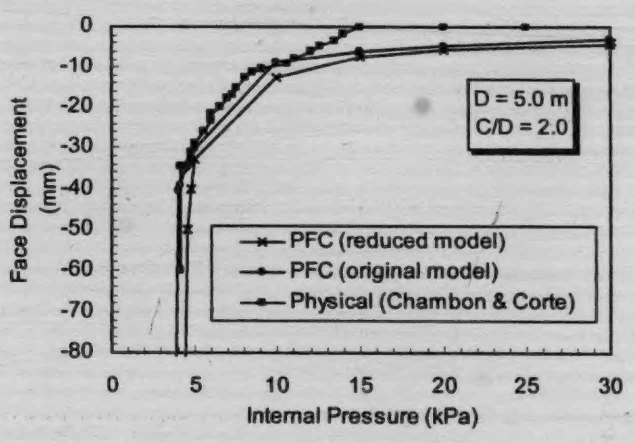

Figure 5.16 Comparison of DEM modeling of tunnel face displacement for two different model sizes ($D/d_{50} = 11.5$, $\mu=0.6$ and $\alpha=0.8$)

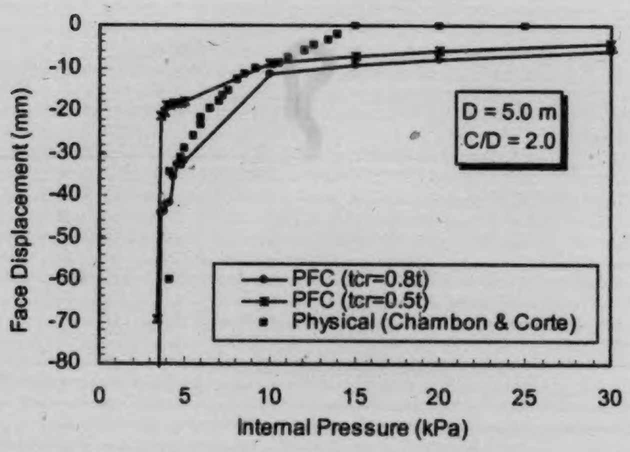

Figure 5.17 Comparison of DEM modeling of tunnel face displacement for two different timestep ($\mu=0.6$, $\alpha=0.8$, $D/d_{50}=11.5$)

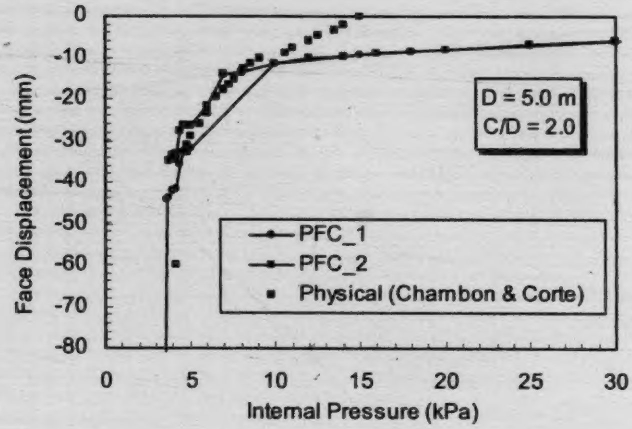

Figure 5.18 Comparison of DEM modeling of tunnel face displacement for different face pressure increment ($D/d_{50} = 11.5$, $\mu=0.6$ and $\alpha=0.8$)

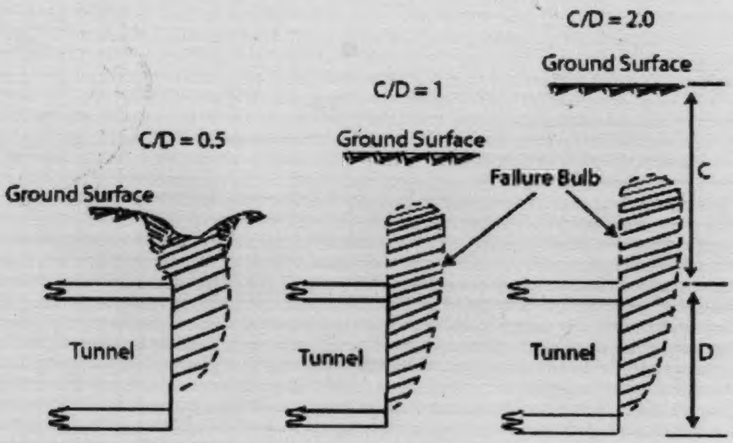
C/D = 2.0
Ground Surface
C/D = 1
Ground Surface
C/D = 0.5
Ground Surface
Failure Bulb
C
D
Tunnel
Tunnel
Tunnel

Figure 5.19 Failure bulbs for different C/D ratios observed in small-scale model (after Chambon & Corte, 1994)

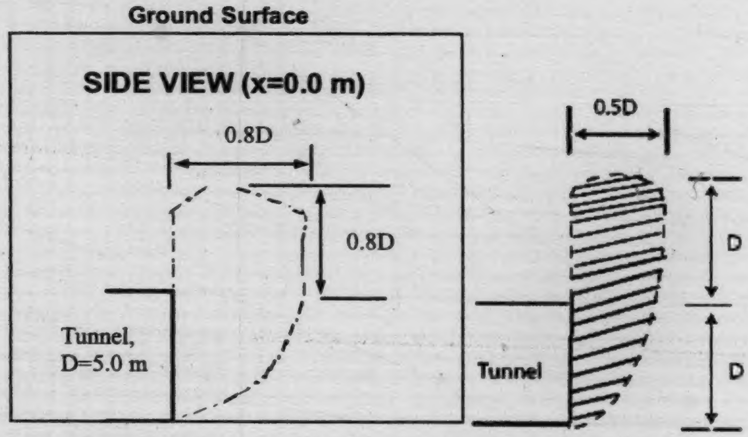
Ground Surface
SIDE VIEW (x=0.0 m)
0.8D
0.8D
Tunnel,
D=5.0 m
0.5D
D
D
Tunnel

(a) DEM result

(b) Physical result

Figure 5.20 Failure bulb from discontinuum modeling (D=5.0 m, C/D=2.0)

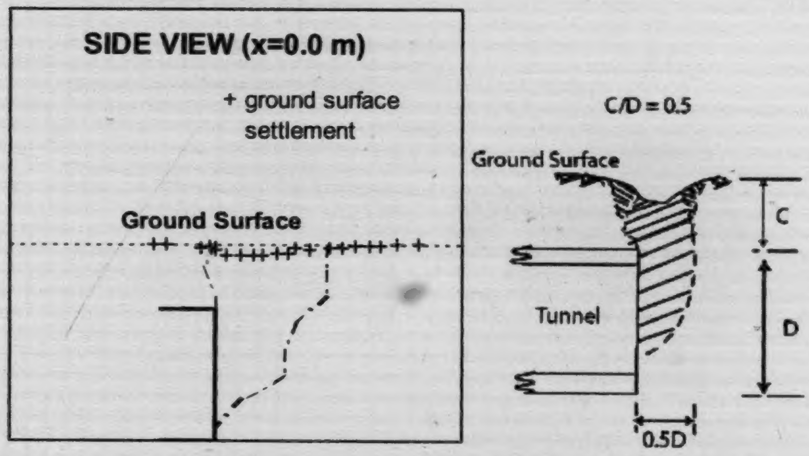
SIDE VIEW (x=0.0 m)
+ ground surface
settlement
Ground Surface
C/D = 0.5
Ground Surface
C
Tunnel
D
0.5D

Figure 5.21 Failure bulb from discontinuum modeling (D=5.0 m, C/D=0.5)

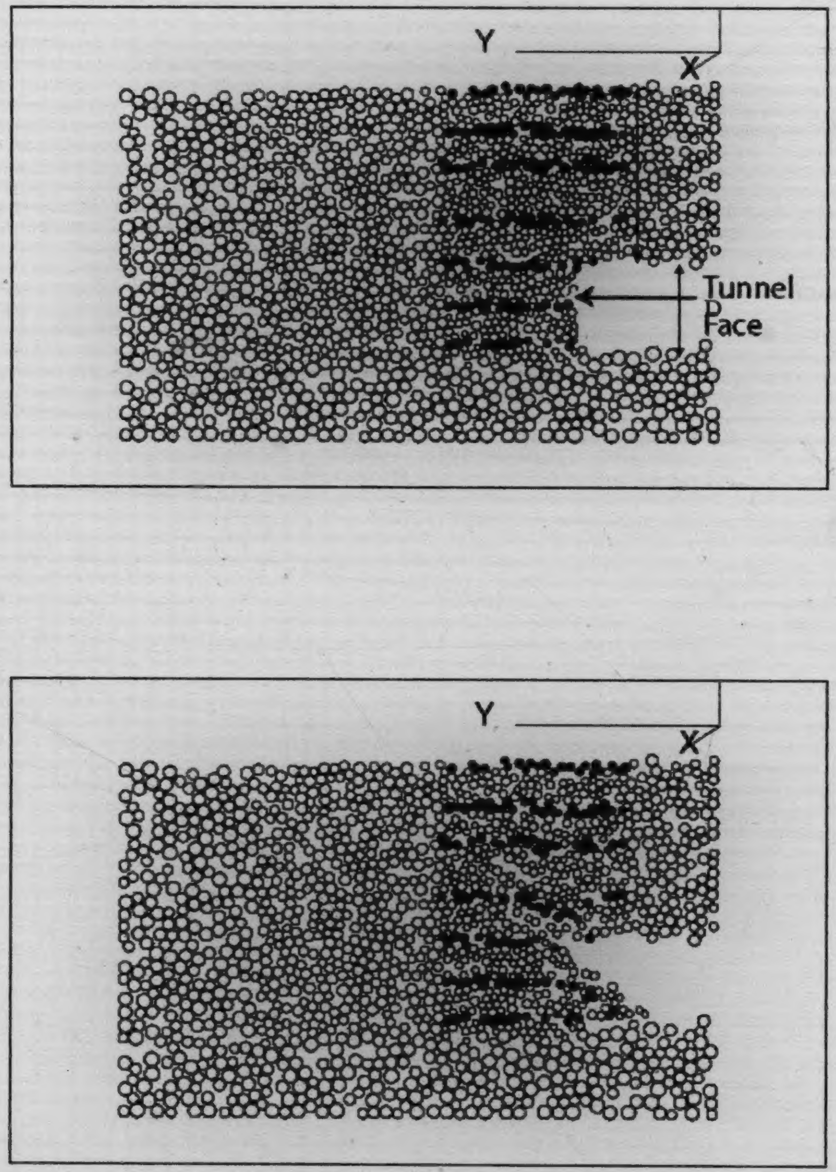

Figure 5.22 Initial face condition (a) and subsequent flow of granular material into collapsed tunnel (b) from discontinuum modeling: plane view (D=5.0 m, C/D=2.0)

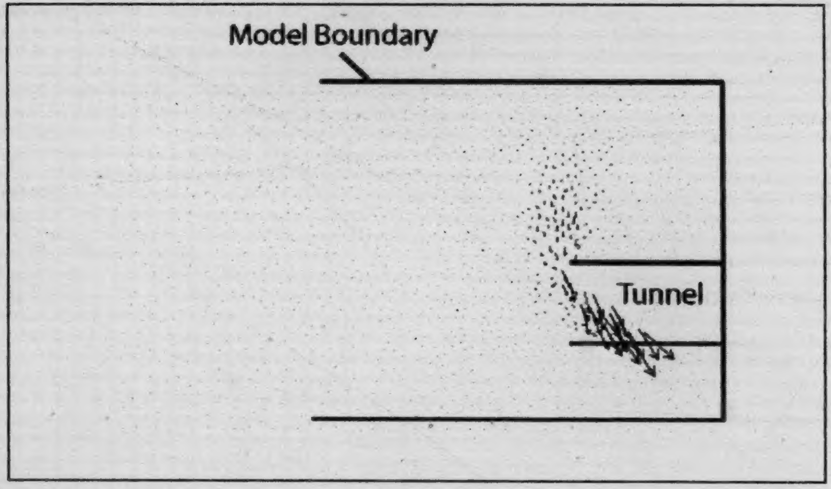
Model Boundary
Tunnel

Figure 5.23 Dwasplacement vectors under complete tunnel collapse: plane view (D=5.0 m, C/D=2.0)

CHAPTER 6

Application Of 3D-DEM To Investigate Surface Settlement above a 6.5-m-Diameter Shallow Tunnel

In Chapter 5 it was shown that the discrete element formulation in DEM could be scaled to model the centrifuge tests with a modification (slightly higher interparticle friction) of the calibrated micro-parameters. It was also shown that particle shape was not a significant issue as far as comparison of face collapse pressure was concerned, which was the main objective. This chapter describes the formulation and application of a three-dimensional discrete element modeling (DEM) to simulate a 6.5-m-diameter South Light Rail Transit (SLRT) tunnel excavated within the City of Edmonton. The primary objective of these analyses was to evaluate whether the same micro-parameters calibrated from the triaxial test (Chapter 4), with the same modification as in Chapter 5, and smooth spherical shaped particles could be used without further scaling of the parameters for the modeling of the SLRT tunnel. The other equally important objectives were to investigate: (1) whether a 6.5-m-tunnel excavation can be practically modeled using DEM, (2) whether the observed displacement pattern can be replicated using DEM, and (3) whether the influence of mixed-face tunneling conditions (sand and till) encountered along the SLRT route could be observed in the settlement pattern calculated by DEM.

6.1 SLRT project background

The recently completed southern extension of the City of Edmonton's light rail transit consists of twin tunnels approximately 6.5 m in diameter and 300 m long passing under St. Joseph's College and the Education Car Park of the University of Alberta Campus (Figure 6.1a). In addition to these buildings the tunnels also pass beneath a major utility tunnel that provides heating and water services to the University. One of the major constraints to the tunnel construction was limiting the settlements, particularly below the buildings, to less than 30 mm (Washuta and Martin 2004).

The tunnels started at a depth of 12-m below the ground surface and were driven on a 6% downward grade to connect to the existing University of Alberta Station at a depth of about 25 m. As a result of this 6% grade the tunnels were driven through a number of geological units that provided a variety of mixed-face tunneling conditions. As shown in Figure 6.1b, five geological units were encountered along the tunnel route, consisting, from the ground surface downward, of: (1) fill, (2) lacustrine silt and clay, (3) outwash sand and silt, (4) glacial till, and (5) Edmonton formation bedrock (Washuta and Martin 2004). Washuta and Martin (2004) classified the outwash sand and silt as varying from raveling/running ground to flowing ground conditions. Consequently, face and roof support was required during tunnel construction. Figure 6.1b also shows the zones of different cover to depth ratio (C/D) encountered along the tunnel route.

The construction of the tunnel started in July 2003 using an Earth Pressure Balance (EPB) tunnel boring machine (TBM) manufactured by Lovat. Figure 6.2 shows the details of the Lovat EPB TBM provided by the manufacturer. As with all EPB machines the mixing of the soil and fluid injection takes place at the cutter head and face. This machine also had injection ports for lubricating the overcut (the excavation of ground larger than the shield diameter thereby producing a gap between tunnel shield and ground) at the cutter head but these were seldom used during construction (Walter, 2004). The EPB pressure was applied through ports at the face as shown in Figure 6.2b. Figure 6.3 is a photograph of the TBM just prior to commencing the excavation of the Southbound tunnel in July. The southbound tunnel was completed in November 2003. Construction of the northbound tunnel was subsequently completed in March 2004. Figure 6.4 shows a photograph of the break through.

The entire project route was instrumented within the zone of influence of tunnel excavation. These included deep and shallow settlement points, slope indicators, building monitoring points, and tiltmeters (for monitoring inclination and vertical rotation for convergence and other movements in structures such as tunnels) which are described further in Section 6.3. Only the results from the shallow settlement points are discussed in this thesis.

6.2 Geotechnical characteristics of soil

Boone et al. (2004) described the characteristics of glacial deposits (mainly outwash and glacial till deposits) along the tunnel route. Figure 6.5 shows the variability in grain size distribution within the outwash deposits. For a typical curve the fines content (percent smaller than 0.075 mm by mass) is less than 5% by mass. Figure 6.6 shows the variation of natural gravimetric water content with elevation. The soil matric suction for sands at a water content of 5% would be around 10 kPa. This is a negative pressure or tension forces acting on the soil. The effect of ignoring this suction on the DEM analyses is discussed in section 6.6.

The low water content (average of 5% compared to an average of 20% in silt and clay) above the ground water level in sand and silt also indicates low fines content within the outwash deposit. It is therefore reasonable to assume, based on Figures 6.5 and 6.6, that the sand within the outwash deposit is relatively clean (low fines content) with uniform gradation (the average uniformity coefficient of the outwash deposit is 8.6). As discussed by Brachman et al. (2004), based on visual observations, the outwash sand deposit varies from clean and dry sand sediments with thin (< 10 mm) silt layers to saturated silty sand and silt outwash closer to the interface with the till. Figure 6.7 shows a photograph of the sand showing the clean nature of the outwash sand exposed in the open-cut excavation for the TBM portal. Table 6.1 gives the geotechnical engineering parameters for the major stratigraphic units used in the design of the project (Washuta and Martin, 2004).

6.3 Field Monitoring

Details of the instrumentation monitoring program and the observed settlements were presented and discussed by Bosse (2005). Only a few of the settlement plots from the southbound tunnel are reproduced here and these will be used to evaluate the DEM modelling results. Figure 6.8 shows the measured shallow settlements (recorded at a depth of 1.5 m) in the region from the portal to the Education Car Park (C/D between 1 and 0.5) for the construction of the southbound tunnel. The measurement accuracy was within ±1 mm (personal communication, Robin Tweedie, P.Eng.). Each data set on the plot represents the settlement profile of an individual settlement point located along the centre line of the route ('ss' refers to surface settlement). The chainage of each settlement point is noted in the legend. The geology as well as the C/D relative to the chainage can be obtained from Figure 6.1b. Figure 6.8 indicates that the settlements between the tunnel portal (chainage +674) and the Education Car Park (chainage +580) were between –11 mm and –18.6 mm. As discussed by Bosse (2005), considerable settlement (up to 10 mm) is observed over the length of the shield of the TBM (the steel cylindrical plate, the body of the TBM, which permits the excavation of soil and the erection of primary lining) with additional settlement occurring at the transition from the tail shield (the tail of the shield extending behind the body) to the segmental lining (circular ring in segments to support permanent ground pressure). These tunneling terms have been explained in section 2.2.3 of Chapter 2. This is in contrast to practical experience from other projects (see Figure 2.6) where the source of majority of the construction settlement is only induced at the tail void.

Figure 6.9 shows the observed shallow settlement response during tunnel construction under the Education Car Park (C/D equal to 1.5–2; chainage between +515 and +585). This figure shows dramatically reduced settlements of approximately –4mm compared to the region prior to reaching the Education Car Park. This is may be due to the tunnel traversing mixed face conditions of sand and till (see the geological sections in Figure 6.1b). Figure 6.10 shows the maximum settlement along the centerline of the tunnel route in conjunction with the tunnel face geology, expressed as a percentage of sand and silt. Figure 6.10 shows that at the tunnel portal the tunnel face is 100% sand and silt, but by the beginning of the Education Car Park the tunnel face has changed to 50% sand and silt in the crown and 50% till in the invert. At the end of the Education Car Park the tunnel face is 100% till. From Figure 6.10 it appears that the surface settlements correlate with the percentage of sands and silts in the tunnel face, at least partially. There could also be an effect of tunnel depth and effectiveness of tail-shield grouting. This important point will further be discussed in section 6.6.

In the following sections three-dimensional DEM is used to model the SLRT tunnel to determine the settlement profile for the portion of the route with portions of sand and silt in the tunnel face, and to evaluate if the reduced settlements under the Education Car Park could be attributed to the mixed-face tunneling conditions.

6.4 MODELING PROCEDURE

6.4.1 Model description

Only half of the tunnel was modeled as shown in Figure 6.11 (C/D equal to 1) because of symmetry along the centre line. The dark tunnel surface represents the rigid TBM shield and lining which was formed by bonding the DEM particles together with strong bond properties equal to those in Table 5.3, Chapter 5. The model size was made as small as practical balancing scale and boundary effects. Figure 6.12 presents the geometry of the domain that has been modeled for a C/D equal to 1. The length in front of the tunnel face was 3 tunnel diameters, the width from the tunnel springline was 1.8 times the tunnel diameter, and the height of the model was 3 tunnel diameters. The tunnel was excavated through the centre of the model height resulting in a cover depth to diameter ratio of 1.0. A total of three different C/D ratios were modeled, 0.5, 1.0 and 2.0. Typical model dimensions and material discretization for a C/D equal to 1.0 are shown in Figure 6.12. In order to create a model with a C/D equal to 0.5, the model in Figure 6.12 was used with the top half of the particles above the tunnel crown being deleted after application of gravitational forces and cycling to equilibrium.

Table 6.2 provides the size distribution and number of particles in each zone shown in Figure 6.12. Particles are drawn at random from a uniform statistical distribution of radii with specified upper (r_{max}) and lower (r_{min}) limits. The material discretization pattern is similar to the one described in Chapter 5 (centrifuge modeling) but has more discretization zones (a total of 13) in order to reduce the model size. The tunnel model shown in Figure 6.13 was a simplified version of the EPB shield tunnel used in the SLRT project, which did not include the exact details of how the face pressure was applied and maintained during EPB shield operation or EPB tunnel motion.

The simulation utilized a ball size distribution of $r_{min} = 120$ mm and ratio $r_{max}/r_{min} = 1.5$ in the zone of interest (zone 1 in Figure 6.12) to $r_{min} = 200$ mm at the boundaries (zone 7, 9, and 11), which resulted in 124734 particles. The ratio of tunnel diameter to average particle diameter was 16 in the zone of interest. This ratio was not considered a significant issue because the purpose of the DEM simulation was to assess settlement at the ground surface and not face collapse pressure as simulated in the centrifuge tests. The parametric study on particle size in Chapter 5 where it was observed that particle size has effects only near the face collapse pressure also supports this notion.

The face pressure applied by the EPB-TBM was assumed to be uniform in the vertical and horizontal directions. In reality, the pressure likely varies across the face as the pressure is applied using a soil paste, and hence the pressure at the bottom of the TBM face will be greater than at the top of the TBM face. This face pressure was controlled by the TBM operator and monitored using 6 pressure sensors distributed over the EPB-TBM face. An average face pressure of 200 kPa was typically used for tunneling in the outwash sands and silt and this pressure was used in the DEM modeling and applied in the same fashion as in centrifuge modeling.

The most challenging part of the DEM modeling was simulation of the gap due to the overcut and the gap between the bore-diameter and the outer dimension of the tunnel lining. The gap was modeled by kinematically displacing the shield and liner elements (here particles) inward by the specified gap amounts (discussed below). This was performed by application of a radial velocity to the particles comprising the shield and liner, i.e., in a vertical plane each ball was assigned two perpendicular but equal velocity components (x- and z-direction) while the third component (longitudinal or y-direction) was kept at zero. This is shown schematically in Figure 6.14. Particle friction for particles comprising the shield and liner were kept at zero during the process. The magnitudes of velocities were specified based on the required gap above the shield and liner. The model was then cycled to reach the desired gap dimension. Finally, equilibrium of the model was checked by more cycles while maintaining the velocities at zero. It was observed that movement along the shield and liner ring was uniform. A similar modeling process was used by Augarde et al. (2001) to simulate a tunnel liner using a 3D finite element technique (see section 2.2.4, Chapter 2).

6.4.2 Boundary conditions

The model boundary walls were rigid in this DEM modelling. The wall that was used for the line of symmetry, the wall above the tunnel excavation and the wall where the excavation begins were frictionless. All other boundaries were assigned the same friction coefficient as the DEM particles. The free surface above the tunnel was formed under 1 g gravitational acceleration.

6.4.3 Initial conditions and tunnel construction

The first step of the modeling procedure was to generate the initial conditions before tunneling. After generation of an initial assembly of particles and formation of the TBM shield and liner, a gravitational acceleration of 1 g was applied to all the particles and the assembly was brought to equilibrium. The free ground surface was automatically created at the end of the equilibrium stage. A unit weight of 15.2 kN/m^3 was obtained by specifying the initial porosity ($n_0 = 0.4$) during the generation of particles and by applying a particle surface friction coefficient of 0.1 during application of gravitational acceleration. A nominal value of 0.1 for particle surface friction was needed to obtain the required density. The unit weight of the outwash sand and silt varied between 16.3 and 22.8 kN/m^3 with an average of 19 kN/m^3.

Table 6.5 shows the specified porosity during ball generation stage and obtained porosity in zone 1 after the initial stage. Also shown are the initial stress distributions from the tunnel centerline upward close to the surface. Locations of the measurement spheres within the zone of interest, zone 1, are shown in Figure 6.15. For each location a collection of two measurement spheres of decreasing radius is generated and the average of these two spheres are reported in Table 6.4 (see Figure 6.15). This would ensure the accuracy of the stress measurement as recommended by the PFC manual. As seen in Table 6.4 the Ko values ranged from 0.77 to 0.92 with 0.84 in front of the face. These values are higher than the observed Ko value for outwash sand based on Poisson's ratio of 0.3 as shown in Table 6. However, the lower observed value could be due to the fact that the small-scale laboratory samples missed the highly layered sedimentation in the outwash deposit (see Figure 6.7) with locked in horizontal stresses. There is limited information available on the determination of Ko values in outwash sand based on in situ tests. The actual Ko value could be between 0.6 and 0.8 (personal communication with Dr. Derek Martin and Mr. Robin Tweedie).

The excavation due to the shield advancement and subsequent lining construction was simulated in the second stage. Unlike centrifuge modeling, the face pressure in the pressure chamber was applied instantly as was the case in the field. Also the objective of the modeling and the modeling procedure were quite different here than in Chapter 5 which was to model surface displacement pattern as opposed to tunnel face displacement. However, the model was run by applying face pressure in increments to check the accuracy of the model results (surface displacement). Face pressure was applied in 10 increments with 100 cycles between the increments. The calculated settlement was higher by a maximum of only 2 mm in front of the face for the case of 10 increments of face pressure and gradually matched with the one increment case. There was no effect on the maximum settlement. This is shown in Figure C1 in Appendix C. In order to be consistent with the field conditions, in the following simulations face pressure was applied in one increment.

The model was not run at this stage, i.e., no cycling was performed until it was taken to the next and final stage—the creation of gaps between the tunnel shield and the ground and between the tunnel lining and the ground. This simulated the field situation where the gaps around the shield and liner were produced under a constant face pressure. In other words, the tunnel face was maintained stable as the shield was advanced generating the gaps. Finally the model was cycled to equilibrium after the desired gaps around the shield and liner were achieved and with the face pressure in place. Figure 6.16 summarizes the various modeling steps in a flow chart.

6.5 PARAMETRIC STUDIES

This thesis was intended to model granular materials only. As can be seen from Figure 6.1b as part of the DEM modeling in this chapter cohesive material needed to be considered. Simplification and idealization were needed to model the overlying clay and fill layer and hard clay till/bedrock materials. The fill/clay layer was modeled as an elastic cap on top of the sand by bonding the particles in the zone of the elastic cap using the DEM parallel bond concept. The hard clay till/bedrock was modeled as a rigid material by specifying higher stiffness and strength numbers to the parallel bond properties used for the elastic cap.

In this Chapter no attempt was made to model the excavation sequence. The focus was on the magnitude and shape of the longitudinal profile of ground displacements induced by radial gaps around the shield and liner. The gap between the ground surface and the TBM shield due to overcutting was assumed to be uniform (Figure 6.13). The theoretical gap between the bore diameter and the outer diameter of the lining is 119.5 mm (see section A-A, Figure 6.13). However, a couple of factors might have resulted in a different gap scenario in the field such as the efficiency of grouting and workmanship during erection of the concrete lining. Therefore, it is difficult to know the exact gap width. A parametric study was performed by varying the distribution of the gap around the liner and evaluating the effect on the surface settlement. In the case of non-uniform distribution of the gap, the gap between the liner and the surrounding ground was gradually increased from the crown and invert up to a value at the tunnel spring which was equal to the value of a uniform gap. The analysis showed that the settlement profile from the non-uniform gap distribution compared to the settlement profile from the uniform gap analysis resulted in an average settlement difference of approximately 1 mm (see Figure C2 in Appendix C). Both the shield and lining were modeled using a similar procedure for modeling a rigid liner as discussed in Chapter 5.

6.5.1 Elastic cap to model fill/clay layer

As mentioned above, for the sake of simplicity and idealization the "Lake Edmonton Clay" was modeled as an "elastic cap" by bonding (parallel-bond) the spherical particles in the zone of interest (the upper particles close to the surface). Assuming the clay behaves as an elastic medium is not unrealistic as the TBM advanced between 10 and 15 metres per day, hence the settlement profiles would have been established when the clay behaviour was undrained. The parallel-bond model describes the constitutive behaviour of a finite-sized piece of cementatious material deposited between two particles and the effective stiffness of this additional material acts in parallel with the contact point stiffness (PFC3D, Theory and Background, 1999). The parallel bond in PFC is defined by four parameters: normal (n) and shear (s) strength and stiffness (Kn_1, Ks_1, Kn_2, and Ks_2 where: 1 and 2 refer to strength and stiffness, respectively). It was taken that $Kn_1 = Ks_1$ and $Kn_2 = Ks_2$. The dimensions of parallel bond stiffness and strength are stress/displacement and stress, respectively. Figure 6.17 shows the effect of parallel bond properties on the surface settlement pattern for the case of C/D equal to 1.0. The geology around the tunnel is also shown in Figure 6.17, which consists of a 3.25 m clay cover overlying sand (case Geo_2 in Table 6.3). Note that in order to reduce the computational time, the material above and below the tunnel invert was modeled as sand, although the field material was till and/or bedrock below the tunnel invert. Three different cases were considered: (A) $Kn_1 = Ks_1 = 1 \times 10^5$ kPa and $Kn_2 = Ks_2 = 1 \times 10^5$ kPa/m, (B) $Kn_1 = Ks_1 = 1 \times 10^5$ kPa and $Kn_2 = Ks_2 = 1 \times 10^{10}$ kPa/m, and (C) $Kn_1 = Ks_1 = 1 \times 10^{10}$ kPa and $Kn_2 = Ks_2 = 1 \times 10^{10}$ kPa/m. The field curve related to C/D equal to 1 (ss103) was considered for comparison.

In addition, two more cases, one with only spherical particles throughout the model without any elastic cap at the surface and another with an elastic cap using $Kn_1 = Ks_1 = 1 \times 10^{10}$ kPa and $Kn_2 = Ks_2 = 1 \times 10^5$ kPa/m were also considered but no noticeable difference in surface displacements were noted compared to case A. The results revealed the following (for a 19.5 mm gap around the shield and a 78-mm gap around the liner):

- Surface displacement is reduced by an average of 8 mm (uniform upward translation) when Kn_2 and Ks_2 is increased to 1×10^{10} kPa/m (case B) and case B agreed well with ss107 up to the tail shield; and
- Displacement is reduced further, especially beyond the tail shield portion, when Kn_l and Ks_l in increased to 1×10^{10} kPa (case C). But the pattern of the displacement curve did not match with the field curve compared to cases A and B and the settlement curve reflected a stiffer and stronger cap material than Edmonton clay.

From the above discussion it is reasonable to believe that the elastic cap with $Kn_l = Ks_l = 1 \times 10^5$ kPa and $Kn_2 = Ks_2 = 1 \times 10^{10}$ kPa/m (case B) produced results comparable to the field data with sand at the tunnel face and a clay cap. This statement will be further tested in sections 6.5.2 and 6.5.3.

6.5.2 Magnitude of gaps around shield and liner

Figure 6.17 revealed that the calculated surface settlement beyond the tail shield is relatively high compared to the field curves. This could be an effect of the specified large gap of about 80 mm between liner and ground. In the actual tunneling process, the gap between liner and ground was filled with grout. Bosse (2005) showed that this grout did not set until after approximately 8 hrs by which time the tunnel had advanced about 10 m. Investigative drilling of this gap at the end of construction indicated that grout thickness varied significantly around the tunnel (Bosse, 2005). An attempt was made to quantify the effects of shield and liner gaps on the calculated surface settlement. Three combinations were considered taking case B of Figure 6.17 as the basis; that is, other parameters are same as Case B; this is shown in Table 6.3. While B3 is close to the theoretical gaps, the other numbers were arbitrarily chosen to see the effect of gap magnitude. The results are shown in Figure 6.18.

Figure 6.18 shows clearly that the larger the gap, the higher the settlement. While the liner gap is the same in B1 and B2, the difference in settlement is proportional to that of the shield gap (5 mm). Also, cases B1 and B2 provided surface settlement within the range of field data while case B3 showed much larger settlement compared to the field settlement magnitude.

The DEM modeling showed that there is a correlation between the gaps around shield and liner and the surface settlement and it is capable of capturing the effects of these gaps on the settlement.

6.5.3 Modeling gaps

As was mentioned earlier the gap around the shield and liner were modeled by applying velocities to the particles comprising the shield and liner and by cycling the model to reach the specified gaps. Therefore, two factors contributed to the final gap value: (1) particle velocity and (2) number of cycles. In Figure 6.18, different gaps were produced by changing the velocities while keeping the cycle constant at 10000. In this parametric study, the gap was kept constant at B1 (Figure 6.18) while the cycle was changed from 10000 (B1) to 15000 (B1_1) and then to 20000 (B1_2) and 5000 (B1_3) corresponding to velocities of 0.02 m/s, 0.068 m/s; 0.015 m/s, 0.05 m/s, and 0.04 m/s; 0.135 m/s to particles comprising the shield and liner, respectively. The objective was to find the combination of velocity and cycle at which minimum changes in surface settlement is noticed. Once again a C/D ratio equal to 1 was considered. The result is shown in Figure 6.19.

Figure 6.19 shows that the greater the number of cycles, the smaller the particle velocity comprising the shield and liner, the larger the settlement. However, the difference becomes smaller as the number of cycles is increased and velocity is decreased. This is quite similar to the effect of platen velocity found in the DEM triaxial test set up (Chapter 4), that is, the higher the platen velocity, the greater the material strength. To achieve specific gaps of 17 mm and 55 mm around the shield and liner, respectively, in the DEM model, a combination of 0.015 m/s (velocity to the particles comprising the shield) and 0.05 m/s (velocity to the particles comprising the liner) were specified.

6.6 CALIBRATION AGAINST FIELD DATA

In order to accommodate the varying geology and C/D ratio along the tunnel route, three cases were considered (Table 6.3). In each case a common clay layer was modeled at the surface overlying sand. Modeling the till underlying the sand was not considered in cases Geo_1 and Geo_2, which has only sand at the tunnel face (uniform face). This was done to simplify the analyses and reduce the modeling time. It was assumed that the stiff till below the tunnel invert had a minimal effect on the relationships among the face pressure, gap around the shield, and liner and surface settlements. The glacial till in the Edmonton area is heavily over consolidated and local tunneling experience has shown that this soil has significant standup time (Bobey et al. 2004). Hence, ignoring the effect of the till for the cases Geo_1 and Geo_2 appears reasonable. Modeling of the till was only considered in case Geo_3 which is a mixed face condition of till and sand. These three cases along with the modeling results and comparison with the field data are discussed below.

In the following simulations the micro-parameters used are: G (particle shear modulus) = 1.0 GPa, ν (particle poisson ratio) = 0.2 and μ (inter-particle friction) = 0.6. The reason for using μ = 0.6 rather than 0.5 was to attempt to compensate for higher strength arising from non-spherical shape, as discussed in Chapter 5. In line with the findings in Chapter 5, the damping coefficient, α, was equal to 0.8.

6.6.1 Uniform face: sand

The uniform tunnel face condition of sand represents the first two cases in Table 6.3. In the following section the settlement prediced by the DEM model is compared to the field data for the cases of C/D equal to 1 and 0.5.

6.6.1.1 C/D=1

The surface displacement along the centerline of the DEM model for a C/D ratio equal to 1 has been calibrated against field data to some degree and has been demonstrated in

Figures 6.17 to 6.19. It appears that case B1_4 in Figure 6.19 represents the best possible DEM curve within the model limitations such as saturation and corresponding suction of the geological material in the field; size and shape of the particles; model dimensions (only half of the tunnel was modeled rather than the full cylindrical tunnel), and tunnel motion. A further discussion and comparisons are provided below.

Figure 6.19 is reproduced in this section showing only the plots of interest that is the best calculated curve found through Figures 6.16 to 6.18 and a range of field measurements (Figure 6.20). Comparing the calculated settlement curve from DEM to the field data (Figure 6.8) the following observations are made regarding the capability of DEM to model a 6.5-m-diameter shallow tunnel response in uniform sand:

- Despite the restrictions in model size and the simplified geometry, the surface settlement predicted by the DEM model was in reasonable agreement with field observations.
- For a specific gap around the shield and liner, the DEM model calculated ground displacement as somewhat an average of two field curves whereas in the field ground displacement around the liner could vary (depending on grout effectiveness), indicating that the surface displacement from the DEM model is quite comparable to that of the field situation.
- Figure 6.20 indicates that the applied face pressure of 200 kPa was adequate for controlling the surface settlements ahead of the tunnel face.
- Approximately 3 mm of surface settlement was calculated immediately above the tunnel face. This is within the range of observed surface settlements above the tunnel face.

The calculated surface settlement curve from the DEM model shows three distinctive zones of settlement: (1) a zone ahead of the tunnel face where the settlement remains close to zero up to 3 m (~ 1/2 the tunnel diameter) ahead of the tunnel face where the settlement curve starts to increase, (2) a zone above the TBM shield which is a linear extension of the settlement rate from a point 3 m ahead of the tunnel face, and (3) at and beyond the tail shield where the settlements accelerate. These zones can be observed in the field settlement profile (e.g., see ss103 in Figure 6.8) which is located at the start of the tunneling near the portal. This settlement profile is in contrast to that provided in Figure 6.8 for ss106 for a TBM-EPB machine and likely reflects the interaction of the ground conditions with the geometry of the gaps around the TBM and the contactor's construction practice with respect to grouting from the tail shield.

6.6.2 Other C/D ratios and mixed face

Figure 6.21 shows the calculated settlement for a C/D ratio of 0.5 and comparison with the field data. The model simulated in the first case is described in Table 6.3. This represents the section close to the Education Car Park underneath the utility tunnel as shown in Figure 6.1b. The field settlement curves shown in Figure 6.20 were used to represent the observed settlements from portal to Education Car Park. All other model parameters are similar to that of Figure 6.20. The results in Figure 6.21 show some distinct characteristics compared to C/D = 1. First, heave ranging between 1.9 and 3 mm was observed in front of the face followed by a sharp increase in the settlement profile just in front of the face. The settlement becomes constant with a negligible rate just before the transition from shield to liner; it goes to negative rate within a distance of 1 m then drops sharply once again. The magnitude of settlement, however, was similar to that in Figure 6.20 for a C/D ratio of 1.

Figure 6.21 clearly shows a surface heave using a face pressure of 200 kPa. This is no surprise as the same face pressure of 200 kPa for C/D = 1 was applied for C/D = 0.5. In the actual construction, underneath the Education Car Park heave was observed and the face pressure was lowered to 160 kPa (personal comment, D. Martin). A DEM model with a face pressure equal to 160 kPa resulted in the heave ranging from 1 to 1.6 mm (see Figure C3 in Appendix C).

So far tunneling with uniform face conditions were simulated. As shown in Figure 6.9, the surface settlement measured along the tunnel centerline changed significantly as the portion of the tunnel face changed from 100% sand to almost 100% till. One of the major difficulties in mixed face tunneling conditions is maintaining a face pressure that can prevent excessive surface settlements. To model this change in face composition using the DEM model, several simplifications were made.

Local tunneling experience in the City of Edmonton, supports the notion that the till (a heterogeneous cohesive material containing a trace–to-some-amount of silt, sand, gravel, and coal) when first exposed will stand unsupported for considerable time. The consistency of till is somewhere between stiff to hard with both the strength and modulus higher than that of Edmonton clay (Bobey et al., 2004; Washuta and Martin, 2004). To represent the till in the DEM model, the spherical particles were glued (similar to the method used to represent the clay as an "elastic cap") to achieve both high strength and stiffness. In order to do that, the strength and stiffness of the bonds between particles were assigned values of 1×10^{20} kPa and 1×10^{20} kPa/m, respectively. A model with the face percentage of 90% till to 10% sand was analyzed with a C/D approximately equal to 2 to assess the impact of the mixed-face conditions on the surface settlements (see Figure 6.2). The particle size distribution and micro-parameters were unchanged from those used for uniform face simulations.

To meet the modeling objectives of calculating surface settlement due to changing tunnel face condition from uniform to mixed face, the spherical particles representing the till were integrated with the spherical particles representing the shield and lining at the level of till. This implied that all the deformations were concentrated in the outwash sands overlying the till and surrounding the tunnel; this is consistent with the SLRT monitoring experience (schematically shown in Figure 6.22). Therefore, the closure due to the construction gap was modeled only in the portion of shield and lining in contact with granular material. This is a reasonable assumption as it was expected that the gap between the higher strength till and shield and liner would not translate into immediate deformation and gap closure (till has considerably higher stand up time than sand). The magnitude of the gap was kept the same as for the uniform face case. The model was initiated from the same initial condition as the uniform face and the 200 kPa face pressure was also maintained.

Figure 6.22 shows the surface settlement curve from the DEM model for a C/D ratio of 2 compared with the field settlement curve. Figure 6.22 clearly shows that the mixed face with 90% till had a significant impact on reducing ground settlements and in particular changing the shape of the settlement profile. As in the previous cases the DEM model over predicts the total settlements. As discussed previously, this is likely due to the uncertainty in the gap between lining and ground; in the DEM model the maximum possible value of 55 mm was used.

Another aspect of the mixed face scenario at the SLRT project is that the presence of sand and silt at the tunnel face gradually reduced as the tunnel advanced toward University Station (Figure 6.1b and 6.10). The modeling in Figures 6.20 and 6.22 represent the limits between full face sand and 10% sand occupying the face, respectively. The maximum settlements from these calculations are plotted in Figure 6.10 and reproduced here as Figure 6.23. The settlement points from the DEM models are similar to those observed in the field, especially for a C/D ratio equal to 1, and clearly show the effects of till in the tunnel face on the maximum surface settlements. The lower field settlement underneath the Education Car Park are likely the result of the combined effects of till in the tunnel face and the contractor's grouting methodology for the tail shield in this sensitive area.

6.7 Summary

A series of analyses were carried out to assess the application of the discrete element method in simulating the surface settlements induced by a 6.5-m-diameter shallow tunnel under uniform and mixed face conditions. Several model simplifications were made to capture construction details that were known to impact surface settlements, e.g., face pressure, shield gap, liner gap. In all cases model deformations were obtained that were in reasonable agreement with measured deformations. A detailed summary of the findings is given below.

1. Due to the limitation of not being able to model non-spherical particles to

simulate a full-scale problem, micro-parameter values obtained through calibration of the DEM model consisting of spherical particles against the small-scale centrifuge testing of shallow tunneling in uniform sand (Chapter 5), were used without further scaling of parameters to simulate the tunnel response.

2. Although not perfect, deformations obtained by the DEM model captured reasonably well the measured deformations. This implies, as discussed by Cundall (2001), although far fewer particles exist in the tunnel model than in the physical system, the internal mechanisms remain essentially unchanged. Hence, equivalent continuum measures of granular material such as deformation can be captured realistically. This implies that the behaviour of sand is derived mainly from microscopic contact behaviour and/or microscopic geometric changes induced by loading.
3. The discrete element method has been successfully used to model a 6.5 m diameter tunnel in three-dimensions with a uniform face. The critical construction issues known to affect surface settlements, e.g., face pressure, shield gap, and liner gap, were successfully implemented in the model. The model size was kept relatively small and the simulation was run within a reasonable time frame (20 hrs on a 1.7 GHz CPU with 1 GB RAM workstation with an Intel Xeon processor).
4. The calculated settlement profiles were in reasonable agreement with the observed settlement profile, particularly in front of and up to 5 m behind the tunnel face. In the liner portion, the model over predicted the surface settlement and this over prediction could be controlled by controlling the size of the gap in the numerical model.
5. The effects of mixed face conditions of till/sand on surface settlements was also examined. The displacement profile from the numerical model when the tunnel face was 10% sand and 90% till was very similar in shape with the measured results. While the maximum settlement was over predicted, this over prediction can be controlled by the size of the gap used in the model. The modelling result showed that the settlement decreases as the till portion of the material at face increased. These findings imply that for the SLRT tunnel the geology of the mixed-face tunneling conditions was likely the controlling factor in reducing the

surface settlements as the tunnel advanced from the portal to the Education Car Park.

Table 6.1 Geotechnical engineering parameters for major stratigraphic units (Washuta and Martin, 2004)

Material	Unit Weight (kN/m^3)	Shear Strength		Modulus of Elasticity (MPa)	Poisson's Ratio
		c' (kPa)	ϕ' (degree)		
Lacustrine Clay	19	15	20	20	0.4
Outwash Sand and Silt	19	0	35	40	0.3
Glacial Till (Cohesive Zone)	21.5	10	35	60	0.3

Table 6.2 Ball size distributions (material discretization) in DEM tunnel model

Ball Zone	Ball Size Distribution, millimeters	Number of Particles
1	$r_{min} = 120$, $r_{max} = 240$	25013
2	$r_{min} = 120$, $r_{max} = 240$	3589
3	$r_{min} = 130$, $r_{max} = 260$	6050
4	$r_{min} = 140$, $r_{max} = 280$	4844
5	$r_{min} = 160$, $r_{max} = 320$	4588
6	$r_{min} = 200$, $r_{max} = 400$	2349
7	$r_{min} = 240$, $r_{max} = 480$	3370
8	$r_{min} = 160$, $r_{max} = 320$	8952
9	$r_{min} = 200$, $r_{max} = 400$	4583
10	$r_{min} = 160$, $r_{max} = 320$	18203
11	$r_{min} = 200$, $r_{max} = 400$	9320
12	$r_{min} = 100$, $r_{max} = 150$	23281
13	$r_{min} = 130$, $r_{max} = 260$	10592
Total number of particles, before excavation		124734

Table 6.3 Magnitude of gaps around shield and liner

Case #	Gap around Shield (mm)	Gap around Liner (mm)
B1	17	55
B2	25	55
B3	17	120

Table 6.4 Tunnel geology modelled in DEM

Case #	Tunnel Location	C/D ratio	Geology	Tunnel Face Geology
Geo_1	Under the utility tunnel	0.5	Clay up to tunnel crown ovelying sand	Uniform sand
Geo_2	Between Portal and Education Car Park	1.0	3.25 m of Clay overlying sand; sand both above and below tunnel crown	Uniform sand
Geo_3	Education Car Park and beyond.	1.5 -2.0 and >2	3.25 m of Clay overlying sand over clay till/bedrock	Mixed face: with the face percentages of till to sand of 90/10

Table 6.5 Initial conditions in DEM model (specified porosity = 0.4, 1g gravity, C/D=1.0)

Parameters	**Measurement Spheres (radius = 1.5 and 1.2 meter)**					
		Ko		**Ko**		**Ko**
	(1,2)		**(3,4)**		**(5,6)**	
Depth from ground, m	9.75		7		5	
Porosity	0.372		0.373		0.386	
σ_z, kPa	150		108		80	
σ_x, kPa	122		96.5		59.5	
σ_y, kPa	127	0.84	100	0.92	61.8	0.77

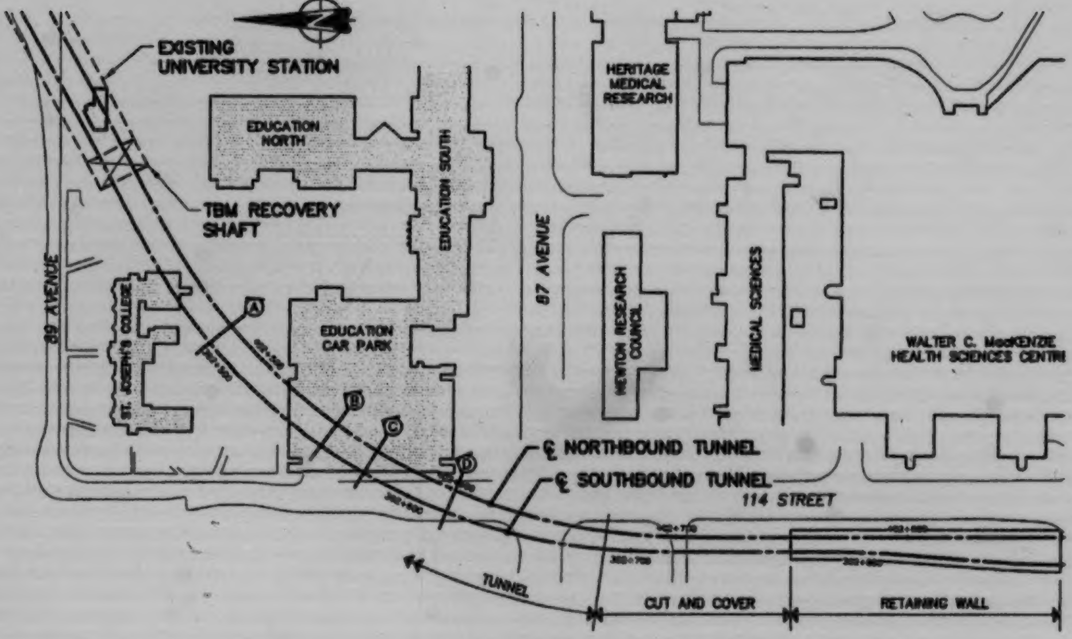
EXISTING UNIVERSITY STATION
TBM RECOVERY SHAFT
EDUCATION NORTH
EDUCATION SOUTH
EDUCATION CAR PARK
ST. JOSEPH'S COLLEGE
89 AVENUE
87 AVENUE
HERITAGE MEDICAL RESEARCH
NEWTON RESEARCH COUNCIL
MEDICAL SCIENCES
WALTER C. MacKENZIE HEALTH SCIENCES CENTRE
A
B
C
D
℄ NORTHBOUND TUNNEL
℄ SOUTHBOUND TUNNEL
114 STREET
TUNNEL
CUT AND COVER
RETAINING WALL

(a) *PLAN*

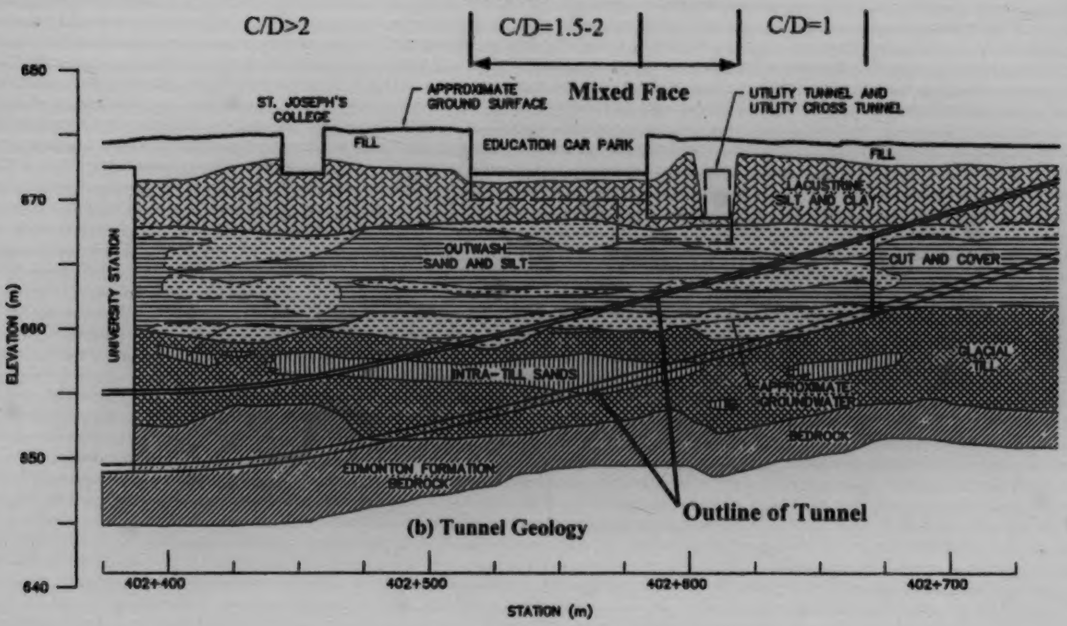
C/D=0.5
C/D>2
C/D=1.5-2
C/D=1
Mixed Face
ST. JOSEPH'S COLLEGE
APPROXIMATE GROUND SURFACE
UTILITY TUNNEL AND UTILITY CROSS TUNNEL
FILL
EDUCATION CAR PARK
LACUSTRINE SILT AND CLAY
UNIVERSITY STATION
OUTWASH SAND AND SILT
CUT AND COVER
INTRA-TILL SANDS
GLACIAL TILL
APPROXIMATE GROUNDWATER
BEDROCK
EDMONTON FORMATION BEDROCK
Outline of Tunnel
ELEVATION (m)
680
670
660
650
640
402+400
402+500
402+600
402+700
STATION (m)

(b) Tunnel Geology

Figure 6.1 Project Location Plan and Simplified Geology (after Bobey et al., 2004)

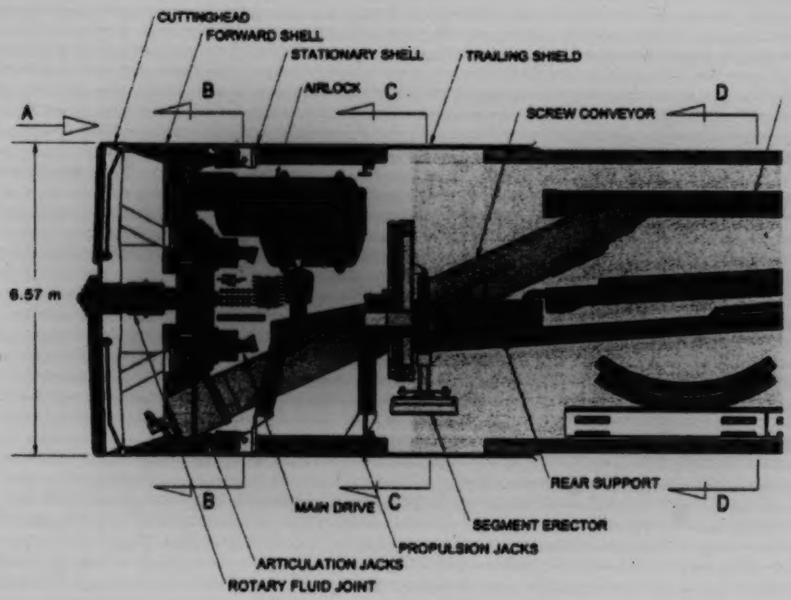
CUTTINGHEAD
FORWARD SHELL
STATIONARY SHELL
TRAILING SHIELD
AIRLOCK
SCREW CONVEYOR
A
B
C
D
6.57 m
REAR SUPPORT
B
MAIN DRIVE
C
D
SEGMENT ERECTOR
PROPULSION JACKS
ARTICULATION JACKS
ROTARY FLUID JOINT

Figure 6.2a Longitudinal section of Lovat EPB-TBM used for constructing the City of Edmonton LRT tunnels (figure provided by Lovat)

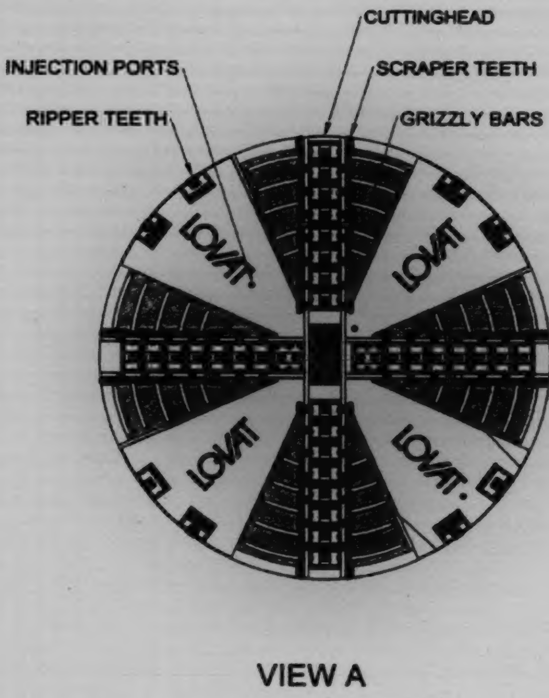
CUTTINGHEAD
INJECTION PORTS
SCRAPER TEETH
RIPPER TEETH
GRIZZLY BARS
LOVAT
LOVAT
LOVAT
LOVAT
VIEW A

Figure 6.2b Face section of Lovat EPB-TBM used for constructing the City of Edmonton LRT tunnels (figure provided by Lovat)

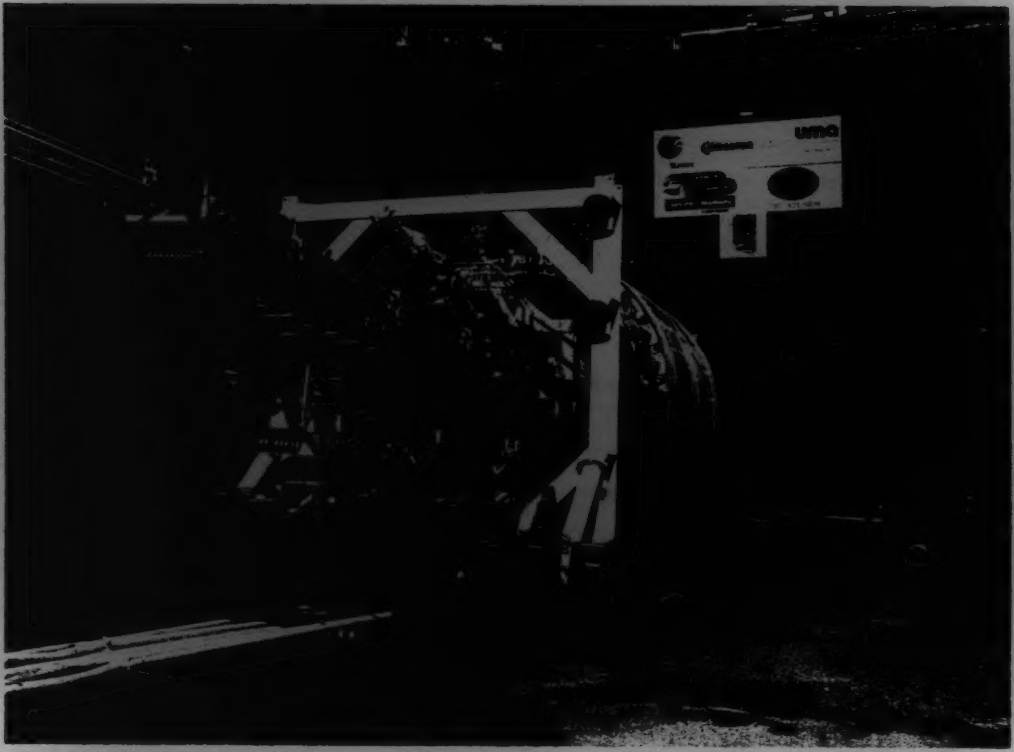

Figure 6.3 Photograph of the Lovat EPB_TBM in position to commence the driving of the southbound LRT tunnel. Note the approximately 6-m of cover (1 tunnel diameter) above the tunnel crown (photo taken during a tour of the site by the author)

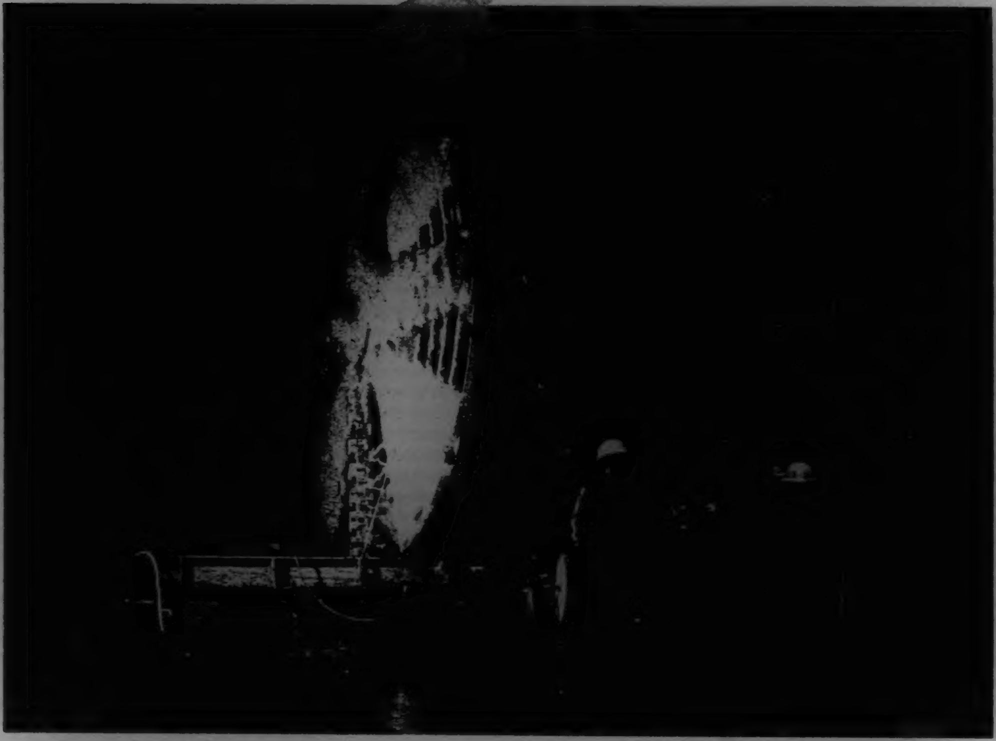

Figure 6.4 The cutting head of the Lovat EPB-TBM after breaking through on the Northbound tunnel (photo taken during a tour of the site by the author)

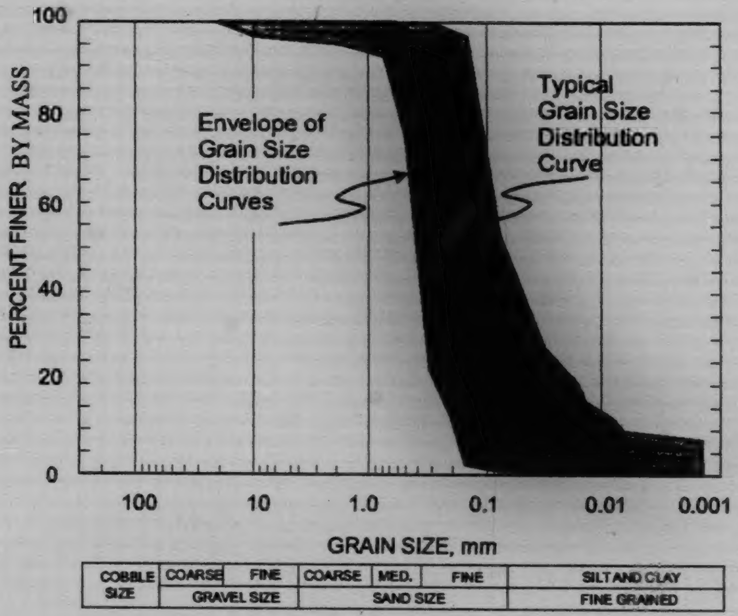

Figure 6.5 Variability in grain size distribution of soils in outwash deposit (after Boone et al, 2004)

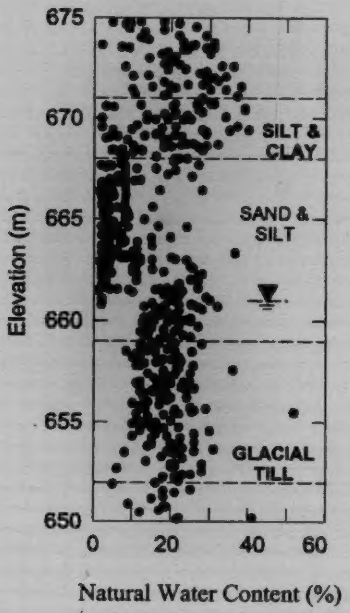

Figure 6.6 Profile of natural water content related to elevation (after Boone et al, 2004)

Figure 6.7: Photograph showing the clean nature of the outwash sand exposed in the open-cut excavation for the TBM portal (photo taken during a tour of the site by the author)

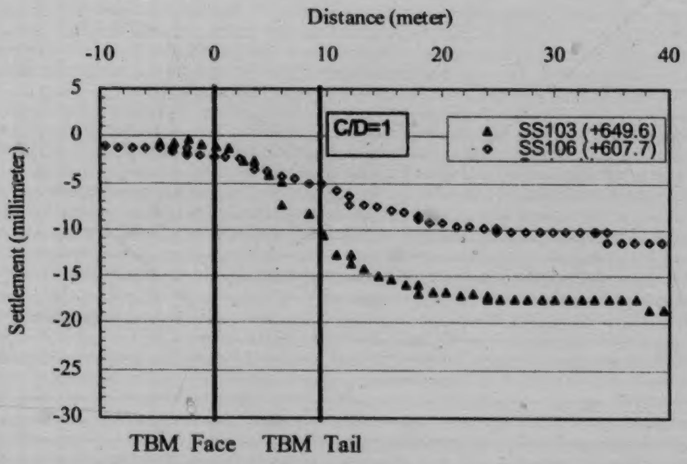

Figure 6.8 Observed shallow settlements range along the centre line of the tunnel during construction of Southbound tunnel with proximity to TBM face, from Portal to Education Car Park (after Bosse, 2005)

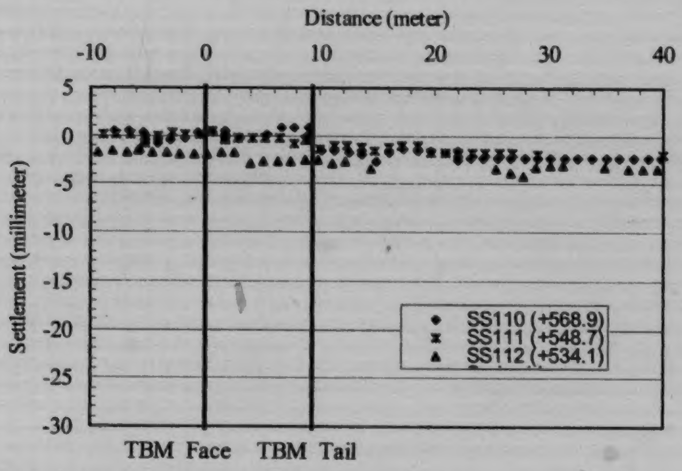

Figure 6.9 Observed shallow settlements along the centre line of the tunnel during construction of Southbound tunnel with proximity to TBM face, Education Car Park (after Bosse, 2005)

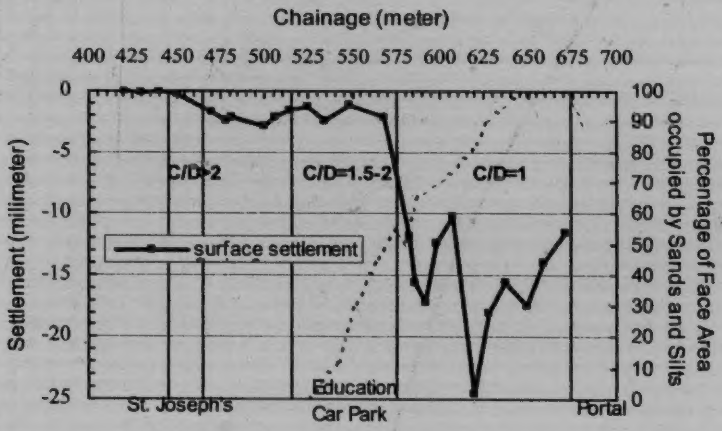

Figure 6.10 Observed shallow settlements during construction of Southbound tunnel and mixed-face condition (after Bosse, 2005)

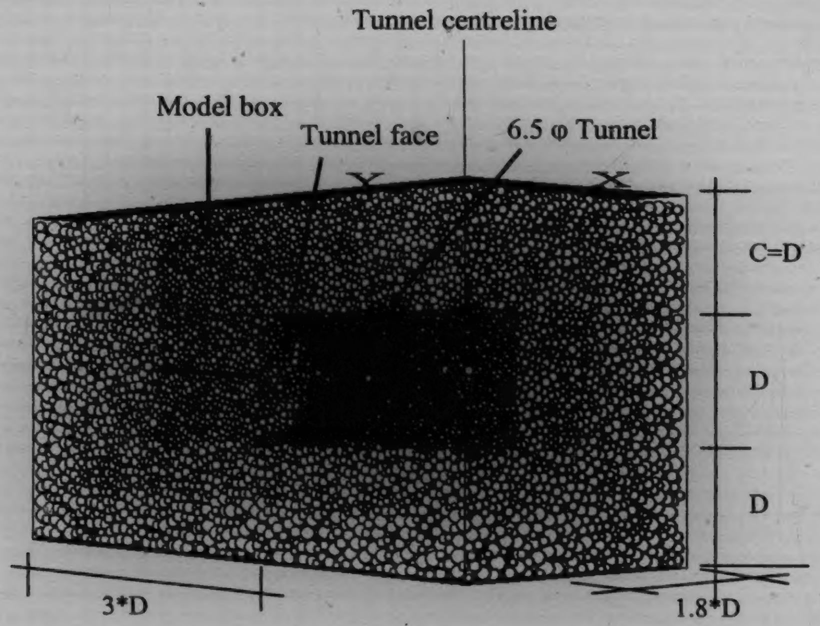
Tunnel centreline
Model box
Tunnel face
6.5 φ Tunnel
C=D
D
D
3*D
1.8*D

Figure 6.11 Three-dimensional view of shallow tunnel model by DEM (half tunnel; 118999 particles)

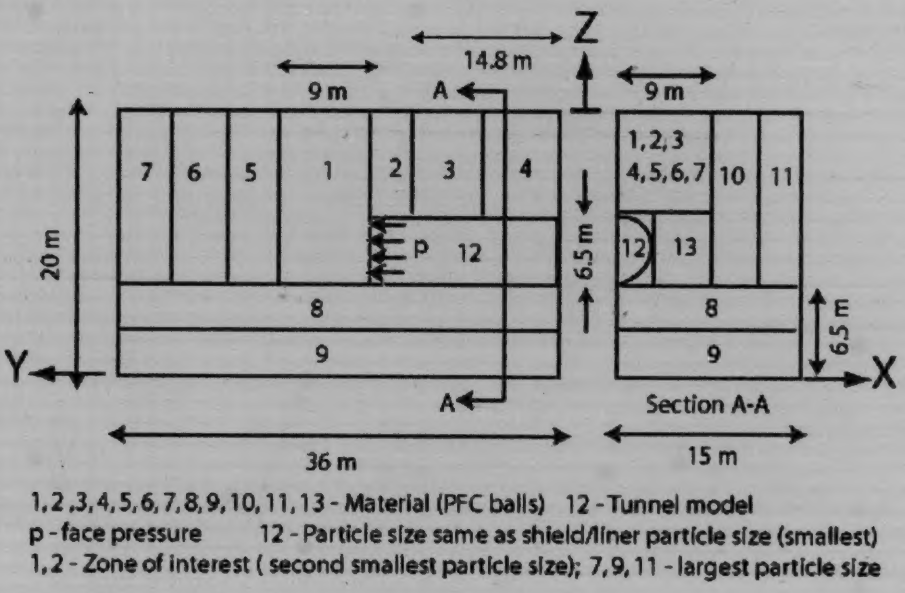
Z
14.8 m
9 m
A
9 m
7
6
5
1
2
3
4
1,2,3
4,5,6,7
10
11
P
12
12
13
20 m
6.5 m
8
8
9
9
6.5 m
Y
X
A
Section A-A
36 m
15 m
1,2,3,4,5,6,7,8,9,10,11,13 - Material (PFC balls)   12 - Tunnel model
p - face pressure   12 - Particle size same as shield/liner particle size (smallest)
1,2 - Zone of interest (second smallest particle size); 7,9,11 - largest particle size

Figure 6.12 DEM model of SLRT tunnel construction

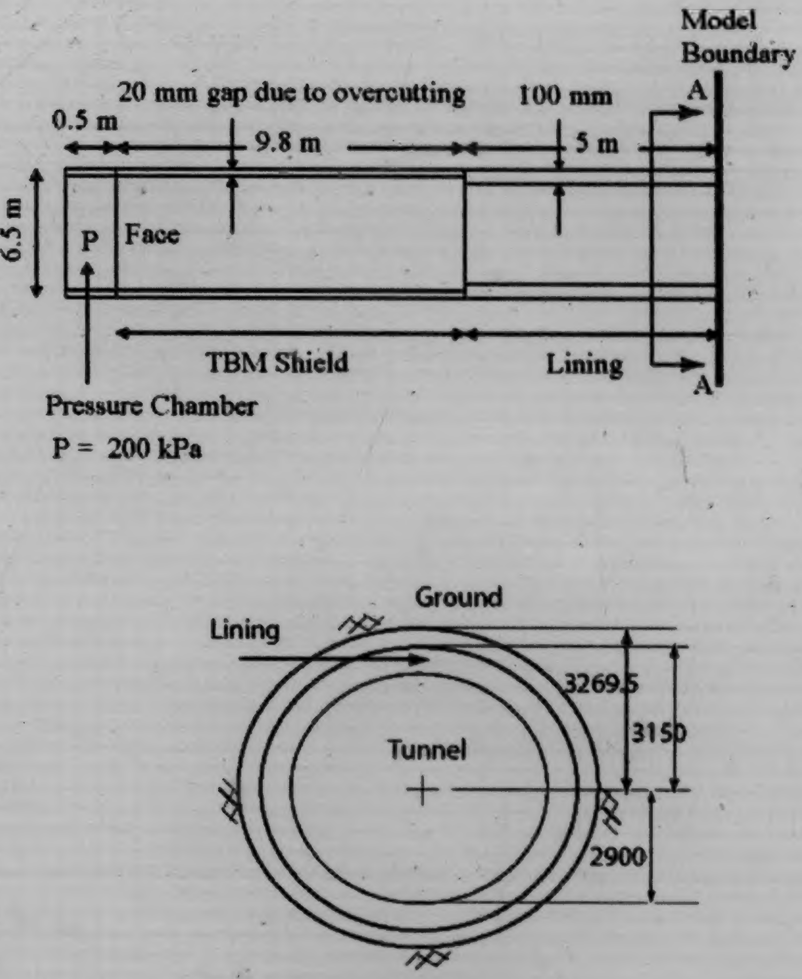
Model
Boundary
20 mm gap due to overcutting
100 mm
A
0.5 m
9.8 m
5 m
6.5 m
P
Face
TBM Shield
Lining
A
Pressure Chamber
P = 200 kPa
Ground
Lining
3269.5
3150
Tunnel
2900

Section A-A
All dimensions are in mm

Figure 6.13 Tunnel model used in SLRT modeling and X-section along the tunnel lining and surrounding ground

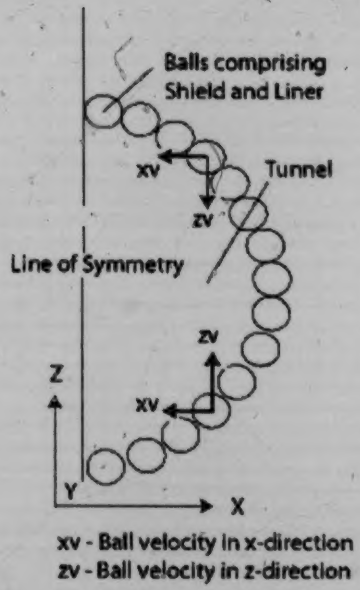
Balls comprising
Shield and Liner
xv
Tunnel
zv
Line of Symmetry
zv
Z
xv
Y
X
xv - Ball velocity in x-direction
zv - Ball velocity in z-direction

Figure 6.14 Uniform radial displacement of Shield/Liner in DEM to create the gaps between the TBM shield/liner and the tunnel bore

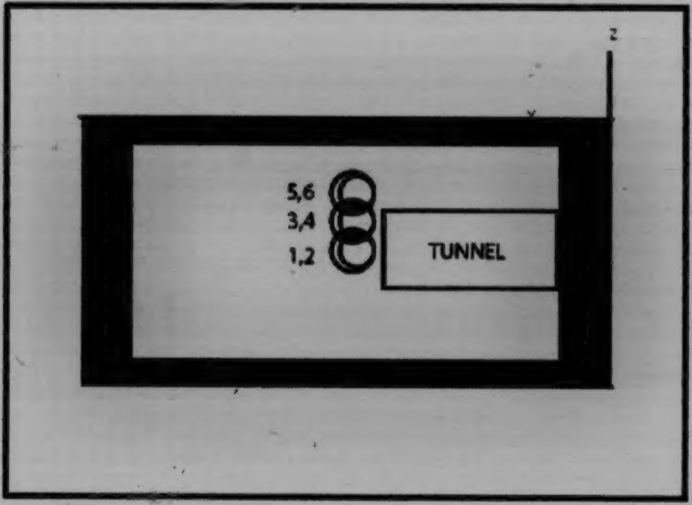
z
x
5,6
3,4
1,2
TUNNEL

Figure 6.15 Location of measurement spheres to measure stresses around the tunnel

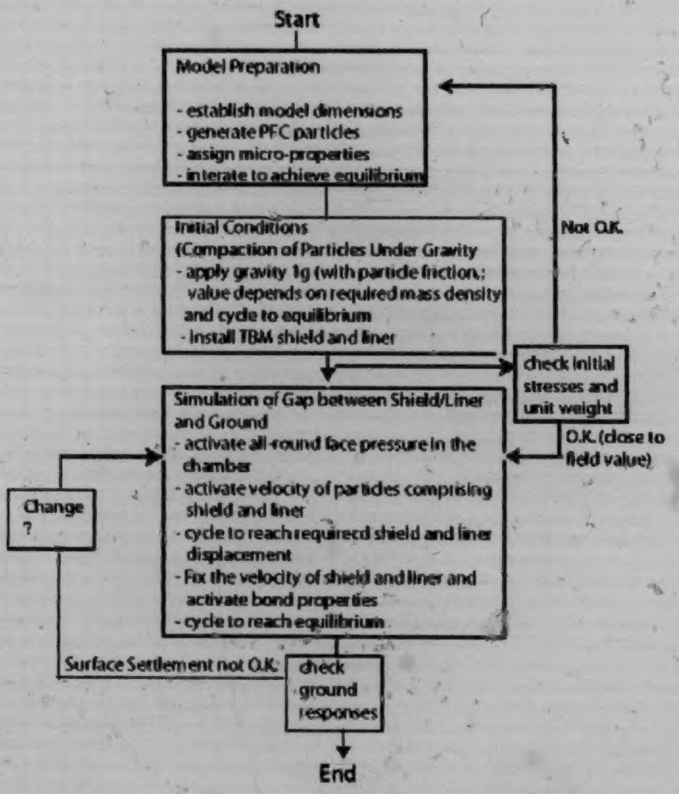
Start
Model Preparation
- establish model dimensions
- generate PFC particles
- assign micro-properties
- interate to achieve equilibrium
Not O.K.
Initial Conditions
(Compaction of Particles Under Gravity
- apply gravity 1g (with particle friction;
value depends on required mass density
and cycle to equilibrium
- Install TBM shield and liner
check initial
stresses and
unit weight
O.K. (close to
field value)
Simulation of Gap between Shield/Liner
and Ground
- activate all-round face pressure in the
chamber
- activate velocity of particles comprising
shield and liner
- cycle to reach required shield and liner
displacement
- Fix the velocity of shield and liner and
activate bond properties
- cycle to reach equilibrium
Change
?
Surface Settlement not O.K.
check
ground
responses
End

Figure 6.16 Flow chart for SLRT simulation by DEM

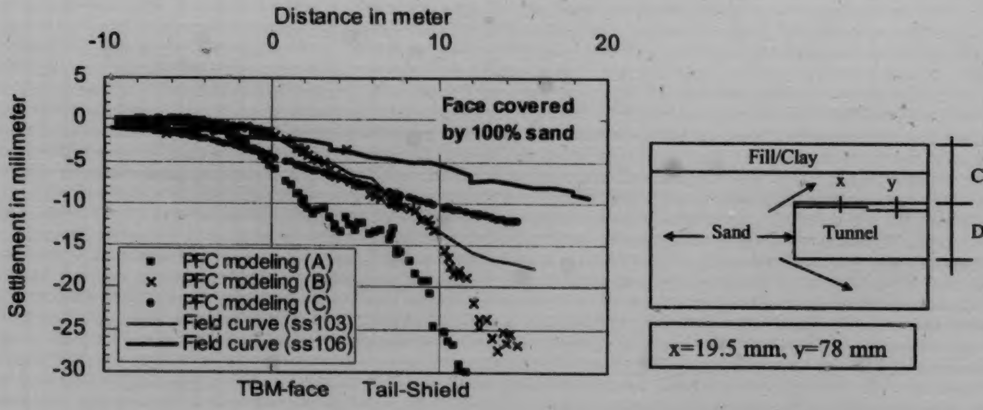

Figure 6.17 Quantification of 'clay cap' in DEM model of 6.5 m-diameter tunnel in sand: uniform face and C/D=1.0 (G=1 GPa, $\nu=0.2$, $\mu=0.6$, spherical particles)

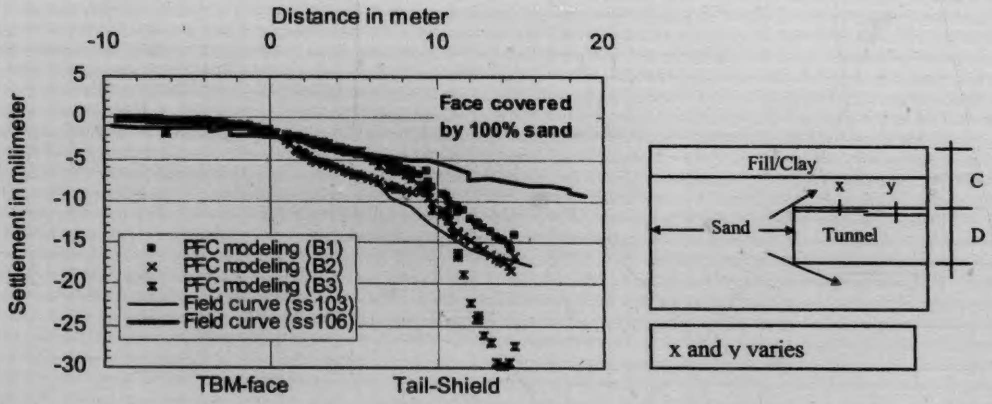

Figure 6.18 Quantification of gaps in DEM model of 6.5 m-diameter tunnel in sand: uniform face and C/D=1.0 (G=1 GPa, ν=0.2, μ=0.6, spherical particles)

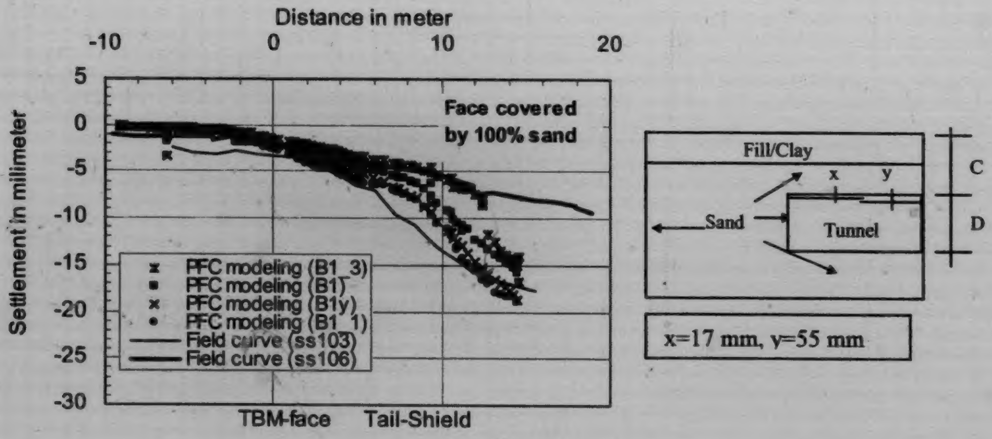

Figure 6.19 Quantification of particle velocity to produce gaps in DEM model of 6.5 m-diameter tunnel in sand: uniform face and C/D=1.0 (G=1 GPa, ν=0.2, μ=0.6, spherical particles)

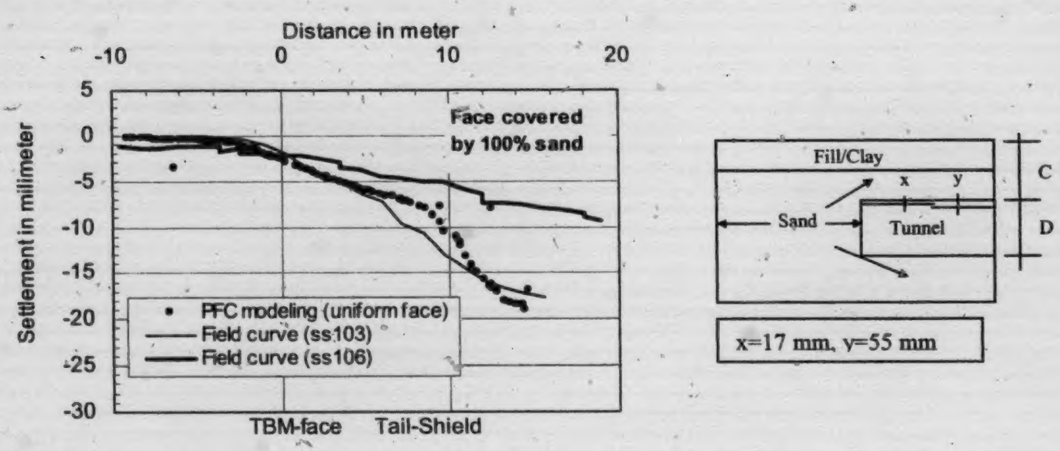

Figure 6.20 Surface settlement from DEM model of 6.5 m-diameter tunnel in sand: uniform face (G=1 GPa, ν=0.2, μ=0.6, spherical particles)

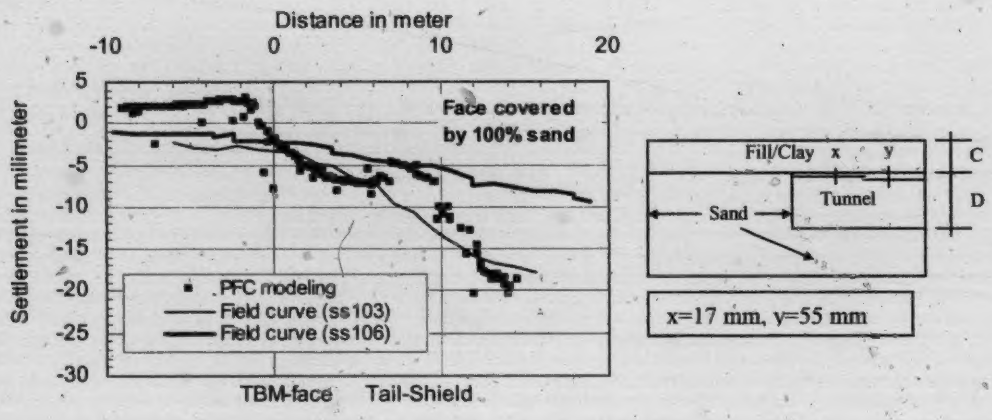

Figure 6.21 Surface settlement from DEM model of 6.5 m-diameter tunnel in sand: uniform face (C/D=0.5, G=1 GPa, ν=0.2, μ=0.6, spherical particles)

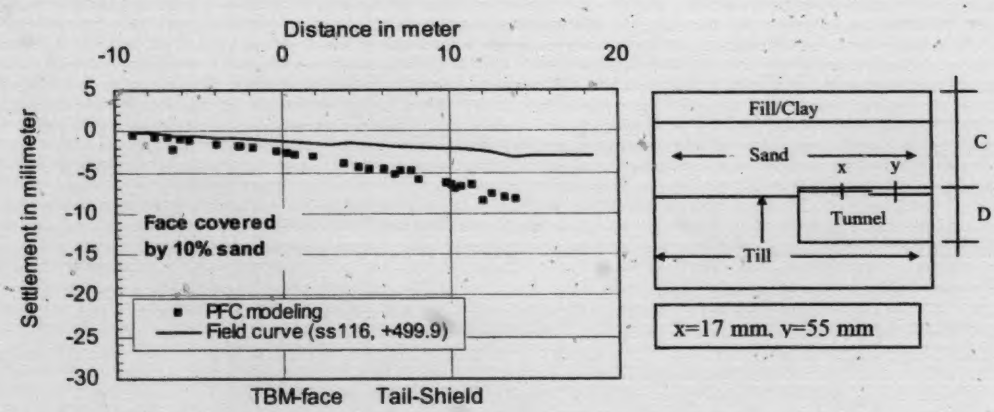

Figure 6.22 Surface settlement from DEM model of shallow tunnel in sand: mixed face consisting 90 percent 'idealized' till (C/D=2, G=1 GPa, ν=0.2, μ=0.6, spherical particles)

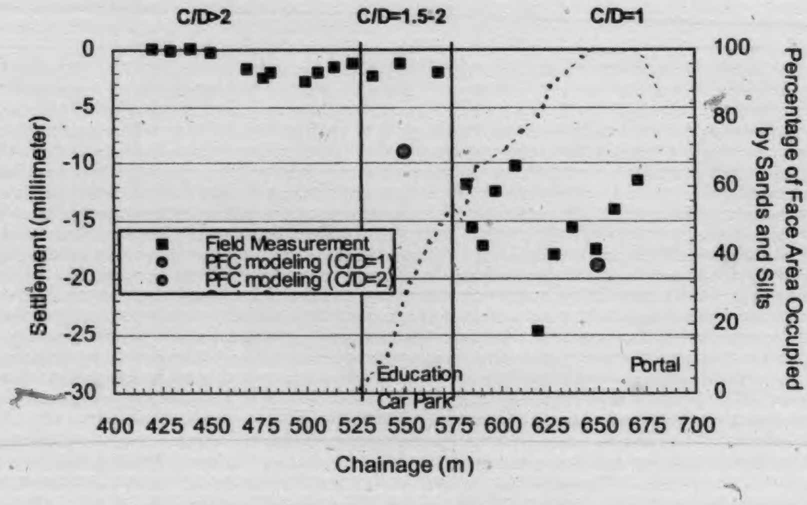

Fig. 6.23 Settlement variation with tunnel geology

CHAPTER 7

Conclusions and Recommendations

7.1 Conclusions

A series of three-dimensional numerical analyses of tunnel face stability and ground deformations in dry sand were carried out using Discrete Element Modeling (DEM). The simulation results obtained from a commercially available DEM code, PFC^{3D}, were compared with the results from physical models of shallow tunnels in dry sand as well as with field data from a recently constructed 6.5-m-diameter South Light Rail Transit (SLRT) tunnel excavated in the City of Edmonton under conditions of sand and mixed face.

The following conclusions are reached about DEM capabilities to model the face collapse pressure and deformations associated with shallow tunnels in dry, uniform sand:

A) Material behaviour

- The calibration of the PFC material against the laboratory standard triaxial test results for uniform sand (standard Ottawa sand) resulted in the following values for the micro-parameters:
    - Elastic properties of DEM particles (Hertz-Mindlin contact law):
      Shear modulus (G) = 1.0 GPa
      Poisson's ratio (ν) = 0.2
    - Interparticle friction coefficient (μ) = 0.5

- The above-mentioned values for the particle contact parameters are applicable to both dense and loose densities. Also the stress-strain-volumetric response of the PFC materials compared well to that of laboratory triaxial test results at different confining stresses using the same values for the contact parameters.

- For a model size close to that of a triaxial sample (165 mm × 70 mm × 70 mm), there is no size or scale effect as long as the average particle size (d_{50}) of the numerical sample remains close to or less than 4 mm (for uniformity coefficient $C_u = 1.5$) and the internal damping is equal to 0.8.

- PFC samples of smooth spherical particles failed to match both the peak strength and the initial modulus of dense standard Ottawa sand. Non-spherical particle shape was needed to capture both the peak strength and the modulus of the sand.

- The sub-rounded shape of the Ottawa sand grains was modeled by bonding two spherical particles of equal size with a slight overlap. This approach to capture the shape of the Ottawa sand grain worked well and replicated the laboratory peak strength of standard Ottawa sand.

- While the stress-strain response of PFC samples determined for non-spherical particles under triaxial compression loading matched well the stiffness and post-peak softening of laboratory triaxial test results of uniform sand, slight differences were observed in the volumetric responses. Initial contraction in PFC sample was higher and occurred over a wider strain level compared to the laboratory sample. The onset of dilation in both physical and synthetic samples occurred before peak stress but at smaller axial strain (0.5%) in the laboratory triaxial sample compared to 1% in PFC samples. This small difference in initial volumetric response could be attributed to the specified particle elastic properties, especially the particle shear modulus, in PFC samples.

- Bulging of PFC samples was obtained using discretized lateral walls. The stress-strain behaviour of dense PFC samples showed a clear peak, and post-peak strain softening.

B) Discrete element modeling of centrifuge testing of tunneling in sand:

- The three-dimensional discrete element simulations of small-scale centrifuge tests of shallow tunnels in sand gave results comparable to that of the physical testing as far as tunnel face stability is concerned. Somewhat less stiff DEM material response obtained from using smooth spherical particles compared to that of sand produced little deviation from the physical response as far as comparison of collapse pressure was concerned.
- Simulated collapse pressure converged with the measured data as the particle sizes were reduced. The study indicated that among the analytical methods, the Vermeer and Ruse method gave reasonable agreement with the numerical predictions for both 5.0 m and 10 m diameter tunnels.

- DEM response of tunneling in sand is sensitive to the following parameters (while keeping the particle elastic parameters and numerical damping coefficient constant):

    - Particle size: The smaller the particle size from the original size (d_{50}) of 8.75 mm the better the response, particularly up to 20 kPa face pressure.
    - Particle friction coefficient (μ): the value of 0.6 (or ϕ_μ = 31 degrees) better matched the centrifuge results than 0.5 (or ϕ_μ = 26.5 degrees). The slightly higher μ value than found through calibration in Chapter 4 (μ = 0.5) was needed to compensate for the spherical particles used in tunnel simulation.
    - Increment of face pressure: DEM results showed the collapse pressure tends to approach the measured value as the increment of face pressure grows smaller.

- The near face displacement pattern from DEM simulations reasonably matched the physical observations, at least qualitatively. With the deeper tunnel, the displacement stops at a certain distance above the tunnel crown and does not propagate to the surface. The opposite was observed for the tunnel at shallower depth where displacement, starting at the face, continued to the surface.

C) Application of 3D-DEM to investigate surface settlement above a 6.5 m diameter tunnel in sand:

- Like the case of centrifuge simulations of shallow tunnel stability in sand, discrete element modeling (using simple spherical shaped particles) has been successfully used to model a 6.5 m diameter tunnel in three-dimensions. The critical tunnel parameters known to affect surface settlements, e.g., face pressure, shield gap, and liner gap, were successfully implemented in the model.

- For the case of uniform face conditions, considerable settlement was observed over the length of the shield of the TBM. Despite restrictions in the model size and the simplified geometry, the calculated settlement profiles were in reasonable agreement with the observed settlement profile, particularly in front of and up to 5 m behind the tunnel face. In the portion over the liner, the model over predicted the surface settlement and this over prediction could be controlled by controlling the size of the gap in the numerical model.

- For the case of mixed face conditions of till/sand, it was found that the maximum settlement was over predicted. However, this over prediction can be controlled by the size of the gap used in the model. The modeling results showed that the settlement decreased as the till portion of the tunnel face increased. These findings imply that for the SLRT tunnel the geology of the mixed-face tunneling conditions was likely the controlling factor in reducing the surface settlements as the tunnel advanced from the portal to the Education Car Park.

7.2 Recommendations

A great deal of opportunity exists to apply DEM to solve full-scale engineering problems involving granular particles and flow of materials. Assuming that computing power will continue to increase, the following are some recommendations for future research.

- Material calibration should be extended to include data from tests other than triaxial tests including plane strain and true triaxial tests. These latter two tests can be used to capture shear band formation in DEM.

- The effects of boundary on material behaviour can be explored through modeling of flexible membranes in DEM.
- More Improvements are needed to realistically capture particle shape.
- Effects of material saturation (due to suction when ground water is below the tunnel) and the ground water table on the DEM tunnel response should be explored.

REFERENCES

Anagnostou, G. and Kovari, K. (1996). Face stability conditions with earth pressure balanced shields. Tunnelling and Underground Space Technology. 11(2): 165-173.

Anagnostou, G. and Kovari, K. (1994). The face stability of slurry-shield-driven tunnels. Tunnelling and Underground Space Technology. 91(2): 165-174.

Atkinson, J. H. and Potts, D. M. (1977). The stability of shallow circular tunnel in cohesionless soil. Geotechnique. 27(2):203-215.

Atkinson, J. H., Potts, D. M., and Schofield, A. N. (1977). Centrifugal model tests on shallow tunnels in sand. Tunnels and Tunnelling: 9 (1): 59-64.

Augarde, C. E. and Burd, H. J. (2001). Three-dimensional finite element analysis of lined tunnels. International Journal for Numerical and Analytical Methods in Geomechanics. 25 (3): 243-262.

Augarde, C. E., Burd, H. J., and Houlsby, G. T. (1998). Some experiences of modeling tunnelling in soft ground using three-dimensional finite elements. Proceedings of the 4th European Conference on Numerical Methods in Geotechnical Engineering – NUMGE98 (ed. Annamaria Cividini): 603-612

Bandini, P. (1999). Static response and liquifaction of silty sands. M.Sc thesis. Purdue University.

Bardet, J. P. (1998). Introduction to computational granular mechanics. In Behavior of Granular Materials (ed. B. Cambou). SpringerWien, NewYork.

Bardet, J. P. (1994). Observations on the effects of particle rotations on the failure of idealized granular materials. Mechanics of Materials. 18: 159-182.

Bardet, J. P. (1986) Bounding surface plasticity model for sands. Journal of Engineering Mechanics, 112(11): 1198-1217.

Bardet, J. P. and Proubet, J. (19[illegible]). Shear-band analysis in idealized granular material. Journal of Engineering Mechanics. 118 (2):397-414.

Bardet, J. P. and Proubet, J. (1991). A numerical investigation of the structure of persistent shear bands in granular media. Geotechnique. 41 (4):599-613.

Bathe, K. J. and Wilson, E. L. (1976). Numerical methods in finite element analyses. Englewood Cliffs: Prentice-Hall.

Bathurst, R. J. and Rothenburg, L. (1988). Micromechanical aspects of isotropic granular assemblies with linear contact interactions. Journal of Applied Mechanics. 55:17-23.

Biarez, J. and Hicher, P. Y. (1987). Simplified hypotheses on mechanical properties equally applicable to sands and clays. Proceedings of the International Workshop on Constitutive Equations for Granular Non-cohesive Soils (eds. A. Saada.and G. Biancini). A.A.Balkema/Rotterdam/Brookfield: 19-32.

Bishop, A. W. and Green, G. E. (1965). The influence of end restraint on the compression strength of a cohesionless soil. Geotechnique. 15(3): 243-266.

Bobet, A. (2001). Analytical solutions for shallow tunnels in saturated ground. Journal of Engineering Mechanics. 127 (12):1258-1266.

Bolton, M. D., Lu, Y. C. and Sharma, J. S. (1996). Centrifuge models of tunnel construction and compensation grouting. Proceedings of International Symposium on Geotechnical Aspects of Underground Construction in Soft Ground, London (eds R.J. Mari and R.N. Taylor), Balkema: 471-478.

Bolton, M. D. (1986). The strength and dilatancy of sands. Geotechnique. 36 (1):65-78

Bobey, L., Tweedie, R., and Broere, R. (2004). Ground and structure monitoring of the Edmonton south LRT tunnel from University station to health sciences station. Proceedings of the 18th Tunneling Association of Canada (TAC) conference, Edmonton, Alberta, Canada.

Boone, S. J., Poot, S., Haley, D., and Pelly, D. (2004). Characterization of glacial deposits for tunnel design. Proceedings of the 18th Tunnelling Association of Canada (TAC) conference, Edmonton, Alberta, Canada.

Bosse, M. C. (2005). Performance of EPB-TBM in mixed face conditions: City of Edmonton South LRT Extension – University Station to Health Sciences Station. Master's thesis. University of Alberta.

Cambou, B. (1998). Micromechanical approach in granular materials. Behaviour of granular materials (ed. Bernard Cambou). International Centre for Mechanical Sciences. Courses and Lectures-No. 385. SpringerWienNewYork.

Carter, J. P., Desai, C. S., Potts, D. M., Schweiger, H. F., and Solan, S.W. (2000). Computing and Computer modeling in geotechnical engineering. GeoEng2000: An International Conference on Geotechnical and Geological Engineering. Volume 1: Invited Papers. Melbourne, Australia.

Chambon, P. and Corté, J. F. (1994). Shallow tunnels in cohesionless soil: Stability of tunnel face. Journal of Geotechnical Engineering. 120(7):1148-1165.

Chambon, P., Corté, J. F., Garner, J. and Konig, D. (1991). Face stability of shallow tunnels in granular soils. Centrifuge 91, Ko (ed.). Balkema, Rotterdam.

Chang, C.S. and Misra, A. (1990a). Packing structure and mechanical properties of granulates. Journal of engineering mechanics. 116 (5): 1077-1093.

Chang, C. S. and Misra, A. (1990b). Application of uniform strain theory to heterogeneous granular solids. Journal of engineering mechanics. 116 (10): 2310-2328.

Chang, C .S., Kabir, M. G., and Chang, Y. (1992a). Micromechanics modeling for stress-strain behavior of granular soils. I: theory. Journal of Geotechnical Engineering. 118 (12): 1959-1973.

Chang, C. S., Kabir, M. G., and Chang, Y. (1992b). Micromechanics modeling for stress-strain behavior of granular soils. II: evaluation. Journal of Geotechnical Engineering. 118 (12): 1975-1992.

Christoffersen, J., Meharabadi, M. M., and Nemat-Nasser, S. (1981). A micromechanical description of granular material behavior. ASME Journal of Applied Mechanics. 48: 339-344.

Clough, G. W. and Schmidt, B. (1981). Design and performance of excavations and tunnels in soft clay. In Soft Clay Engineering, Elsevier: 569-634.

Cundall, Peter A. (2001). A discontinuous feature for numerical modeling in geomechanics? Geotechnical Engineering (Proceedings of the Institution of Civil Engineers). 149 (1):41-47.

Cundall, P. A. (1988). Formulation of three-dimensional distinct element method – Part I: a scheme to detect and represent contacts in a system composed of many polyhedral blocks. International Journal of Rock Mechanics, Mining Science and Geomechanics Abstracts. 25 (3):107-116.

Cundall, P. A. (1971). A computer model for simulating progressive, large-scale movements in blocky rock systems. Proceedings of symposium of International Society of Rock Mechanics. 2 (8).

Cundall, P. A. and Carranza-Torres, C. (2004). Micromechanical models for rock behavior. International Journal of Rock Mechanics and Mining Sciences. Submitted.

Cundall, P. A. and Hart, R. D. (1992). Numerical Modeling of Discontinua. Engineering Computations. 9: 101-113.

Cundall, P. A. and Strack, O. D. L. (1979). A discrete numerical model for granular assemblies. Geotechnique. 29 (1):47-65.

Cundall, P. A. and Strack, O. D. L. (1978). The distinct element method as a tool for research in granular media, Parts I and II, Report to National Science Foundation, Eng. 76-20711, Department of Civil and Mineral Engineering, University of Minnesota, Minneapolis, MN.

Davis, G. de .V (1986). Numerical methods in engineering and science. Chapman and Hall. London, UK.

Davis, R. O. and Selvadurai, A. P. S. 2002. Plasticity and Geomechanics. Cambridge University Press.

Dobry, R. and Ng, T.-T. (1992). Discrete modeling of stress-strain behavior of granular media at small and large strain. Engineering Computations. 9:129-143.

Drescher, A. and Vardoulakis, I. (1982). Geometric softening in triaxial tests on granular material. Geotechnique. 32: 291-303.

Ehlers, W., Diebels, S., and Michelitsch, T. (2001). Microscopic modelling of granular materials taking into account particle rotations. Lecture Notes in Physics 568 (eds. P. A. Vermeer). Springer-Verlag Berlin Heidelberg. 259-274.

Eisenstein, Z. (2000). The challenges of urban tunnelling. Proceedings of the International Conference on Tunnels and Underground Structures, Singapore (eds. Jian Zhao, J.N. Shirlaw and R. Krishnan): 15-33.

Fortin, J., Hjiaj, M., and Saxce, G. de (2002). An improved discrete element method based on a variational formulation of the frictional contact law. Computers and Geotechnics. 29 (8):609-640.

Gioda, G. and Locatelli, L. (1999). Back analysis of the measurements performed during the excavation of a shallow tunnel in sand. International Journal for Numerical and Analytical Methods in Geomechanics. 23: 1407-1425.

Gioda, G. and Swoboda, G. (1999). Developments and applications of the numerical analysis of tunnels in continuous media. International Journal for Numerical and Analytical Methods in Geomechanics. 23: 1393-1405

Graham, J. (1992). The key material properties in geotechnical engineering need to be measured instead of being specified. Predictive Soil Mechanics. Proceedings of the Wroth Memorial Symposium. St Catherine's College, Oxford. G.T. Houlsby and A.N. Schofield (eds.).

Guest, A. R. and Cundall, P. A. (1994). A three dimensional particle flow code for block cave modeling. The Application of Numerical Modeling in Geotechnical Engineering. International Society for Rock Mechanics. South African National Group. Pretoria.

Harr, M. E. (1977). Elastic theory and continuum. In Mechanics of Particulate Media: A probabilistic Approach. McGraw-Hill, Inc.

Hart, R., Cundall, P. A., and Lemos, J. (1988). Formulation of a three-dimensional distinct element model – Part II: mechanical calculations for motion and interaction of a system composed of many polyhedral blocks. International Journal of Rock Mechanics, Mining Science and Geomechanics Abstracts. 25 (3):117-125.

Hitcher, P.-Y. (1996). Elastic properties of soils. Journal of Geotechnical Engineering. 122 (8):641-648.

Holubec, I. (1966). The yielding of cohesionless soils. PhD thesis. University of Waterloo.

Horne, M. R. (1965a). The behavior of an assembly of rotund, rigid, cohesionless particles. I, II. Proceedings of the Royal Society of London. Series A. 286: 62-78, 79-97

Horne, M. R. (1965b). The behavior of an assembly of rotund, rigid, cohesionless particles. III. Proceedings of the Royal Society of London. Series A. 310: 21-34.

Honda, T., T., Hibino, A., Takahashi, and Kuwano, J. (2001). Arching effects on the deformation of sandy ground induced by tunneling. Modern Tunneling Science and Technology, Adachi et al (eds.). Swets and Zeitlinger.

Imam, R. (1999). Modeling the constitutive behaviour of sand for the analysis of static liquefaction. PhD dessertation. Deptarment of Civil and Environmental Engineering, University of Alberta, Edmonton, Alberta, Canada.

Imamura, S., T. Nomoto, K. Mito, K., Ueno, and Kusakabe, O. (1996). Design and development of underground construction equipment in a centrifuge. Proceedings of International Symposium on

Geotechnical Aspects of Underground Construction in Soft Ground, London (eds R.J. Mari and R.N. Taylor), Balkema: 531-536.

Itasca Consulting Group, Inc, Minneapolis, Minnesota.

Iwashita, K. and Oda, M. (1998). Rolling resistance at contacts in simulation of shear band development by DEM. Journal of Engineering Mechanics. 124(3): 285-292.

Jensen, R. P., Bosscher, P. J., Plesha, M. E., and Edil, T. B. (1999). DEM simulation of granular media-structure interface: effects of surface roughness and particle shape. International Journal for Numerical and Analytical Methods in Geomechanics. (23):531-547.

Johnson, K. L. (1985). Contact mechanics. Cambridge University Press. London.

Kirkpatrick, W. M. and Belshaw, D. J. (1968). On the interpretation of triaxial tests. Geotechnique. 18(3): 336-350.

Kim, H. J. and Eisenstein, Z. (1998). Estimation of tunnel lining loads for tunnels in Edmonton. Proc. 51st Canadian Geotechnical Conference, Edmonton. 215-222. Bitech Publishers Ltd., Richmond.

Koerner, R. M. (1968). The behavior of cohesionless soils formed from various minerals. Ph.D thesis. Duke University.

Kuhn, M. R. (1999). Structured deformation in granular materials. Mechanics of Materials. 31: 407-429.

Kuhn, M.R. (1997). Deformation measures for granular materials. Mechanics of deformation and flow of particulate materials (eds. Ching S. Chang, Anil Misra, Robert Y. Liang and Marijan Babic). 91-104

Kolymbas, D. and Herle, I. (1998). Hypoplasticity: a framework to model granular materials. In Behavior of Granular Materials (ed. B. Cambou). SpringerWienNewYork.

Kovari, K. and Lunardi, P. (2000). On the observational method in tunneling. GeoEng2000: An International Conference on Geotechnical and Geological Engineering. Volume 1: Invited Papers. Melbourne, Australia.

Lade, P. V. (1977). Elasto-plastic stress-strain theory for cohesionless soil with curved yield surfaces. International Journal of Solids and Structures, 13: 1019-1036.

Lade, P. V. and Wang, Q. (2001b). Analyses of shear banding in true triaxial tests on sand. Journal of engineering mechanics. 127 (8):762-768.

Lamb, T. W. and Whitman, R. V. (1979). Soil mechanics: SI Version. John Wiley and Sons, New York.

Last, N.C. and Harkness, R. M. (1991). The explicit finite difference technique applied to geomechanics. Part I: Continua. Advanced Geotechnical Analysis. Developments in Soil Mechanics and Foundation Engineering-4. P.K. Banerjee and R. Butterfield (eds.). Elsevier Applied Science. London and New York.

Last, N.C. (1991). The explicit finite difference technique applied to geomechanics. Part II: Discontinua – the distinct element method. Advanced Geotechnical Analysis. Developments in Soil Mechanics and Foundation Engineering-4. P.K. Banerjee and R. Butterfield (eds.). Elsevier Applied Science. London and New York.

Leca, E. and Dormieux, L. (1990). Upper and lower bound solutions for the face stability of shallow circular tunnels in frictional material. Geotechnique. 40 (4):581-606.

Leca, E., Leblais, Y., and Kuhnhenn, K. (2000). Underground works in soils and soft rock tunneling. GeoEng2000: An International Conference on Geotechnical and Geological Engineering. Volume 1: Invited Papers. Melbourne, Australia.

Lee, K. L. and Seed, H. B. (1967). Drained strength characteristics of sands. Journal of the Soil Mechanics and Foundations Division (ASCE). SM 6:117-141.

Lin, X. and Ng, T.-T. (1997). A three-dimensional discrete element model using arrays of ellipsoids. Geotechnique. 47 (2):319-329.

Lorig, L. J., Board, M. P., Potyondy, D. O., and Coetzee, M. J. (1995). Numerical modeling of caving of using continuum and micro-mechanical models. CAMI'95: 3rd Canadian Conferences on Computer Applications in the Mineral Industry. Montreal, Quebec, Canada.

Lunardi, P. (2000). Design and construction of tunnels using the approach based on the analysis of controlled deformation in rocks and soils. Tunnels and Tunnelling International Special Supplement. May: 3-30.

Maconochie, D. J. and Suwansawat, S. (2001). Tunneling for the Chaloem Ratchamongkhon line in Bangkok. Proceedings 2001 of Rapid Excavation and Tunneling Conferenc (RETC). Society for Mining, Metallurgy, and Exploration. p 113-128

Mair, R. J. and Taylor, R. N. (1998). Theme lecture: Bored tunnelling in the urban environment. In Proceedings of the Fourteenth International Conference on Soil Mechanics and Foundation Engineering (Ed. Publications Committee of XIV ICSMFE). (4):2353–2385. A.A. Balkema, Rotterdam.

Masson, S. and Martinez, J. (2001). Micromechanical analysis of the shear behavior of a granular material. Journal of engineering mechanics. 127 (10): 1007-1016.

Mindlin, R.D. (1949). Compliance of elastic bodies in contact. Journal of Applied Mechanics, Transaction ASME. 71: 259-268.

Mindlin, R.D. and Deresiewicz, H. (1953). Elastic spheres in contact under varying oblique forces. ASME Journal of Applied Mechanics. 20: 327-344.

Mirghasemi, A. A., Rothenburg, L., and Matyas, E. L. (2002). Influence of particle shape on engineering properties of assemblies of two-dimensional polygon-shaped particles. Geotechnique. ?

Misra, A. (1995). Interfaces in particulate materials. Mechanics of Geometrical Interfaces. A.P.S. Selvadurai and M.J. Boulon (eds.). Elsevier Science: 513-536.

Moh, Z. C., Ju, D.H., and Hwang, R. N. (1996). Ground movements around tunnels in soft ground. Proceedings of International Symposium on Geotechnical Aspects of Underground Construction in Soft Ground, London (eds R.J. Mari and R.N. Taylor), Balkema: 725-730.

Mustoe, G. G. W., Williams, J. R., and Hocking, G. (1987). The discrete element method in geotechnical engineering. Developments in Soil Mechanics and Foundation Engineering-4: Dynamic Behavior of Foundations and Buried Structures. P.K. Banerjee and R. Butterfield (eds.). Elsevier Applied Science. London and New York.

Ng, T.-T. (2004). Triaxial simulations using DEM with hydrostatic boundaries. Journal of Engineering Mechanics. ASCE, 130(10).

Ni, Q. (2003). Effects of particle properties and boundary conditions on soil shear behaviour: 3-D numerical simulations. PhD thesis. University of Southhampton. UK.

Ni, Q., Powrie, W., Zhang, X., and Harkness, R. (2000). Effect of particle properties on soil behavior: Three-dimensional numerical modeling of shearbox tests. Numerical Methods in Geotechnical Engineering (eds. George M. Filz and D.V. Griffiths). Geotechnical Special Publication No. 96 (ASCE).

Nomoto, T., S., Imamura, T., Hagiwara, O., Kusakabe, O. and Fujii, N. (1999). Shield tunnel construction in centrifuge. Journal of Geotechnical and Geoenvironmental Engineering. 125 (4). 289-300.

Nomoto, T., K., Mito, S., Imamura, K., Ueno, K., and Kusakabe, O. (1996). Centrifuge modelling of construction processes of shield tunnel. Proceedings of International Symposium on Geotechnical Aspects of Underground Construction in Soft Ground, London (eds R.J. Mari and R.N. Taylor), Balkema: 567-572.

Norris, G. M. (1977). The drained shear strength of uniform quartz sand as related to particle size and natural variation in particle shape and surface roughness. Ph.D thesis. University of California, Berkeley.

Oda, M. (1997). A micro-deformation model for dilatancy of granular materials. Mechanics of deformation and flow of particulate materials (eds. Ching S. Chang, Anil Misra, Robert Y. Liang and Marijan Babic). 24-37.

Oda, M. (1977). Coordination number and its relation to shear strength of granular material. Soils and Foundations. 17 (2): 29-42.

Oda, M. (1972). Initial fabrics and their relations to mechanical properties of granular material. Soils and Foundations. 12 (1): 17-36.

Oda, M., Konishi, J., and Nemat-Nasser, S. (1982). Experimental micromechanical evolution of strength of ganular materials: effects of particle rolling. Mechanics of Materials. 1: 269-283.

Oda, M., Konishi, J., and Nemat-Nasser, S. (1980). Some experimentally based fundamental results on the mechanical behavior of granular materials. Geotechnique. 30(4): 479-495.

Oda, M. and Iwashita, K. (2000). Study on couple stress and shear band development in granular media based on numerical simulation analyses. International Journal of Engineering Science. 38:1713-1740.

O'Reilly, M. P. and New, B. M. (1982). Settlements above tunnels in the United Kingdom – their magnitude and prediction. Tunnelling 82, London, IMM: 173-181.

O'Sullivan, C., Bray, J. D., and Riemer, M. F. (2002). Influence of particle shape and surface friction variability on response of rod-shaped particulate media. Journal of Engineering Mechanics. 128 (11):1182-1192.

Panet, M. and Guenot, A. (1982). Analysis of convergence behind the face of a tunnel. Proceedings of Tunnelling 82, Institution of Mining and Metallurgy, London: 197-204.

Parry, R. H. G. (2000). Shear strength of geomaterials – A brief historical perspective. GeoEng2000: An International Conference on Geotechnical and Geological Engineering. Volume 1: Invited Papers. Melbourne, Australia.

Peck, R. B. (1969). Deep excavations and tunnelling in soft ground. Proceedings of 7th International Conference Soil Mechanics and Foundation Engineering, Mexico City, State of the Art Volume: 225-290.

Potts, D. M. and Addenbrooke, T. I. (1997). A structure's influence on tunnelling-induced ground movements. Proceedings of Institution of Civil Engineers, Geotechnical Engineering. 125(4): 109-125.

Proctor, D. C. and Barton, R. R. (1974). Measurements of the angle of interparticle friction. Geotechnique. 24 (4):581-604.

Proctor, R. V. and White, R. L. (1946). Rock tunneling with steel supports Youngstown, Ohio, Commercial Shearing and Stamping Co. Harvard soil mechanics series, 25.

Rodriquez-Roa, F. (2002). Ground subsidence due to shallow tunnel in dense sandy gravel. Journal of Geotechnical and Geoenvironmental Engineering. 128 (5):426-434.

Rowe, P. W. (1962). The stress-dilatancy relation for static equilibrium of an assembly of particles in contact. Proceedings of the Royal Society of London. Series A. 269: 500-527.

Rowe, P. W. and Barden, L. (1964). ASCE Journal of Soil Mechanics and Foundation Engineering. 90(SM 1): 1-27.

Rowe, R. K., Lo, K. Y., and Kack, G. J. (1983). A method of estimating surface settlement above tunnels constructed in soft ground. Canadian Geotechnical Journal. 20(8): 11-22.

Rutledge, P. C. (1947). Cooperative triaxial shear research program. Progress Report on Soil Mechanics Fact Finding Survey, USAE, Waterways Experiment Station, Vicksburg, Miss.

Saada, A. S. and Townsend, F. C. (1981). State of the art: Laboratory strength testing of soils. Laboratory Shear Strength of Soil (eds. R. N. Yong and F. C. Townsend). ASTM STP 740: 7-77.

Sagaseta, C. (1998). On the role of analytical solutions for the evaluation of soil deformation around tunnels. Proceedings of the 4th European Conference on Numerical Methods in Geotechnical Engineering – NUMGE98 (ed. Annamaria Cividini): 3-24.

Sagaseta, C. (1987). Analysis of undrained soil deformation due to ground loss. Geotechnique. 37(3): : 301-320.

Sagaseta, C. (1992). Soil properties and their measurement. Predictive Soil Mechanics. Predictive Soil Mechanics. Proceedings of the Wroth Memorial Symposium. St Catherine's College, Oxford. G.T. Houlsby and A.N. Schofield (eds.).

Salgado, R., Bandini, P., and Karim, A. (2000). Shear Strength and Stiffness of Silty Sand. Journal of Geotechnical and Geoenvironmental Engineering. 126 (5):451-462.

Santamaria, J. C. (2001). Soils and Waves: Particulate Materials Behavior, Characterization and Process Monitoring, John Wiley and Sons, Ltd, England.

Satake, M. (1993). New formulation of graph-theoretical approach in the mechanics of granular materials. Mechanics of Materials. 16: 65-72.

Satake, M. (1992). A discrete-mechanical approach to granular materials. International Journal of Engineering Science. 30(10): 1525-1533.

Satake, M., Chang, C.S., and Tobita, Y. (1999). Fundamentals for mechanics of granular materials. In Mechanics of Granular Materials: an introduction (eds. M. Oda and K. Iwashta). A.A.Balkema/Rotterdam/Brookfield.

Schanz, T. and Vermeer, P.A. (1998). On the stiffness of sands. Prefailure Deformation Behavior of Geomaterials. Geotechnique Symposium:383-387.

Schmidt, B. (1969). Settlements and ground movements associated with tunnelling in soils, PhD Thesis, University of Ilinois, Urbana.

Schuller, H. and Schweiger, H. F. (1999). Application of Multilaminate Model for Shallow Tunnelling. FELSBAU. 17 (1): 44-47.

Scott, R. F. (1987a). Failure. Geotechnique. 37 (4): 423-466.

Scott, R. F. (1987b). Constitutive relations for soil: present and future. Proceedings of the International Workshop on Constitutive Equations for Granular Non-cohesive Soils (eds. A. Saada.and G. Biancini). A.A.Balkema/Totterdam/Brookfield: 723-725.

Shin, J. H., Potts, D. M., and Zdravkovic, L. (2002). Three-dimensional modelling of NATM tunnelling in decomposed granite soil. Geotechnique. 52 (3):187-200.

Shirlaw, J. N., Ong, J. C. W., Rosser, H. B., Tan, C. G., Osborne, N. H., and Heslop, P. E. (2003). Local settlements and sinkholes due to EPB tunnelling. *Proceedings of the Institution of Civil Engineers: Geotechnical Engineering*. 156 (4): 193-211

Sitharam, T. G., Dinesh, S. V., and Shimizu, N. (2002). Micromechanical modeling of monotonic drained and undrained shear behavior of granular media using three-dimensional DEM. International Journal for Numerical and Analytical Methods in Geomechanics. (26):1167-1189.

Sitharam, T. G. and Nimbkar, M. S. (2000). Micromechanical modeling of granular materials: effect of particle size and gradation. Geotechnical and Geological Engineering. (18):91-117. Kluwer Academic Publishers, Netherlands.

Suiker, A. S. J., de Borst, R., and Chang, C. S. (2000). Micro-mechanically based higher-order continuum models for granular materials. Constitutive Modelling of Granular Materials (ed. Dimitrios Kolymbas). Springer.

Swoboda, G. (1979). Finite element analysis of the New Austrian Tunnelling Method (NATM). Proceedings of 3rd International Conference on Numerical Methods In Geomechanics, Aachen. 2: 581-586.

Taylor, D. W. (1941). Seventh progress report on shear research to U.S. engineers. MIT Publication. Massachusetts Institute of Technology, Cambridge, Mass.

Taylor, R. N. (1998). Modelling of tunnel behviour. Geotechnical Engineering (Proceedings of the Institution of Civil Engineers). 131:127-132.

Taylor, R. N. (1995). Buried structures and underground excavations. Geotechnical Centrifuge Technology (ed. R.N. Taylor). Blackie Academic and Professional.

Terzaghi, K. (1950). Geologic aspects of soft ground tunneling, Chap. 2. Applied Sedimentation. Parker D. Trask (ed.). Wiley, New York. 193-209.

Terzaghi, K. (1946). Rock defects and loads on tunnel supports. In R. V. Proctor and T.L. White. Rock Tunnelling with Steel Supports. Youngstown, Ohio, Commercial Shearing and Stamping Co., Section 1: 17-99. Harvard soil mechanics series, 25.

Thomas, P. A. and Bray, J. D. (1999). Capturing nonspherical shape of granular media with disk clusters. Journal of Geotechnical and Geoenvironmental Engineering. 125 (3):169-178.

Thornton, C. (2000). Numerical simulations of deviatoric shear deformation of granular media. Geotechnique. 50 (1):43-53.

Tordesillas, A., Peters, J. F. and Gardiner, B. S. (2004). Insights into 1D localisation theory and micromechanical constitutive laws. Geotechnique, 54 (00):1-4

Tweedie, R. W., Bean, S. M., Thompson, S., and Eisenstein, Z. (1991). Stability of the north slope and portal at the Edmonton Light Rail Transit crossing of the North Saskatchewan River. *Canadian Geotechnical Conference*, n pt 2, 1991, p 85/1-85/9

Vardoulakis, I. and Drescher, A. (1985). Behavior of granular soil specimens in the triaxial compression test. Stress-Strain Modeling of Soils (eds. P. K. Banerjee and R. Butterfield). Developments in Soil Mechanics and Foundation Engineering – 2. Elsevier Applied Science Publishers.

Vermeer, P. A. (1978). A double hardening model for sand. Geotechnique, 28 (4): 413-433.

Vermeer, P. A. and Ruse, N. 2000. Face stability when tunnelling in soil and homogeneous rock. Developments in Theoretical Geomechanics, Smith and Carter (eds.).

Verruijt, A. and Booker, J. R. (1996). Surface settlements due to deformation of a tunnel in an elastic half plane. Geotechnique. 46 (4): 753-756.

Wang, Q. and Lade, P. V. (2001a). Shear banding in true triaxial tests and its effects on failure of sand. Journal of engineering mechanics. 127 (8):754-761.

Washuta, A. and Martin, C. (2004). Design and contracting strategy for a short tunnel in mixed ground conditions. Proceedings of the 18th Tunneling Association of Canada (TAC) conference, Edmonton, Alberta, Canada.

APPENDIX A

Measurement of Particle Rotation

1. Rotational Velocity: x-component

Middle-third Particles **Top Particles**

Axial Strain: 0.5 %

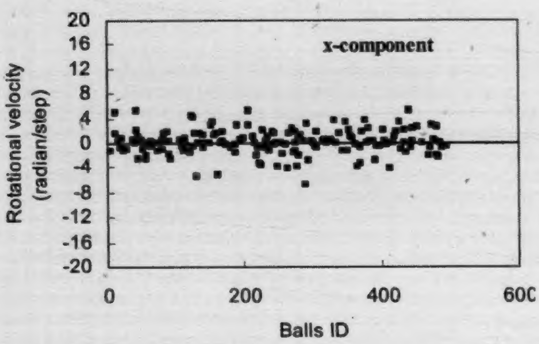

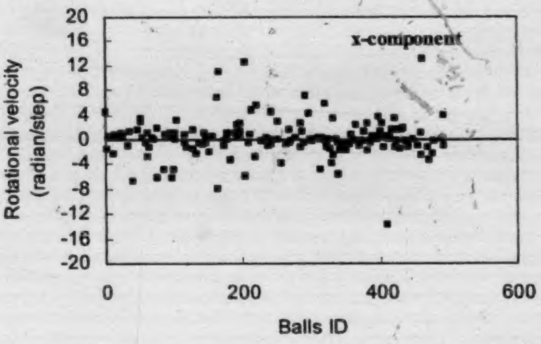

Axial Strain: 1.0 %

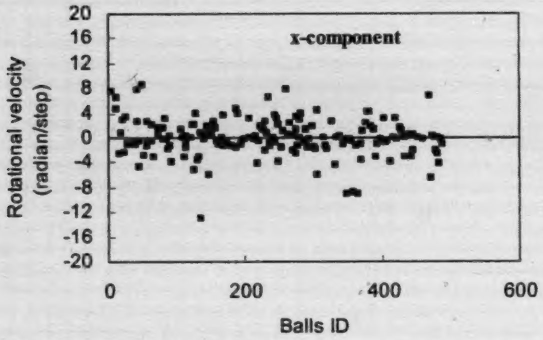

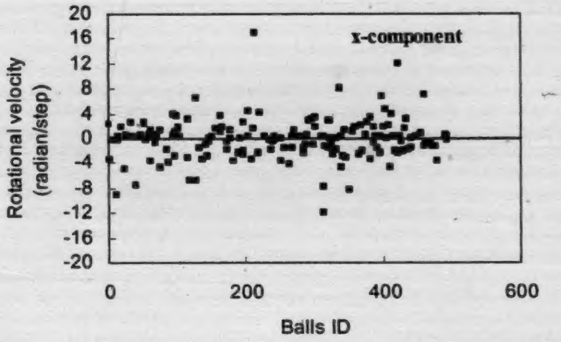

Axial Strain: 2%

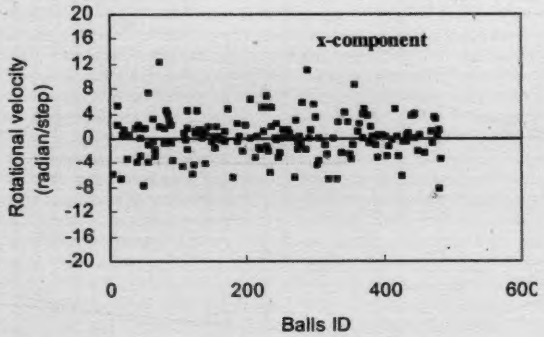

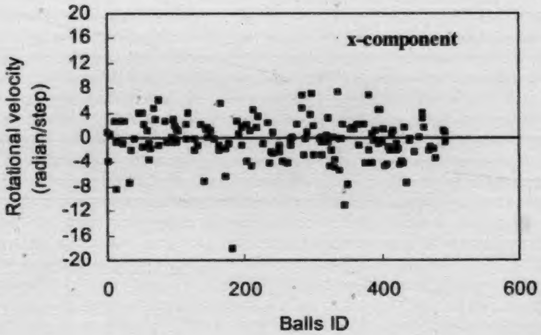

Middle-third Particles **Top Particles**

Axial Strain: 4%

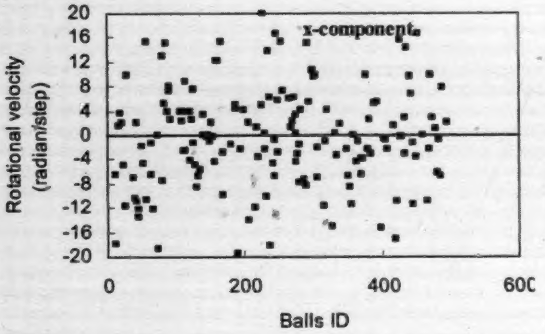

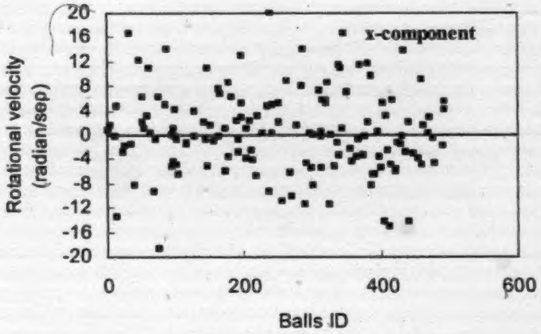

Axial Strain: 10%

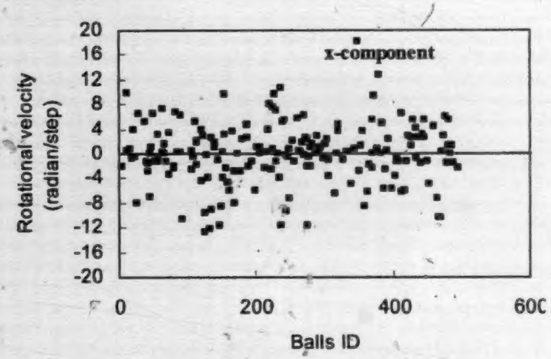

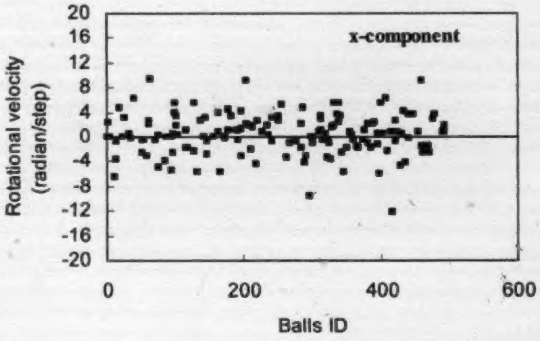

2. Rotational Velocity: y-component

Axial Strain: 0.5 %

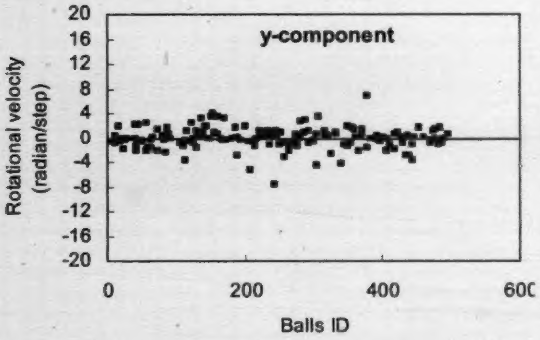

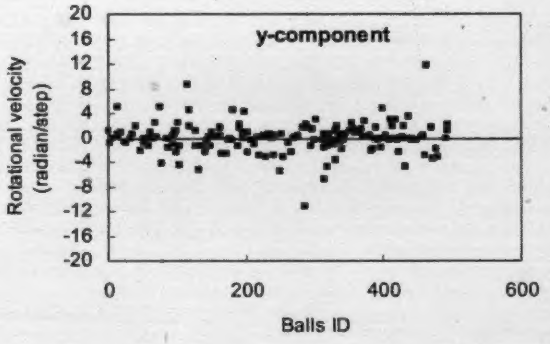

Middle-third Particles **Top Particles**

Axial Strain: 1 %

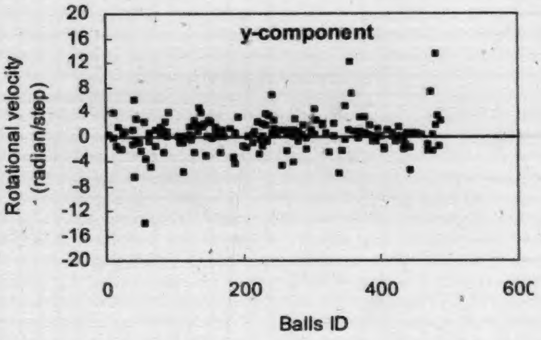

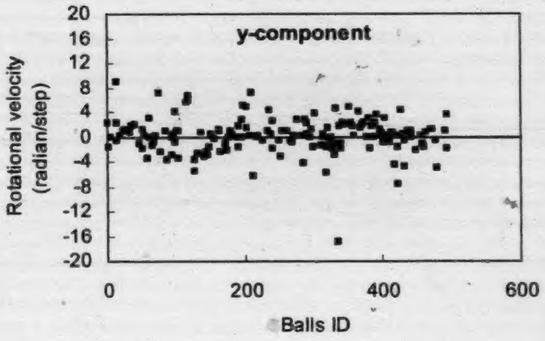

Axial Strain: 2 %

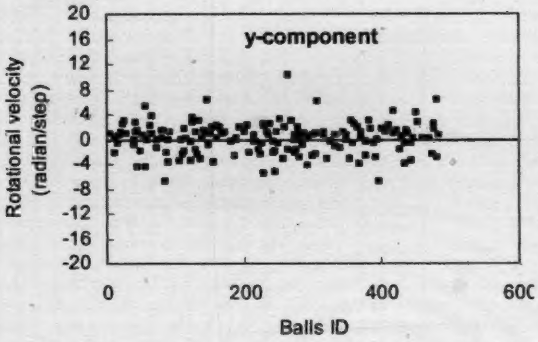

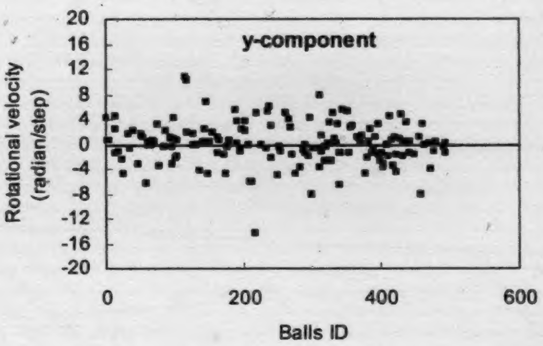

Axial Strain: 4 %

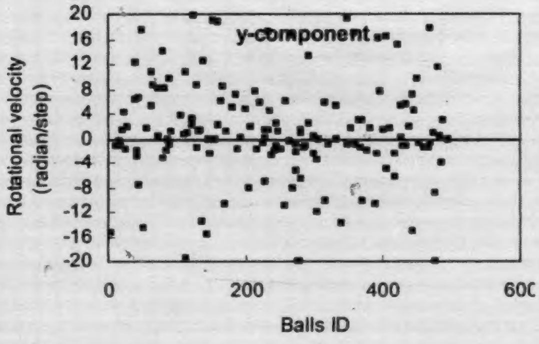

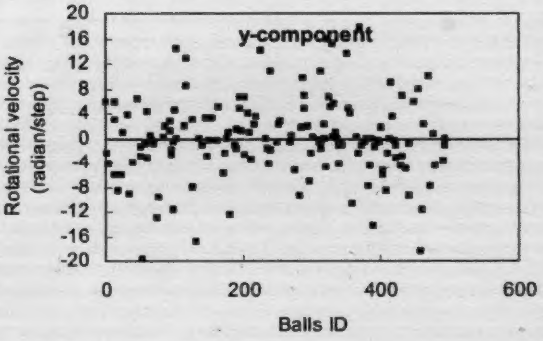

Middle-third Particles **Top Particles**

Axial Strain: 10 %

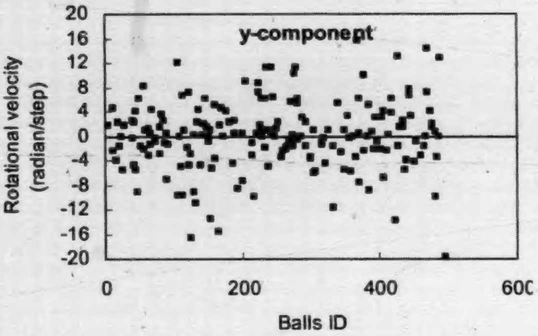

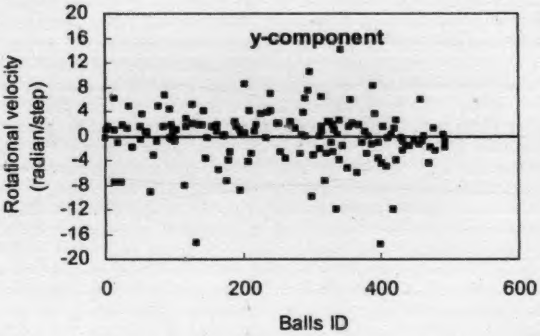

3. Rotational Velocity: z-component

Axial Strain: 0.5 %

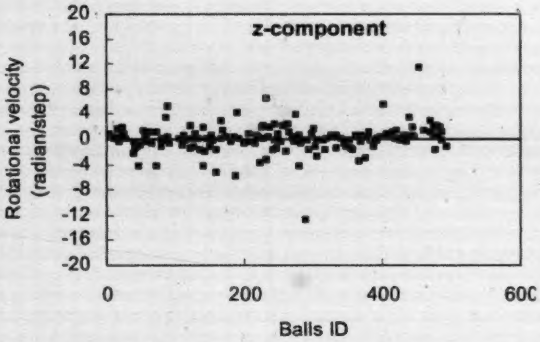

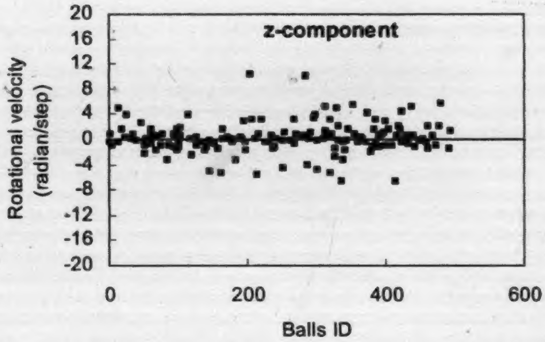

Axial Strain: 1 %

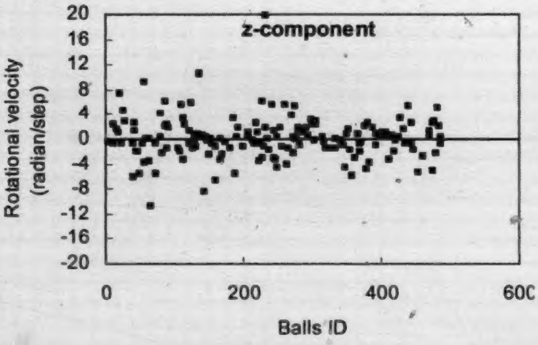

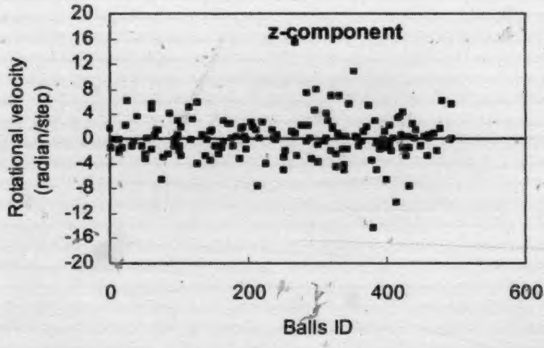

APPENDIX B

Measurement of Failure Zone (C/D=2.0)

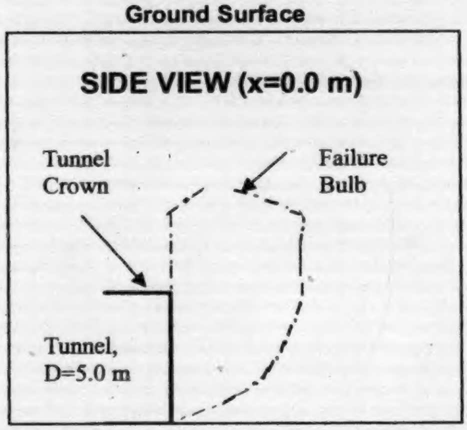
Ground Surface
SIDE VIEW (x=0.0 m)
Tunnel Crown
Failure Bulb
Tunnel, D=5.0 m

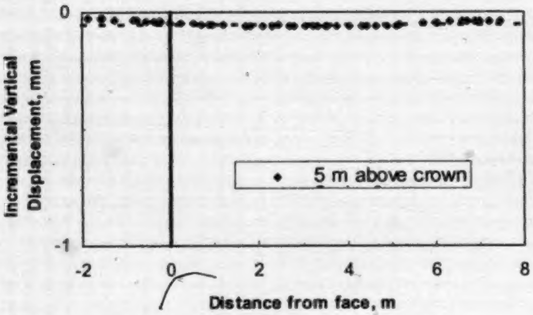

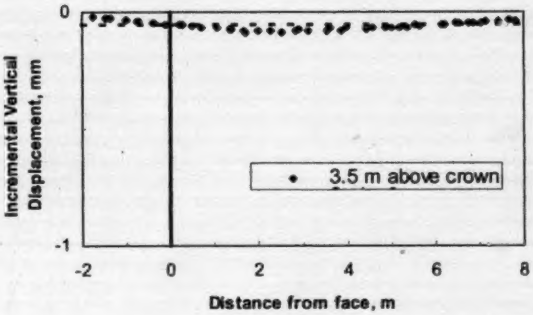

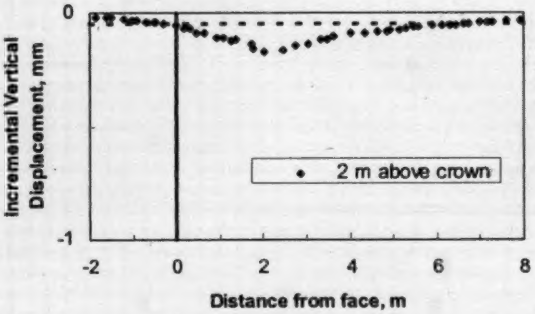

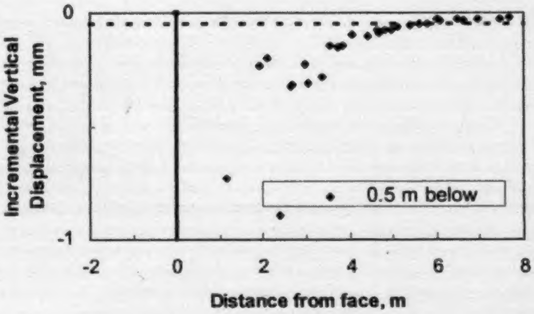

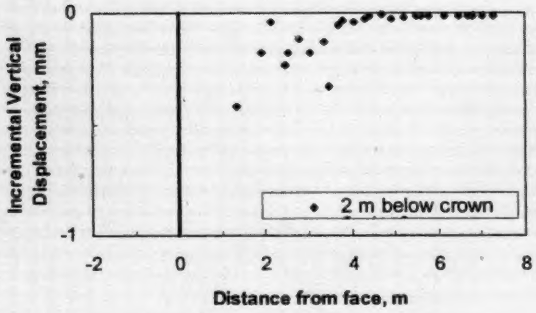
0
-1
Incremental Vertical Displacement, mm
2 m below crown
-2
0
2
4
6
8
Distance from face, m

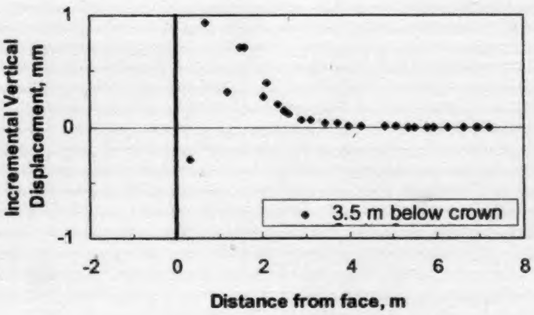
1
0
-1
Incremental Vertical Displacement, mm
3.5 m below crown
-2
0
2
4
6
8
Distance from face, m

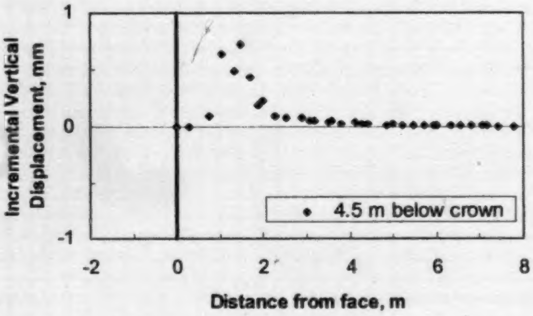
1
0
-1
Incremental Vertical Displacement, mm
4.5 m below crown
-2
0
2
4
6
8
Distance from face, m

Measurement of Failure Zone (C/D=0.5)

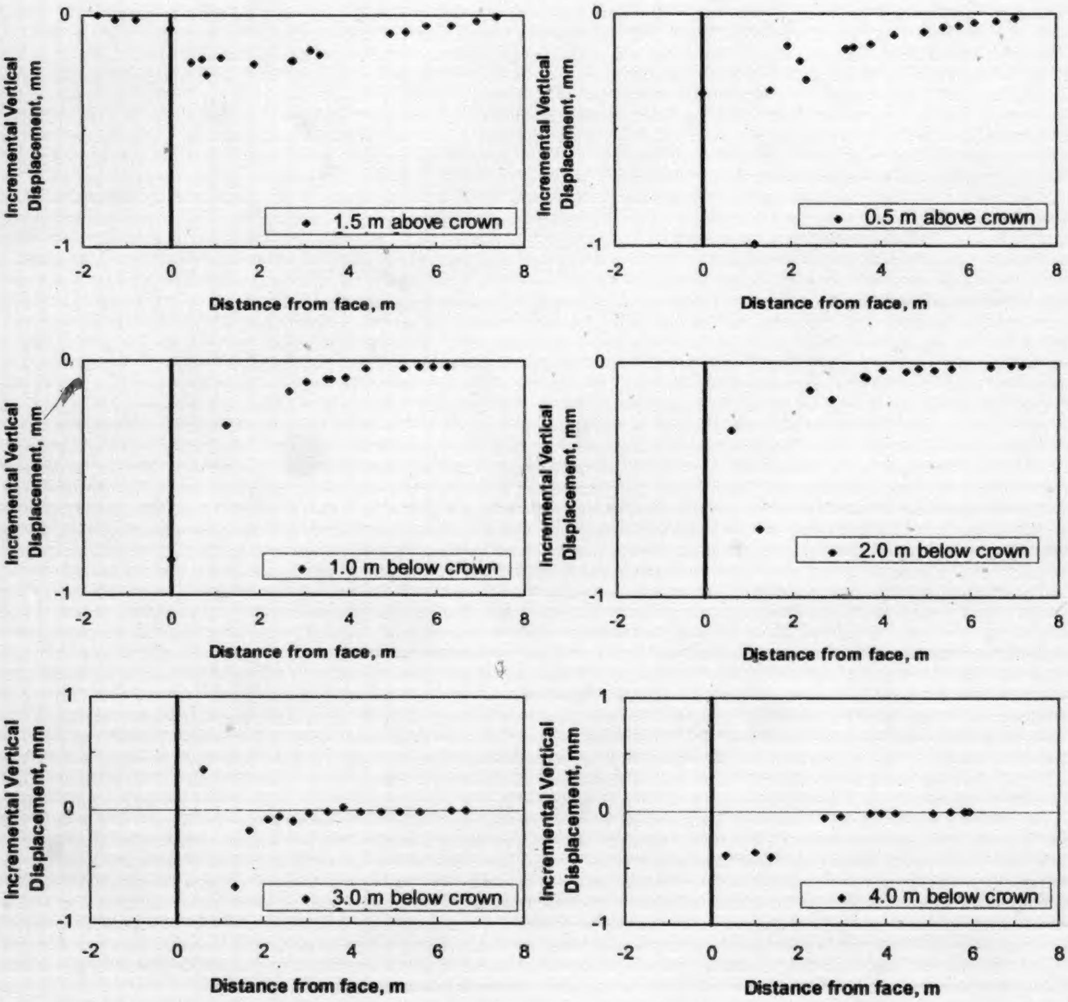

APPENDIX C

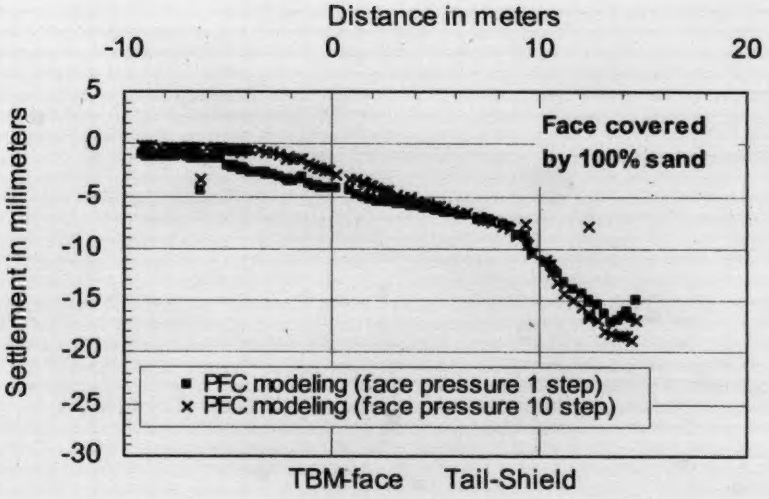
Distance in meters
-10
0
10
20
Settlement in milimeters
5
0
-5
-10
-15
-20
-25
-30
Face covered by 100% sand
■ PFC modeling (face pressure 1 step)
× PFC modeling (face pressure 10 step)
TBM-face
Tail-Shield

Figure C1

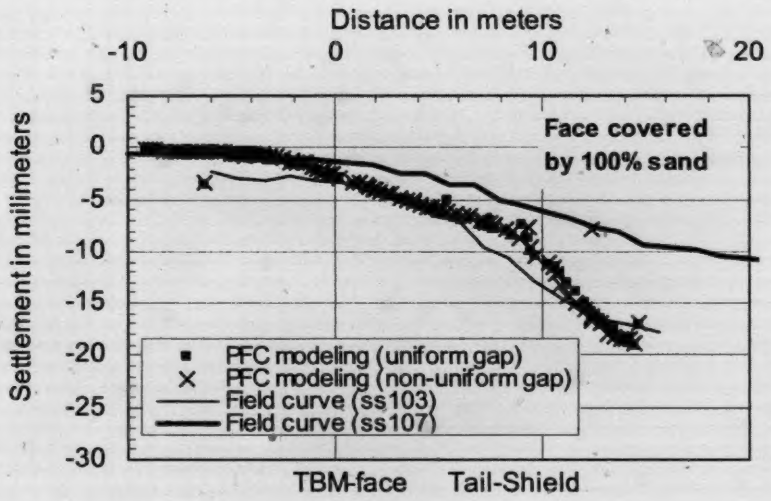
Distance in meters
-10
0
10
20
5
0
-5
-10
-15
-20
-25
-30
Settlement in milimeters
Face covered by 100% sand
■ PFC modeling (uniform gap)
× PFC modeling (non-uniform gap)
Field curve (ss103)
Field curve (ss107)
TBM-face
Tail-Shield

Figure C2

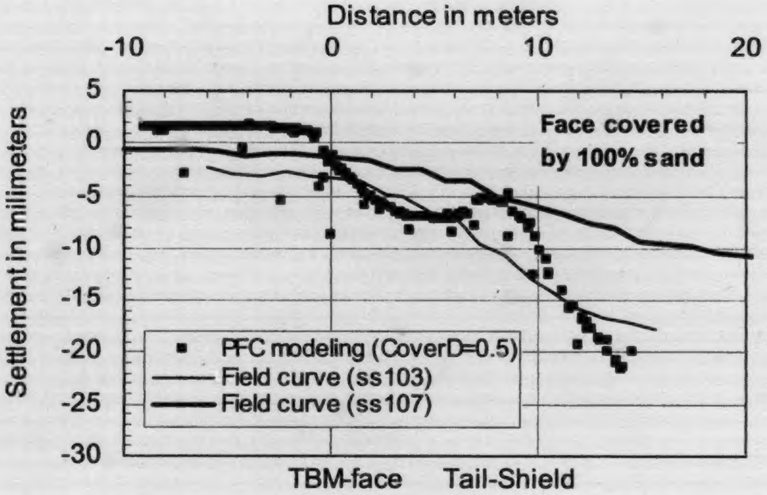
Distance in meters
-10
0
10
20
5
0
-5
-10
-15
-20
-25
-30
Settlement in milimeters
Face covered by 100% sand
PFC modeling (CoverD=0.5)
Field curve (ss103)
Field curve (ss107)
TBM-face
Tail-Shield

Figure C3